PB87-133252

Boundary-Layer Computational Model for Predicting the Flow and Heat Transfer in Sudden Expansions

Iowa State Univ., Ames

Prepared for

National Aeronautics and Space Administration
Washington, DC

Jul 86

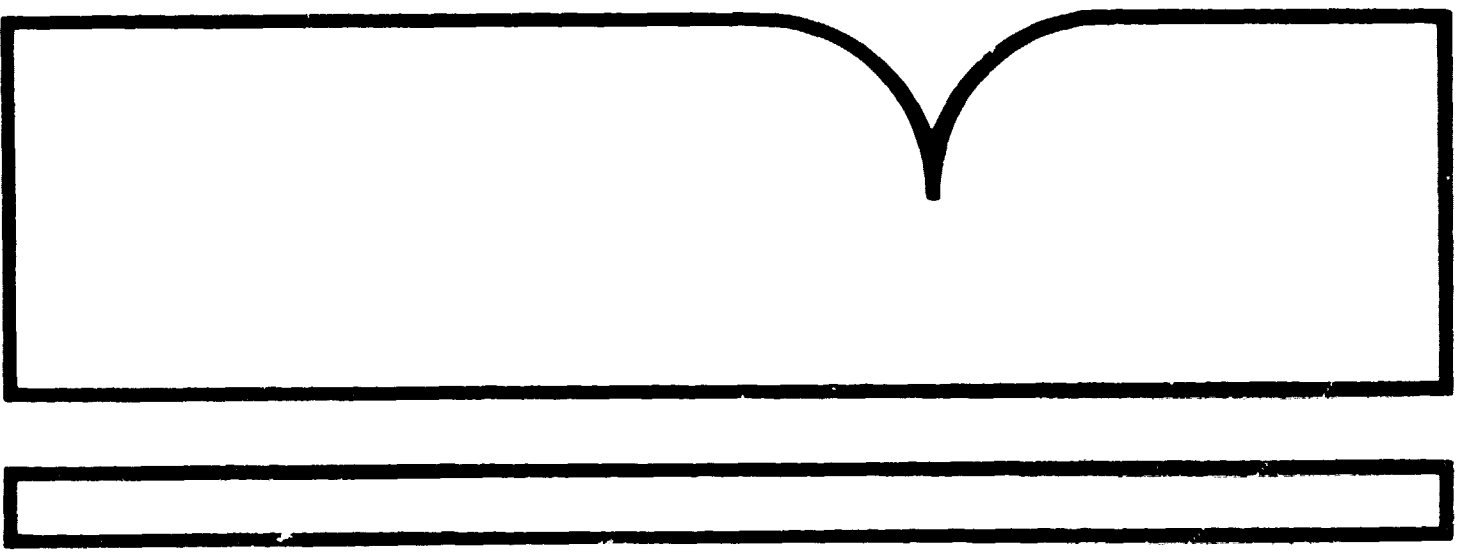

PB87-133252

J. P. Lewis R. H. Pletcher

A Boundary-Layer Computational Model for Predicting the Flow and Heat Transfer in Sudden Expansions

July 1986
National Science Foundation

National Aeronautics and Space Administration
HTL-41, CFD-14
ISU-ERI-Ames-87018

technical report

College of Engineering
Iowa State University

50272-101

REPORT DOCUMENTATION PAGE

1. REPORT NO. ISU-ERI-AMES-87018

2.

3. Recipient's Accession No. PB87 133252/AS

4. Title and Subtitle

A Boundary-Layer Computational Model for Predicting the Flow and Heat Transfer in Sudden Expansions

5. Report Date July 1986

6.

7. Author(s) J. P. Lewis and R. H. Pletcher

8. Performing Organization Rept. No.

9. Performing Organization Name and Address
Department of Mechanical Engineering
Engineering Research Institute
Iowa State University
Ames, IA 50011

10. Project/Task/Work Unit No.

11. Contract(C) or Grant(G) No.
(C) NSF CBT-8211713
(G) NASA NGT-016-002-801

12. Sponsoring Organization Name and Address
National Science Foundation
Division of Engineering
Washington, D.C. 20550

National Aeronautics and Space Administration
Washington, D.C. 20546

13. Type of Report & Period Covered
Technical

14.

15. Supplementary Notes

16. Abstract (Limit: 200 words)

Fully developed turbulent and laminar flows through symmetric planar and axisymmetric expansions with heat transfer were modeled using a finite-difference discretization of the boundary-layer equations. By using the boundary-layer equations to model separated flow in place of the Navier-Stokes equations, computational effort was reduced permitting turbulence modeling studies to be economically carried out. For laminar flow, the reattachment length was well predicted for Reynolds numbers as low as 20 and the details of the trapped eddy were well predicted for Reynolds numbers above 200. For turbulent flows, the Boussinesq assumption was used to express the Reynolds stresses in terms of a turbulent viscosity. Near-wall algebraic turbulence models based on Prandtl's-mixing-length model and the maximum Reynolds shear stress were compared. The near-wall models were used with the standard high-Reynolds-number k-ε turbulence model. A low turbulent-Reynolds-number k-ε model was also investigated but found to be unsuitable for separated flow. The maximum-shear-stress near-wall model gave better predictions than the Prandtl-mixing-length models, especially for heat transfer. The predicted turbulent heat transfer is primarily dependent on the turbulence model used in the near-wall region.

17. Document Analysis a. Descriptors

Viscous flow
Heat transfer
Turbulence modeling
Separated flow

b. Identifiers/Open-Ended Terms

Finite-difference methods

c. COSATI Field/Group

18. Availability Statement
No restriction on distribution. Available from National Technical Information Service, Springfield, Virginia 22161

19. Security Class (This Report) Unclassified

20. Security Class (This Page) Unclassified

21. No. of Pages 235

22. Price

(See ANSI-Z39.18) See Instructions on Reverse

OPTIONAL FORM 272 (4-77)
(Formerly NTIS-35)
Department of Commerce

TABLE OF CONTENTS

LIST OF TABLES

LIST OF FIGURES

ABSTRACT

Fully developed turbulent and laminar flows through symmetric planar and axisymmetric expansions with heat transfer were modeled using a finite-difference discretization of the boundary-layer equations. By using the boundary-layer equations to model separated flow in place of the Navier-Stokes equations, computational effort was reduced permitting turbulence modeling studies to be economically carried out. The continuity and momentum equations were solved in a coupled manner. The validity of the once-through calculation scheme utilizing the FLARE approximation was studied by using a multiple sweep procedure in which the FLARE approximation is removed after the first sweep.

For laminar constant property flow, the equations were nodimensionalized so that the solution was independent of Reynolds number. Two different dependent hydrodynamic variable sets were tried: the primitive variable set (u-v), and the streamwise velocity stream function variable set (u-ψ). The predictions of the boundary-layer equations were identical regardless of the variable set used. The predictions of the boundary-layer equations for parameters associated with the trapped eddy compared well with the predictions of the Navier-Stokes equations and experimental measurements for laminar isothermal flow when the Reynolds number was above 200 and the ratio of inlet to outlet channel diameter(width) was less than 1/3. The reattachment length and the flow field outside of the trapped eddy were well predicted for Reynolds numbers as low as twenty for laminar flow.

The Boussinesq assumption was used to express the Reynolds stresses in terms of a turbulent viscosity. Near-wall algebraic turbulence models based on Prandtl's-mixing-length model and the maximum Reynolds shear stress were compared. The near-wall models were used with the standard high-Reynolds-number k-ε turbulence model. A low-turbulent-Reynolds-number k-ε model was also investigated but found to be unsuitable for separated flow. The maximum-shear-stress near-wall model gave better predictions than the Prandtl-mixing-length models, especially for heat transfer. The predicted turbulent heat transfer is primarily dependent on the turbulence model used in the near-wall region. Globally iterating over the flow field had a more pronounced effect on the heat transfer solution than on the hydrodynamic solution.

NOMENCLATURE

A_j, a_j	coefficients appearing in the finite-difference expressions
A^+	empirical constant used in turbulence modeling
[A]	2×2 coefficient matrix (Eq. 3.21, Eq. 3.42)
B_j, b_j	coefficients appearing in the finite-difference expressions
[B]	2×2 coefficient matrix (Eq. 3.21, Eq. 3.42)
BL	boundary-layer equations
c	FLARE constant
c_f	skin-friction coefficient ($= 2\tau_w/(\rho u_i^2)$)
C_j, c_j	coefficients appearing in the finite-difference expressions
$c_\mu, c_D, c_1, c_2, c_3, c_4, c_{\theta 1}, c_{\theta 2}, c_{\theta 1w}, c_w$	turblence modeling constants (Table 2)
c_p	specific heat
{C}	2×1 matrix (Eq. 3.21, Eq. 3.42)
d	inlet plate spacing or inlet pipe diameter
D	outlet plate spacing or outlet pipe diameter, van Driest damping function (Eq. 2.57), diffusion difference operator (Eq. 3.10)
D_j, d_j	coefficients appearing in the finite-difference expressions
D_{15}	modified van Driest damping function (based on $A^+ = 15$)
[D]	2×2 coefficient matrix (Eq. 3.21, Eq. 3.42)
E_j, e_j	coefficients appearing in the finite-difference expressions
FDE	finite-difference equation
h	step height (except for Eq. 2.23 where it is the enthalpy)

H	total enthalpy (Eq. 2.23)
H_j	coefficient appearing in the finite-difference expressions
k	turbulent kinetic energy (Eq. 2.67), thermal conductivity coefficient
k_t	effective turbulent thermal conductivity coefficient
ℓ	turbulent length scale (= κDy)
ℓ_r	reattachment length
L	turbulent length scale (Eq. 2.68)
NJ	j-index corresponding to the centerline
Nu_i	Nusselt number based on inlet diameter
Nu_o	Nusselt number based on outlet diameter
Nu_{db}	$0.023\ Re_o^{0.8}\ Pr^{0.4}$
NS	Navier-Stokes equations
p	pressure
P	production of turbulent kinetic energy (= $\mu_t/\rho(\partial u/\partial y)^2$)
Pe	Peclet number (Re × Pr)
Pr	Prandtl number
Pr_t	turbulent Prandtl number
q	heat flux rate
Q	dimensionless heat flux rate (Eq. 2.51)
r	distance from the centerline
r_o	outlet channel radius
R	dimensionless distance from the centerline (= r/d)
Re	Reynolds number (= $\rho u_i d/\mu$)
Re_h	Reynolds number based on the step height (= $\rho u_i h/\mu$)

S_ϕ	source term (Table 4)
$S_{\phi,c}, S_{\phi,d}$	see Eq. (3.32)
St	Stanton number
T	temperature
T_b	bulk temperature
TE	truncation error
u_i	average inlet velocity in the x-direction
u_c	collision velocity (Eq. 2.34)
U	dimensionless velocity (= u/u_i)
u^+	dimensionless velocity (= u/u_τ)
u_τ	turbulent velocity scale (= $(\tau_w/\rho)^{1/2}$)
$-\overline{u'v'}_m$	maximum Reynolds stress at a given x-position
{U}	2×1 unknown matrix (Eq. 3.21, Eq. 3.42)
v	velocity in the y-direction
V	velocity vector
x	distance from the step (Fig. 2)
X	dimensionless distance from the step (= x/(d Re))
X_r	dimensionless reattachment length
Δx_+	$x^{i+2} - x^{i+1}$
Δx_-	$x^{i+1} - x^i$
ΔX_-	$X^{i+1} - X^i$
y	distance from the wall (Fig. 2)
Y	dimensionless distance from the wall (= y/d)
y^+	dimensionless distance from the wall (= $yu_\tau\rho/\mu$)
Δy_+	$y_{j+1} - y_j$

Δy_- $y_j - y_{j-1}$

ΔY_+ $Y_{j+1} - Y_j$

ΔY_- $Y_j - Y_{j-1}$

Greek symbols

α turbulence modeling constant (Table 2)

β dimensionless pressure gradient (Eq. 2.43b)

γ turbulence modeling constant (Table 2)

Γ_ϕ surrogate symbol (Table 4)

δ^* displacement thickness

δ_y central difference operator (Eq. 3.8)

ψ stream function

Ψ dimensionless stream function ($= \psi_{cp}/(d^{1+m}u_i)$)

ε dissipation rate of turbulent kinetic energy

η dimensionless total enthalpy ($= H/u_i^2$)

ζ coordinate having equal grid spacing

$\Delta\zeta$ $\zeta_j - \zeta_{j-1}$

κ von Karman constant ($= 0.41$)

μ viscosity

μ_t turbulent viscosity (Eq. 2.18)

ρ density

τ shear stress

ϕ surrogate symbol for variables

χ $-dp/dx$

ω vorticity

Subscripts

b	bulk
cp	constant property
e	edge of the boundary layer
i	inlet
j	y-index
min	minimum
max	maximum
o	outlet
r	reattachment
w	wall

Superscripts

i	x-index
m	constant (= 1 if axisymmetric; = 0 if 2-D planar)
$( )'$	instantaneous variation from a mean turbulent quantity (Eq. 2.2)
$( )''$	instantaneous variation from a mass averaged quantity (Eq. 2.7)
$( )^{*}$	designates a modified coefficient
$(\bar{})$	time averaged turbulent quantity (Eq. 2.3)
$(\tilde{})$	mass averaged turbulent quantity (Eq. 2.8)
$(\hat{})$	provisional variable used in Newton linearization

I. INTRODUCTION

A. Overview of Separated Flow

Flow with separation is often encountered in fluid mechanics. Separation can occur due to adverse pressure gradients, as on the upper surface of an airfoil that has "stalled" or in a pipe with a sudden expansion or contraction. This latter type of separation occurs in engineering practice in heat exchangers and combustion chambers. The flow separation causes a region of flow reversal immediately downstream of the expansion that is sometimes referred to as a trapped eddy or trapped vortex due to its "swirling" nature. The region of flow reversal caused by the the flow separation can have an important effect on the flow field.

Figure 1 introduces the physical nature of reattaching flow. The boundary layer at the step develops into a shear layer which has high levels of shearing stress. The recirculation region develops behind the face of the expansion. The streamline that divides the recirculating region from the rest of the flow is called the dividing streamline. The point where the dividing streamline meets the wall is called the point of reattachment. For "steady" turbulent flow, the point of reattachment varies with time due to large turbulent eddies in the shear layer [1]. Thus, for turbulent flow, it may be more appropriate to define a reattachment region that extends 20% of the reattachment length on both sides of the average distance to reattachment [2]. After reattachment,

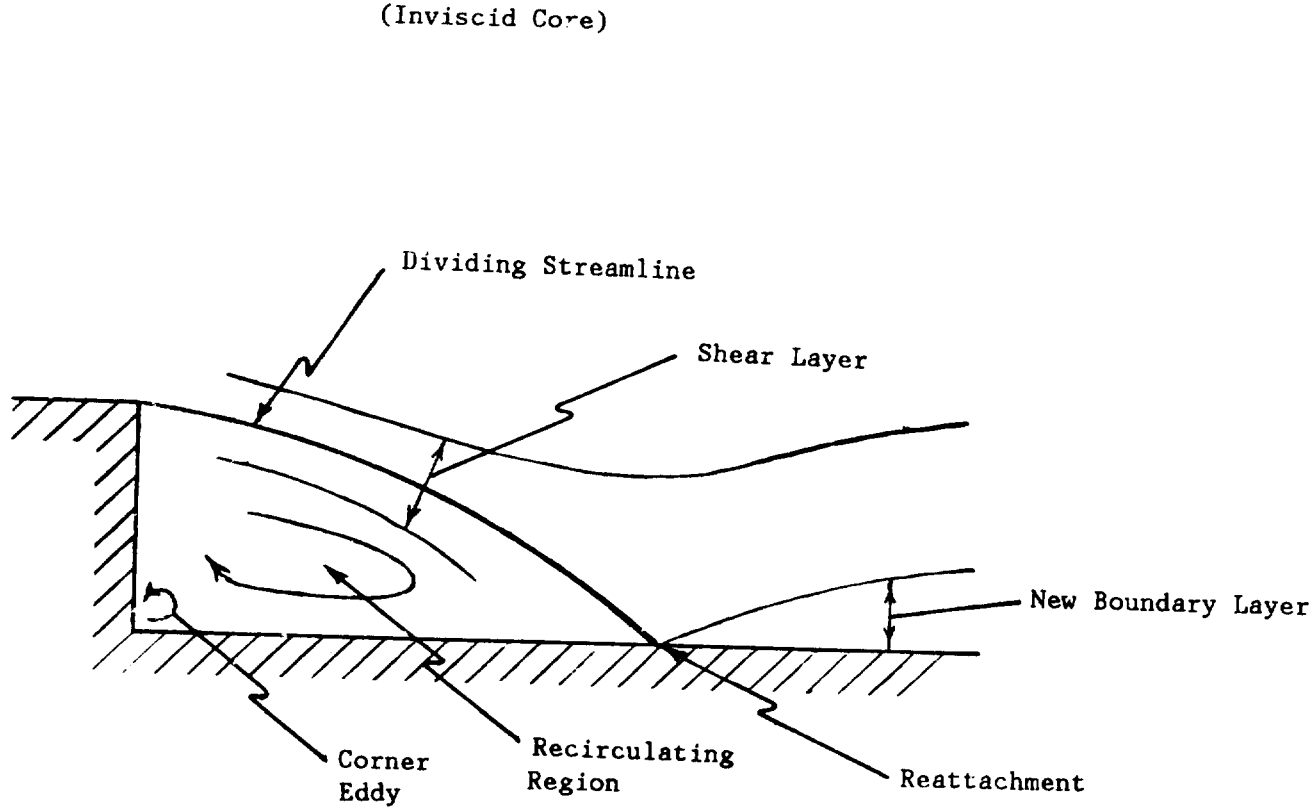

Figure 1. Physical description of reattaching flow

sides of the average distance to reattachment [2]. After reattachment, a new sub-boundary layer begins to form. In the corner formed by the step and the wall downstream of the step, a smaller eddy is formed that rotates in a direction opposite to that of the larger eddy. An inviscid core above the shear layer may or may not exist depending on whether the flow is fully developed at the step.

The present study deals with finite-difference solutions to partial differential equations that govern the velocity and temperature of fluid flow through rapid expansions. Since this geometry is one of the simpler geometries involving regions of flow reversal, it is of value as a test case to develop algorithms to be used with complex geometries.

The Navier-Stokes equations are the general set of governing equations that are applicable for predicting the velocity field for this geometry. However, solving the Navier-Stokes equations requires more programming effort and computer time than solving equation sets that are more approximate. One such equation set consists of the boundary-layer equations.

In general, the boundary-layer equations provide a good model of the flow field when the Reynolds number is very high. The boundary-layer equations can be obtained from the Navier-Stokes equations by assuming that the change of any variable of interest in the streamwise direction and the transverse velocity are both very small. The conservation of momentum equation in the transverse direction, y, reduces to a statement that the pressure varies only in the streamwise direction and is constant in the transverse direction ($\partial p/\partial y=0$).

For flows in which the boundary-layer assumptions are valid, the boundary-layer equations can be solved in place of the Navier-Stokes equations with relative ease. However, with rapid expansions, there exists a region of low Reynolds number flow immediately after the expansion in the recirculating eddy where the fluid velocity is low. The limitations of using the boundary-layer equations for this geometry has not been thoroughly addressed in previous studies.

The boundary-layer equations are a parabolic set which means that no information from the downstream direction can influence the solution. Parabolic equation sets are applicable to flows in which a predominant direction of flow can be defined. This is in contrast to an elliptic equation set (such as the Navier-Stokes equations) in which events anywhere in the flow domain of interest can influence the solution. Elliptic equations can be used to model flow with no predominant flow direction. In regions of flow reversal, a predominant flow direction cannot be clearly defined. This indicates that flow regions with flow reversal are elliptic in nature.

If the flow is not fully developed at the sudden expansion, a core region of inviscid fluid can be identified. Laplace's equation (elliptic in type) can be effectively used to model flow in this inviscid core if the flow is irrotational, making it unnecessary to solve the full Navier-Stokes equations in this region. By using the boundary-layer equations in the viscous region near the wall and Laplace's equation in the inviscid free stream, elliptic effects can be

included through the solution of Laplace's equation. The idea of using an equation set valid for the inviscid region and the boundary-layer equations near the wall is commonly known as viscous-inviscid interaction. However, if the flow is fully developed at the expansion, no internal core of inviscid fluid can be identified, so viscous-inviscid interaction cannot be used. For the flows predicted in this study, no inviscid core existed.

When predicting turbulent flow, the governing equations are time averaged over a short period of time. As a result of averaging, extra terms are introduced into the momentum and energy equations and the original variables are replaced with time averaged variables. The extra terms in the momentum equations are called Reynolds stresses. Turbulence modeling of the Reynolds stresses in regions of flow reversal has been particularly challenging since many of the assumptions usually made in turbulence modeling are invalid when recirculation is present.

The algebraic mixing length models neglect the diffusion and convection of turbulent kinetic energy and turbulent length scales. These algebraic models show good correlation with experimental data for turbulence that is in equilibrium. In equilibrium boundary layers, the production of turbulent kinetic energy equals the dissipation of turbulent kinetic energy The turbulence encountered in recirculation flow is not equilibrium turbulence, so convection and diffusion of turbulence parameters need to be accounted for by using turbulence models more complex than the algebraic mixing length models.

More complex turbulence models that require the solution of partial-differential equations (PDEs) for the turbulence parameters are at the present time being refined. These models employ additional PDEs to take into account diffusion and convection of turbulence parameters. The turbulent kinetic energy equation (k-equation) is a PDE generally used in regions of high turbulence Reynolds number. Some modifications have been proposed to make it applicable for regions of low turbulence Reynolds number and reversed flow. The k-equation requires the specification of a turbulent length scale either algebraically or through the solution of an ordinary differential equation (ODE) or another PDE. A popular PDE to provide this length scale is the ε-equation (equation for the dissipation rate of turbulent kinetic energy). The ε-equation, usually used in conjunction with the k-equation, is the weakest link of the k-ε model [3]. The k-ε model is the most widely used two equation model of turbulence. The k-ε model is used with the assumption that the Reynolds stresses are proportional to the mean rate of strain [4]. Other models do not make this assumption but impose PDEs for the Reynolds stresses themselves. These Reynolds stress models have not been widely used due to their complexity. However, algebraic equations that approximate the Reynolds stress PDE are often used in conjunction with the k-ε model [5].

If the temperature field is desired, the energy equation is used to solve for the temperature and to predict the heat transfer. If the flow is turbulent, the turbulent transport of energy must be modeled. As

with hydrodynamic turbulence models, there is a wide range of complexity involved with modeling the turbulent heat transport. In general, turbulence greatly enhances the heat transfer (and the skin friction).

B. Literature Review

In the last fifteen years, there has been a wealth of new literature on the subject of reversed flow caused by a sudden contraction or expansion. However, for laminar flow heat transfer data sets are very scarce. There have been several studies of the heat transfer for turbulent flow, but until recently these studies have not included hydrodynamic data. Therefore, if differences appeared when comparing the temperature field or heat transfer rates with other data sets, one did not know if they were due to a faulty hydrodynamic solution or if they were due to problems with the solution of the energy equation itself.

1. Laminar rapid expansion studies

a. Experimental hydrodynamic The laminar experimental hydrodynamic data sets are divided into two groups. Those dealing with axisymmetric and symmetric planar expansions are discussed in the symmetric section; those dealing with asymmetric planar expansions (also called backsteps or rearward-facing steps) are grouped in the asymmetric section

1) Symmetric The first experimental study of an abrupt pipe expansion was carried out by Macagno and Hung [5] who used flow

visualization with aluminum powder in oil. They considered only an expansion ratio of 1:2 (inlet diameter to outlet diameter) and found that the flow remained axisymmetric and stable for Reynolds numbers less than 4500. They also found that the distance from the step to the point of reattachment varied linearly with Reynolds number.

Back and Roshko [6] used flow visualization to find the point of reattachment for flows in a circular channel abrupt expansion for Reynolds numbers between 20 and 4200. Dye was injected into water. They used a nearly uniform inlet profile with a very thin boundary layer at the expansion and reported that as the Reynolds number was increased, the distance to reattachment increased, reached a maximum, decreased, and then stayed constant when the flow became turbulent. The shear layer undulated for moderate Reynolds numbers with vortices appearing in it as the Reynolds number was increased further. For most of the range of Reynolds numbers studied, the flow was turbulent at reattachment.

A 1:2 pipe expansion was studied by Iribarne et al. [7]. They found wave-like disturbances of the flow over a range of Reynolds numbers varying from 9 to 1355. The velocity profile at the step was nearly uniform with a very thin boundary layer. The shear layer downstream of the expansion developed wave-like disturbances. They reported that the frequency of the disturbances was a function of the square root of the Reynolds number. The irregular sinusoidal motion of the shear layer turned varicose for a Reynolds number of 350 which corresponded to the maximum reattachment length. There was considerable

turbulence at reattachment when the Reynolds number was above 350. The mean flow field remained symmetric.

Durst et al. [8], using a laser-Doppler anemometer, studied the flow through a symmetric 1:3 plane expansion over a range of Reynold numbers. The flow was fully developed at the inlet. Only for the lowest Reynolds number tried (56 based on the maximum velocity upstream of the expansion) was the flow symmetric. For Re of 252, the flow was stable but very asymmetric with additional separation regions downstream of the step. The two trapped eddies were of different length. An additional region of separation appeared after the shorter of the primary eddies for some Reynolds numbers. For Re above 252, the flow was unsteady.

Feuerstein et al. [9] studied the fully developed flow through three different axisymmetric channel expansions using high speed photography of a fluid with tracer particles. They used the measured velocity profiles after reattachment as inlet conditions to a linearized boundary-layer problem to study the flow redevelopment. They gave a correlation for the distance to reattachment for d/D = 0.63 and 300 < Re < 1000 as

$$\ell_r/h = 0.048\ Re_d^{1.1} \tag{1.1}$$

Equation (1.1) predicts longer reattachment lengths than were predicted in this study.

Cherdron et al. [10] used a laser-Doppler anemometer to study flow that was fully developed at a 1:2 planar symmetric expansion. They found unequal reattachment lengths due to oscillations of the velocity if the Reynolds number based on the maximum inlet velocity was over 150. This caused antisymmetry due to the confinement of the flow. The reattachment length was close to an integral number of the wavelength of the disturbance in the shear layer. Disturbances at the lip were amplified in the shear layer to cause the unsteadiness.

Restivo and Whitelaw [11] used the same channel as Durst et al. [8] but with a uniform inlet profile with a very thin boundary layer at the step. A laser-Doppler anemometer was used to measure the flow velocities. The flow was asymmetric for all Reynolds numbers studied (494 to 3865 based on the maximum inlet velocity). They studied a 1:2 and a 1:3 symmetric planar expansion with a uniform velocity profile at the inlet. They reported a higher frequency of disturbance and so a shorter wavelength than reported by Cherdron et al. [10]. They believed that this caused the shorter distances to reattachment than those measured by Cherdron et al. [10] since the distance to reattachment remained the same integral number of wavelengths that Cherdron reported. However, Pollard [12] used the Navier-Stokes equations to study the effect of inlet conditions on flow over a step. He found that the reattachment length for a uniform inlet was less than that of a fully developed inlet for the same Reynolds number. Since Pollard's analysis did not take into account any wave-like disturbances, it is likely that

the shorter reattachment lengths measured by Restivo and Whitelaw [11] are only a result of the uniform inlet velocity profile and not the higher frequency of the shear layer disturbance.

It is important to note that all of the symmetric laminar expansion experiments indicated that the flow has wave-like instabilities when the Reynolds number is of order 100 to 1000. The instabilities are worse for flows in which the boundary-layer thickness is approximately an order of magnitude less than the step height. Those having a boundary-layer thickness approximately the same order of magnitude as the step height are more stable [13]. The planar expansions are more unstable than the axisymmetric expansions because of the influence of the end walls of the planar expansions which introduce three-dimensional effects.

When the boundary layer is fully developed at the expansion, experiments show that a laminar, two-dimensional, steady flow solution commonly exists. For a planar expansion the steady, two-dimensional flow was verified for a Reynolds number of 39 for a 1:3 expansion [8] and 100 for a 1:2 expansion [10]. For an axisymmetric expansion, steady, symmetric flow was observed for Reynolds numbers up to 4500 by Macagno and Hung [5].

2) Asymmetric Since most of the asymmetric channel expansion (backward facing step) studies appearing in the literature involved a thin boundary layer at the step and an inviscid core or inviscid free stream, they were not used for comparison in the present

work. For this reason, some of the backward facing step data sets will only be briefly mentioned.

Moore [14] was the first to study flow over a rearward-facing step. His study was carried out with air in a low speed wind tunnel. Leal and Acrivos [15] studied the effect of base bleed on the separated flow. O'Leary and Mueller [16] studied the flow over a backward facing step that had a thin boundary layer at the expansion using flow visualization with a water channel. Goldstein et al. [17] used a hot wire anemometer and raised some doubts concerning the earlier measurements of Moore [14]. The flow studied by Goldstein et al. had a thin boundary layer at the step. Denham and Patrick [18] used a laser anemometer to measure nominally fully developed flow over a back step. Matsui et al. [19] used flow visualization. Armaly and Durst [20], using a laser-Doppler anemometer to study the flow over a backward facing step, found additional regions of recirculation not found by Denham and Patrick [18]. Sinha et al. [21] studied flow in which the flow at the step had a thick boundary layer in relation to the step height but thin in relation to the channel height.

Armaly et al. [22] found qualitative similarities between the stability of two-dimensional flow for symmetric and asymmetric expansions. They used a laser-Doppler anemometer with air as the fluid and found that the flow was two-dimensional for Reynolds numbers less than 400 and greater than 6600, corresponding to laminar and turbulent flow respectively. In the laminar range, the flow four step heights

upstream of the inlet was nearly parabolic. At the step, there was only a small variation from the parabolic profile. As the velocity was increased, the reattachment length increased when the flow was laminar, continued to increase as transition was reached, peaked, and then decreased until the flow was totally turbulent. This is similar to the findings of Back and Roshko [6] for an axisymmetric expansion. Once the flow was totally turbulent, the reattachment length remained constant.

b. Experimental heat transfer It is important to note that there is no literature concerning experimental studies of heat transfer for symmetric laminar sudden expansions. Those investigators considering heat transfer for asymmetric planar expansions were Aung [23, 24] and Armaly et al. [25].

Aung [23,24] used a Mach-Zender interferometer to measure the heat transfer after a rearward-facing step. He used a uniform wall temperature and a fairly thick ($\delta^*/h \sim 1$) boundary layer at separation. Aung gives reattachment lengths, free stream velocities, heat transfer coefficients, average Stanton numbers, temperature distributions, and the following correlation for the average Stanton number.

$$St = 0.787\ Re_s^{-.55}(s/x_s)^{0.72} \qquad (1.2)$$

where Re_s is the Reynolds number based on the step height, s, and the free stream velocity above the step, and x_s is the distance from the step. Aung found that the local heat transfer coefficient increased monotonically in the separated region but was always lower than that for

flow over a flat plate. Regardless of this, for transitional flow, the total heat transfer can be significantly higher than for flow over a flat plate. The maximum heat transfer was downstream of reattachment. Aung also found that the distance to reattachment peaked while the flow was in transition, then decreased until it became turbulent. The stream line curvature before the step was said to have increased the heat transfer upstream of the step.

Armaly et al. [25] measured the momentum, heat and mass transfer in backward-facing step flows that were fully developed at the step. Their reported heat transfer data show that the Reynolds analogy is invalid in the region of reversed flow. At Reynolds numbers near 400, the laminar flow became three-dimensional.

c. Numerical hydrodynamic The numerous numerical solutions for flows through rapid expansions can best be summarized in tabular form. Table 1 shows the majority of the available computational solutions for laminar flows through rapid expansions to date.

1) Symmetric Hung [26] was the first to calculate laminar two-dimensional flows of this type using the Navier-Stokes equations. He predicted the flow through a 1:2 symmetric planar expansion and a 1:2 axisymmetric expansion for Reynolds numbers less than 360. He found that the distance from the step to the point of reattachment varied linearly with Reynolds number. Macagno and Hung [5] compared the axisymmetric Navier-Stokes solutions with their own measurements. The correlation was excellent. Hung [26] and Macagno and Hung [5] used the

Table 1. Summary of laminar numerical solutions for sudden expansions

Author(s)	Method	Expansion Type	Inlet Condition
Acrivos & Schrader [27]	BL,Finite Dif.	Sym. Planar	Parabolic, Uniform
Agarwal [28]	NS,Finite Dif.	Sym. Planar	Parabolic
Armaly et al. [22]	NS,Finite Dif.	Back-Step	Parabolic
Atkins et al. [29]	NS,Finite Dif.	Back-Step	Experimental[a] Parabolic
Chen et al. [30]	NS,Finite Analytic	Back-Step	Parabolic
Durst et al. [8]	NS,Finite Dif.	Sym. Planar	Parabolic
Giaquinta [31]	NS,Finite Dif.	Sym. Planar	Uniform
Hackman et al. [32]	NS,Finite Volume	Back-Step	Parabolic, Experimental
Halim & Hafez [33]	PPNS,Finite Dif.	Sym. Planar	Parabolic
Hall & Pletcher [34]	Viscous/Inviscid Interaction	Back-Step	Thin boundary layer
Hung, T.K.[26]	NS,Finite Dif.	Sym. Planar, Axisymmetric	Parabolic
Hutton & Smith [35]	NS,Finite Elem.	Back-Step	Parabolic
Huyakorn et al. [36]	NS,Finite Elem.	Back-Step	Parabolic
Kumar & Yajnik [37]	BL,eigenfunction expansion	Sym. Planar	Parabolic
Kwon et al. [38]	BL,Finite Dif.	Sym. Planar	Parabolic, Experimental
Kwon & Pletcher [39]	Viscous/Inviscid Interaction	Sym. Planar	Parabolic,Thin boundary layer, Experimental
Leschziner [40]	NS,Finite Dif.	Back-Step, Axisymmetric	Parabolic
Macagno & Hung [5]	NS,Finite Dif.	Axisymmetric	Parabolic
Morihara [41]	NS,Finite Dif.	Sym. Planar	Parabolic
Oosthuizen [42]	BL,Finite Dif.	Back-Step	Parabolic, 4th order poly
Osswald et al. [43]	NS,Finite Dif.	Sym. Planar Axisymmetric	Parabolic

[a] All the inlet conditions listed as experimental where nearly parabolic.

Table 1. (continued)

Author(s)	Method	Expansion Type	Inlet Condition
Plotkin [44]	BL,Fourier Series approx.	Sym. Planar	Parabolic
Pollard [12,45]	NS,Finite Dif.	Axisymmetric	Parabolic Uniform
Roache & Mueller [46]	NS,Finite Dif.	Back-Step	4th order Polhausen poly
Taylor et al. [47]	NS,Finite Elem.	Back-Step	Parabolic Experimental
Thomas et al. [48]	NS,Finite Elem.	Back-Step	Parabolic

stream function and the vorticity (ψ-ω) as variables in both a steady and an unsteady approach.

Morihara [41] was next to solve the Navier-Stokes equations for flow through symmetric channels. Instead of using the vorticity-stream function variables he developed a primitive variable technique with the pressure terms eliminated from the equations. He coupled the continuity equation with the momentum equations and thus circumvented the need to use a relaxation parameter. The algorithm appeared stable but required large computer storage if the coefficient matrix was not broken into smaller submatrices. He predicted shorter reattachment lengths than those predicted by Hung [26] for a 1:2 symmetric planar expansion.

Durst et al. [8] solved the Navier-Stokes equations using the vorticity-stream function method first developed by Gosman et al. [49] to compare with their experimental measurements through a 1:3 (d:D as in

Fig. 2) symmetric planar expansion. However, since the flow was symmetric and two-dimensional for only the lowest Reynolds number tried (56 based on the maximum inlet velocity), this was the only comparison they were able to make.

Giaquinta [31] used two types of differencing molecules to solve the unsteady ψ-ω form of the Navier-Stokes equations as a model for the flow through a 2:5 symmetric planar expansion. He studied the difference between an explicit time method and an implicit time method. The flow was started from rest and allowed to reach a steady state. He found that the implicit method was good for long time analyses, particularly after flow initiation. The explicit time method was good for predicting sudden changes in the fluid motion such as at start up. The inlet velocity profile was uniform. The flows studied had Reynolds numbers of 10 and 100.

Leschziner [40] used primitive variables to test the predictions of the Navier-Stokes equations for three different types of finite differencing of the convective terms for an axisymmetric and asymmetric planar expansion. His predicted reattachment length compared well with the measurements of Macagno and Hung [5] for an axisymmetric expansion. He stated that artificial diffusion due to skewness of grid and streamlines is unimportant for laminar flow.

Pollard [12,45] used a primitive variable formulation of the Navier-Stokes equations to predict the flow through axisymmetric expansions by finite-difference discretization. His computational

algorithm was similar to the SIMPLE algorithm developed by Patankar and Spalding [50]. He studied the effect of varying the Reynolds number, expansion ratio, and inlet profile and found that the distance to reattachment varied linearly with Reynolds number and nonlinearly with expansion ratio. Reattachment lengths were shorter for uniform inlet profiles than for parabolic inlet profiles. It should be noted that for some Reynolds numbers his predictions of c_f exceeded the known fully developed c_f values by as much as 11%. His predicted reattachment lengths compared well with those predicted by Macagno and Hung [5].

Agarwal [28] used a third-order accurate upwind differencing scheme to solve the ψ-ω form of the Navier-Stokes equations. However, his predictions do not compare well with the measurements of Durst et al. [8] for a 1:3 symmetric planar expansion. For a 1:2 symmetric planar expansion, the results compared well with the predictions of Kumar and Yajnik [37] and Kwon and Pletcher [39]. The algorithm was stable and accurate for high Reynolds numbers.

Osswald et al. [43] used a direct implicit time-dependent technique to solve the vorticity-stream function form of the Navier-Stokes equations to predict the flow through a 1:3 symmetric planar expansion and a 1:2 axisymmetric expansion. A generalized orthogonal coordinate system with a cluster conformal transformation technique packed the grid in the regions where the length scale was shorter. An ADI (alternating direction implicit) scheme was used to solve the vorticity transport equation; a block-Gaussian elimination scheme was used to solve the stream function equation.

Those who used the partially-parabolized Navier-Stokes equations (PPNS) include Madavan [51] and Chiu [52]. They neglected the streamwise diffusion terms in the Navier-Stokes equations.

Only recently have the boundary-layer equations been used to predict the flow through the large regions of reversed flow behind sudden expansions. Acrivos and Schrader [27] felt that the boundary-layer equations were not valid near the step. In this "near region" close to the step, they stated that the flow was inviscid in nature, the length of the inviscid region being of the same order of magnitude as the inverse of the Reynolds number. To overcome this, they modified the initial velocity profile at the step to account for upstream influence in the near region. Acrivos and Schrader used the unsteady boundary-layer equations by marching in time until a steady state solution was reached. They added damping to the viscous term in the momentum equation to suppress instabilities in the finite-difference procedure. They predicted the flow through symmetric planar expansions for various expansion ratios.

Kumar and Yajnik [37] reported that by properly scaling the coordinate parallel to the channel centerline, the region of inviscid flow was shrunk to zero. They argued that a form of the boundary-layer equations, as a set of limit equations to the Navier-Stokes equations, is applicable for this geometry for sufficiently high Reynolds numbers. Kumar and Yajnik used an eigenfunction expansion to reduce the set of partial differential equations to a set of ordinary differential

equations. They predicted the flow through symmetric planar expansions. Plotkin [44] solved the boundary-layer equations in a way similar to Kumar and Yajnik [37]. However, instead of an eigenfunction expansion, Plotkin used a concise Fourier series approximation technique. Plotkin's results were similar to those of Kumar and Yajnik. Both Plotkin [44] and Kumar and Yajnik [37] reported singular behavior when attempting to predict separated flow if too many expansion terms were included.

Kwon et al. [38] solved the boundary-layer equations with a once through marching procedure. In regions of reversed flow, the FLARE approximation [53] removed the streamwise convective terms. The momentum and continuity equations were solved in coupled manner. The predicted reattachment length compared well with that predicted by the Navier-Stokes equations and that measured experimentally.

2) Asymmetric Roache and Mueller [46] used a finite-difference discretization of the unsteady Navier-Stokes equations to predict the flow field passing over an asymmetric planar expansion or back-step. They used a ψ-ω form of the Navier-Stokes equations. They marched explicitly in time until the solution stabilized.

Atkins et al. [29] solved the ψ-ω form of the Navier-Stokes equations with finite differences. Their laminar predictions used the experimental inlet profile of Denham [54] (2:3 asymmetric expansion). They tried upwind and central differencing of the convective terms. The predictions of both differencing schemes were very close to the

measurements of Denham. For Reynolds numbers lower than those measured by Denham, the upwind differences predicted reattachment lengths and eddy intensities that were 8% less than those predicted by the central differences.

Leschziner [40] used primitive variables to test three methods of finite differencing the convective terms of the Navier-Stokes equations. He compared his predictions with the measurements of Denham and Patrick [18] for 2:3 asymmetric expansion. He predicted the minimum stream function value in the eddy measured by Denham and Patrick but over predicted the measured reattachment length. He stated that artificial diffusion due to skewness of grid and streamlines is unimportant for laminar flow.

The TEACH code [55] was used by Armaly et al. [22] to solve the Navier-Stokes equations. Their measurements and predictions compared well as long as they used their measured inlet condition in their computations and as long as the experimental flow remained two-dimensional. The back-step they studied had an exparsion ratio of 1:1.94.

Hackman et al. [32] used a finite volume discretization of the primitive variable Navier-Stokes equations to test two different differencing schemes. They predicted the flow over a backward facing step and compared the results with Denham and Patrick [18] for Reynolds numbers of 73 and 229 based on the step height and average inlet velocity. When the measured inlet profile at the step was used as the

inlet condition for computations, the numerical predictions compared well with experimental measurements. Their predictions did not compare well with measurements when a parabolic inlet condition was used.

There have been three studies that used viscous-inviscid interaction for back-step flows that had a thin boundary layer at the step. Kwon and Pletcher [39] developed a hydrodynamic solution method. In the viscous region, they used the boundary-layer equations with the FLARE approximation [45]; in the inviscid region they solved Laplace's equation. Halim and Hafez [33] solved a fourth-order equation for the stream function in the viscous region derived from the PPNS equations. Halim and Hafez introduced an implicit coupling procedure for coupling the viscous and inviscid solutions.

There have been several finite element solutions of the Navier-Stokes equations for flow over back-steps. The usual method of using the Galerkin formulation with weighted residuals that is so widely used in structural mechanics often produces oscillations in the solution. This is because the convection terms cannot be easily treated by the symmetrical operators that are commonly used in structural mechanics.

Huyakorn et al. [36] predicted the fully developed flow through an asymmetric expansion using different interpolation elements. Hutton and Smith [35] predicted the same flow case.

Taylor et al. [47] used a weighted residual finite element discretization of the primitive variable Navier-Stokes equations to predict the laminar and turbulent flow over a back-step. They compared

their predictions with the experimental measurements of Denham and Patrick [18] and the finite-difference predictions of Atkins et al. [29]. The predictions of Taylor et al. did not match the measurements as well as the finite-difference predictions of Atkins et al.

Thomas et al. [48] predicted the laminar and turbulent flow over a back-step using primitive variables. They had to substitute upwind weighting functions for the Galerkin weighting functions to get convergence. This is similar to the need to sometimes use upwind differencing instead of central differencing of the Navier-Stokes equations to reach a stable finite-difference solution. The variable coefficients of the convective terms were set to the previous global iteration values. This provided a means of linearization and a means of global iteration. The predictions of Thomas et al. compare reasonably well with the measurements of Denham and Patrick [18] and the finite-difference predictions of Atkins et al. [29].

Chen et al. [30] used what they termed a finite-analytic procedure to solve the Navier-Stokes equations. They predicted the flow over a 2:3 back-step. They predicted more mass trapped in the eddy behind the step than that measured by Denham and Patrick [18].

Chiu [52] used the PPNS equations to predict the incompressible flow over a back-step (see Numerical-symmetric section). His predictions are in good agreement with the predictions of the full Navier-Stokes equations and experimental measurements, indicating that the streamwise diffusion terms are unimportant for moderate Reynolds numbers.

Kwon and Pletcher [39] and Oosthuizen [42] used a finite-difference formulation of the boundary-layer equations to predict fully developed flow over an asymmetric expansion. Oosthuizen was able to predict the additional region of separation on the wall opposite the step that was first reported by Armaly and Durst [20]. Both Kwon and Pletcher [39] and Oosthuizen [42] used the FLARE approximation to march through regions of reversed flow.

The previous studies that used the boundary-layer equations have provided only isolated comparisons indicating that the solution to the boundary-layer equations may provide useful information for some sudden expansion flows. However, the limitations of the boundary-layer equations have not been clearly defined.

d. Numerical heat transfer Hall and Pletcher [34] modified the algorithm of Kwon and Pletcher [39] to include a solution of the energy equation. Theirs is the only laminar solution of the energy equation for flow over a back-step in the literature.

2. Turbulent rapid expansion studies

The experimental studies are discussed first, followed by the numerical studies. Both the experimental and numerical studies are divided into two groups according to whether or not they include heat transfer data.

Turbulent measurements are more difficult to make than laminar flow measurements. The early studies used flow visualization, pitot tubes, hot wires, and surface pressure transducers to measure flow parameters.

At first, these data provided mostly qualitative, but important, flow field information. Later as hot wire techniques were refined, more accurate measurements were taken. With the introduction of laser-Doppler anemometers and pulsed-wire anemometers, the measurements again increased in accuracy. At the present time, refinements are still being made to increase the accuracy of turbulence measurements [2].

a. Experimental hydrodynamic The experimental-hydrodynamic studies are divided into two groups. Those dealing with flow through an axisymmetric or a planar symmetric channel expansion are grouped in the symmetric category; those dealing with flow over a backward-facing step are grouped in the asymmetric category.

1) Symmetric The studies giving only hydrodynamic data for symmetric sudden expansions are summarized as follows:

Flow visualization: Drewry [56]

Pitot tubes: Kangovi and Page [57], Ha Minh and Chassaing [58], Mehta [59]

Hot-wire anemometers: Abbot and Kline [60], Chaturvedi [61], Ha Minh and Chassaing [58], Mehta [59]

Laser-Doppler anemometers: Moon and Rudinger [62], Freeman [63], Smyth [64], Lu [65], Stevenson et al. [66]

Abbot and Kline [60], Smyth [64], and Mehta [59] all studied the flow through symmetric (double-sided) planar expansions. Abbot and Kline [60] were the first to experimentally study the flow in asymmetric and symmetric planar expansions using hot wire probes. Smyth [64] was

the first to study the flow through a symmetric planar expansion using a laser-Doppler anemometer. He provided mean velocity, turbulent kinetic energy, Reynolds stress, and fluctuating velocity profiles. The flow was fully developed and turbulent at the step. He found no appreciable flow asymmetries. Mehta [59] found asymmetric unsteady flow through a symmetric expansion when d/D was greater than 1.5. For d/D smaller than 1.5, the flow remained steady and symmetric. The asymmetries may have been due to three dimensional effects caused by the small channel aspect ratio (the ratio of the channel height to the width was only 1/4). Mehta used hot wires and pitot tubes.

There have been numerous axisymmetric rapid expansion studies. Chaturvedi [61] used pitot tubes and hot wire anemometry to study axisymmetric expansion flow. He provided velocity, pressure, and turbulence data for different step face wall angles.

Moon and Rudinger [62] studied fully developed turbulent flow through a axisymmetric expansion using a laser-Doppler anemometer (LDA). They published velocity profiles, centerline velocity curves, and eddy shape diagrams. For the range of Reynolds numbers studied (10^3-10^6 based on the inlet diameter), the reattachment length was approximately 1.25 outlet tube diameters from the step and independent of Reynolds number. They also compared their measurements with numerical predictions.

Freeman [63] studied flows that had hot and cold co-flowing streams at the expansion. He measured the reattachment length as 5 step heights

from the expansion for Reynolds numbers between 20,000 and 40,000 using a laser anemometer. For this range of Reynolds numbers, he found that the temperature profiles were independent of the Reynolds number.

Kangovi and Page [57] used pitot tubes to measure the flow through an axisymmetric sudden expansion. They measured a reattachment length of 8 step heights.

Ha Minh and Chassaing [58] used hot wires and pitot tubes to measure flow that had a very thin boundary layer through a 1:2 pipe expansion. They reported a turbulence intensity that was 19% of the centerline velocity in the reattachment region. The turbulence intensity decayed rapidly downstream of reattachment. They measured reattachment at nine step heights from the step.

Stevenson et al. [66] measured the velocities of flow through an axisymmetric expansion and an asymmetrical backstep using a laser anemometer. They used frequency shifting and control of the seeding density to eliminate bias errors. The axisymmetric case had a short entry length before the expansion. The axisymmetric inlet profile was measured with a pitot tube and found to be "very flat". They found the peak Reynolds stress was at the edge of the recirculation zone. They published turbulent kinetic energy, Reynolds stress, and some fluctuating velocity data. They also predicted the flow using a modified version of the SIMPLE computer code with a k-ε turbulence model. The strength of their paper is in the experimental measurements.

Drewry [56] and Lu [65] studied flows having a constriction at the inlet of a relatively short pipe. Lu [65] used a laser anemometer to determine the velocities in a short tube with constrictions at both ends. He provided the centerline velocity and a few velocity profiles. The inlet conditions, which were not provided, were not that of fully developed turbulent flow. Drewry used flow visualization.

2) Asymmetric Eaton and Johnston [1] gave an excellent summary of the backward facing step experiments that were done before 1981. Rather than repeat their work, the main points of their summary will now be listed and a detailed sketch of the experiments they summarized will not be given.

Upon reviewing the early experiments, Eaton and Johnston made the following conclusions.

- The reattaching shear layer is like a free shear layer except on the "wall side" where the flow is highly turbulent. Since the outer part of the reattaching shear layer is similar to a free plane shear layer, turbulence models that work well for free shear layers should work well for the reattaching shear layer except near the wall and reattachment point. Some refinement will undoubtedly have to be done for these regions. The outer part of the reattaching layer retains the characteristics of a free shear layer for as many as 50 step heights downstream of the step.

- There is a rapid decrease in Reynolds stresses near reattachment that is caused by either streamline curvature, pressure gradient, wall interaction or some combination of the above.
- The maximum reversed flow velocity is usually over 20% of the free stream velocity.
- The boundary layer state (turbulent or not) at the step has an important effect on the downstream flow. For fully turbulent boundary layers, the flow is independent of the Reynolds number. However, it is not clear how much the boundary layer thickness affects the flow.
- Increasing the free stream turbulence tends to decrease reattachment lengths; increasing the expansion ratio tends to increase reattachment lengths.
- Hot-wire probes tend to measure lower turbulence quantities than laser anemometers. It was concluded that the hot-wire anemometers under measure turbulence quantities.
- The y-position of the maximum turbulence intensity moves toward the wall as reattachment is approached; it moves away from the wall as reattachment is passed.
- There still remains controversy on whether spanwise vortices are the dominant structure in the plane mixing layer. Eaton and Johnston concluded that this is the case. They concluded that these vortices are the cause of the unsteady reattachment point noted in several studies.

- There is also controversy on what happens to the large eddies at reattachment. Some feel these eddies are ripped apart while others feel that some of the large eddies go upstream and some go downstream.

Since Eaton and Johnston's review of backward facing step experiments, there have been several new studies that have added insight to the physics of the flow. Since the review, Driver and Seegmiller [67], Pronchick and Kline [68], Adams [69], and Stevenson et al. [66] have used laser anemometers to study the recirculating flow. Pronchick and Kline also used flow visualization. Cheun et al. [70] and Moss and Baker [71] used pulsed wire anemometers; Westphal et al. [2] used a pulsed wall probe.

Along with using a pulsed wire anemometer, Moss and Baker [71] also measured the surface pressure for flow over small protuberances and a backward facing step in a large wind tunnel. They found that "the line of peak stresses diverges progressively outwards from the dividing streamline with values rising to a maximum before falling away with reattachment", which is in agreement with the summary of Eaton and Johnston [1].

Cheun et al. [70] studied the effects of the free stream turbulence and the boundary layer thickness at the step. They reported that for their experiments, the free stream turbulence had little effect on the flow. This is different from the conclusion reached by Eaton and Johnston [1] in their review. Cheun et al. also reported that the

thinner the boundary layer at the step, the shorter the reattachment length.

Chandrsuda and Bradshaw [72] studied the turbulent stresses and turbulent energy balance in the reattachment region with hot-wire anemometers. They concluded, in agreement with everyone else, that the shear layer upstream of reattachment is similar to a plane mixing layer. They said that the change of the turbulence structure near reattachment is due to the confinement of the large eddies. They felt that an accurate turbulence model should have a fairly sophisticated model for the triple products, i.e., a triple product transport equation and that the dissipation equation should include a wall effect term.

Driver and Seegmiller [67] measured the thickness of an oil film with a laser to determine c_f. They reported a sudden increase in turbulent stress after separation which started to decrease two step heights before reattachment. The triple cross products rapidly disappeared at reattachment which suggested that the eddies were being torn apart. They reported that the wall side of the shear layer was highly turbulent. In comparing with numerical predictions, they concluded that using an algebraic stress model improved predictions because streamline curvature was important.

Pronchick and Kline [68] hopefully settled the dispute concerning what happens to the eddies at reattachment. According to Pronchick and Kline, the two earlier theories concerning the fate of the large eddies are both correct. Pronchick and Kline concluded that some eddies are

broken apart at reattachment and some are either swept upstream or downstream. Those swept downstream are the cause of the slow recovery of the flow to typical boundary layer flow. They reported that the unsteadiness of the reattachment point was caused by three-dimensional eddies.

Westphal et al. [2] mainly used a newly developed pulsed wall probe to study the flow in the back-flow region. They found a strong dependence of the reattachment length on the boundary layer thickness. The flows they studied became similar when the x-coordinate was scaled about the reattachment point. They felt that there was a laminar-like thin region of strong backflow next to the surface upstream of reattachment that was not similar to attached turbulent boundary layers.

The investigation by Stevenson et al. [66] was mainly to study the errors in velocity biasing when using laser anemometers for turbulent flow. Velocity bias is due to the fact that for turbulent flow, more particles per unit time traverse the probe volume when the velocity is high than when it is low. Velocity bias can be overcome by high uniform seeding density and equal time velocity sampling. They found the peak Reynolds stress at the edge of the recirculation zone. The channel was so narrow that the measurements were not truly two-dimensional since the side walls undoubtedly affected the flow. For this reason, the asymmetric planar expansion measurements cannot be used as a comparison for two-dimensional numerical predictions.

Walterick et al. [73] found relatively high free stream turbulence in their backward facing step measurements. They concluded this was caused by the unsteady motion of the shear layer that was noticed at the reattachment point. However, it may have been due to inadequate flow conditioning upstream of the test section [74]. The importance of free stream turbulence is still unclear [1,70].

Lamb and McCotter [75] made surface pressure measurements over a small step and protuberances in a large wind tunnel. They were able to correlate the pressure in the recirculation region using reference values at reattachment and the point of minimum pressure.

Adams [69] found that a laminar boundary layer at separation gave shorter reattachment lengths than a turbulent boundary layer. The flow remained Reynolds number independent for the range of Reynolds numbers studied (under 36,000 based on the step height). He, like Westphal et al. [2], argued that the boundary layer in the recirculating region was laminar-like. He found no bursting mechanism like that observed in typical turbulent boundary layers.

The reversed flow studied by Simpson et al. [76] and Simpson [77] was for flow that had separation induced by a pressure gradient on a flat plate but has application to rapid expansion flows. Simpson et al. [76] reported that the eddy viscosity and mixing length models are poor in the separation region. They claim that the normal law of the wall in u^+ and y^+ coordinates is not valid in the recirculation bubble near the wall. They say that the turbulence stress must be modelled according to

the turbulence structure and not by the mean velocity gradients. They state that the reason the eddy viscosity models are not good in the reversed flow is because $\partial u/\partial y$ is based on averaging the large turbulent fluctuations. These averages are not meaningful due to the relative magnitudes of the instantaneous velocity and the time averaged velocity. Simpson [77] divides the flow into three layers: (1) a viscous layer near the wall, (2) an intermediate layer that acts as an overlap or buffer, and (3) an outer layer which is part of the large scale outer flow. For the viscous layer near the wall, he proposes the following equation

$$\frac{u}{u_N} = g\left(\frac{y}{N}\right) \tag{1.3}$$

where N is the location of the maximum negative velocity in the bubble and u_N is the absolute value of the maximum negative velocity. Using Eq. (1.3), he developed wall functions that can be used in place of the law of the wall.

b. Experimental heat transfer There have been several reviews of the heat transfer data for turbulent separated flows. Hanson and Richardson [78] and Chilcott [79] were the earliest. Fletcher et al. [80] reviewed a large number of papers published previous to 1974 for both subsonic and supersonic separating reattaching flows for various geometries. Aung and Watkins [81] and Aung [24] reviewed the turbulent subsonic heat transfer studies in 1978 and 1983 respectively.

Aung's review [24] emphasized the studies of recirculating flows over steps and cavities for laminar, transitional, and turbulent flows that were done after 1978. He noted that downstream of the step, the pressure reaches a low value and then remains almost constant in the axial direction for some distance. He concluded that the curvature effect of the streamlines enhances the heat transfer. The studies he reviewed indicated that the thermal boundary layer redeveloped to a form that was typical of flat plate flow quicker than the velocity field redeveloped. He also pointed out the difference between laminar and turbulent separation heat transfer. For laminar heat transfer, the heat transfer rate in the recirculation bubble is always less that that for a flat plate. It starts low and increases monotonically. On the other hand, turbulent heat transfer greatly exceeds that of fully developed flat plate flow in the recirculating region. The turbulent heat transfer rate peaks at reattachment then drops to fully developed flat plate or channel flow values. Aung states that high levels of turbulence are generated in the shear layer where the turbulence dissipation is small. The dissipation remains small until the length scale decreases due to the flow approaching the wall. This is why the turbulent stresses increase in the reattaching shear layer only to decrease when reattachment is approached.

The different heat transfer studies listed by geometry are:

- Axisymmetric expansion: Ede et al. [82], Krall and Sparrow [83], Zemanick and Dougall [84], Runchal [85], Back et al. [86], Kang et al. [87], Sparrow and O'Brien [88],

Amano et al. [89], and Baughn et al. [90]

- Planar symmetric: Filetti and Kays [91], Seki et al. [92], and Seki et al. [93]
- Asymmetric rearward-facing step: Seban et al. [94], Seban [95], Aung and Goldstein [96], Kottke [97], and Vogel and Eaton [74]

There is some disagreement concerning the effect of Reynolds number on the heat transfer. Most of the planar symmetric and axisymmetric expansion studies indicated that the maximum Nusselt number is proportional to $Re^{2/3}$ [83, 84, 90, 92, 93]. However, Amano et al. [89] found that for the smallest expansion ratio they studied (d/D = 0.195), the Nusselt number was not a function of the Reynolds number and varied according to $Re^{0.5}$ for the larger two expansion ratios that they studied. Ede et al. [82], who used water as a fluid with heating upstream of the expansion as well as downstream, found the variation of the convective heat transfer coefficient substantially independent of Re over a wide range of Reynolds numbers (3700-45,000). Filetti and Kays [91] predicted two different reattachment lengths for their symmetric planar expansion and so measured the Nusselt number as being proportional to Re^{m}, where the measured values of m bracketed 2/3. Filetti and Kays [91] reported that the Nusselt number was proportional to $Re^{0.6}$. For rearward-facing step flows, Seban et al. [94] found the maximum Nusselt number proportional to $Re^{0.8}$. Sparrow and O'Brien [88] measured the heat transfer along the face of an axisymmetric expansion and concluded that for high Reynolds numbers, the heat transfer rate became less and less dependent on Re.

Most of the studies indicate that the maximum Nusselt number is at the reattachment point [83, 93, 94]. Vogel and Eaton [74] used a newly developed pulsed wall probe that measures c_f to verify that the point of maximum heat transfer and zero shear stress correspond. However, Kang et al. [87] using flow visualization measured it to be upstream of reattachment by 15% of the reattachment length. The value of the maximum Nusselt number was higher than the fully developed Nusselt number by a factor of 2.7 to 11, depending on the reference. The maximum Nussult number is very geometry dependent [84].

Zemanick and Dougall [84] reported a small effect of Re on the reattachment point except for very high and very low Reynolds numbers. For the very high Reynolds numbers, compressibility might have had an effect. They found that reattachment was a function of the expansion ratio with smaller values of d/D giving longer reattachment lengths. Baughn et al. [90], whose test was very similar to that of Zemanick and Dougall, found that for a given expansion size, the bubble length varied little with Re. Both the studies by Zemanick and Dougall and Baughn et al. utilized fully developed flow at the axisymmetric expansion. Krall and Sparrow [83] measured a reattachment length of 1.25 to 2.5 diameters from the step. The reason why some studies showed little effect of Reynolds number and expansion size on the distance to maximum Nusselt number and others showed a large effect is probably due to differences in the boundary layer thickness at the expansion.

Several investigators found evidence of a small eddy in the corner near the step rotating in a direction opposite to that of the larger eddy. Zemanick and Dougall [84] and Baughn et al. [90] both conclude that since there is a local maximum in the heat transfer rate very near the step, this indicates the existence of the small eddy. Sparrow and O'Brien [88] said their napthalene sublimation method made the existence of a secondary eddy obvious.

The studies point out that the heat transfer through the near wall layer does not behave like that through a normal turbulent boundary layer in the reattachment and redevelopment regions. Seban [95] found large temperature gradients near the wall downstream of the step. Aung and Goldstein [96] stated that near the step, the largest temperature difference was in the shear layer. As the reattachment point was reached, half of the temperature drop was across the shear layer and the other half was across the fluid near the wall. Sogin [98] found that for separation behind bluff bodies, most of the temperature drop was in the thin layer near the body. Vogel and Eaton [74] studied both the fluid dynamics and the heat transfer of flow through an asymmetric planar expansion. They found that the near wall region is important in determining the heat transfer rate. The sublayer dominates the heat transfer and is the reason the Stanton number and skin-friction coefficient are not well-correlated by the Reynolds analogy. This indicates that a constant turbulent Prandtl number is not correctly modeling the physical behavior in the recirculating region. They found

that the momentum thickness was much larger than the enthalpy thickness following reattachment.

The reversed flow region affects the heat transfer well-beyond reattachment. The flow measured by Filetti and Kays [91] had not reached fully developed values after 14 step heights downstream of the step. Aung and Goldstein [96] said that their results indicated that the heat transfer values approached the flat plate values after 12 step heights.

c. Numerical hydrodynamic Turbulent recirculating flows are much more difficult to predict than laminar recirculating flows. Turbulence models are well developed for attached boundary layers but experimental evidence has shown that the attached boundary layer assumptions are many times not valid in the recirculating flow. Most of the recent numerical predictions have used a variation of the k-ε model of turbulence. Although relations for k and ε can be rigorously derived from the Navier-Stokes equations, new unknowns are introduced that require modeling assumptions. These assumptions render the k-ε transport equations approximations at best. Much of the computational research in turbulent recirculating flow has been carried out to improve the k-ε model for recirculating flow.

In the latter part of the 1970s, there was a sudden interest in numerical predictions of rapid expansion flow. Briggs et al. [99] predicted the flow measured by Abbot and Kline [60]. Le Balleur and Mirande [100] and Kim et al. [101] used viscous-inviscid interaction.

Ha Minh and Chassaing [102] predicted flow through an asymmetrial expansion. Gosman et al. [103] predicted the flow through symmetric and axisymmetric expansions using primitive variables. Oliver [104] and Mehta [105] used vorticity-stream function variables. Taylor et al. [47] used a finite element method to solve the primitive variable form of the Navier-Stokes equations for flow over a backstep. He used a k-equation turbulence model with an empirical mixing length formula. Atkins et al. [106] predicted the flow through an asymmetric channel expansion. The above numerical predictions are discussed in more detail in Kwon and Pletcher [39].

Kwon and Pletcher [39] used viscous-inviscid interaction to predict the flow measured by Kim et al. [107]. They solved Laplace's equation in the inviscid region and the boundary layer equations in the viscous region. The FLARE approximation was used to march the boundary-layer equations through regions of reversed flow. They used the k-equation and an ODE for the length scale upstream of the step, and the k-equation and an algebraic equation for the length scale downstream of the step.

Lokrou and Shen [108] solved a form of the boundary-layer equations by using a normalization of the velocity profiles to make them invariant in the streamwise direction. This reduced the PDEs to a system of ODEs. However, the theory fails near reattachment due to flow curvature and instability.

Sindir [109, 110] used four different turbulence models to predict the flow through asymmetric expansions with parallel walls and

nonparallel walls respectively. Two of the turbulence models were the k-ε model and an algebraic stress model (which still requires solutions of the k and ε equations). The other two were obtained by modifying the production term in the ε-equation. He found the modified algebraic stress model superior in the reversed flow region. However, it predicted too slow a recovery after reattachment. He found that the best approach was to use the modified algebraic stress model in the reversed flow region and the nonmodified algebraic stress model after reattachment. The "best" model is thus regionally dependent. For the near wall region, he used the wall functions of Chieng and Launder [111].

Hackman et al. [32] predicted the flow through an asymmetric expansion with two types of differencing schemes: (1) an upstream weighted difference scheme (UWDS) and (2) a skew hybrid upstream differencing scheme (SHUDS) for both Cartesian and curvilinear meshes. They solved the Navier-Stokes equations with the standard k-ε turbulence model with law-of-the-wall type wall functions near the wall. They found that the UWDS predicted shorter reattachment lengths, gave generally inferior predictions, and was much more sensitive to the mesh size. SHUDS was less grid dependent and gave better overall correlation with measurements. Hackman et al. thought that some of the poor predictions for turbulent flows was a result of the numerical scheme and not an inadequate turbulence model. Their computations over predicted the turbulent stress in the shear layer. This may be the reason for the

general under prediction of reattachment length by k-ε turbulence models. Their model predicted a sharper return to low kinetic energy in the inviscid core than was measured. This effect is a common ailment of the k-ε turbulence model for this type of flow.

Srinivas and Fletcher [112] used a variation of an algebraic turbulence model to predict flow over the trailing edge of a flat plate and backward facing step. They used the finite element method to solve the compressible Navier-Stokes equations by a pseudo transient time marching technique. Since their wall pressure and maximum shear stress predictions were in good agreement with measurements, they argued that the algebraic eddy viscosity models predict most flow features well for wake and separated flow.

Walterick et al. [73] predicted the flow over a backstep (asymmetric planar expansion) by solving the Navier-Stokes equations with a k-ε turbulence model with the pressure fluctuation term of the k-equation modeled in a nonstandard way. Their method predicted reattachment well. Their predictions using plug flow at the inlet gave shorter reattachment lengths than for the inlet condition with a boundary layer.

d. Numerical heat transfer Chieng and Launder [111] used a modification of the TEACH-2E code to predict the flow through axisymmetric expansions. They tried the standard high-Reynolds-number k-ε equation turbulence model with much attention given to a new set of wall functions, and a low-Reynolds-number k-ε model. The low-Reynolds-

number model converged very slowly and predicted heat transfer rates 5 times that of the measurements of Zemanick and Dougall [84]. The high-Reynolds-number turbulence model gave better predictions. However, in a later publication [113] it was reported that the original code had errors in it. When these errors were corrected, the predicted heat transfer was lowered by about 25%. The model was "fixed" by defining a variable turbulent Reynolds number related to the laminar sublayer thickness rather than assuming this turbulent Reynolds number to be a constant as in the first paper. This shows a common ingredient of turbulence modeling. Some models are so complex and contain so many constants and ad hoc functions, that these can be altered until the numerical predictions agree with experimental measurements. Even coding errors can apparently be overcome with appropriate turbulence modeling.

Kang and Suzuki [114] computed the flow for a high speed jet in a pipe using the standard k-ε turbulence model with law-of-the-wall type wall functions with constant values for c_μ and Pr_t. They had to alter the enthalpy law of the wall to make their heat transfer rate predictions agree with experiments.

Watkins and Gooray [115] and Gooray et al. [116] predicted the flow through asymmetric planar expansions and pipe expansions using a k-ε turbulence model. The model was altered to include the effects of pressure-strain interactions and streamline curvature by using functional relations for c_μ in the viscosity definition and Pr_t. The expressions for c_μ and Pr_t were derived by using algebraic stress

relations. They used a two pass procedure. The first pass was with a high-Reynolds-number k-ε with wall functions to find the point of reattachment. The second pass consisted of the high-Reynolds-number k-ε turbulence model upstream of reattachment and the low-Reynolds-number k-ε equations of Jones and Launder [117] downstream of reattachment. The correlation between their predictions and experiments was very good. However, their expression for Pr_t for the Cartesian grid can be shown to be between 0.2 and 0.3 for fully developed equilibrium flow in a channel rather than the well accepted value of 0.9.

Chieng [118] used a low-Reynolds-number k-ε turbulence model to predict the heat transfer in abrupt pipe expansions. Chieng's predictions do not agree with the measurements of Zemanick and Dougall [84].

Amano [119] and Amano et al. [89] expanded on the two equation wall function method of Chieng and Launder [111]. Amano used a three zone wall function and did not require local equilibrium between production and dissipation in the ε-equation. The predictions compare well with those of Zemanick and Dougall [84] for the d/D=0.54 expansion and high Reynolds number but do not compare as well for the d/D=0.43 expansion. The computations indicated that the maximum Stanton number was before reattachment and that the dependency of the level of heat transfer on Re is slightly less than that of the experimental data. In Amano et al. [89], the computer predictions were compared with a concurrent set of experimental measurements.

C. Scope and Contributions of the Present Study

The purpose of this study is to determine the degree to which the boundary-layer equations can be used to model the flow through a region of flow reversal caused by an abrupt channel expansion. Since the previous studies that used the boundary-layer equations [39, 27, 42] provided only isolated comparisons with experiments and Navier-Stokes solutions, the limitations of the boundary-layer equations have not been previously defined. The purpose of the present work is to more clearly define the limitations of such solutions for both two-dimensional and axisymmetric expansion flows with respect to Reynolds number and expansion ratio. Determining the range of applicability of the boundary-layer equations is of practical importance since the effort required to solve the boundary-layer equations is an order of magnitude less than that required for the full Navier-Stokes equations. Furthermore, the constant property laminar boundary-layer equations are independent of Reynolds number. Therefore, the boundary-layer equations need to be solved only once for any given expansion ratio and the solution can then be applied through proper scaling for any channel Reynolds number.

Figure 2 shows the geometry of the flows considered. Since both axisymmetric and symmetric planar expansions occur in applications, both types of geometry were considered. This allowed comparison with the results of as many other studies as possible. Only flows that were fully developed at the step were included in this work, so viscous-

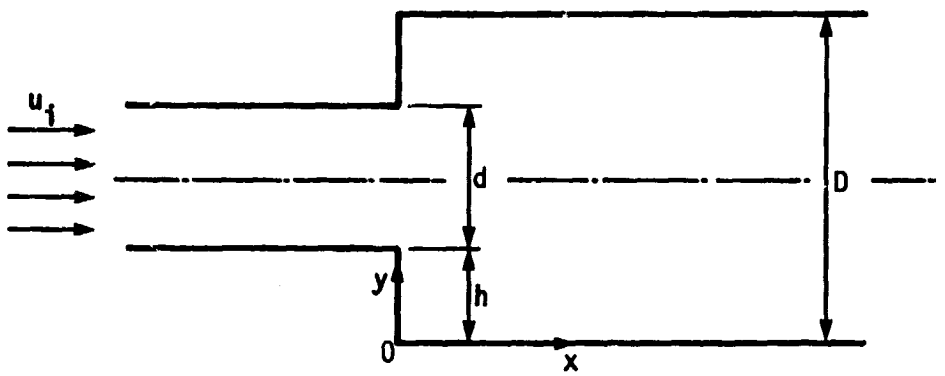

Figure 2. Symmetric expansion geometry

inviscid interaction was not applicable. Compressibility effects were negligible in the flow regimes considered so compressibility effects could be neglected. However, for flows with heat transfer, the variation of fluid properties with temperature was taken into account.

Turbulence modeling of rapid expansion flows, especially with heat transfer, is a major challenge. None of the conventional algebraic or two-equation models work satisfactorily for the rapid expansion geometry. A number of model combinations were evaluated in this study. Turbulent flows were predicted by adding a turbulent viscosity to the molecular viscosity as was first proposed by Boussinesq [120]. The effect of various improvements and modifications of the k-ε turbulence

model was considered. Some of the modifications tried included extra terms in the k and ε equations, algebraic stress models, and variable turbulent Prandtl numbers. Special attention was given to different methods of modeling the near-wall turbulence. The hydrodynamic and heat transfer predictions of the boundary-layer formulation were compared with other numerical results and with experimental measurements.

The contributions of the present study are as follows.

1. The limiting Reynolds number at which the laminar prediction begins to be poor is defined.
2. The circumstances under which global iteration improves predictions are found.
3. Those flow parameters well predicted by the boundary-layer formulation for laminar and turbulent flow are defined.
4. Near-wall turbulence modeling was considered that did not assume a special form for velocity or temperature, i.e., the momentum, continuity, and energy equations were solved throughout the flow field including the near-wall region.
5. A modification of the turbulent viscosity model of Johnson and King [121] was developed that gives improved results over the law-of-the-wall viscosity model in the separated flow.
6. This is the first study using the boundary-layer equations to predict turbulent flow with heat transfer through rapid expansions.
7. An inexpensive numerical procedure is developed that has practical applications in predicting the flow and heat transfer in devices having large regions of separated flow.

II. GOVERNING EQUATIONS

In this chapter, the theoretical background needed to solve the problem of flow and heat transfer in a sudden expansion is developed. The relevant partial-differential equations will be developed with their associated boundary and initial conditions. The compressible, variable property, turbulent boundary-layer equations will be developed first. These equations are the most general needed in this thesis. Particular simplifications of the compressible turbulent boundary-layer equations will be made as needed. It is a simple matter to make the necessary simplifications of the general turbulent boundary-layer equations to obtain, for instance, the laminar incompressible equations. A special form of the laminar incompressible equations can then developed that is independent of the Reynolds number. The turbulence models used will then be discussed. Finally, the relevant engineering parameters are presented.

A. Variable Property Turbulent Boundary-Layer Equations

The continuity equation is by far the easiest equation to derive. For this reason, this equation will be developed in more detail than the momentum or energy equations in order to show the methodology and introduce the necessary background information.

1. Conservation of mass

A mass balance of the fluid passing through a fixed control volume produces the following equation

$$\frac{\partial \rho}{\partial t} + \nabla \cdot (\rho \vec{V}) = 0 \tag{2.1}$$

Equation (2.1) is valid for any nonreacting continuum of fluid, including fluid with turbulence. However, to discretize the equation for computer simulation of the turbulent motion, a grid fine enough to capture the very small length scales of the turbulent motion must be used. For a practical problem, this would require the solution of a number of algebraic equations that is beyond the capabilities of a present day computer. Since turbulent motion is characterized as random motion in which statistical averages are meaningful [122], time averaged equations can be used in place of the instantaneous set. To average the equations, the instantaneous velocity of the fluid certain properties) is considered as the sum of an averaged value and its fluctuating value [123].

$$\bar{f} = f + f' \tag{2.2}$$

Here, f represents a velocity component or property of the fluid and is defined as

$$\bar{f} = \int_{t}^{t+\Delta t} f(t)dt \tag{2.3}$$

Note that by definition $\bar{f}' = 0.0$, and $\overline{\bar{f}'\bar{g}} = 0.0$ where $\bar{g}$ is some averaged variable. The time of averaging Δt is long enough to average out the fluctuations due to turbulence but not long enough to influence the variation of the mean flow with time. The density and velocity vector are written in the following form

$$\rho = \bar{\rho} + \rho' \tag{2.4}$$

$$\vec{V} = \bar{\vec{V}} + \vec{V}' \tag{2.5}$$

Equations (2.4) and (2.5) are substituted into (2.1) and the equation is time averaged. After canceling the terms that are zero, a time averaged equation results:

$$\nabla \cdot (\bar{\rho}\bar{\vec{V}} + \overline{\rho'\vec{V}'}) = 0 \tag{2.6}$$

It is now convenient to introduce the following type of averaging that is often used for gas mixtures [123]

$$f = \tilde{f} + f'' \tag{2.7}$$

where

$$\tilde{f} = \frac{\overline{\rho f}}{\bar{\rho}} \tag{2.8}$$

It can be shown that

$$\overline{\rho' u'} = -\bar{\rho}\tilde{u}'' \tag{2.9}$$

Using (2.9) in (2.6) and making the assumption of steady flow, Eq. (2.6) becomes

$$\nabla \cdot (\bar{\rho}\vec{\tilde{V}}) = 0 \tag{2.10}$$

Under the boundary-assumptions [123],

$$\bar{u} = \tilde{u} \tag{2.11}$$

Equation (2.10) is now written in expanded form for two dimensional planar and axisymmetric flow with $\tilde{u}$ substituted for $\tilde{u}$.

$$\frac{\partial}{\partial x}(r^m \bar{\rho}\tilde{u}) + \frac{\partial}{\partial y}(r^m \bar{\rho}\tilde{v}) = 0 \tag{2.12}$$

Equation (2.12) is valid for compressible flow for both two-dimensional Cartesian and axisymmetric geometries. When the geometry is Cartesian, m is taken as zero; when axisymmetric, m is taken as one.

It is convenient (but not essential [39]) when using the present scheme to employ the stream function, ψ, in place of v as a variable. This is done merely to make the equations more suitable for external flows with separation. When using the boundary-layer equations for external flows with separation, the displacement thickness is specified as a boundary condition to overcome the singularity at separation. If u-v variables are used, the displacement thickness must be obtained by integration of the velocity profile; if u-ψ variables are used it is obtained directly without integration. An expression for the stream function is

$$\frac{\partial \psi}{\partial x} = - r^m \bar{\rho}\tilde{v} \tag{2.13}$$

Substituting Eq. (2.13) into the continuity Eq. (2.12) gives a new form of the continuity equation

$$\frac{\partial \psi}{\partial y} = r^m \bar{\rho}\bar{u} \tag{2.14}$$

Note that the definition of ψ for compressible flow corresponds to a mass flow rate rather than a volumetric flow rate as for incompressible flows.

Equation (2.12) is the same as the continuity equation for laminar flow neglecting the tilda and bar notation above the averaged variables.

2. Conservation of momentum

The momentum equation is merely a statement of Newton's second law for fluid flowing through a nonaccelerating control volume. In vector form for compressible flows, it is [124]

$$\rho \frac{D\vec{V}}{Dt} = - \nabla p - [\nabla \cdot \vec{\tau}] + \rho \vec{g} \tag{2.15}$$

Note that $\vec{\tau}$ is the stress tensor and $\vec{g}$ is the gravity vector. To obtain the equation valid for compressible turbulent boundary layers, a derivation similar to that followed for the continuity equation must be followed. However, for the momentum and energy equations this is so lengthy that the steps will only be outlined here. (See Cebeci and Smith [123] and Anderson et al. [4] for the details of the derivation.)

The main steps required to obtain the compressible turbulent boundary-layer momentum equations are as follows.

(1) Substitute the sum of the averaged and fluctuating value for each of the instantaneous velocity components, density, and pressure.

(2) Time average the equations and cancel the terms that are zero due to the time averaging.

(3) Substitute the continuity equation into the momentum equation.

(4) Neglect the body forces and the mean or averaged unsteady terms.

(5) Make the boundary-layer assumptions and cancel the higher order terms by doing an order of magnitude analysis. The main assumptions made are:

$$\frac{\partial}{\partial y} >> \frac{\partial}{\partial x} \ , \ u >> v \ , \ \bar{u} = \tilde{u}$$

For subsonic flow, the x-momentum boundary-layer equation is then

$$\bar{\rho}\tilde{u}\frac{\partial \tilde{u}}{\partial x} + \bar{\rho}\tilde{v}\frac{\partial \bar{u}}{\partial y} = -\frac{d\bar{p}}{dx} + \frac{1}{r^m}\frac{\partial}{\partial y} r^m(\mu\frac{\partial \bar{u}}{\partial y} - \bar{\rho}\overline{u'v'}) \qquad (2.16)$$

The y-momentum equation reduces to

$$-\frac{\partial \bar{p}}{\partial y} - \frac{\partial}{\partial y}(\bar{\rho}\overline{v''v''}) = 0 \qquad (2.17)$$

The pressure gradient in the y-direction is assumed to be small compared to the one in the x-direction, so the y-momentum equation can be neglected [4].

Equation (2.16), neglecting the bars indicating a time averaged quantity and the Reynolds stress term, $\bar{\rho}\overline{u'v'}$, is the same as the x-momentum equation governing laminar boundary-layer flow. The extra term $(-\bar{\rho}\overline{u'v'})$ arises due to the convection of turbulence. It is grouped with

the laminar-like viscous term because $\overline{u'v'}$ can be thought of as increasing the stress through exchange of momentum in the fluid. Due to the $-\bar{\rho}\overline{u'v'}$ term, there are presently more unknowns than equations. The extra equations needed to solve the system are obtained through turbulence modeling.

At this point, it is convenient to introduce a turbulent viscosity μ_t defined as

$$\mu_t \frac{\partial \bar{u}}{\partial y} = - \bar{\rho}\overline{u'v'} \tag{2.18}$$

as was first suggested by Boussinesq in 1877 [122]. The Boussinesq assumption is actually the first turbulent modeling assumption made. Further turbulence modeling assumptions and the evaluation of the turbulent viscosity is discussed in Section C of this chapter. Of course if the flow being predicted is laminar, all turbulent fluctuation velocities are zero, so μ_t is also zero.

At this point, it is convenient to drop the bars and tildas in Eqs. (2.12) and (2.16). By substituting Eq. (2.18) into Eq. (2.16), the momentum equation becomes

$$\rho u\frac{\partial u}{\partial x} + \rho v\frac{\partial u}{\partial y} = -\frac{dp}{dx} + \frac{1}{r^m}\frac{\partial}{\partial y}\, r^m(\mu+\mu_t)\frac{\partial u}{\partial y} \tag{2.19}$$

The unbarred variables are recognized to represent time averaged quantities in turbulent flow.

Equation (2.19) is a parabolic equation in x. It is normally solved by marching from a starting position to the desired location in

the x-direction. As the solution is marched down the channel for $u > 0$, the solution should only be influenced by the domain behind the x-position that has been reached by marching. What is beyond the point reached by marching in the x-direction (downstream) should not influence the solution of a truly parabolic equation, or the formulation becomes unstable. However, with flow reversal, flow moving in the negative x-direction will influence the solution from downstream. This downstream influence causes the streamwise marching solution of the parabolic equations to be unstable unless special measures are taken. The problem lies in the x-convective term $u\partial u/\partial x$ since it is the term that contributes the downstream influence.

Reyhner and Flugge-Lotz [53] proposed that the convective term in the x-direction be replaced by $c|u|\partial u/\partial x$ where c is a small positive constant or zero. This approximation is referred to as the FLARE approximation. For rapid expansions, the velocity in the reversed flow is about 10% to 20% that of the main flow stream, so this assumption seems valid. For the momentum and energy equations, c will be taken as one if u is positive; c will be taken as zero if u is negative. Thus, any downstream influence to the parabolic equations is cancelled and the formulation is stable. Governing partial-differential equations for variables associated with turbulence will be developed in following sections that have an x-convective term similar to Eq. (2.19). In solving these turbulence modeling equations, taking c as 0.0 when u was negative caused numerical instabilities near the wall associated with

round-off errors in the computer. For stability reasons, c was set to 1.0 in the turbulence modeling equations when using the FLARE approximation.

Repetitive global iteration through the flow field can be used in place of the FLARE approximation to provide stability to the boundary-layer equation marching procedure. The x-convective term can be approximated with a local-upwind finite-difference as opposed to disregarding or approximating this term as is done with the FLARE approximation.

We can also use the previously introduced stream function to eliminate v from Eq. (2.19). After making the FLARE approximation and using Eq. (2.13) to eliminate v from Eq. (2.32a), the resulting x-momentum equation valid for turbulent compressible flow is

$$c\rho u\frac{\partial u}{\partial x} - \frac{1}{r^m}\frac{\partial \psi}{\partial x}\frac{\partial u}{\partial y} = -\frac{dp}{dx} + \frac{1}{r^m}\frac{\partial}{\partial y}r^m(\mu+\mu_t)\frac{\partial u}{\partial y} \tag{2.20}$$

Equation (2.20) is singular at the centerline for axisymmetric geometries. When r = 0, the y-convective term can be removed from Eq. (2.20) since v is zero and no convection in the y direction will occur. l'Hospital's rule can then be used to find the valid representation of the diffusion term as r approaches zero. The momentum equation valid for axisymmetric flow with r = 0 is

$$c\rho u\frac{\partial u}{\partial x} = -\frac{dp}{dx} + 2\frac{\partial}{\partial y}(\mu+\mu_t)\frac{\partial u}{\partial y} \tag{2.21}$$

3. Conservation of energy

The energy equation is simply a statement of the first law of thermodynamics for fluid passing through a stationary control volume. For flows which are not isothermal, the energy equation must be solved along with the continuity and momentum equations. There are two main reasons why the energy equation must be introduced: (1) heat transfer quantities or temperature fields are desired or (2) the change of the fluid properties with temperature will affect the hydrodynamic predictions.

The energy equation can be written in terms of the total enthalpy, H.

$$\frac{\partial}{\partial t}(\rho H) + \nabla\cdot(\rho H\vec{V}) = \frac{\partial p}{\partial t} + \nabla\cdot\{[\vec{\tau}\cdot\vec{V}] - \vec{q}\} \tag{2.22}$$

H is defined as

$$H = h + \frac{1}{2}u_i u_i \tag{2.23}$$

The stress tensor, $\vec{\tau}$, depends on the coordinate system (see Anderson et al. [4] for the different forms). The heat flux vector, $\vec{q}$, can be written in indicial form as

$$q_i = - k\frac{\partial T}{\partial x_i} \tag{2.24}$$

The body forces have been neglected.

Cebeci and Smith [123] show the details of obtaining the form of the energy equation used in this thesis. An outline of the steps

required to obtain the desired form of the energy equation follows. Equation (2.22) is time averaged in the same way as the continuity and momentum equations discussed in the previous sections. The boundary-layer assumptions are then used to eliminate the higher order terms through an order of magnitude analysis. Under boundary-layer assumptions, $\bar{H} = \tilde{H}$. For steady, subsonic, compressible flow, the energy equation becomes

$$\rho u\frac{\partial H}{\partial x} + \rho v\frac{\partial H}{\partial y} = \frac{1}{r^m}\frac{\partial}{\partial y}\left\{r^m\left(\frac{\mu}{Pr}\frac{\partial H}{\partial y} - \rho c_p\overline{v'T'} + u\left[(1-\frac{1}{Pr})\mu\frac{\partial u}{\partial y} - \rho\overline{u'v'}\right]\right)\right\} \tag{2.25}$$

Equation (2.25) is the same as the laminar energy equation except for the two extra terms involving the fluctuating turbulent quantities, $-\rho c_p\overline{T'v'}$ and $-\rho\overline{u'v'}$. The heat flux caused by the $\overline{T'v'}$ term is assumed to be proportional to $\partial T/\partial y$. A turbulent Prandtl number, Pr_t, is defined by the following equation

$$-\rho c_p\overline{v'T'} = \frac{c_p\mu_t}{Pr_t}\frac{\partial T}{\partial y} \tag{2.26}$$

Pr_t must be determined by turbulence modeling. When Eqs. (2.18), (2.26), and (2.13) are substituted into Eq. (2.25) and after making the FLARE approximation in the same way as was done for the momentum equation, the turbulent compressible boundary-layer energy equation becomes

$$c\rho u\frac{\partial H}{\partial x} - \frac{1}{r^m}\frac{\partial \psi}{\partial x}\frac{\partial H}{\partial y} = \frac{1}{r^m}\left[\frac{\partial}{\partial y}\, r^m\left(\left[\frac{\mu}{Pr} + \frac{\mu_t}{Pr_t}\right]\frac{\partial H}{\partial y} + \left[\mu(1-\frac{1}{Pr}) + \mu_t(1-\frac{1}{Pr_t})\right]u\frac{\partial u}{\partial y}\right)\right] \tag{2.27}$$

The bars have been dropped from Eq. (2.27) and all the flow variables are understood to be averaged values.

Equation (2.27) is singular when r = 0 for axisymmetric geometries. By removing the y-convective term and using l'Hospital's rule, the singularity can be removed. Equation (2.27) becomes

$$\rho u\frac{\partial H}{\partial x} = 2\frac{\partial}{\partial y}\left(\left[\frac{\mu}{Pr} + \frac{\mu_t}{Pr_t}\right]\frac{\partial H}{\partial y} + \left[\mu(1-\frac{1}{Pr}) + \mu_t(1-\frac{1}{Pr_t})\right]u\frac{\partial u}{\partial y}\right) \qquad (2.28)$$

Equation (2.28) is the governing momentum equation when r = 0 for axisymmetric geometries.

4. Boundary and initial conditions

a. Boundary conditions Two boundary conditions for both u and H were used, one at y = 0 and one at the centerline. One boundary condition at the wall was specified for ψ. In addition to the wall boundary condition for ψ, another restriction the solution must satisfy is the channel mass flow constraint. The mass flow constraint is merely a mass balance across the entire channel cross section. The channel mass flow constraint is not actually used as a boundary condition but will be necessary later in order to solve for dp/dx.

The no-slip condition at the wall and the symmetry condition at the channel centerline give the boundary conditions for the velocity as

$$u(x,0) = 0 \ , \ \frac{\partial u}{\partial y}(x,y_{centerline}) = 0 \qquad (2.29)$$

The stream function boundary condition and mass flow constraint for the channel cross section are respectively

$$\psi(x,0) = 0 \ , \ \psi(x,y_{centerline}) = \int_0^{D/2} \rho r^m u(0,y)dy \tag{2.30}$$

The boundary condition for H at the centerline is the symmetry condition

$$\frac{\partial H}{\partial y}(x,y_{centerline}) = 0 \tag{2.31}$$

Two different H boundary conditions are possible at the wall depending on whether the temperature or the heat transfer rate is specified. For specified wall temperature, $T_w(x)$, the boundary condition is

$$H(x,0) = c_p T_w(x) \tag{2.32a}$$

For specified heat flux, $q_w(x)$, the boundary condition is

$$-k\frac{\partial}{\partial y}(H-\frac{u^2}{2}) = c_p q_w(x) \tag{2.32b}$$

b. Initial conditions The initial conditions depend on whether the flow is turbulent or laminar. Above the lip of the step ($y > h$), a fully developed turbulent or fully developed laminar inlet profile was used as the inlet condition for u. Along the face of the step, the logical condition due to the no slip requirement is

$$u(0,y) = 0, \qquad 0 \le y < h \tag{2.33}$$

However Acrivos and Schrader [27] argue that this is not correct for the boundary-layer equation set. They say that a nonzero velocity should be used to take into account the effect of the fluid returning from downstream in the recirculating region. Acrivos and Schrader used the following initial condition on the face of the step.

$$u(0,y) = u_c(y), \qquad 0 \le y \le h/2 \tag{2.34}$$

$$u(0,y) = - u_c(h-y), \qquad h/2 < y \le h$$

The fluid velocity was taken as zero for this study except for in a few cases used to determine the effect of the nonzero velocity on the face of the step.

Once the initial velocity is decided upon, the following integral gives ψ

$$\psi(0,y) = \int_0^y \rho r^m u(0,\xi) d\xi \tag{2.35}$$

where ξ is a dummy variable of integration.

Since the experimental studies compared with used an insulated step face and a fully developed temperature profile, the inlet condition for H is

$$\frac{\partial H}{\partial x}(0,y) = 0, \qquad 0 \le y \le h \tag{2.36a}$$

$$H(0,y) = c_p T(0,y) + \frac{1}{2} u^2(0,y), \qquad h < y \le D/2 \tag{2.36b}$$

For a fully developed inlet profile and an unheated entry length,

$$T(0,y) = T_b(0) \tag{2.37}$$

Where $T_b(x)$ is the mean or bulk temperature.

5. Equation of state

In order to solve the above conservation equations, ρ, μ, k, and Pr must be specified. This is done by introducing an equation of state.

In general, any property of the fluid, f, is a function of temperature and pressure, i.e.,

$$f = f(T,P) \tag{2.38}$$

Since one of the main purposes of this study is to compare with experimental measurements, the fluids of interest are water and air at moderate temperatures and nearly atmospheric pressures. For these restrictions, all the properties of water are very weak functions of pressure [125]. The density of water for all practical purposes is constant. For air near atmospheric pressure, μ, k, and Pr are all very weak functions of pressure. For air, the density is found from the ideal gas equation

$$\rho = \frac{p}{RT} \tag{2.39}$$

where R is the gas constant. Thus, all properties except the density for air vary only with temperature and can be expressed as

$$f = f(T) \tag{2.40}$$

The particular functions used to approximate the fluid properties as a function of temperature for air and water are given in Appendix A.

B. Laminar Constant Property Nondimensionalized Equations

For laminar constant property flows, the boundary-layer equations can be nondimensionalized such that they are independent of the Reynolds

number. The method of nondimensionalizing has been previously used for developing flow in channels. It reduces the hydrodynamic solution to a function of the size of the expansion, the inlet conditions, and the boundary conditions.

For constant density, ρ can be removed from the partial-differential operators of Eq. (2.12) and canceled from the equation. A different stream function must be defined for the incompressible case than was used for the compressible case in the previous section. The stream function for incompressible flow is defined as

$$v = - \frac{\partial}{\partial x}(\psi_{cp}) \tag{2.41}$$

The constant property continuity equation can be written as

$$u = \frac{\partial}{\partial y}(\psi_{cp}) \tag{2.42}$$

To nondimensionalize the conservation equations, the following dimensionless variables are introduced:

$$U = \frac{u}{u_i} \quad , \quad X = \frac{x}{dRe} \quad , \quad Y = \frac{y}{d} \quad , \quad \eta = \frac{H}{u_i^2} \tag{2.43a}$$

$$\Psi = \frac{\psi_{cp}}{d^{1+m} u_i} \quad , \quad R = \frac{r}{d} \quad , \quad \beta = - \frac{dRe}{\rho u_i^2} \frac{dp}{dx} \tag{2.43b}$$

Again, m is zero if the geometry is two-dimensional; m is one if the geometry is axisymmetric. The Reynolds number is based on u_i and d.

Using Eq. (2.43) in Eq. (2.42) gives the dimensionless continuity equation

$$U = \frac{1}{R^m} \frac{\partial \Psi}{\partial Y} \tag{2.44}$$

Substituting Eq. (2.43) into the laminar form of Eq. (2.16) gives the dimensionless x-momentum equation

$$cU\frac{\partial U}{\partial X} - \frac{1}{R^m}\frac{\partial \Psi}{\partial X}\frac{\partial U}{\partial Y} = \beta + \frac{1}{R^m}\frac{\partial}{\partial Y}\left(R^m \frac{\partial U}{\partial Y}\right) \tag{2.45}$$

Equations (2.43) with the laminar energy equation (Eq. 2.27) gives the dimensionless energy equation

$$cU\frac{\partial \eta}{\partial X} - \frac{1}{R^m}\frac{\partial \Psi}{\partial X}\frac{\partial \eta}{\partial Y} = \frac{1}{R^m}\frac{\partial}{\partial Y}\left(R^m\left[\frac{1}{Pr}\frac{\partial \eta}{\partial Y} + \left(1 - \frac{1}{Pr}\right)U\frac{\partial U}{\partial Y}\right]\right) \tag{2.46}$$

Note that the FLARE approximation has been made in the same way as done for the dimensional equations in the previous section.

The boundary conditions for U are

$$U(X,0) = 0 \ , \ \frac{\partial U}{\partial Y}\left(X,1 + \frac{h}{d}\right) = 0 \tag{2.47}$$

The stream function is set to zero at the channel wall ($\Psi(X,0) = 0$). The stream function at the centerline is determined from the inlet profile at the step. For a parabolic, fully developed inlet

$$\Psi\left(X,1 + \frac{h}{d}\right) = \frac{1}{2}, \quad \text{planar expansion} \tag{2.48a}$$

$$\Psi\left(X,1 + \frac{h}{d}\right) = \frac{1}{8}, \quad \text{axisymmetric expansion} \tag{2.48b}$$

The boundary condition for η at the centerline is the symmetry condition

$$\frac{\partial \eta}{\partial Y}\left(X,1 + \frac{h}{d}\right) = 0 \tag{2.49}$$

There are two possible boundary conditions for η at the wall depending on if the heat flux or the wall temperature is specified. If the wall temperature is specified, the condition is

$$\eta(X,0) = \frac{i}{u_i^2} c_p T_w(X,0) \tag{2.50a}$$

If the heat flux at the wall is specified, the condition is

$$-\frac{\partial \eta}{\partial Y}(X,0) = Q_w + \frac{\partial}{\partial Y}\frac{U^2}{2}\Big|_{y=0} \tag{2.50b}$$

where Q_w is a dimensionless wall heat flux given by

$$Q_w = \frac{Pe\ q_w}{\rho u_i^3} \tag{2.51}$$

Pe is the Peclet number (Pe = Re × Pr).

A parabolic initial condition for U at the inlet was specified. U was taken as zero along the face of the step. The initial condition for the stream function is obtained by integrating U from the wall to the centerline as follows

$$\Psi(0,Y) = \int_0^Y R^m U(0,\xi)d\xi \tag{2.52}$$

The initial condition for the nondimensional total enthalpy is

$$\eta(0,Y) = \frac{c_p T(0,Y)}{u_i^2} + \frac{1}{2}U^2(0,Y) \tag{2.53}$$

C. Turbulence Modeling

In a previous section, Eq. (2.18) defined a turbulent viscosity, μ_t according to the Boussinesq approximation. Equation (2.26) defined a turbulent Prandtl number, Pr_t. In order to predict turbulent flow, μ_t and Pr_t must be approximated by turbulence modeling. The modeling used in this work is discussed in this section.

1. Equilibrium turbulence equations

Turbulent boundary-layer flow with no separation can be divided into two main regions: (1) the inner region which is not highly influenced by the pressure gradient, and (2) the outer region which is highly affected by the pressure gradient. The inner region can be further divided into three parts: a laminar sublayer, a buffer region, and a fully turbulent region. In the laminar sublayer, the molecular viscosity dominates; in the fully turbulent region, the Reynolds stresses dominate. Both the stresses due to molecular viscosity and Reynolds stresses are important in the buffer region.

Dimensional analysis shows that a nondimensional velocity, u^+, and a nondimensional distance from the wall, y^+, are important in describing the flow in the inner region. They are defined as

$$y^+ = \frac{u_\tau y \rho}{\mu}, \quad u^+ = \frac{u}{u_\tau} \tag{2.54}$$

where u_τ is a turbulent velocity scale $(\tau_w/\rho)^{1/2}$ and τ_w is the shear stress at the wall. When y^+ and u^+ are used to plot turbulent boundary-

layer velocity profiles with no separation, the profiles collapse into one curve in the inner region. Experiments have shown that the time averaged thicknesses of these three layers for smooth walls are approximately

laminar sublayer	$0 < y^+ < 5$
buffer layer	$5 < y^+ < 30$
fully turbulent layer	$30 < y^+$

The molecular viscosity of gases can be calculated by

$$\mu_t = \rho(\text{length scale})(\text{velocity scale}) \tag{2.55}$$

Prandtl adopted this idea for turbulent flow and proposed a length scale, ℓ, for the inner region that is proportional to the distance from the wall. Van Driest later modified ℓ by multiplying it by an experimentally determined damping function D [126]. The modified length scale becomes

$$\ell = \kappa D y \tag{2.56}$$

where $\kappa = 0.41$. The van Driest damping function, D, is given by

$$D = 1 - \exp(-y^+/A^+) \tag{2.57}$$

where A^+ is usually taken as 25 or 26. Prandtl proposed a velocity scale as

$$(\text{velocity scale}) = \ell \left|\frac{\partial u}{\partial y}\right| \tag{2.58}$$

The turbulent viscosity for the inner region can then be expressed as

$$\mu_t = \rho \ell^2 \left|\frac{\partial u}{\partial y}\right| \tag{2.59}$$

Equation (2.59) is known as the Prandtl mixing length model for turbulent viscosity. With μ_t specified, the governing equations can be integrated for the inner region.

By making the Couette flow assumption ($\partial u/\partial x$ is very small and can be neglected) the momentum equation is reduced to an ODE [127]. This assumption is valid near the wall. By neglecting the turbulent viscosity, this ODE can be integrated in the laminar sublayer of the inner region to show that

$$u^+ = y^+ \tag{2.60}$$

This is equivalent to saying that the shear stress is constant in the near-wall region. Similarly, by neglecting the laminar viscosity in the fully turbulent part of the inner region and using Eq. (2.59), this ODE can be integrated to show that

$$u^+ = \frac{1}{\kappa}\ln(y^+) + B \tag{2.61}$$

where B is a constant near 5.0. The region for which Eq. (2.61) is valid is sometimes referred to as the logarithmic layer. Equation (2.61) is often called the "law of the wall". The velocity in the buffer region, $u^+ = f(y^+)$ must be obtained experimentally.

There have been attempts to modify Eq. (2.56) to make the mixing length more applicable for reversed flow. Reeves [123] and McD Galbraith and Head [129] recommend that Eq. (2.56) be multiplied by $(\tau_{max}/\tau_w)^{1/2}$ The mixing length for the inner region then becomes

$$\ell = \kappa \frac{\tau_{max}}{\tau_w} Dy \tag{2.62}$$

Carter and Wornom [130] and Pletcher [131] recommend that the van Driest damping function, D, by based on the maximum shear stress in the boundary layer instead of the wall shear stress. The modified van Driest damping factor is then

$$D = 1 - \exp[-(\frac{\rho}{\mu}\left|\frac{\partial u}{\partial y}\right|_{max})^{1/2} y/A^+] \tag{2.63}$$

For an attached boundary layer, Eqs. (2.63) and (2.63) reduce to Eqs. (2.56) and (2.57).

The value of 25 for A^+ corresponds to a boundary layer with a zero pressure gradient. Kays and Moffat [132] proposed an empirically based function for A^+ valid for nonzero pressure gradients as

$$A^+ = 25.0/(ap^+ + 1) \tag{2.64}$$

where p^+ is given by

$$p^+ = \frac{\mu(dp/dx)}{\rho^{1/2}\tau_w^{3/2}}$$

and

$$a = 30.2, \quad p^+ < 0$$

$$a = 20.6, \quad p^+ > 0$$

Johnson and King [121] expressed the turbulent viscosity according to Eq. (2.55) but used the square root of the maximum Reynolds stress, $(\overline{u'v'}_m)^{1/2}$, as the turbulent velocity scale. They used $D_{15}^2 \kappa y$ as the length scale where D_{15} is the van Driest damping function based on an A^+ value of 15 instead of the usual 25. The expression for μ_t then becomes

$$\mu_t = \rho D_{15}^2 \kappa y (-\overline{u'v'}_m)^{1/2} \tag{2.65}$$

Equation (2.65) can be used in place of Eq. (2.59) for the turbulent viscosity expression in the inner region.

For the outer region, ℓ is often taken as proportional to the boundary layer thickness with Eq. (2.58) used as the velocity scale [4]. Another common method is to use a constant times the displacement thickness as the length scale and the velocity at the outer edge of the boundary layer as the velocity scale. The expression for the turbulent viscosity in the outer region then becomes

$$\mu_t = \rho(K\delta^*)(u_e) \tag{2.66}$$

where K is a constant ($\simeq 0.016$), δ^* is the displacement thickness as evaluated for incompressible flow [145], and u_e is the velocity at the edge of the boundary layer.

Equations (2.59), (2.65), and (2.66) describe zero equation turbulence models. One way of classifying turbulence models is to add the number of PDEs used in the turbulence model. Each PDE counts as one equation; each ODE counts as one-half an equation; each algebraic equation counts as zero equations.

Zero equation turbulence models are not able to take into account the effects of diffusion or convection of turbulence length scales or velocity scales. They only balance the production and dissipation of turbulence quantities [3]. To account for convection and diffusion, PDEs are required to introduce directional rates of change. When the

dissipation of turbulence balances the production, the turbulence is said to be in local equilibrium. Therefore, zero or algebraic turbulence models are valid for regions in local equilibrium. In the shear layer for flow over a step, turbulent kinetic energy production exceeds dissipation [24]. This turbulent kinetic energy must be convected and diffused away. This indicates that in the region affected by the shear layer, a zero equation model is inadequate and models involving one or more PDEs or ODEs must be used.

2. k-ε equations

In this section, the two-equation turbulence models investigated in this work are described. For the k-ε model, turbulent length and velocity scales for use in Eq. (2.55) are described by PDEs [3]. The velocity scale used is $k^{1/2}$, where k is called the turbulent kinetic energy and is defined as

$$k = \frac{1}{2} \overline{(u'^2 + v'^2 + w'^2)} \tag{2.67}$$

The length scale is defined as

$$L = c_D \frac{k^{3/2}}{\varepsilon} \tag{2.68}$$

where c_D is a constant listed in Table 2 and ε is the dissipation rate of k. The expression for the turbulent viscosity is given by

$$\mu_t = \rho c_\mu \frac{k^2}{\varepsilon} \tag{2.69}$$

where c_μ is usually 0.09.

Table 2. Turbulent Modeling Constants

Constant	Value	Reference	Constant	Value	Reference
c_μ	0.09	[133]	α	2.2	[134]
c_D	0.164	[39]	γ	0.55	[134]
c_1	1.35	[135]	$c_{\theta 1}$	3.0	[115]
c_2	1.8	[135]	$c_{\theta 2}$	0.33	[115]
c_3	0.0115	[135]	$c_{\theta 1w}$	0.5	[115]
c_4	0.5	[135]	c_w	2.44	[115]

At this point, the unknown μ_t has been expressed in terms of two other unknowns, k and ε. Transport PDEs can be derived for both k and ε from the Navier-Stokes equations, but these PDEs involve other unknowns. The formulation must be "closed" by modeling assumptions to provide the necessary equations for the additional unknowns. After these modeling assumptions, the k and ε equations can be written as

$$c\rho|u|\frac{\partial \phi}{\partial x} - \frac{1}{r}\frac{\partial \psi}{\partial x}\frac{\partial \phi}{\partial y} = \frac{1}{r}\frac{\partial}{\partial y}\left[r\Gamma_\phi \frac{\partial \phi}{\partial y}\right] + S_\phi \qquad (2.70)$$

where ϕ is either k or ε, depending on the equation desired. S_ϕ is a source term.

Two different sets of source ter- and Γ's were used in this study: a high Reynolds number form used by Launder and Spalding [133], and a low Reynolds number form developed by Chien [135]. Chien added extra

terms to Γ_ϕ and S_ϕ to make the original high turbulent Reynolds number equations used by Launder and Spalding applicable in regions of low turbulent Reynolds number flow near the wall.

In referring to turbulence models, the Reynolds number of turbulence or turbulent Reynolds number is not the same as the Reynolds number based on the the channel width or pipe diameter and the average inlet velocity. The dividing line between the low and high turbulent Reynolds number regions is not universally or clearly defined for all types of flow. There are several ways to define the turbulent Reynolds number depending on the velocity scale and the length scale used. If y is the length scale and u_τ the velocity scale, the turbulent Reynolds number is merely y^+. For this definition, the high turbulent Reynolds number flow for an attached boundary layer would be that part of the flow for which $y^+ > 30$. The low Reynolds number flow would correspond to $y^+ < 30$. Hereafter, the high and low turbulent Reynolds number k-ε models will be referred to as the high-Reynolds-number k-ε model and the low-Reynolds-number k-ε model respectively, realizing that the Reynolds number referred to in these cases is the Reynolds number of turbulence.

The expressions for Γ_ϕ and S_ϕ for the k and ε equations for both the high and low Reynolds number cases are given in Table 3. Those terms within the dotted vertical lines are those added by Chien in his low Reynolds number model. Chien also found it necessary to modify the turbulent viscosity relation by multiplying Eq. (2.69) by an empirical function as follows

$$\mu_t = \rho c_\mu \frac{k^2}{\varepsilon} [1-\exp(-c_3 y^+)] \qquad (\quad)$$

Table 3. Expressions for S_ϕ and Γ_ϕ for the k-ε turbulence model

ϕ	Γ_ϕ	S_ϕ
k	$\mu + \mu_t$	$\mu_t(\frac{\partial u}{\partial y})^2 - \rho\varepsilon - \frac{2\mu k}{y^2}$
ε	$\mu + \frac{\mu_t}{1.3}$	$c_1 \frac{\varepsilon}{k}\mu_t(\frac{\partial u}{\partial y})^2 - \rho\frac{\varepsilon}{k}[c_2 f \varepsilon + \frac{2\mu k}{\rho y^2}e^{(-c_4 y^+)}]$ $(f = 1 - 0.222e^{[(-\rho k^2/6\mu\varepsilon)^2]})$

The boundary conditions for the low-Reynolds-number k-ε equation are applied at the wall as

$$k = \varepsilon = 0 \tag{2.72}$$

The high-Reynolds-number k-ε equations are not valid near the wall. Boundary conditions must be applied away from the wall or wall functions must be used to approximate k and ε near the wall [4].

Two expressions for k and ε in the near-wall region were used in this study when solving the high Reynolds number k-ε equations. One is based on the turbulent viscosity near the wall as expressed by Eq. (2.59) and the other is based on μ_t as given by Eq. (2.65).

The wall model based on Prandtl's mixing length model was derived as follows. For flow in equilibrium (production = dissipation), the convective and diffusive terms of the high Reynolds number case of Eq. (2.71) are neglected. Inserting the expression for the mixing length gives

$$\mu_t\left(\frac{\partial u}{\partial y}\right)^2 = \rho c_D \frac{k^{3/2}}{L} \tag{2.73}$$

For this equilibrium case and the constants given in Table 2, it can be shown that [3]

$$\ell = c_\mu^{3/2}/c_D\, L = 1.002\, L \simeq L$$

Using Eq. (2.59) to eliminate μ_t gives

$$\ell^2 \left|\frac{\partial u}{\partial y}\right|^3 = c_D \frac{k^{3/2}}{\ell}$$

Solving for k gives

$$k = c_D^{-2/3} \ell^2 \left(\frac{\partial u}{\partial y}\right)^2 \tag{2.74}$$

Equation (2.74) can be used to find k in the near-wall region and as a boundary condition for the k-equation PDE. Once k is known, ε is found from

$$\varepsilon = c_D \frac{k^{3/2}}{L} \tag{2.75}$$

Equations (2.74) and (2.75) should be used in place of the PDEs expressing k and ε for $y^+ < 30$ to 100.

Simpson et al. [76] argues that measurements in a separation bubble on a flat plate caused by pressure gradients indicates that that the law-of-the-wall model (which is based on Eq. 2.54) is not valid even at the wall in the separated flow. He states that the flow is dominated by turbulent fluctuations that are comparable in magnitude to the mean velocities. However, several investigators have used the equilibrium

law-of-the-wall model for the near-wall flow in conjunction with two-equation models away from the wall with good success [32, 116].

The near-wall expressions for k and ε based upon the inner viscosity model of Johnson and King [121] were derived by first substituting Eq. (2.65) into the equilibrium expression given by Eq. (2.73). After assuming L is given by κDy and solving for k gives

$$k = [\frac{1}{C_D}(\kappa y D_{15} \frac{\partial u}{\partial y})^2 D(-\overline{u'v'}_m)^{1/2}]^{2/3} \tag{2.76}$$

Once k is known, the expressions for μ_t given by Eqs. (2.65) and (2.69) are equated and solved for ε to give

$$\varepsilon = c_\mu k^2 / [D_{15}^2 \kappa y (-\overline{u'v'}_m)^{1/2}] \tag{2.77}$$

Equations (2.76) and (2.77) provide alternative expressions for k and ε in the near-wall region.

3. Algebraic stress model

The algebraic stress model (ASM) is becoming a popular variation of the k-ε turbulence model. In the ASM, an expression for c_μ is derived that is used in place of the constant value of 0.09. The functional c_μ is used in conjunction with the k-ε equations and Eq. (2.69) to calculate the turbulent viscosity. The ASM includes some effects of pressure-strain interaction and streamline curvature.

The algebraic stress model used is that developed by Rodi [3]. Exact PDEs can be derived for the six different Reynolds stresses of which only $\overline{u'v'}$ is significant for boundary-layer flow. After modeling,

these transport equations for the Reynolds stresses contain gradients of the Reynolds stresses only in the convection and diffusion terms. Rodi assumes that the transport of $\overline{u_i'u_j'}$ is proportional to the transport of k. An equation for the transport of k can be obtained from Eq. (2.70) as

$$\frac{Dk}{Dt} - \text{Diff}(k) = S_k$$

where D( )/Dt represents the total derivative, and Diff( ) represents the diffusion operator. Rodi assumes the proportionality constant between the transport of $\overline{u_i'u_j'}$ and the transport of k as $\overline{u_i'u_j'}/k$. The following equation can then be written for the transport of the Reynolds stresses

$$\frac{D}{Dt}\overline{u_i'u_j'} - \text{Diff}(\overline{u_i'u_j'}) = \overline{u_i'u_j'}/k \left[\frac{Dk}{Dt} - \text{Diff}(k)\right] \tag{2.78}$$

Equation (2.78) is used in the Reynolds stress transport equations with modeling assumptions to derive algebraic equations for the Reynolds stresses. This is possible since the gradient terms have been removed by the proportionality assumption expressed as Eq. (2.78). For thin shear layers with no bouyancy terms included, $\overline{u'v'}$ is

$$-\overline{u'v'} = c_\mu \frac{k^2}{\varepsilon}\frac{\partial u}{\partial y} \tag{2.79}$$

(an eddy viscosity relationship) where c_μ is now a function given by

$$c_\mu = \frac{2}{3}(1-\gamma)\frac{\alpha - 1 + \gamma P/\varepsilon}{(\gamma - 1 + P/\varepsilon)^2} \tag{2.80}$$

and P is

$$P = \mu_t \frac{1}{\rho}\left(\frac{\partial u}{\partial y}\right)^2$$

The values of α and γ are given in Table 2.

4. Turbulent prandtl number

When solving the energy equation for turbulent flow, the effects of turbulent mixing are included in the turbulent Prandtl number, Pr_t, as defined by Eq. (2.26). The Reynolds analogy [127] states that the turbulent diffusivity for momentum, μ_t/ρ, is equal to the turbulent thermal diffusivity, $k_t/(\rho c_p)$, where k_t is an effective thermal conductivity coefficient. This is based on the idea that if the turbulent motion of the fluid is dominant over molecular diffusion, the heat and the momentum turbulent diffusion should proceed at nearly the same rate since the same mechanism is responsible for both. For molecular diffusion, the Prandtl number is equal to the molecular diffusivity of momentum (kinematic viscosity) divided by the molecular thermal diffusivity. If the turbulent Prandtl number is described in the same way, it would equal one, since the two diffusivities are equal under the Reynolds analogy.

Experimental measurements have shown that for molecular Prandtl numbers greater than 0.5, Pr_t is closer to 0.9 if it must be a constant. However, Pr_t can be as high as 2.0 near the wall and as low as 0.8 in the fully turbulent region [127]. $Pr_t = 0.9$ seems to be an average value that works well for air. Several recent turbulent heat transfer predictions have used $Pr_t = 0.9$ with reasonable success [111, 115].

It is possible to derive expressions for Pr_t in a method similar to that used to derive an expression for c_μ. First, transport equations for the three turbulent scalar fluxes $\overline{u_i'T'}$ are derived. The gradient terms in these equations are removed by modeling assumptions to leave an algebraic expression for Pr_t. Gibson and Launder [136] assumed that the transport of the scalar fluxes was proportional to the transport of k as Rodi did to derive an expression for c_μ.

Watkins and Gooray [115] derived an expression for Pr_t in streamline and Cartesian coordinates. Their derivation was for a general elliptic problem. When the boundary-layer assumptions are applied in Cartesian coordinates, Pr_t is given by

$$Pr_t = \frac{1}{\phi_t} c_\mu \left[1 + \frac{k}{\varepsilon} \phi_t (1 - c_{\theta 2}) \frac{\partial u}{\partial y}\right] \tag{2.81}$$

where

$$\phi_t = c_{\theta 1} + c_{\theta 1 w} f' + 0.5(P/\varepsilon - 1)$$

$$f' = 0.41 \frac{k^{3/2}}{\varepsilon} (y^{-1/2} + x^{-1/2})^2$$

The last term in the brackets in the expression for f' is to include the effect of the step face in rapid expansion flow. For normal boundary-layer flow, this term would be deleted [137].

D. Engineering Parameters

This section introduces the form of the engineering parameters used later in this study.

It is possible to derive expressions for Pr_t in a method similar to that used to derive an expression for c_μ. First, transport equations for the three turbulent scalar fluxes $\overline{u_i'T'}$ are derived. The gradient terms in these equations are removed by modeling assumptions to leave an algebraic expression for Pr_t. Gibson and Launder [136] assumed that the transport of the scalar fluxes was proportional to the transport of k as Rodi did to derive an expression for c_μ.

Watkins and Gooray [115] derived an expression for Pr_t in streamline and Cartesian coordinates. Their derivation was for a general elliptic problem. When the boundary-layer assumptions are applied in Cartesian coordinates, Pr_t is given by

$$Pr_t = \frac{1}{\phi_t} c_\mu \left[1 + \frac{k}{\varepsilon} \phi_t (1 - c_{\theta 2}) \frac{\partial u}{\partial y}\right] \tag{2.81}$$

where

$$\phi_t = c_{\theta 1} + c_{\theta 1 w} f' + 0.5(P/\varepsilon - 1)$$

$$f' = 0.41 \frac{k^{3/2}}{\varepsilon} (y^{-1/2} + x^{-1/2})^2$$

The last term in the brackets in the expression for f' is to include the effect of the step face in rapid expansion flow. For normal boundary-layer flow, this term would be deleted [137].

D. Engineering Parameters

This section introduces the form of the engineering parameters used later in this study.

1. Wall shear stress

The shear stress at the wall for internal flow can be evaluated in two ways. The first way is by using the definition of τ for a Newtonian fluid as follows

$$\tau_w(x) = \tau(x,0) = \mu\frac{\partial u}{\partial y}(x,0) \tag{2.82}$$

For internal flows, a second expression for τ_w can be derived by equating the forces and momentum fluxes entering and leaving a control volume spanning the channel width. The following expression results

$$\tau_w(x) = -(2^{-m} r_o \frac{dp}{dx} + r_o^m \frac{dM}{dx}) \tag{2.83}$$

where

$$M = \int_0^{r_o} \rho r^m u^2 dy \tag{2.84}$$

Equation (2.83) applies since, for the boundary-layer equations, the pressure gradient is aligned with the x-coordinate and so can be expressed as a total derivative. The fact that the two expressions for τ_w should be equal, was used as an internal check in the computer program.

2. Bulk temperature

The mean or bulk temperature for variable property flow is given by the equation

$$T_b = (\int_0^{r_o} \rho r^m u c_p T dy)/(\int_0^{r_o} \rho r^m u c_p dy) \tag{2.85}$$

A second expression for the bulk temperature can be derived by an energy balance on a control volume spanning the channel. The resulting expression is

$$T_b(x_2) = \int_{x_1}^{x_2} q_w dx - \frac{1}{2}\int_0^{r_o} \rho_2 u_2^3 dy + \frac{1}{2}\int_0^{r_o} \rho_1 u_1^3 dy + T_b(x_1)\int_0^{r_o} \rho_1 u(x_1,y) c_{p1} dy \Big/ \int_0^{r_o} \rho_1 u(x_1,y) c_{p1} dy \qquad (2.86)$$

The "1" and "2" subscripts refer to two different x-positions. The two expressions for T_b should be equal and so provide an internal check on the present predictions.

III. METHOD OF SOLUTION

This chapter describes the method used to solve the equations developed in the previous chapter. The computational grid will be presented. The finite-difference discretization will then be discussed followed by the method used to solve the resulting system of equations. The method used to discretize the boundary conditions will also be presented. Finally, convergence, truncation error, and stability will be discussed.

The equations are discretized in an implicit manner. When using implicit methods for parabolic marching problems, a system of equations must be solved for the unknowns at the next station beyond the known values. It is generally felt that implicit procedures are well-suited for parabolic marching problems [4].

A. Computational Grid

The finite-difference equations used are valid for uniform and nonuniform grids. A representative example of the orthogonal Cartesian grid used for this study is shown in Fig. 3. The mesh shown in Fig. 3 is much coarser than those actually used. Grid refinement studies showed that 81 to 121 y-grid points and 135 x-grid points were adequate to resolve the flow field. The j index is used to specify y-position with j = 1 corresponding to the points on the wall, and j = NJ corresponding to the points on the centerline. The i index is used to specify x-position. For x = 0, i = 1.

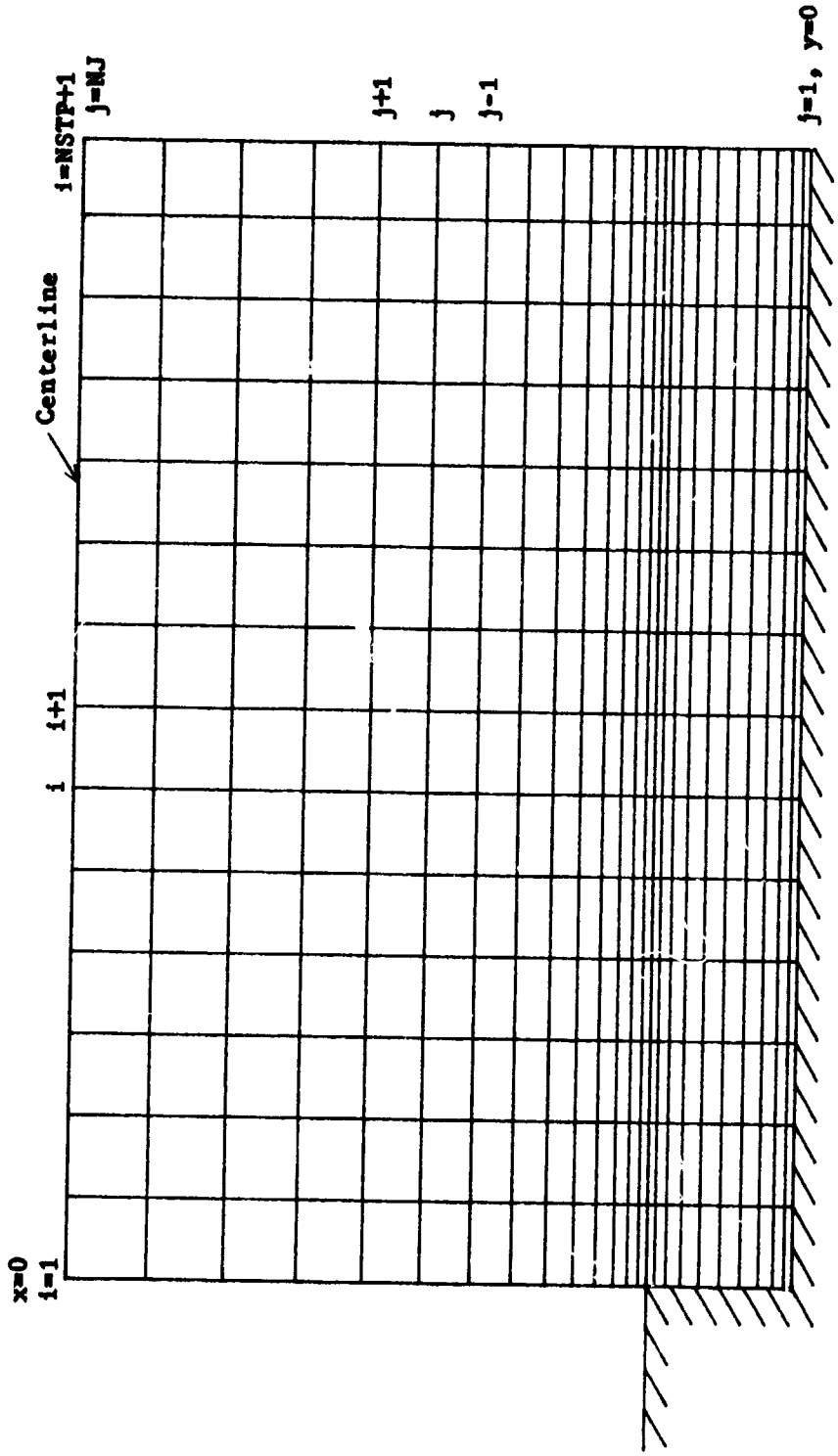

Figure 3. Finite-difference grid

Constant y-grid spacing was used for laminar flows. When predicting turbulent flows, it was necessary to use variable y-grid spacing in order to have a small Δy near the wall and a larger Δy away from the wall. For turbulent flow, inverses of the general stretching transformations of Roberts [138] as given in Anderson et al. [4] provided the y-grid spacing. The exact form of the stretching transformations is given in Appendix F. The y-grid spacing was fine enough near the wall to ensure that at least two to three grid points were in the laminar sublayer.

A geometric progression x-grid spacing was used that was defined by

$$\Delta x_+ = K\Delta x_- \tag{3.1}$$

where K is a variable greater than or equal to one. Δx_-, and Δx_+ are shown in Fig. 3. The distance between x = 0 and the first solution station Δx_1 is given by

$$\begin{aligned} \Delta x_1 &= \frac{x_{stop}}{NSTP}, \qquad K = 1 \\ \Delta x_1 &= \frac{x_{stop}(1-K)}{1-K^{NSTP}}, \qquad K > 1 \end{aligned} \tag{3.2}$$

where NSTP is the number of steps to be taken in the x-direction, and X_{stop} is the largest x-value in the solution domain. For flow with reattachment, K was set to one in order to provide adequate resolution at the point of reattachment. A value of K not equal to one was only used in flows with no step.

B. Velocity/Stream Function (u-ψ) Variable Equations

The stream function and the streamwise velocity were used as the hydrodynamic variables in most of the computations done in this study. This section describes the finite-difference discretization of the governing PDEs with u, ψ, H, k and ε as the variables.

The continuity and momentum equations were solved in a coupled manner in the present study. Since they are coupled, solutions for both u and ψ (or u and v for the u-v equation set) are obtained simultaneously. This is different from the usual method of solving the boundary-layer equations. Usually, the momentum equation is solved first to find u using lagged values of v from the previous marching station. Then, the continuity equation is solved using the recently obtained u values to find v. By using the coupled procedure, the v (or ψ) values are not lagged in the momentum equation so the predictions of u will be more accurate. Solving the momentum and continuity equations in a coupled implicit way is more complicated since the resulting system of equations is block tridiagonal with the tridiagonal elements being two by two matrices. When using an uncoupled implicit method, a tridiagonal system results where the tridiagonal elements are only single elements. Kwon and Pletcher [39] reported that the velocity profiles and pressure gradient predicted by the uncoupled scheme showed wiggles in regions of flow separation. When they coupled the continuity and momentum equations, the wiggles disappeared.

The energy, k and ε equations were solved uncoupled. The continuity and momentum equations were solved first to obtain u and ψ at a specific x. If the temperature field was desired, or if the flow was turbulent, the u's and ψ's were used in the energy, k and ε equations.

1. Continuity equation finite-difference discretization

The discretization of the continuity equation will be discussed first because it does not have the same general form as the other four PDEs. Figure 4a shows the difference molecule used for the continuity equation, Eq. (2.14). The finite-difference approximation of Eq. (2.14) is

$$(\rho r^m u)^{i+1}_{j-\frac{1}{2}} = \frac{1}{\Delta y_-}(\psi^{i+1}_j - \psi^{i+1}_{j-1}) \tag{3.3}$$

When a subscript or a superscript is i or j plus or minus 1/2 as in Eq. (3.3), the value of the variable is taken as the average of the values at the two adjacent nodes, i.e.,

$$\phi_{j-\frac{1}{2}} = (\phi_j + \phi_{j-1})/2.$$

The finite-difference form of the continuity equation is then

$$\frac{1}{2}(\rho^{i+1}_j r^m_j u^{i+1}_j + \rho^{i+1}_{j-1} r^m_{j-1} u^{i+1}_{j-1}) = \frac{1}{\Delta y_-}(\psi^{i+1}_j - \psi^{i+1}_{j-1}) \tag{3.4}$$

At this time, the density, ρ, is unknown at the i+1 station. In order to decouple the momentum and continuity equations from the energy equation, the density values will be lagged in the x-direction by setting

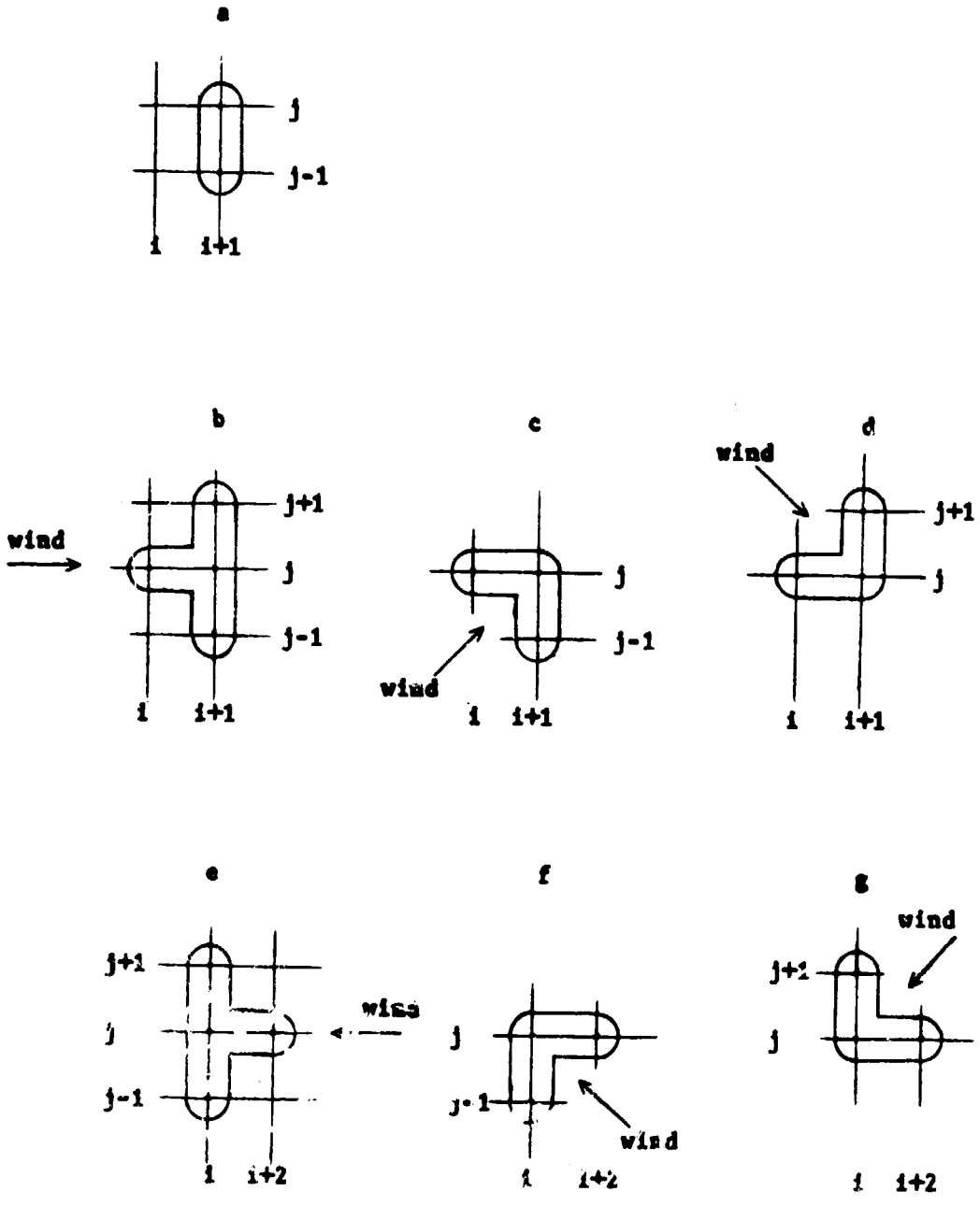

Figure 4. Finite-difference molecules

$$\rho_j^{i+1} = \rho_j^i \tag{3.5}$$

The fluid properties at the i+1 marching station will always be lagged in this way. The continuity equation is now of the form

$$b_j u_{j-1}^{i+1} + e_j u_j^{i+1} - \psi_j^{i+1} + \psi_{j-1}^{i+1} = 0 \tag{3.6}$$

The expressions for b_j and e_j are found in Appendix B.

2. General finite-difference discretization

The momentum (Eq. 2.20), energy (Eq. 2.27), k (Eq. 2.68), and ε (Eq. 2.68) equations can all by written in the same form as Eq. (2.68) as follows

$$c\rho|u|\frac{\partial\phi}{\partial x} - \frac{1}{r}\frac{\partial\psi}{\partial x}\frac{\partial\phi}{\partial y} = \frac{1}{r}\frac{\partial}{\partial y}\left[r\Gamma_\phi \frac{\partial\phi}{\partial y}\right] + S_\phi \tag{3.7}$$

The values of the Γ_ϕ's and the S_ϕ's for each of the different equations are given in Table 4. It is assumed at this point that μ_t and Pr_t have been found through the appropriate turbulence model as discussed in Section II.C. The m superscripts on the r's have been dropped since it is more efficient to simply set r(y) = 1 for planar geometries and let r(y) be the distance from the centerline for axisymmetric geometries. The terms enclosed by the dotted vertical lines in the k and ε equations shown in Table 4 are the low-Reynolds-number terms added by Chien [135] to make the model valid in regions having a low Reynolds number of turbulence.

This section discusses those points of the finite-difference procedure that are common to all of the equations (momentum, energy, k, and ε) fitting the form of Eq. (3.7). In the following sections, the details specific to a particular equation will be discussed.

Table 4. Expressions for S_ϕ and Γ_ϕ for the general equation

ϕ	Γ_ϕ	S_ϕ
u	$\mu_t + \mu$	$-\frac{dp}{dx}$
H	$\frac{\mu}{Pr} + \frac{\mu_t}{Pr_t}$	$\frac{1\partial}{r\partial y}[r(\Gamma_u - \Gamma_H)\frac{\partial}{\partial y}(u^2/2)]$
k	$\mu + \mu_t$	$\mu_t(\frac{\partial u}{\partial y})^2 - \rho\varepsilon - \frac{2\mu k}{y^2}$
ε	$\mu + \frac{\mu_t}{1.3}$	$c_1 \frac{\varepsilon}{k}\mu_t(\frac{\partial u}{\partial y})^2 - \rho\frac{\varepsilon}{k}[c_2 f \varepsilon + \frac{2\mu k}{\rho y^2}e^{(-c_4 y^+)}]$ $(f = 1 - 0.222e^{[(-\rho k^2/6\mu\varepsilon)^2]})$

Six different finite-difference molecules were used to discretize Eq. (3.7). The particular molecule used depended on the direction of the flow. Figure 4 shows the six different molecules and the direction of the "wind" for each. The molecules shown in Figs. 4b and 4e which use central differencing in the y-direction were used for the majority of the grid points. The others were used only when the velocity in the

y direction caused nonviscous behavior when the molecules of Figs. 4b or 4e were used. This nonviscous behavior is discussed further in the Stability section.

a. First global iteration using FLARE Equation (3.7) in finite-difference form for the case when the FLARE approximation is in effect or when the flow is in the positive x-direction is

$$\frac{1}{\Delta x_-} c\rho_j^i u_j^{i+1}(\phi_j^{i+1} - \phi_j^i) - \frac{1}{r_j \Delta x_-}(\psi_j^{i+1} - \psi_j^i)\delta_y^* \phi_j^{i+1} = S_\phi + \frac{1}{r_j} D(r_j, \Gamma_j, \phi_j^{i+1}) \tag{3.8}$$

where δ_y^* is a central difference operator valid for nonuniform grids given by

$$\delta_y^* \phi_j = \frac{1}{\Delta y_+ + \Delta y_-}\left[\frac{\Delta y_-}{\Delta y_+}(\phi_{j+1} - \phi_j) + \frac{\Delta y_+}{\Delta y_-}(\phi_j - \phi_{j-1})\right] \tag{3.9}$$

and D is a specialized diffusion difference operator used to discretize the term

$$\frac{\partial}{\partial y}\left(r\Gamma_\phi \frac{\partial \phi}{\partial y}\right)$$

The form of D is

$$D(r_j, \Gamma_j, \phi_j^{i+1}) = \tag{3.10}$$

$$\frac{2}{\Delta y_+ + \Delta y_-}\left(\frac{\Delta y_-}{(\Delta y_+)^2} r_{j+\frac{1}{2}} \Gamma_{j+\frac{1}{2}}(\phi_{j+1}^{i+1} - \phi_j^{i+1}) + \left[\frac{\Delta y_+}{\Delta y_-} - \frac{\Delta y_-}{\Delta y_+}\right]\frac{\Gamma_j r_j}{\Delta y_+ + \Delta y_-}\right.$$

$$\left.\left[\frac{\Delta y_-}{\Delta y_+}(\phi_{j+1}^{i+1} - \phi_j^{i+1}) + \frac{\Delta y_+}{\Delta y_-}(\phi_j^{i+1} - \phi_{j-1}^{i+1})\right] - \frac{\Delta y_+}{(\Delta y_-)^2} r_{j-\frac{1}{2}} \Gamma_{j-\frac{1}{2}}(\phi_j^{i+1} - \phi_{j-1}^{i+1})\right)$$

b. After first global iteration After the first global iteration, the FLARE approximation was discarded and the x-convective term of Eq. (3.7) was differenced in a local upwind manner according to the local streamwise velocity. If u was positive then the difference molecule shown in Fig. 4b was used; if u was negative, the molecule shown in Fig. 4e was used. For the case with negative u, the finite-difference discretization of Eq. (3.7) is

$$\frac{1}{\Delta x_+}\rho_j^i u_j^{i+1}(\phi_j^{i+2}-\phi_j^{i+1}) - \frac{1}{r_j\Delta x_+}(\psi_j^{i+2}-\psi_j^{i+1})\delta_y^* \phi_j^{i+1} = S_\phi + \frac{1}{r_j}D(r_j,\Gamma_j,\phi_j^{i+1}) \qquad (3.11)$$

This allows downstream flow information in the global sense to influence the solution in the reversed flow region. For positive u, the discretization procedure was the same as that used for the first global iteration with FLARE.

For turbulent flow calculations, the Newton linearization was dropped after the first global iteration and the nonlinear terms were linearized using values from the previous global iteration.

c. Upwind discretization Equations (3.8) and (3.11) can both be written in the form

$$b_j\phi_{j-1}^{i+1} + d_j\phi_j^{i+1} + a_j\phi_{j+1}^{i+1} = c_j \qquad (3.12)$$

For positive d_j, the coefficients b_j and a_j must be negative for Eq. (3.12) to correctly model viscous behavior [4]. For laminar flows, nonviscous behavior was not a problem. However, for turbulent flows, a_j

and b_j did become positive at positions near the step and near the reattachment point.

Upstream differencing of the y-derivative in the y-convective term when either a_j or b_j was positive ensured that both a_j and b_j were both negative. Central differencing was still used in the diffusion operator D. If a_j was positive, the finite-difference molecules "c" and "f" of Fig. 4 were used; if b_j was positive, molecules "d" and "g" were used for the y-convective term. This is easily done by substituting the correct upwind finite-difference for the central difference operator δ_y^* as

$$\delta_y^* \phi_j^{i+1} \Rightarrow (\phi_j^{i+1} - \phi_{j-1}^{i+1})/\Delta y_-, \quad \text{for } a_j > 0$$

$$\delta_y^* \phi_j^{i+1} \Rightarrow (\phi_{j+1}^{i+1} - \phi_j^{i+1})/\Delta y_+, \quad \text{for } b_j > 0$$

3. Momentum equation finite-difference discretization

In this study, the momentum and continuity equations were solved to the wall for laminar and turbulent flows. Most other investigators used wall functions near the wall for turbulent flows so that the solution point nearest the wall is well-away from wall effects. A turbulence model valid in reversed flow that is accurate near the wall as well as in the high-Reynolds-number region away from the wal highly desirable.

a. Linearization For the momentum equation with $\phi = u$, Eq. (3.8) is nonlinear since two unknown u values at the i+1 station are

multiplied together. There are several ways to linearize the coefficients of Eq. (3.8):

- lag the coefficients
- extrapolate the coefficients
- update of the coefficients by simple iteration
- update of the coefficients by Newton linearization

A detailed description of each type of coefficient linearization can be found in Anderson et al. [4].

Kwon and Pletcher [39] studied the effect of several linearization schemes. They reported that only Newton linearization while coupling the continuity and momentum equations gave well-behaved predictions when there were large areas of recirculation. Newton linearization also greatly enhanced the rate of convergence of the linearization iteration. Due to the findings of Kwon and Pletcher, Newton linearization with coupling was the linearization scheme used in the present study.

The main idea behind Newton linearization is to replace the coefficients of the convective terms that cause the nonlinearity with

$$\phi_j^{i+1} = \hat{\phi}_j^{i+1} + \delta_\phi \tag{3.13}$$

where δ_ϕ is a small change between the converged value at the i+1 level and $\hat{\phi}_j$ is a provisional value from a previous Newton linearization iteration. After each of the variable coefficients of Eq. (3.8) is replaced with Eq. (3.13) and the δ_ϕ^2 terms dropped, a linear equation results. For the first Newton iteration, the provisional values are lagged and the solution is stepped from the i marching station to the i+1 marching station. The provisional values are then updated with the

predicted values at the i+1 level and the equation is solved again for the unknowns at the i+1 marching station. In this study, the iteration was continued until the average solution change was less than 5.0×10^{-4}. The average solution change was defined as

$$\text{maximum}\{\Sigma_j|u_j^{i+1}-\hat{u}_j|/\Sigma_j|\hat{u}_j|,\ \Sigma_j|\psi_j^{i+1}-\hat{\psi}_j|/\Sigma_j|\hat{\psi}_j|\}$$

The solution was then advanced to the i+2 marching station in the same way.

After using Newton linearization to linearize Eq. (3.8) and grouping the coefficients for each of the different unknowns, the following equation results

$$B_j u_{j-1}^{i+1} + D_j u_j^{i+1} + A_j u_{j+1}^{i+1} + E_j \psi_j^{i+1} = H_j \chi + C_j \qquad (3.14)$$

The pressure gradient, -dp/dx, has been expressed as χ. The coefficients of Eq. (3.14) are given in Appendix B.

After the first global iteration, if u was negative, Eq. (3.11) was used in place of Eq. (3.8). Equation (3.11) was linearized in the same way as Eq. (3.8). After grouping the coefficients of the unknown variables, the same form as given by Eq. (3.14) results. The variables with i+2 superscripts are considered as knowns since the values used are obtained from the previous global iteration. The coefficients of Eq. (3.14) for the case of negative u are given in Appendix B.

b. Boundary conditions The boundary conditions for u and ψ for use in solving the momentum and continuity equations follow. At the

wall (y = 0), $u_1^{(\ )}$ and $\psi_1^{(\ )}$ are simply set to zero. At the centerline, $\partial u/\partial y = 0$ is specified in the following way. The equation valid on the centerline for both axisymmetric and planar geometries is (see Eq. 2.20 and 2.21)

$$c\rho u\frac{\partial u}{\partial x} = \chi + 2^m \frac{\partial}{\partial y}(\mu+\mu_t)\frac{\partial u}{\partial y} \tag{3.15}$$

To specify the symmetry condition at the wall, a reflection boundary condition is used by defining a pseudopoint, y_{NJ+1}, beyond the y-value corresponding to the centerline, y_{NJ}. Equation (3.15) is finite differenced using the molecule of Fig. 4b to give

$$\frac{1}{\Delta x_-}\rho_{NJ}^{i}u_{NJ}^{i+1}(u_{NJ}^{i+1} - u_{NJ}^{i}) = \chi + 2^m D(1,\Gamma_{u,NJ},u_{NJ}^{i+1}) \tag{3.16}$$

Due to symmetry, for j = NJ

$$u_{NJ+1}^{(\ )} = u_{NJ-1}^{(\ )},\ \Delta y_- = \Delta y_+,\ \Gamma_{u,NJ+\frac{1}{2}} = \Gamma_{u,NJ-\frac{1}{2}} \tag{3.17}$$

Substituting Eq. (3.17) into Eq. (3.16) gives

$$B_{NJ}u_{NJ-1}^{i+1} + D_{NJ}d_{NJ}^{i+1} = H_{NJ}\chi + C_{NJ} \tag{3.18}$$

The expressions for the constants of Eq. (3.18) are given in Appendix B.

4. Solution of coupled finite-difference hydrodynamic equation system

This section outlines the method used to solve the finite-difference approximations of the continuity and momentum boundary-layer equations for compressible variable property flow with u-ψ as the variables. Since Eqs. (3.6) and (3.14) both involve u_{j-1}^{i+1}, u_j^{i+1},

and ψ_j^{i+1}, they must be solved simultaneously. For j = 2 to NJ-1, the following finite-difference equation holds

$$\begin{bmatrix} B_j & 0 \\ b_j & 1 \end{bmatrix} \begin{Bmatrix} u_{j-1}^{i+1} \\ \psi_{j-1}^{i+1} \end{Bmatrix} + \begin{bmatrix} D_j & E_j \\ e_j & -1 \end{bmatrix} \begin{Bmatrix} u_j^{i+1} \\ \psi_j^{i+1} \end{Bmatrix} + \begin{bmatrix} A_j & 0 \\ 0 & 0 \end{bmatrix} \begin{Bmatrix} u_{j+1}^{i+1} \\ \psi_{j+1}^{i+1} \end{Bmatrix} = \begin{Bmatrix} H_j \chi + C_j \\ 0 \end{Bmatrix} \tag{3.19}$$

Assembling the set of equations consisting of Eq. (3.19) written for each y-grid point at a given x-position results in a system of linear equations that must be solved simultaneously. The resulting system is block tridiagonal with each block consisting of a two by two matrix as follows

$$\begin{bmatrix} [D]_1 & [A]_1 & [0] & & & \\ [B]_2 & [D]_2 & [A]_2 & [0] & & \\ [0] & [B]_3 & [D]_3 & [A]_3 & [0] & \\ & [0] & [B]_j & [D]_j & [A]_j & [0] \\ & & [0] & [B]_{NJ} & [D]_{NJ} & \end{bmatrix} \begin{bmatrix} \{U\}_1 \\ \{U\}_2 \\ \{U\}_3 \\ \{U\}_j \\ \{U\}_{NJ} \end{bmatrix} = \begin{bmatrix} \{C\}_1 \\ \{C\}_2 \\ \{C\}_3 \\ \{C\}_j \\ \{C\}_{NJ} \end{bmatrix} \tag{3.20}$$

where

$$[A]_j = \begin{bmatrix} A_j & 0 \\ 0 & 0 \end{bmatrix}; \quad [B]_j = \begin{bmatrix} B_j & 0 \\ b_j & 1 \end{bmatrix}; \quad [D]_j = \begin{bmatrix} D_j & E_j \\ e_j & -1 \end{bmatrix}$$

$$\{C\}_j = \begin{Bmatrix} H_j\chi + C_j \\ G_j\chi + d_j \end{Bmatrix}; \quad \{U\}_j = \begin{Bmatrix} u_j^{i+1} \\ \psi_j^{i+1} \end{Bmatrix} \tag{3.21}$$

The coefficients of Eq. (3.21) are the same as those listed in Appendix B.

Equation (3.20) was reduced to upper triangular form by using a modified Thomas algorithm. The Thomas algorithm is commonly used to efficiently solve tridiagonal systems of equations in which the elements are single coefficients. The same method can easily be applied to solve Eq. (3.20) due to the sparseness of the submatrices $[A]_j$ and $[B]_j$. To eliminate the submatrices below the diagonal on the jth row of submatrices, the j-1 row is multiplied by $-[B]_j[D]_{j-1}^{-1}$ and added to the jth row. $[D]_j^{-1}$ is the inverse of $[D]_j$. Since it is known that $[B]_j$ will be zeroed and that $[A]_j$ will not change because all the elements above it are zero, it is only necessary to modify $[D]_j$ and $\{C\}_j$. The elimination process is started with j = 2 and proceeds to j = NJ. The new diagonal and right hand submatrices become

$$[D]_j^* = -[B]_j[D]_{j-1}^{-1}[A]_{j-1} + [D]_j \tag{3.22}$$

$$\{C\}_j^* = -[B]_j[D]_{j-1}^{-1}\{C\}_{j-1} + \{C\}_j \tag{3.23}$$

The exact form of the new submatrices is given in Appendix C.

The pressure gradient parameter χ has been grouped with known coefficients on the right-hand side of Eq. (3.20) even though it has been unknown to this point. However, after the system of equations is in upper triangular form, the mass flow constraint which specifies ψ at the centerline (Eq. 2.30) is implemented to solve for the unknown pressure gradient, χ. This is done by noting that after Eq. (3.20) is reduced to upper triangular form, the reduced form of the momentum and continuity equations for $j = NJ$ is

$$[D]^{*}_{NJ}\{U\}^{i+1}_{NJ} = \{C\}^{*}_{NJ} \tag{3.24}$$

$\{C\}^{*}_{NJ}$ contains the unknown χ; $\{U\}_{NJ}$ contains only the unknown u^{i+1}_{NJ} since ψ_{NJ} is a known boundary condition. Since there are only two unknowns and two equations, u^{i+1}_{NJ} and χ can be algebraically determined. The resulting expressions for u^{i+1}_{NJ} and χ are given in Appendix C.

After determining u^{i+1}_{NJ} and χ, a matrix form of back substitution was used to find $\{U\}_j$ for $j \neq NJ$ as follows

$$\{U\}_j = ([D]^{*}_j)^{-1}(\{C\}^{*}_{j+1} - [A]_j\{U\}_{j+1}) \tag{3.25}$$

Appendix C shows the specific form of the back substitution.

5. Energy equation finite-difference discretization

As was done when discretizing the momentum equation, two types of discretizations were used depending on whether the FLARE approximation was being used and the sign of u. After the first global iteration, the

FLARE approximation for the energy equation was discarded. The x-derivatives in the energy equation were then differenced in a local upwind manner to allow energy to be convected from the globally downstream direction when flow reversal was present. Upstream differencing for the y-derivative in the y-convective term was used as necessary to ensure viscous behavior of the predictions.

The discretization of the energy equation for a general point removed from the boundaries is given by Eqs. (3.8) and (3.11) with $\phi = H$. Equation (3.8) was used for the first global sweep and when u was positive; Eq. (3.11) was used when for the second and subsequent global sweeps when u was negative. The u's and ψ's are known since the momentum and continuity equations were solved first. Thus, the resulting finite-difference equation is linear in H. The source term of the energy equation as given in Table 4 is discretized as

$$S_{H,j} = \frac{1}{r_j} D(r_j, S_j, \tfrac{1}{2}(u_j^{i+1})^2)$$

When the coefficients of the unknown Hs are grouped, the result is

$$b_j H_{j-1}^{i+1} + d_j H_j^{i+1} + a_j H_{j+1}^{i+1} = c_j \tag{3.26}$$

The expressions for the coefficients are given in Appendix D.

a. Boundary conditions Now that the governing FDEs away from the boundary have been determined, the appropriate boundary conditions must be discretized in order to obtain the complete system of governing equations. The requirement that the flow be symmetric about the

centerline is used as the boundary condition at the centerline. The two possible boundary conditions at y = 0 are: a specified surface temperature (Eq. 2.32a), and a specified heat flux (Eq. 2.32b).

At the centerline, the symmetry condition leads to the following equation for j = NJ

$$\frac{1}{\Delta x}\rho_{NJ}^{i}u_{NJ}^{i+1}(H_{NJ}^{i+1} - H_{NJ}^{i}) =$$

$$2^{m}D(1,\Gamma_{H,NJ},H_{NJ}^{i+1}) + 2^{m}D(1,S_{H,NJ},\tfrac{1}{2}(u_{NJ}^{i+1})^{2}) \qquad (3.27)$$

The symmetry condition states that $H_{NJ-1}^{i+1} = H_{NJ+1}^{i+1}$. Using this fact with Eq. (3.17), Eq. (3.27) becomes

$$b_{NJ}H_{NJ-1}^{i+1} + d_{NJ}H_{NJ}^{i+1} = c_{NJ} \qquad (3.28)$$

The values of the coefficients are listed in Appendix D.

1) Specified wall surface temperature For a specified temperature boundary condition at the wall, $H_1^{(\ )} = c_p T_w(x)$. The wall boundary condition is implemented by using Eq. (3.26) for j = 2 as follows

$$d_2H_2^{i+1} + a_2H_3^{i+1} = c_2 - b_2H_1^{i+1} \qquad (3.29)$$

Since H_1^{i+1} is known, it has been moved to the right hand side with c_2. Using Eq. (3.29), Eq. (3.26) for j=3 to NJ-1, and Eq. (3.28) for j = NJ gives a tridiagonal system that can easily be solved by Gaussian elimination.

2) Specified wall heat flux For a specified heat flux at the wall, a one-sided three point finite-difference approximation of $\partial T/\partial y$ in Eq. (2.32b) gives

$$d_1 H_1^{i+1} + a_1 H_2^{i+1} + \lambda H_3^{i+1} = c_1 \tag{3.30}$$

where d_1, a_1, λ, and c_1 are given in Appendix D. In obtaining Eq. (3.30), c_p was assumed to be locally constant.

Equations (3.30), (3.26) for j = 2 to NJ-1, and (3.28) for j = NJ make up the system to be solved for the case of a specified wall heat flux. Eq. (3.30) destroys the tridiagonal form of the system of equations. This is easily overcome by adding $-\lambda/a_2$ times Eq. (3.26) with j = 2 to Eq. (3.30). This modification of the first row of the coefficient matrix and right hand column matrix does not harm the diagonal dominance of the algebraic system. The Thomas algorithm can now be used to efficiently solve for the unknown Hs at the i+1 x-position.

b. Initial conditions At x = 0, initial conditions must be specified for H. For an unheated channel upstream of the step, the initial condition for the temperature above the step is simply

$$T(0,y) = T_{inlet}$$

Since the experimental data sets to be compared with had an insulated step, the initial condition below the face is $\partial T/\partial x = 0.0$. For the first sweep down the channel, $\partial T/\partial x$ in the x-convective term of the

energy equations was set to zero. This removed any influence of the temperature along the face of the step for the first sweep down the channel. For subsequent sweeps, a three-point finite-difference representation of $\partial T/\partial x = 0.0$ was used to extrapolate backwards to the face of the step from the first two x-grid stations beyond the step. The extrapolated face temperatures were then used in the next sweep down the channel.

6. k-ε equation finite-difference discretization

The ε-equation was solved before the k-equation since it is the more approximate of the two equations [3]. Lagged values of k or values of k from a previous iteration were used in the source term of the ε equation to uncouple the two equations. The k-equation was then solved using the recently computed values of ε. Upon knowing k and ε, μ_t was then calculated by Eq. (2.67).

The convective and diffusive terms of the k and ε equations were finite differenced using Eqs. (3.8) and (3.11) with upwind differencing of the y-derivative in the y-convective term as needed. The resulting equation is of the form

$$b_j k_{j-1}^{i+1} + d_j k_j^{i+1} + a_j k_{j+1}^{i+1} = c_j \tag{3.31}$$

The values of the coefficients in Eq. (3.31) and the similar equation for ε are listed in Appendix D.

a. Source terms Unlike the momentum and energy equations, the source terms of the k and ε equations need special treatment. As the

wall is approached, the source terms begin to dominate the diffusion and convection terms [122]. Special handling of the source terms in the k-equation is needed to ensure that k remains positive [139].

The source term of a PDE must be written in the following linear form when approximating the PDE:

$$S_\phi = S_{\phi,d}\,\phi + S_{\phi,c} \tag{3.32}$$

where $S_{\phi,d}$ is the part that is included in the d coefficient of Eq. (3.31) and $S_{\phi,c}$ is the part that is included in c_j of Eq. (3.31). If $S_{\phi,c}$ is always positive and $S_{\phi,d}$ is always negative, for initial positive ϕ, ϕ will always be positive. The source term of the k-equation written in the form of Eq. (3.32) is

$$S_k = (-\frac{2\mu}{y^2})k + (2\mu_t(\frac{\partial u}{\partial y})^2 - \rho\varepsilon) \tag{3.33}$$

If $S_{k,c}$ was positive, Eq. (3.33) was used as the expression for the source term. When $S_{k,c}$ became negative, $S_{k,c}$ was set to zero and $S_{k,d}$ took the form

$$S_{k,d} = -\frac{2\mu}{y^2} + (2\mu_t(\frac{\partial u}{\partial y})^2 - \rho\varepsilon)/k^* \tag{3.34}$$

where k^* is a lagged value of k or a k given by a previous iteration.

The ε-equation source term is

$$S_\varepsilon = (-\frac{\rho}{k^*}c_2 f\varepsilon^* - \frac{2\mu}{y^2})\varepsilon + c_1\mu_t(\frac{\partial u}{\partial y})^2\,\frac{\varepsilon^*}{k^*} \tag{3.35}$$

Equation (3.35) shows that $S_{\varepsilon,c}$ is always positive and $S_{\varepsilon,d}$ is always negative as they should be to ensure positive ε.

The previous discussion of the source terms for the k and ε equations included the terms added by Chien [135] for low-Reynolds-number regions. If the low-Reynolds-number form is not desired, the terms in the vertical dotted lines of Table 3 must be deleted.

b. Near-wall models For the high-Reynolds-number k-ε model that was used for all the separated flow calculations, the near-wall region must be modeled differently than the rest of the flow. There were three different methods used for specifying the turbulent viscosity near the wall: (1) the maximum-shear-stress model, (2) the Prandtl-mixing-length model and, (3) the Prandtl-mixing-length model with variable A^+.

The maximum shear stress model is based on the inner viscosity model of Johnson and King [121]. The point at which the switch was made from the wall model to the k-ε high-Reynolds-number PDE model was at a constant y value, y_b. The value of y_b was specified as the y corresponding to a y^+ of 30.0 to 50.0 for fully developed turbulent flow at the same Reynolds number (based on D and and the average outlet velocity). The predictions were not sensitive to the value of y_b within this range. The turbulent viscosity in the near wall region for method 1 was given by Eq. (2.65). Equations (2.76) and (2.77) give the expressions used for $k(y_b)$ and $\varepsilon(y_b)$.

For method 2, the boundary conditions were applied at a y^+ value of 30.0 to 50.0 with similar results for both values. For method 3, the boundary conditions for k and ε were applied at

$$y^+ = 2.0\ A^+$$

For method 3, A^+ was varied according to Eq. (2.64). In the recirculation region and near reattachment, A^+ reached values as low as 1.0. Ordinarily, this is well-into the viscous sublayer and much too small a value of y^+ for the high-Reynolds-number k-ε equations to be valid. Johnson and Launder [113] found that by reducing the thickness of the laminar sublayer below that normally found in turbulent boundary layers, the wall functions of Chieng and Launder [111] gave much better predictions of the heat transfer in recirculating flow.

Since the value of y at which the k-ε boundary conditions were applied varied for methods 2 and 3, it was necessary to specify values for k and ε for y values corresponding to y^+ less than 30. For methods 2 and 3, the k and ε values for $y^+ < 30.0$ were given by Eqs. (2.74) and (2.75). Equation (2.69) then gave the near-wall turbulent viscosity.

c. Initial conditions To start the marching procedure for the first sweep down the channel, lagged values for k must be used in the source terms. Since the source terms of the k and ε equations contain k^{-1}, zero k values are inappropriate. To remove the singularity, the values for k and ε on the face of the step were set to the values of the point just above the lip of the step at the inlet to the channel (j =

NH+1, i = 1 as in Fig. 3). Sometimes these values caused the solution to diverge for fine grids and large expansions as the solution was marched from the step on the first iteration. This divergence could sometimes be overcome by using the k and ε values at a point further above the lip for the face values (j = NH+2 or NH+3).

C. Primitive Variable Hydrodynamic Equations

This section describes the method used to solve the constant property continuity and momentum equations in a coupled manner using primitive variables, that is, without introducing the stream function. Previous primitive variable boundary-layer calculations for separated flow with the momentum and continuity equations uncoupled predicted a solution with small unphysical "wiggles" [39]. The main reason for predicting the flow with the primitive variable equations was to see if the use of ψ was essential to obtain a satisfactory solution when large regions of separation were present. It will be shown in Section IV.A.1.d that the primitive variable formulation gives predictions identical to those of the u-ψ predictions under similar assumptions. This indicates that the equation coupling overcomes the small oscillations and not the choice of variables. Only the planar two-dimensional equations for constant property laminar flow will be developed. The predictions of the primitive variable formulation would give the same predictions as the u-ψ variable case for axisymmetric geometries, for problems with heat transfer, and for variable property

flows. The effect of iterating globally over the flow field was not studied for the primitive variable case.

For planar 2-D coordinates, the transverse dimensionless velocity V can be given in terms of the dimensionless stream function as

$$V = -\frac{\partial \Psi}{\partial X} = \frac{vRe}{u_i} \tag{3.36}$$

Substituting Eq. (3.36) into Eq. (2.45) gives

$$cU\frac{\partial U}{\partial X} + V\frac{\partial U}{\partial Y} = \beta + \frac{\partial}{\partial Y}\left(\frac{\partial U}{\partial Y}\right) \tag{3.37}$$

The continuity equation is

$$\frac{\partial U}{\partial X} + \frac{\partial V}{\partial Y} = 0 \tag{3.38}$$

Equations (3.37) and (3.38) are for constant property laminar flow and are nondimensionalized in a way so that they are independent of the Reynolds number.

1. Finite-difference discretization

Equation (3.38) is finite differenced in the following manner

$$\frac{\Delta Y_-}{2\Delta X_-}\left[\left(U_j^{i+1} - U_j^i\right) + \left(U_{j-1}^{i+1} - U_{j-1}^i\right)\right] + V_j^{i+1} - V_{j-1}^{i+1} = 0 \tag{3.39}$$

The finite-difference discretization of Eq. (3.37) is

$$\frac{1}{\Delta X_-}cU_j^{i+1}\left(U_j^{i+1} - U_j^i\right) + \frac{1}{\Delta Y_+ + \Delta Y_-}V_j^{i+1}\left(U_{j+1}^{i+1} - U_{j-1}^{i+1}\right) =$$

$$\beta + \frac{2}{\Delta Y_+ + \Delta Y_-}\left[\frac{1}{\Delta Y_+}\left(U_{j+1}^{i+1} - U_j^i\right) - \frac{1}{\Delta Y_-}\left(U_j^{i+1} - U_{j-1}^{i+1}\right)\right] \tag{3.40}$$

Note that the FLARE approximation is in effect to allow the solution to be marched through regions of reversed flow. Equation (3.40) is linearized with Newton linearization as was done for the u-ψ variable scheme. Equation (3.39) and the linearized form of Eq. (3.40) can be combined into a coupled equation as

$$[B]_j\{U\}_{j-1} + [D]_j\{U\}_j + [A]_j\{U\}_{j+1} = \{C\}_j \tag{3.41}$$

where

$$[A]_j = \begin{bmatrix} A_j & 0 \\ 0 & 0 \end{bmatrix};\ [B]_j = \begin{bmatrix} B_j & 0 \\ b_j & -1 \end{bmatrix};\ [D]_j = \begin{bmatrix} D_j & E_j \\ e_j & 1 \end{bmatrix}$$

$$\{C\}_j = \begin{Bmatrix} H_j\beta + C_j \\ G_j\beta + d_j \end{Bmatrix};\ \{U\}_j = \begin{Bmatrix} u_j^{i+1} \\ V_j^{i+1} \end{Bmatrix} \tag{3.42}$$

Writing Eq. (3.41) for each value of j gives a linear system of equations. Appendix E gives the form of the coefficients of Eq. (3.42).

2. Solution of the system

Two different methods were used to solve the system of equations consisting of Eq. (3.41) for different values of j. Regardless of the method used, the pressure derivative, β, was obtained as part of the solution similar to what is done when using an inverse boundary-layer method. Two different methods were used to solve for β: solving for β algebraically as was done for the u-ψ variable method, and solving for β using an iterative secant numerical procedure.

a. Modified Thomas algorithm When Eq. (3.41) is assembled for all values of j, the resulting equation is the same form as Eq. (3.20), and so can be solved by the modified Thomas algorithm. The submatrices below the diagonal are eliminated by row operations on each row of submatrices. Appendix E gives the resulting values of the components of the submatrices.

After the system of equations is in upper triangular form, the coupled momentum and continuity equations for j = NJ are given by

$$\begin{bmatrix} D^*_{NJ} & E_{NJ} \\ e^*_{NJ} & 1 \end{bmatrix} \begin{Bmatrix} U^{i+1}_{NJ} \\ V^{i+1}_{NJ} \end{Bmatrix} = \begin{Bmatrix} H^*_{NJ}\beta + C^*_{NJ} \\ G^*_{NJ}\beta + D^*_{NJ} \end{Bmatrix}$$

The primes denote that the coefficients are for the upper triangular system of equations. Since $V^{i+1}_{NJ} = 0$, Eq. (3.43) has two unknowns, β and U^{i+1}_{NJ}, which can be obtained algebraically. Now a matrix form of back substitution (Eq. 3.25) is used to solve for the unknown Us and Vs at the i+1 marching station. Appendix E gives the exact form of the submatrices used in the back substitution.

b. Pressure-derivative secant If β were known, the system of equations consisting of Eq. (3.40) for each grid node could be directly solved by any suitable solution scheme for a system of equations. To start the secant procedure, β is simply guessed and the system of equations solved. If the guessed β is correct, then the boundary condition that $V_{NJ} = 0$ will be satisfied. For each incorrect β guessed, there will correspond a nonzero V_{NJ}. After two guesses for β, a secant

procedure can be used to predict a new guess for β that will yield a value of V_{NJ} closer to zero.

Three different variations of the secant method were tried:

1. A secant procedure to find the correct pressure derivative was nested in the Newton linearization loop.
2. The Newton linearization loop was nested in the secant loop to find the correct pressure derivative.
3. The Newton linearization loop was removed resulting in lagged coefficient linearization with a pressure secant procedure to find the correct pressure derivative.

Figure 5 shows a block diagram of the method used for variation 1. For variation 1 above, the provisional values used in the Newton linearization were set to the values from the previous channel station. A secant method was used to determine the correct value of the pressure derivative in the following way. Two guesses for the pressure derivative were obtained by multiplying the pressure derivative at the previous station by 1.04 and 0.96. The pressure gradient for the first step was taken as the pressure gradient that would occur in fully developed channel flow. The general block solver NBTRIP provided by Sukumar R. Chakravarthy of Stanford University [4] provided two solutions to the system resulting from these guessed pressure gradients. For the correct pressure derivative, the transverse velocity at the centerline, V_{NJ} should be zero. The centerline Vs obtained from the first two guesses were used in a secant procedure to predict a new

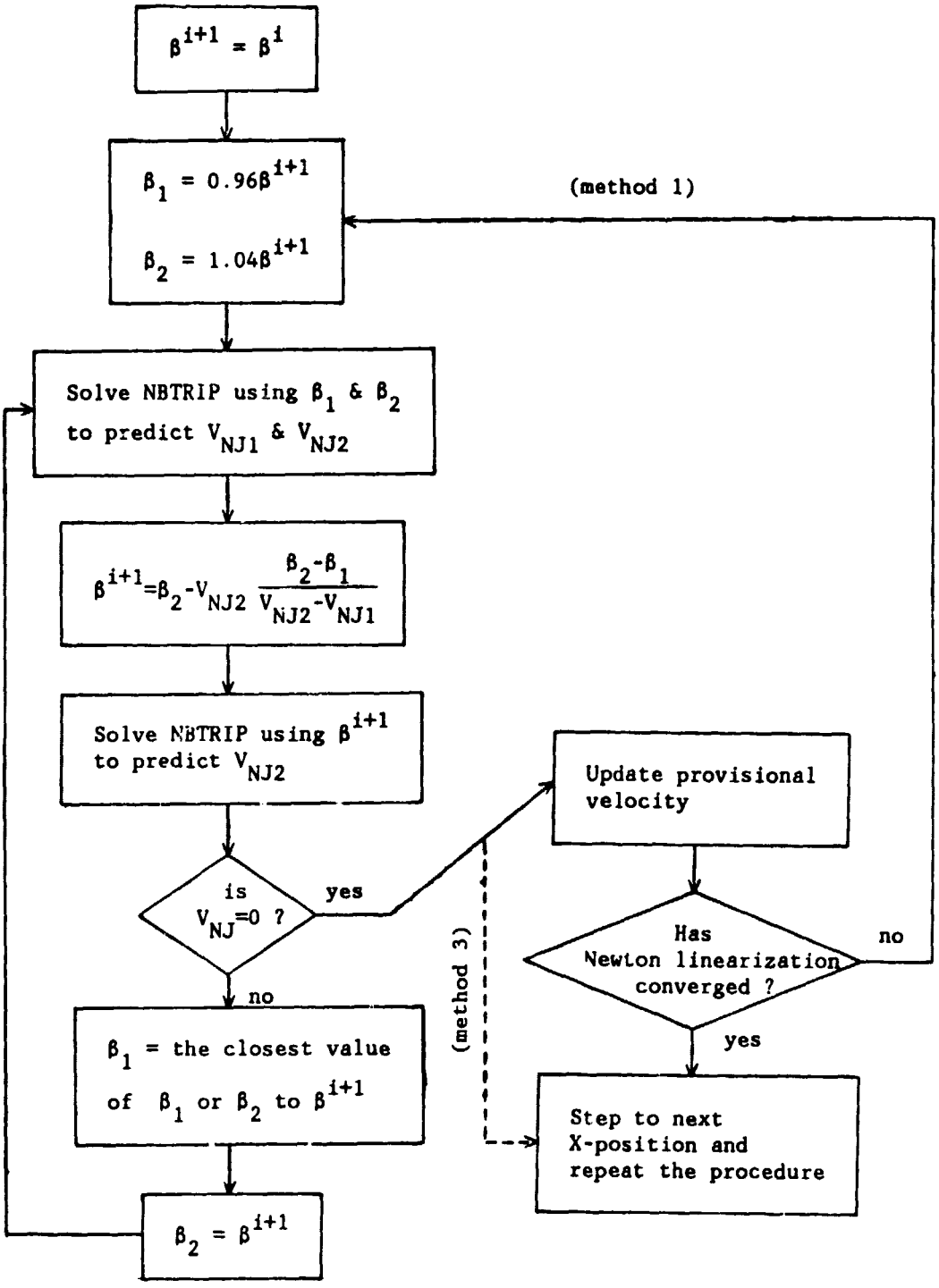

Figure 5. Block diagram for the pressure secant algorithms

pressure derivative. NBTRIP gave a new solution based upon this new pressure derivative. The secant iteration continued trying to force V_{NJ} to zero until the relative change of the pressure derivative was less than some small prescribed value. At this point, the provisional variables used in Newton linearization were updated and the process repeated. Thus, the pressure iteration was nested in the Newton linearization iteration for each step down the channel.

Variation 2 is similar to variation one except that the Newton linearization loop was nested in the pressure secant loop. A first guess for the pressure derivative was chosen in the same way as in variation 1. NBTRIP gave a prediction for the velocity profiles at the new step from the input guessed pressure derivative and the velocity profiles at the previous step. The Newton linearization algorithm then looped until the provisional velocities stopped changing. At this point, a second guess for the pressure derivative was input to the linearization loop and the process repeated. The secant method then predicted a new pressure derivative. This new pressure derivative was used as input to NBTRIP to predict new velocity profiles and the linearization iteration was repeated. The pressure loop (with linearization loop nested in it) was repeated until the pressure derivative change was very small.

Variation 3 only had the pressure secant loop. It is the same as variation 1 except that there was no Newton linearization loop (see Fig. 5).

Section IV.A.1.d gives the results of the different primitive variable schemes.

D. Convergence

With any numerical approximation to a partial differential equation (PDE), one must be concerned with the errors in the approximation. It is hoped that a finite-difference equation (FDE) solution is close to the exact solution of the PDE. If the FDE formulation is consistent and stable, it converges to the solution of the PDE as the grid is refined [4].

1. Consistency and truncation error

A FDE formulation is consistent if the truncation error (TE) goes to zero as the computational grid is refined. The truncation error is defined as

$$TE = PDE - FDE \tag{3.44}$$

The truncation error was found by using Taylor series expansions of the derivatives in the PDEs. The truncation error of the continuity equation is $O(\Delta y_-^2)$; the truncation error of all the other FDEs is $O(\Delta x, \Delta y_- \Delta y_+, \Delta y_- - \Delta y_+)$ when central differencing of $\partial\phi/\partial y$ is used in the y-convective term. (The truncation error degrades to $O(\Delta x, \Delta y)$ for the upwind differencing of the y-convective term but this usually only takes place near the step where the solution procedure is admittedly approximate.) Note that for uniform grid spacing, the TE becomes

formally $O(\Delta x, \Delta y^2)$. Since $\Delta x, \Delta y \to 0$ as the mesh is refined, the FDE discretization is consistent.

Even though the TE is only formally first order in Δy, it can be shown that the TE in the y-direction behaves in a second order fashion as was suggested by Blottner [140]. The dominant term of the truncation error is

$$(\Delta y_+ - \Delta y_-) \frac{\partial^3 u}{\partial y^3} = (y_{j+1} - 2y_j + y_{j-1}) \frac{\partial^3 u}{\partial y^3} \tag{3.45}$$

If y is defined by a stretching transformation, $y = y(\zeta)$, of the ζ space which has a uniform grid spacing, $\Delta\zeta$, then

$$\frac{\partial^2 y}{\partial \zeta^2} = \frac{1}{\Delta \zeta^2}(y_{j+1} - 2y_j + y_{j-1}) + O(\Delta \zeta^2) \tag{3.46}$$

Equation (3.46) is introduced to merely establish a link between the nonuniform y-grid spacing and the uniform ζ-grid spacing. Equation (3.46) can be rearranged to give

$$y_{j+1} - 2y_j + y_{j-1} = O(\Delta \zeta^2) \tag{3.47}$$

The finite-difference discretization has a formal truncation error of $O(\Delta \zeta^2)$ for the uniform grid space. Equation (3.47) indicates, that the largest term of the truncation error of the nonuniform grid behaves in a second order manner with respect to the uniformly divided ζ space. If more y-grid points are added, an additional corresponding number of ζ-grid points will be added. Therefore, the finite-difference discretization in the nonuniform grid space, y, behaves in a second order fashion ($TE = O(\Delta \zeta^2)$) as long as y can be defined as $y = y(\zeta)$.

2. Stability

The second requirement for convergence is stability. A solution method is stable if the round-off errors in the computer and the truncation errors do not grow as the solution progresses. For linear PDEs, a von Neumann stability analysis can determine if a FDE discretization is stable [4]. The implicit method used in this study is unconditionally stable for linear initial-value PDEs and was assumed to be stable for the nonlinear boundary-layer equations of the present study.

For linear initial-value PDEs that are solved in a marching manner, Lax's Equivalence Theorem shows that for a consistent FDE discretization, stability is a sufficient condition for convergence [4]. Lax's theorem has not been proved for the nonlinear case but is generally accepted as valid. Since the present finite-difference formulation is consistent and stable, it is convergent.

Even though most implicit marching schemes for parabolic PDEs can be shown to be unconditionally stable in the von Neumann sense, an inappropriate grid can cause wiggles in the solution due an unphysical modeling of the PDE. This is easily shown by looking at the following momentum equation for an uncoupled implicit marching scheme

$$B_j u_{j-1}^{i+1} + D_j u_j^{i+1} + E_j u_{j+1}^{i+1} = C_j \tag{3.48}$$

To realistically model viscous flows, B_j and A_j should be opposite in sign to D_j [4]. This gives the flowing mesh Reynolds number constraint

$$\frac{v_j \Delta y}{\nu} < 2 \tag{3.49}$$

If Δy or v_j is too large, the mesh Reynolds number constraint is violated and unphysical behavior is predicted.

Nonviscous behavior due to the violation of the mesh Reynolds number has not been documented for the case when the momentum and continuity equations are coupled. Kwon and Pletcher [39] have suggested that proper viscous modeling is achieved because v in the $v\partial u/\partial y$ term is treated as a variable when the momentum equation is solved.

The continuity equation is a mass balance and does not involve the viscosity so its effect when coupled with the momentum equation should not change the required character of the coefficients in the momentum equation. This suggests that A_j and B_j of Eqs. (3.19) and (3.31) should remain negative.

Two common ways to ensure negative off-diagonal terms is to upwind difference the y-derivative in the y-convective term and to refine the grid. Since a large number of grid points were already being used in this study, upwind differencing was used to ensure proper viscous modeling.

IV. RESULTS

This chapter presents the results of this study. The laminar results will be discussed first followed by the turbulent results. The laminar and turbulent sections are each divided into hydrodynamic and heat transfer sections.

A. Laminar

The laminar results were promising in general and shed light on the nature of the boundary-layer equations as compared to the Navier-Stokes equations. The solution algorithm is quite robust and well-behaved for all the cases studied. No artificial damping or overrelaxation of any kind was needed for the laminar predictions. A typical laminar run required 3-5 seconds of NAS AS/6 computer time per global sweep through the flow field.

1. Hydrodynamic constant temperature

The constant temperature laminar results are presented in this section. The continuity and momentum equations (Eqs. 2.44 and 2.45) were nondimensionalized so that the Reynolds number dependence was removed. Calculations were made for expansion ratios of 1:1.2 through 1:4 (d:D as in Fig. 2) for both symmetrical planar and axisymmetrical expansion flows. This range of expansion ratios included the range of those studied by others with experimental tests and numerical predictions for this type of geometry. Comparisons were made with

available experimental results and solutions of the Navier-Stokes equations. Particular attention was given to the influence of expansion ratio and Reynolds number on the level of agreement between the predictions of the boundary-layer equations and measurements or Navier-Stokes solutions. Some flow parameters were predicted better than others. Those generally well-predicted were velocity and reattachment length. The higher the Reynolds number, the better the predictions.

a. Convergence When marching through a region of reversed flow using the boundary-layer equations, it is important to ensure that the solution does not become unstable as the grid is refined. Blottner [141] reported that his solution to the slender-channel equations diverged as he refined the grid when in the reversed flow region. For this reason, grid refinement was carefully studied to verify that the solution by the present method did not become unstable when the grid was refined. Figure 6 shows the effect of reducing ΔX on the reattachment length and the location and value of Ψ_{min}. Figure 6 shows the solution asymptotically approaches definite values as the grid is refined and does not diverge.

Figure 7 shows the relative change of key parameters per global iteration. In Fig. 7, Z is a surrogate variable that takes on the value of X_r, the X-distance to Ψ_{min}, the Y-distance to Ψ_{min}, or Ψ_{min}. Since the relative change of these four parameters goes to zero with increasing iteration number (i), it is obvious that the global iteration converges to steady-state values.

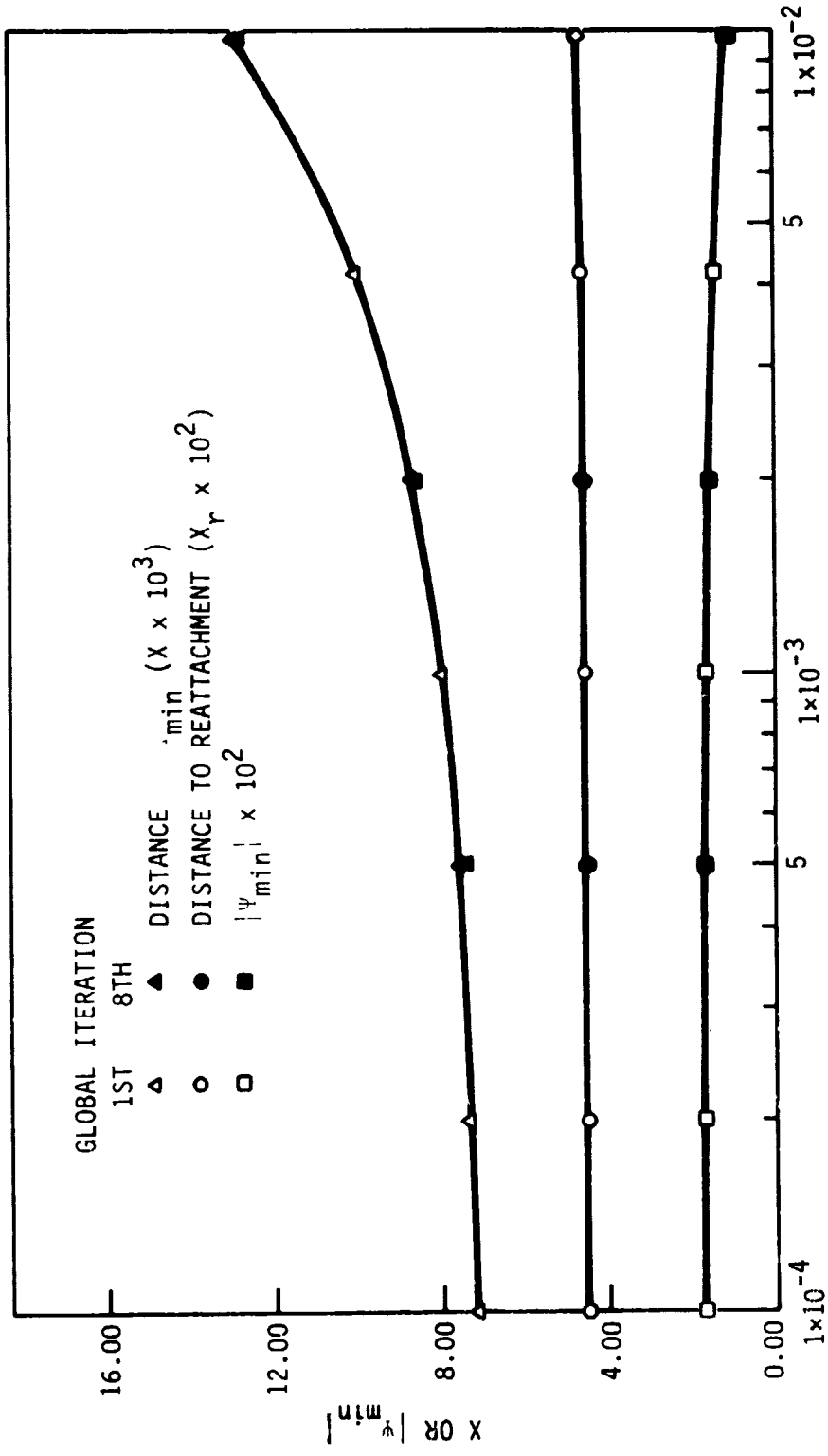

Figure 6. The effect of grid refinement on reattachment length, minimum stream function (Ψ_{min}), and distance to Ψ_{min} for an axisymmetric 1:2 expansion

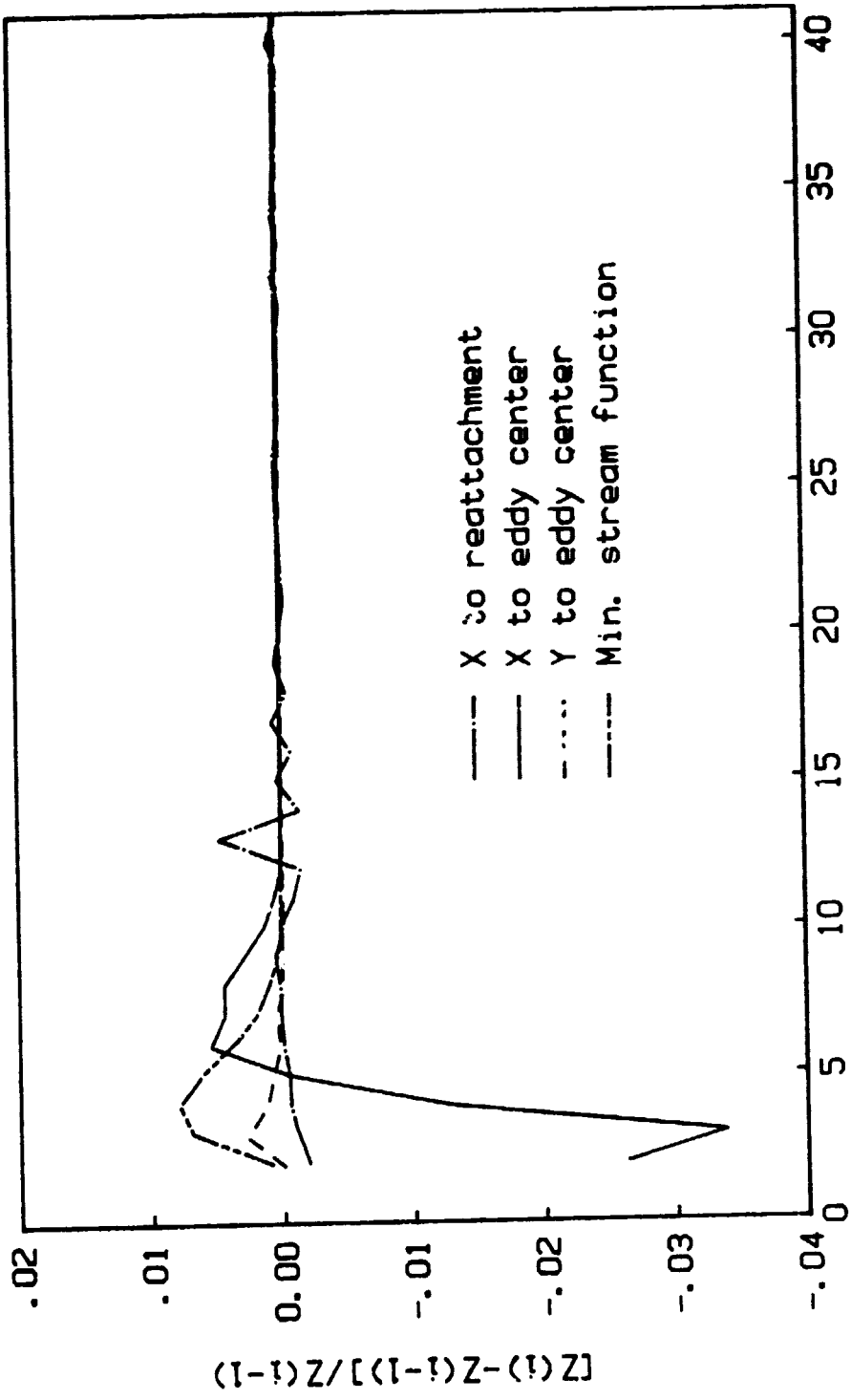

Figure 7. Relative change of hydrodynamic flc parameters with global iteration for a planar 1:2 channel expansion (Z is a surrogate iable)

b. Comparison with other data sets Reattachment length was well-predicted over a wide range of expansion ratios and Reynolds numbers. Figures 8 through 10 compare the reattachment lengths predicted by the boundary-layer equations with those of experiments and other mathematical models. The boundary-layer predictions of Figs. 8, 9, and 10 are all for only one global sweep through the flow domain. Global iteration over the flow field had almost no affect on the reattachment length predicted by the boundary-layer method.

Figure 8 compares the reattachment length and distance to the vortex center predicted by the boundary-layer equations using the FLARE approximation with the experimental and computational results of Macagno and Hung [5] for a 1:2 axisymmetric expansion. The comparison between reattachment lengths predicted by the boundary-layer solution and the results of Macagno and Hung are excellent for Reynolds numbers above twenty.

Figure 9 compares the reattachment lengths from the boundary-layer solution with that of other investigators for different Reynolds numbers and expansion ratios for symmetric planar expansions. The reattachment length measured by Durst et al. [8] was taken from a photo of smoke in air from which it was difficult to tell accurately where reattachment occurred. From Fig. 9 it appears that the agreement is very good for h/d from 0.0 to 0.5 and at least marginal from 0.5 to 1.0.

Table 5 compares the predictions of the boundary-layer equations and the Navier-Stokes equations [43] for the location of flow

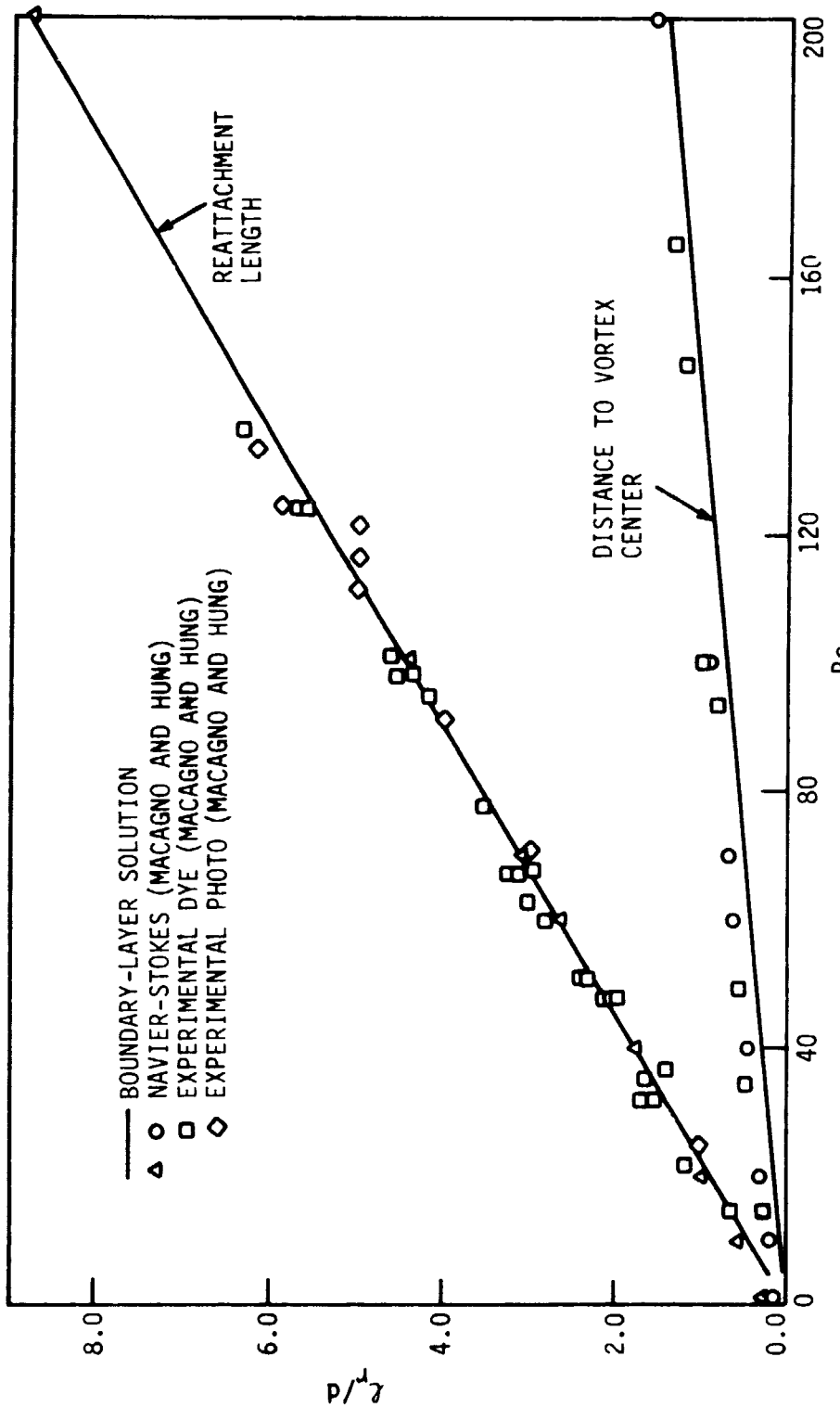

Figure 8. Comparison of the distances to flow reattachment and vortex center for experiment [5], Navier-Stokes solutions [5], and the boundary-layer equation solution with FLARE for a 1:2 pipe expansion

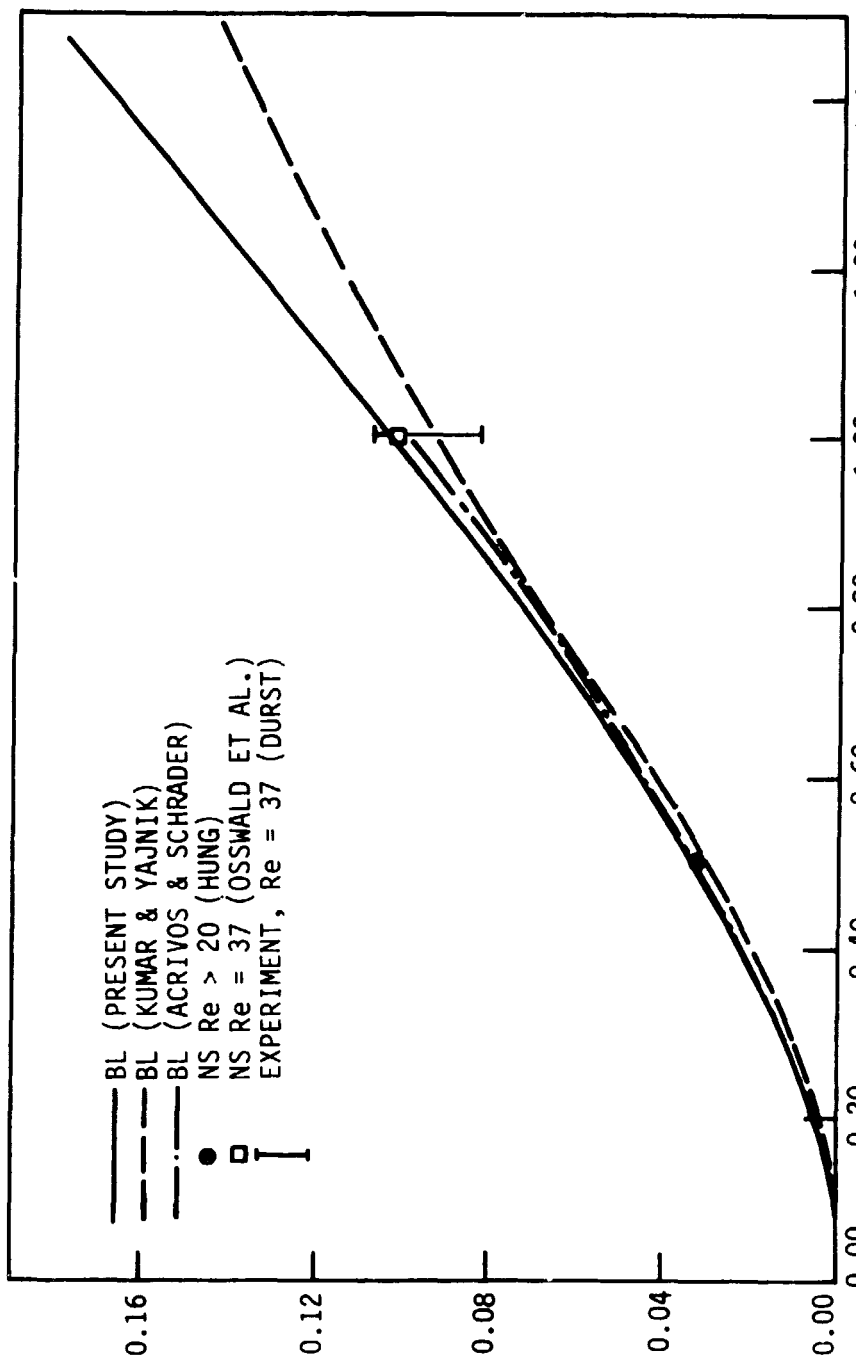

Figure 9. Nondimensional distance to reattachment for a planar channel expansion as a function of expansion ratio predicted by the boundary-layer equations [37,27], the Navier-Stokes equations [26,43], and experiment [8]

reattachment, the location of the minimum stream function (Ψ_{min}), and the absolute value of Ψ_{min}. The ratio of the inlet to outlet plate spacing was 1:3; the Reynolds number was 37.3. Even for this large expansion ratio and low Reynolds number, the distance to reattachment predicted by the boundary-layer equations is within 5% of that predicted by the Navier-Stokes equations.

Table 5. Comparison of Navier-Stokes and boundary-layer predictions for a 1:3 planar expansion

STUDY	X_r	X to Ψ_{min}, Y to Ψ_{min}	Ψ_{min}
Osswald et al. [43]	0.1030	0.0290, 0.615	0.0515
Present	0.0981	0.0227, 0.647	0.0668

Figure 10 shows the axisymmetric analog of Fig. 9. Comparisons are made with Pollard's [12] and Macagno and Hung's [5] solutions of the Navier-Stokes equations. Again the agreement appears excellent for h/d less than 0.5 and good for values as high as 1.0.

A fourth order polynomial fits the boundary-layer predictions of Figs. 9 and 10 to within 3%. The reattachment length can be expressed as

$$X_r = A + B(\frac{h}{d}) + C(\frac{h}{d})^2 + D(\frac{h}{d})^3 + E(\frac{h}{d})^4 \qquad (4.1)$$

Table 6 gives the values of the constants of Eq. (4.1). Equation (4.1) is valid for $0.1 < h/d < 1.5$.

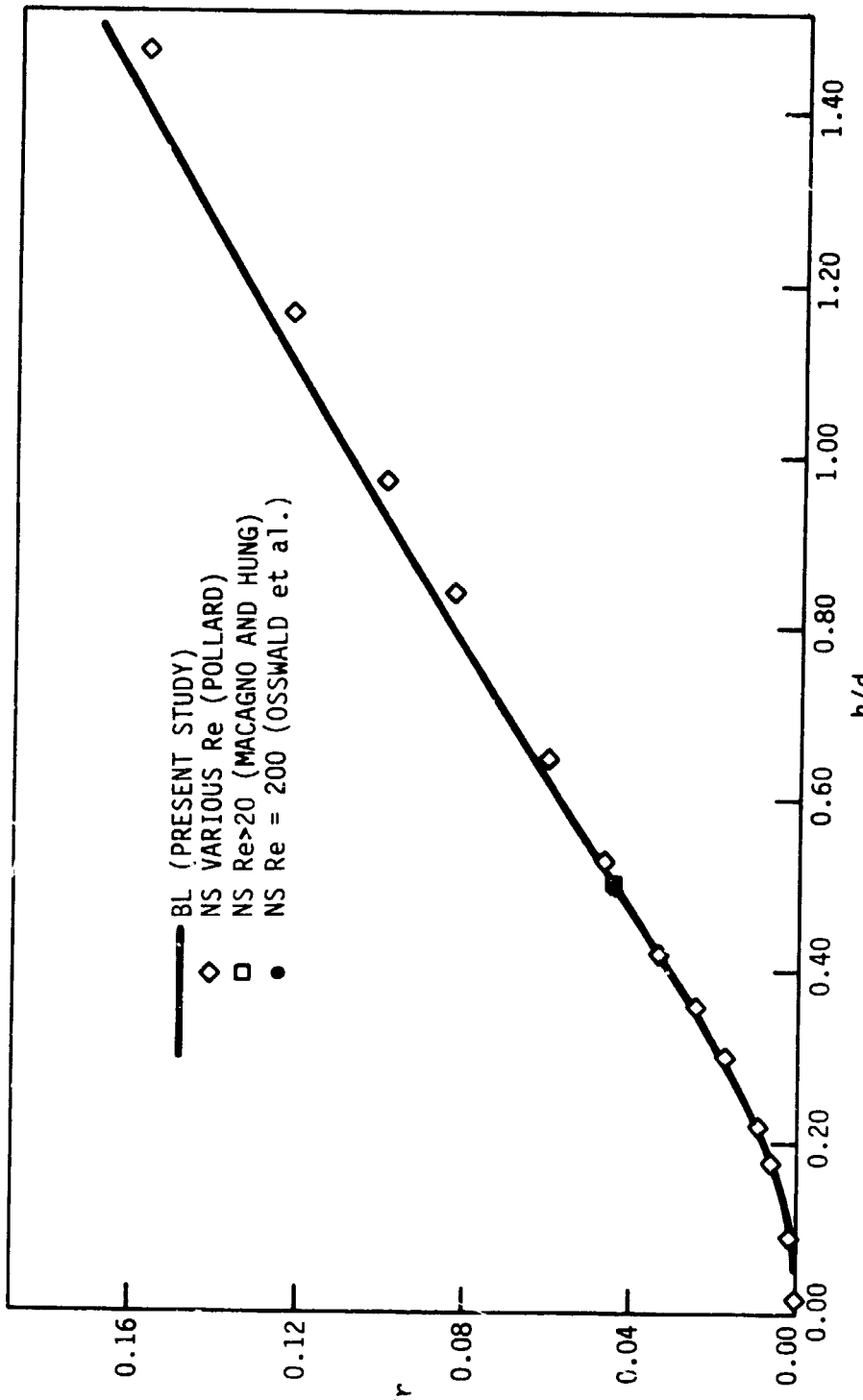

Figure 10. Nondimensional distance to reattachment for an axisymmetric expansion as a function of expansion ratio predicted by the boundary-layer equations and the Navier-Stokes equations [5,12,43]

Table 6. Coefficients for Eq. (4.1)

Geometry	A	B	C	D	E
Symmetric Planar	-0.001277	0.004262	0.1748	-0.09451	0.02086
Axisymmetric	-0.003749	0.0213	0.222	-0.1769	0.04717

Velocity comparisons with the Navier-Stokes predictions were also encouraging. The velocity predicted by the boundary-layer equations compares well with the Navier-Stokes solution of Macagno and Hung [5] (Fig. 11) for Re = 60 and a 1:2 pipe expansion. Even in the region of reversed flow the agreement is good. Figure 12 shows the centerline velocities for axisymmetric flow for three different expansion ratios. The boundary-layer solution used for this plot is again that for just one sweep down the channel since global iteration did not affect this parameter. The agreement between the boundary-layer solution and the Navier-Stokes solution of Macagno and Hung [5] for the 1:2 expansion ratio is almost perfect. Pollard's [12] predictions do not compare as well.

The constant property boundary-layer solution, which is independent of Reynolds number (see Section II.B), can be thought of as the asymptotic limit to the solution of the Navier-Stokes equations as the Reynolds number becomes large. Figure 13 shows the Reynolds number at which the boundary-layer equations can be used in place of the Navier-Stokes equations for symmetric expansions with d/D = 1/2. For Reynolds

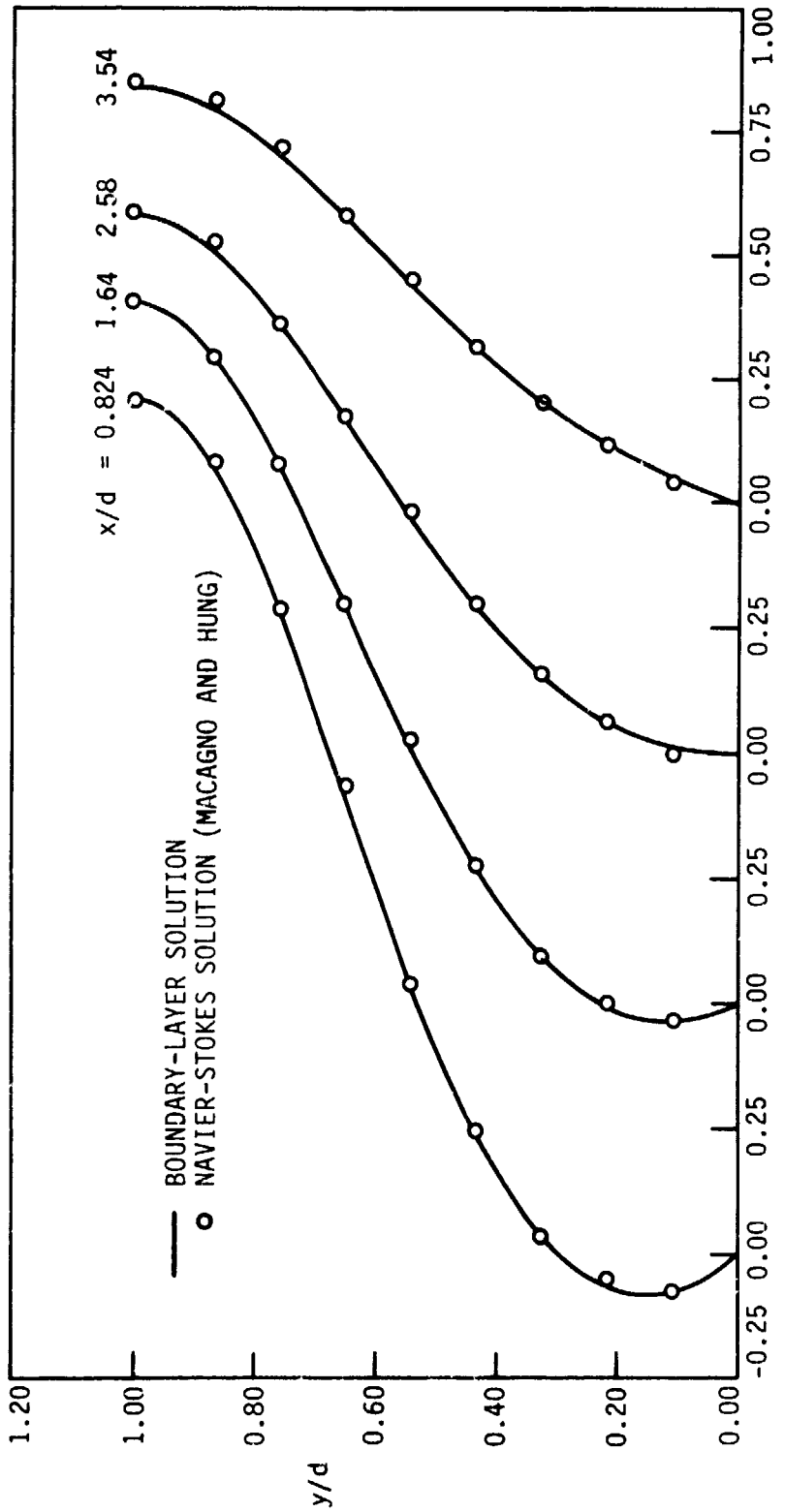

Figure 11. Comparison of velocity profiles predicted by the boundary-layer equations with FLARE and the Navier-Stokes equations [5] for Re = 60 and a 1:2 axisymmetric expansion

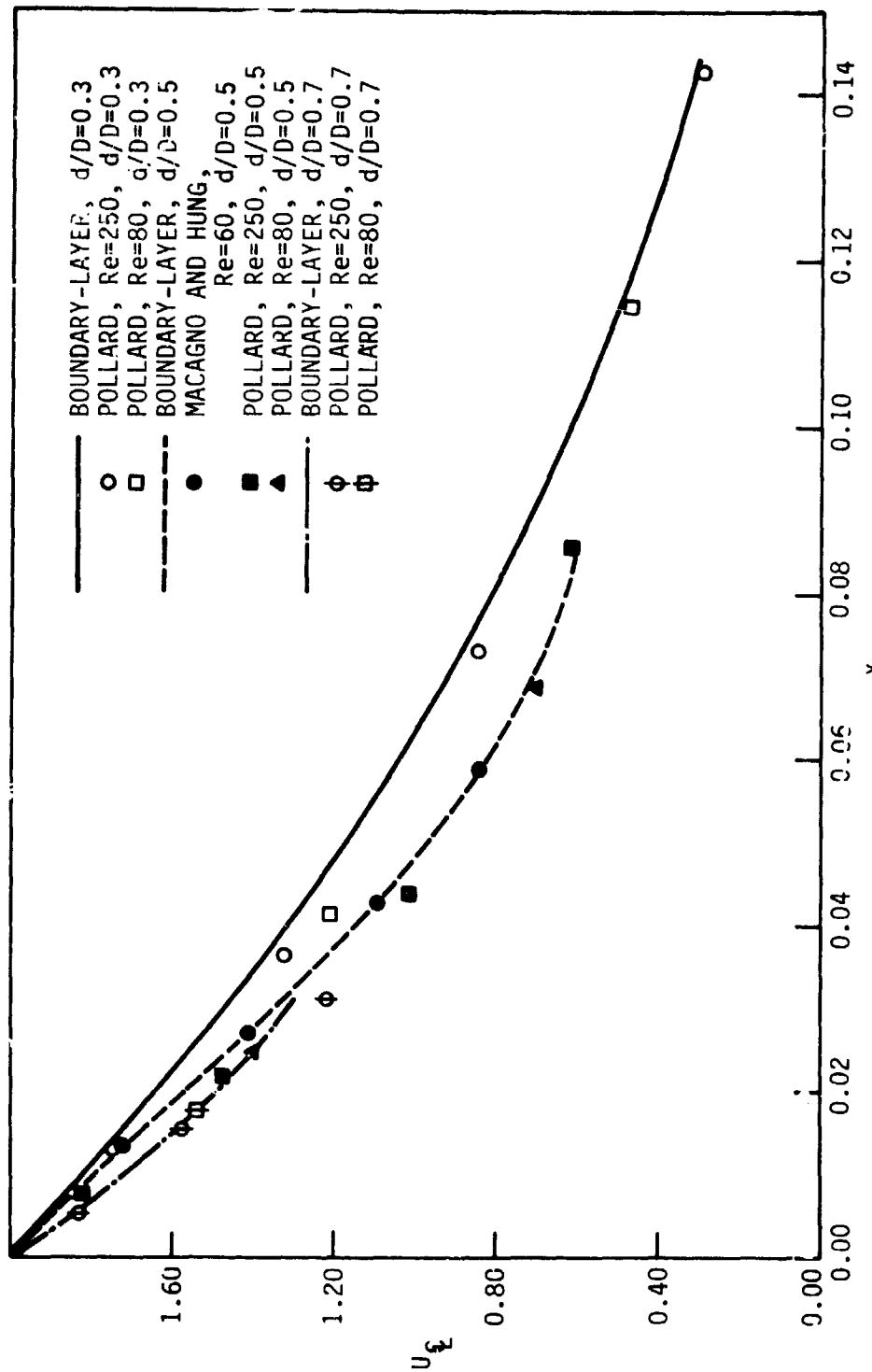

Figure 12. Comparison of centerline velocity for axisymmetric expansions predicted by the boundary-layer equations and the Navier-Stokes equations [5,12]

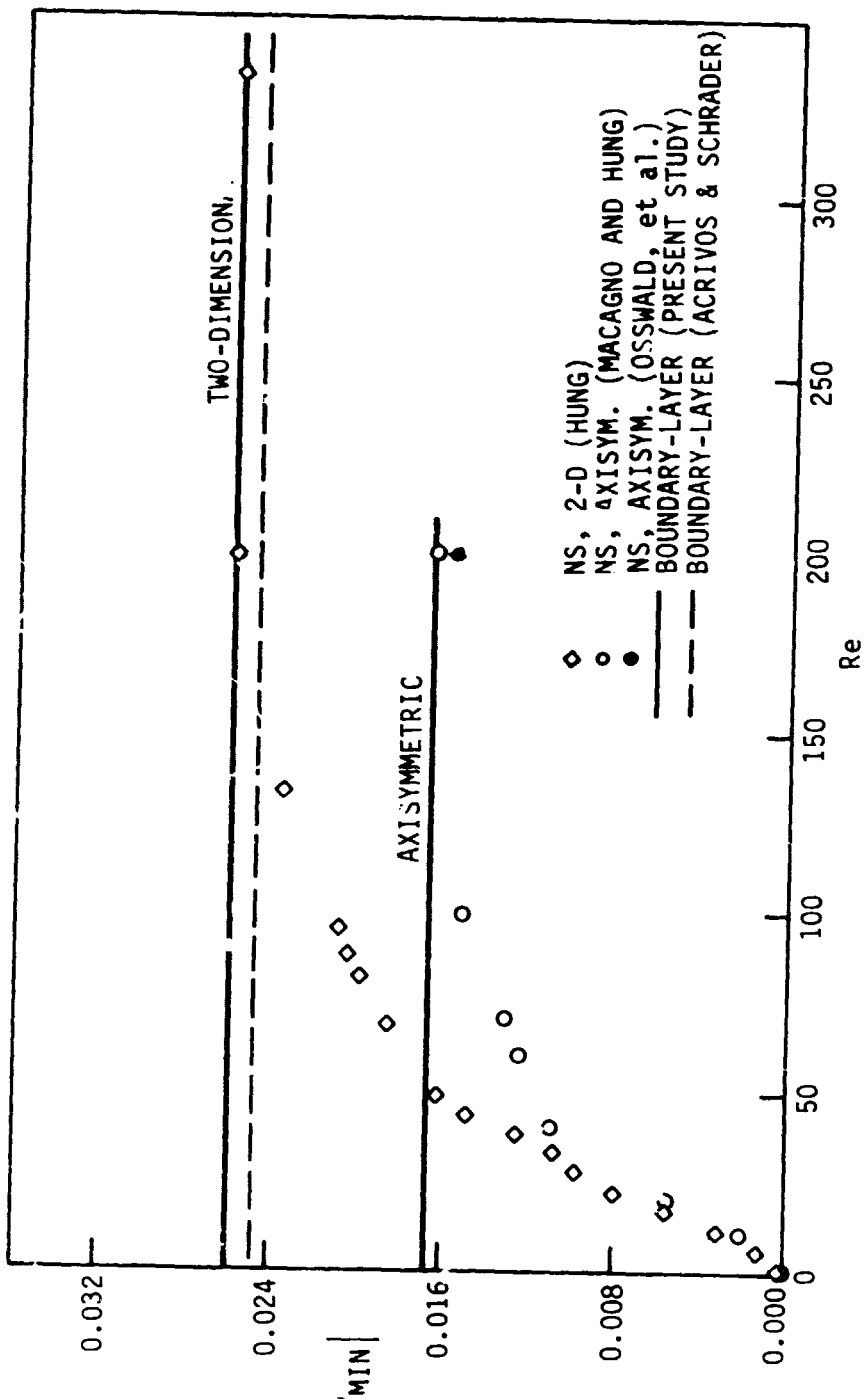

Figure 13. Comparison of the stream function at the center of the trapped vortex predicted by the boundary-layer equations and the Navier-Stokes equations [5,26,43] for a 1:2 expansion

numbers below 100, the boundary-layer predictions of Ψ_{min} are greatly in error. This trend is consistent with the Ψ_{min} comparison shown in Table 5. For the case shown in Table 5 (Re = 37.3), the prediction of Ψ_{min} by the boundary-layer equations was 30% higher than that predicted by the Navier-Stokes equations; the X-location of Ψ_{min} was 22% lower. Figure 8 shows that the distance to the vortex center predicted by the boundary-layer equations is less than that predicted by the Navier-Stokes equations and measured experimentally by what appears to be a constant amount for all Reynolds numbers. The relative error becomes less at larger Reynolds numbers. Global iterative sweeps down the channel affected Ψ_{min} by less than 1%.

Figure 14 compares c_f predicted by the boundary-layer method and that predicted by Chiu [142]. Chiu used a partially-parabolized Navier-Stokes (PPNS) model that neglected the streamwise diffusion terms but included the elliptic effects of pressure and convection. The geometry was that of a 1:3 two-dimensional expansion; the Reynolds number was 39.

Figure 14 shows that global iteration has little effect on the reattachment length (where $c_f = 0.0$). The first sweep down the channel using the boundary-layer equations predicts smaller absolute minimum values of c_f in the reversed flow region than the PPNS equations. Global iteration produces the same minimum value of c_f as the PPNS predictions, but this value occurs at a smaller X. Figure 14 hints that the boundary-layer predictions tend to "squeeze" the region of flow reversal closer to the step. Hence, the c_f curve reaches a minimum

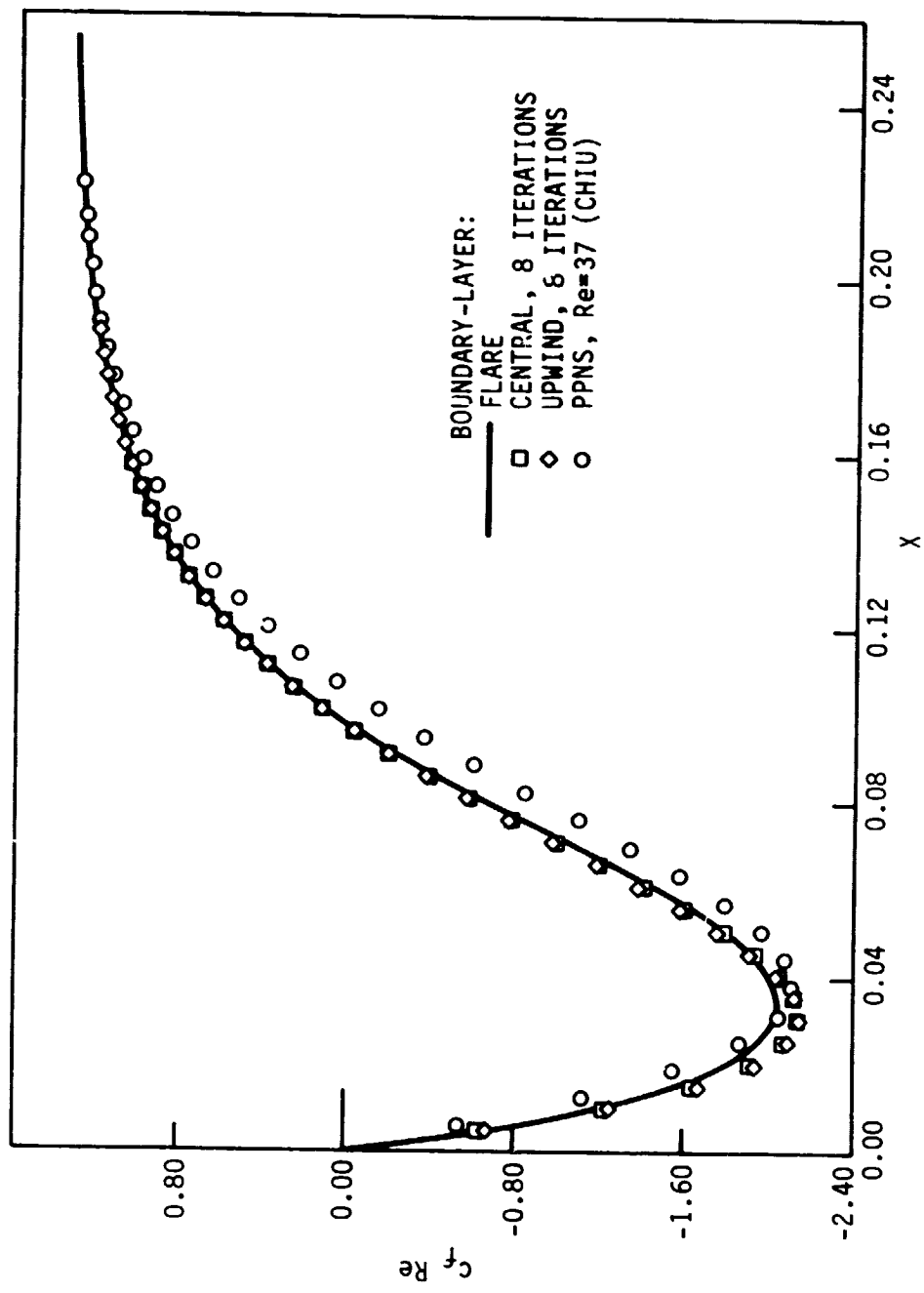

Figure 14. Comparison of friction coefficient predictions between the boundary-layer equations and the PPNS equations [142] for a 1:3 planar expansion

sooner than the PPNS model, and the distance to the vortex center is underpredicted as is shown by Fig. 8.

Figure 14 also compares central differencing and upwind differencing of the X-derivative in the reversed flow region. A few test calculations with central differencing of the X-derivative in the X-convective term were compared with the local upwind differencing that was usually used when FLARE was not in effect. Figure 14 shows that the predictions are very similar for the two types of differencing.

Figure 15 shows a comparison of c_f predicted by the boundary-layer equations and c_f predicted by Pollard [45] using the Navier-Stokes equations for a 1:2 pipe expansion. For less severe pipe expansions, as for the 1:2 expansion case, global iteration has very little effect, as is shown by Fig. 15. It should be noted that Pollard's prediction for the Re = 250 case shown in Fig. 15 overshoots the known fully-developed c_f Reynolds number product of 2.0 by 11%. Since Pollard provides very few details of his computational procedure other than that it is similar to the SIMPLE method of Patankar and Spalding [50], it is not clear why c_f exceeds the fully-developed values in some cases.

Figure 16 shows a plot of c_f similar to Fig. 15 for d/D = 0.7 and Re = 250 which is a relatively mild expansion and a high Reynolds number. For a Reynolds number this large, the agreement was expected to have been better. Pollard's c_f predictions do not support the supposition that the boundary-layer solution tends to "push" the recirculation region closer to the step as does Chiu's [142] and Macagno and Hung's [5].

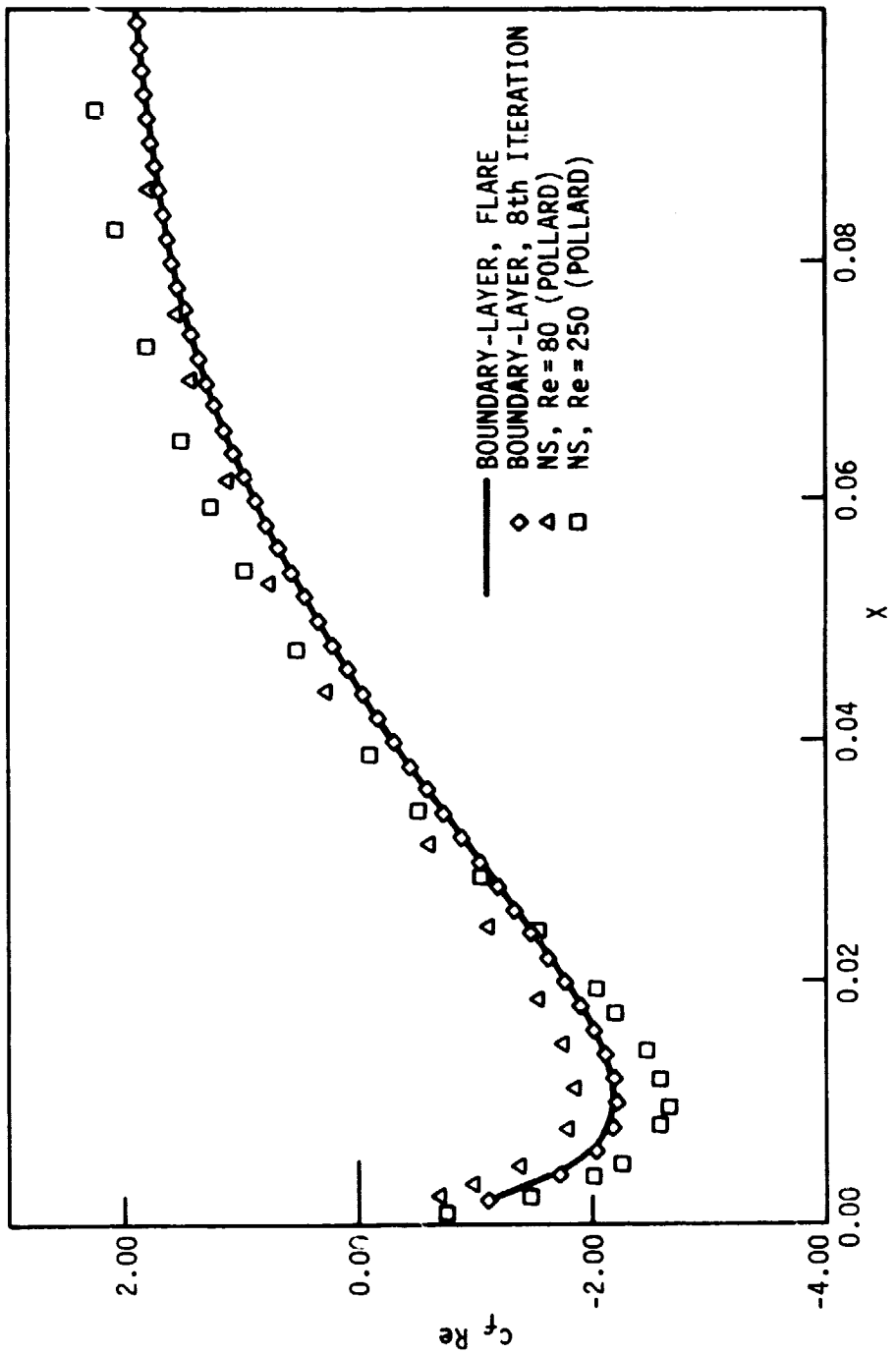

Figure 15. Friction coefficient predicted by the boundary-layer equations with and without global iteration compared with the Navier-Stokes solution [45] for a 1:2 pipe expansion

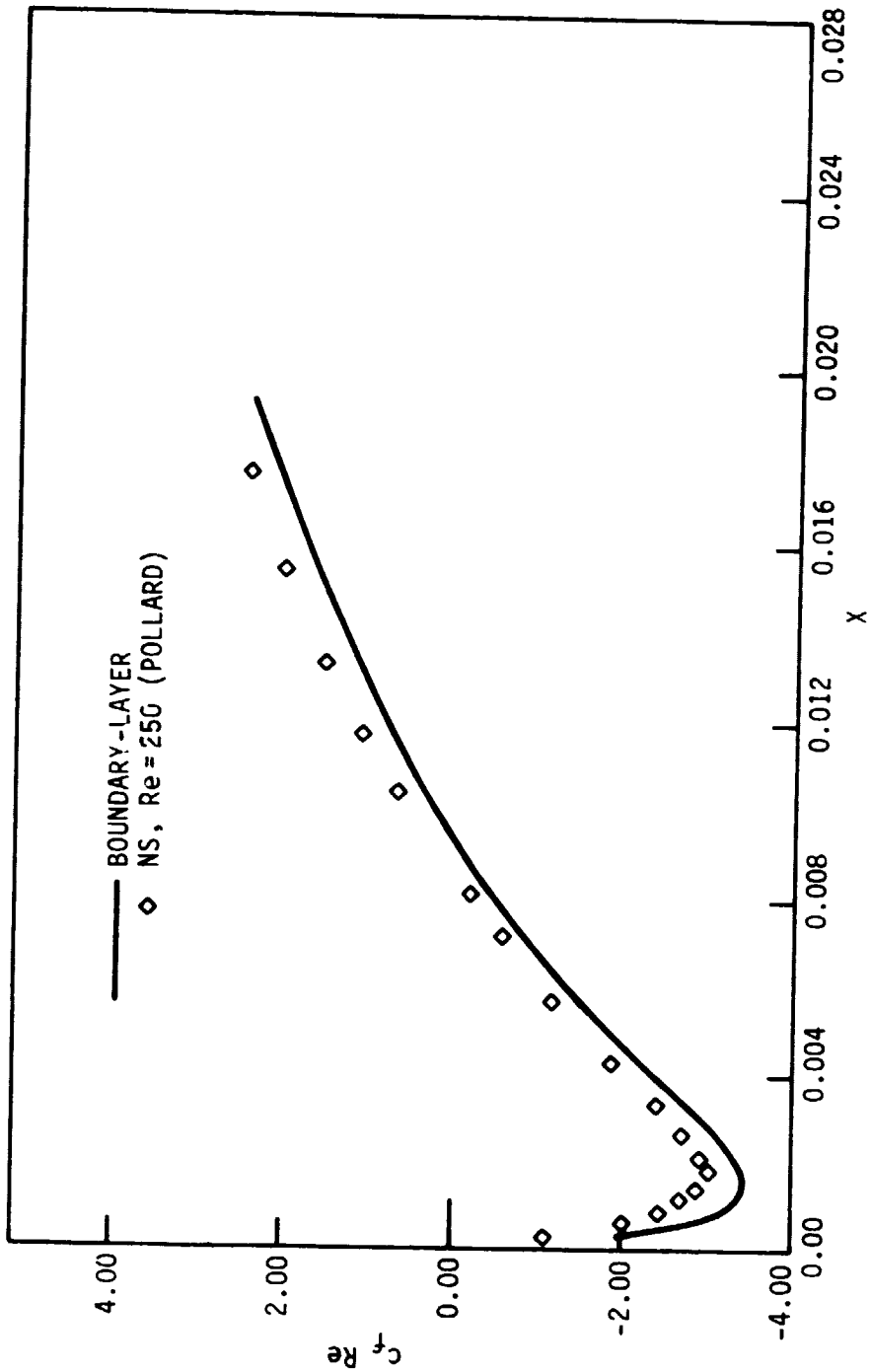

Figure 16. Friction coefficient predicted by the boundary-layer equations compared with the Navier-Stokes solution [45] for a pipe expansion with d/D = 0.7

Figures 17 and 18 show predicted values of the skin-friction coefficient for different values of h/d for planar and axisymmetric expansions respectively. Both figures show results obtained using the "once-through" method with the FLARE approximation. When using these curves, one should realize that they many not be accurate in the recirculation region for low Reynolds numbers (less than 100).

Figure 19 shows the effect of global iteration on the pressure gradient for a 1:3 two-dimensional expansion. The pressure gradient appears to be the parameter most affected by global iteration. The predicted dP/dX was very similar whether local upwind or central differencing of the X-derivative in the X-convective term was used when flow reversal was present.

One interesting prediction of the boundary-layer equations using FLARE was the existence of a small secondary eddy in the corner formed by the wall and the step. For d/D = 0.5, this eddy was less than 1/220th the length of the primary eddy. This eddy was discovered while using an extremely small ΔX for mesh refinement studies. The second eddy rotates in a direction opposite that of the large one. The flow situation very near the corner is similar to Stokes flow across the top of a wedge cut in a wall. The solution to this Stokes flow is a "stack" of eddies in the wedge, decreasing in size and intensity as one moves down in the wedge [143]. For runs employing global iteration, a grid fine enough to predict the secondary eddy was not used due to expense. (ΔX would had to have been less that 1/400th the distance to

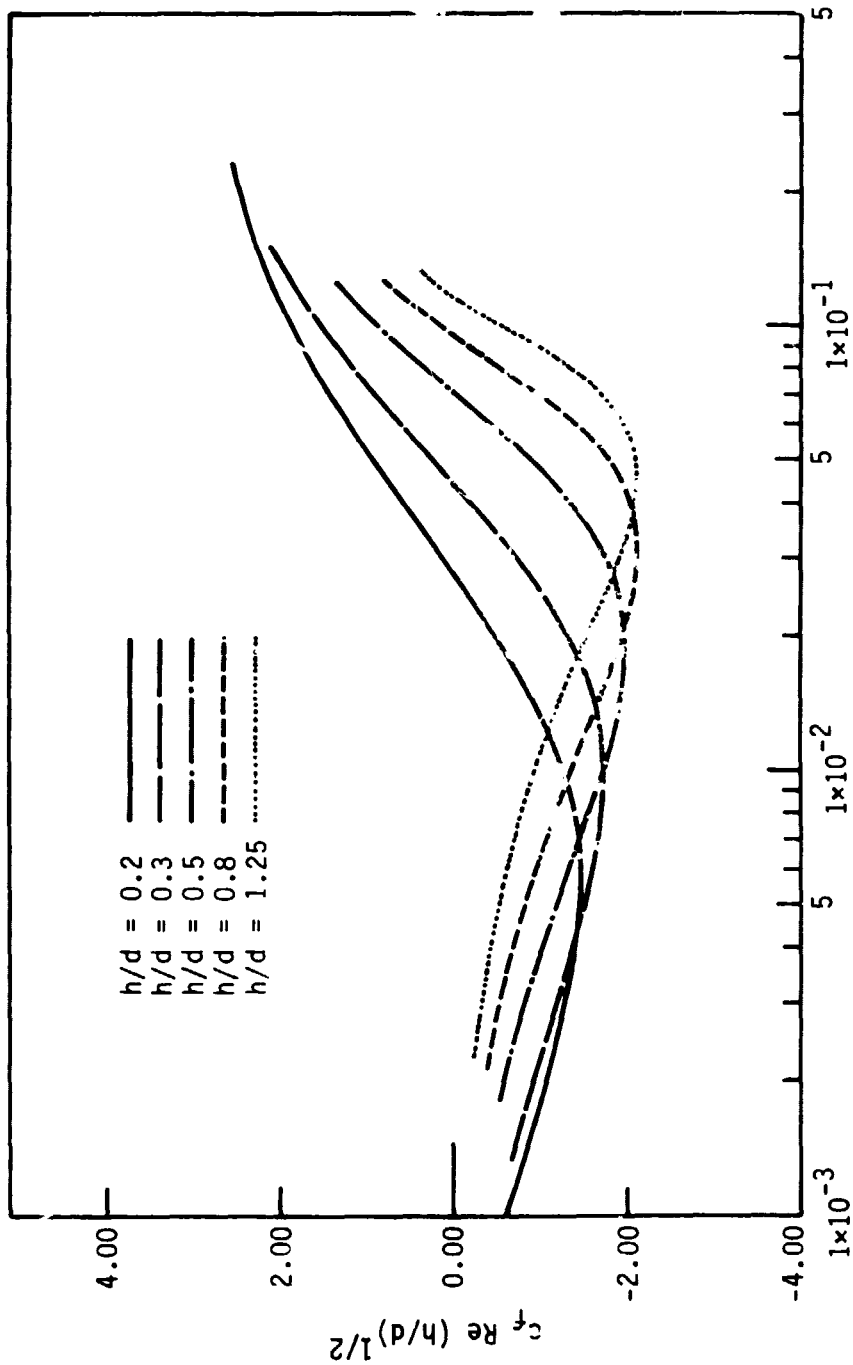

Figure 17. Friction coefficient predicted by the boundary-layer equations using FLARE for different expansion ratios for symmetric planar expansions

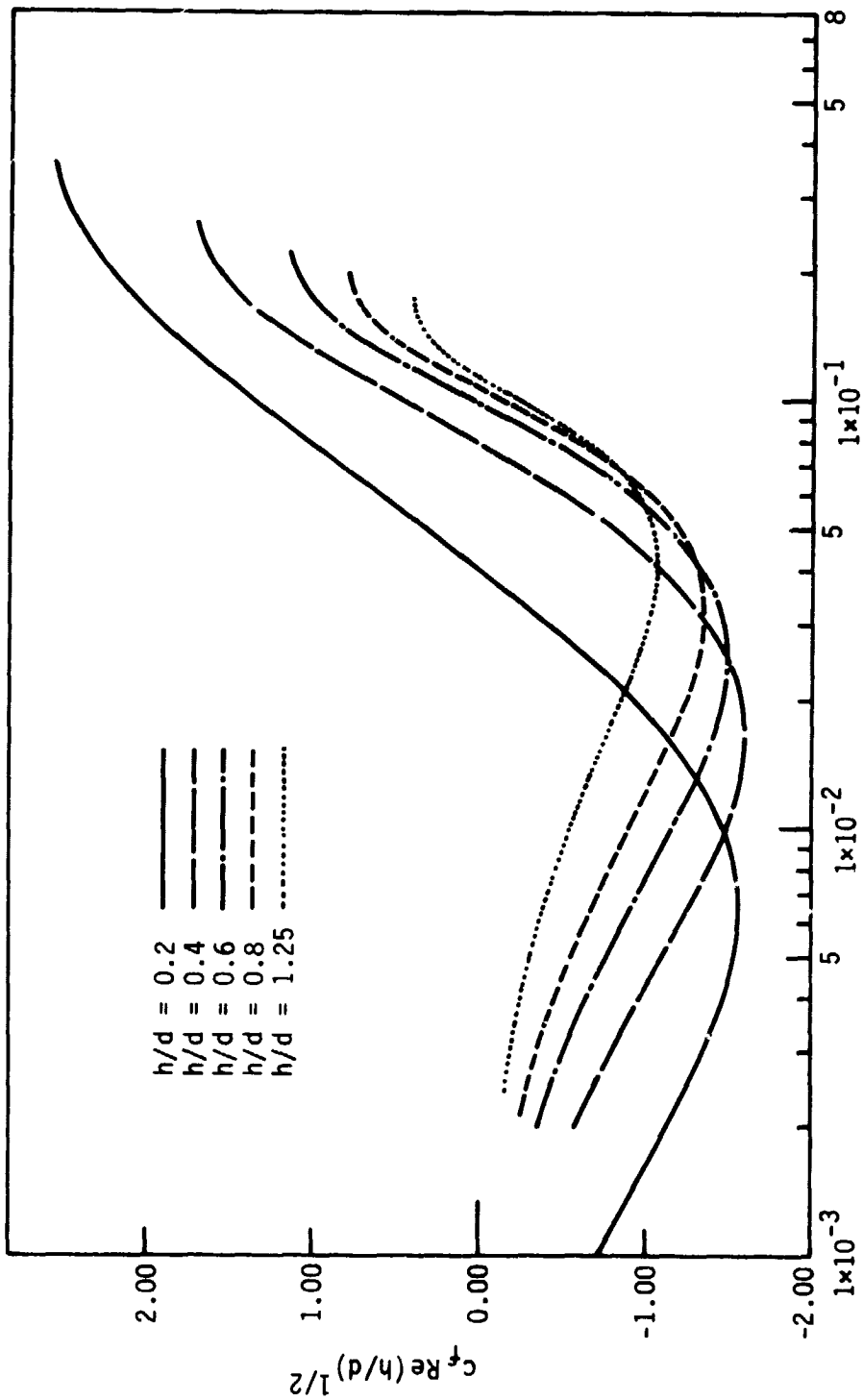

Figure 18. Friction coefficient predicted by the boundary-layer equations using FLARE for different expansion ratios for axisymmetric expansions

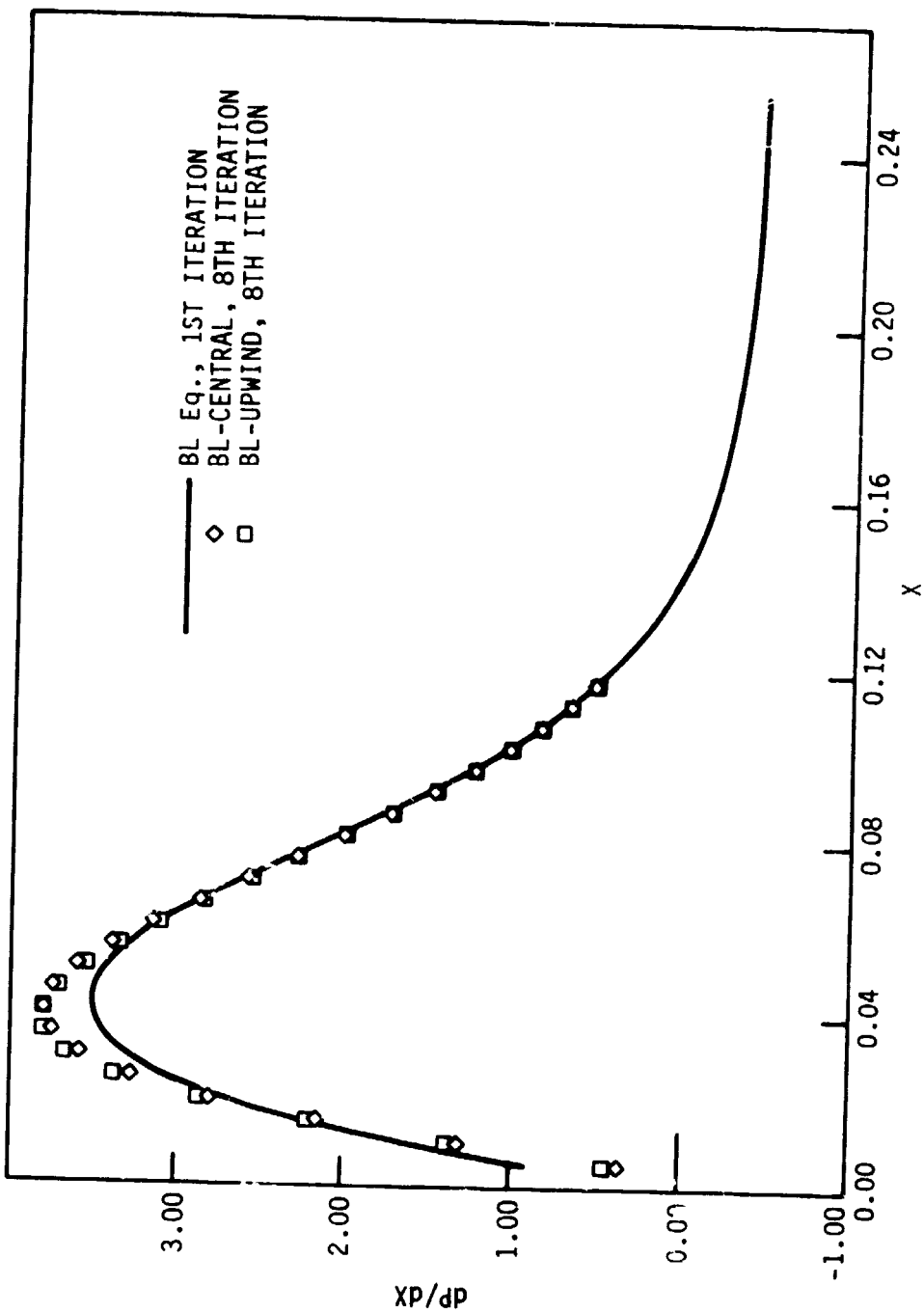

Figure 19. Effect of global iteration on the dimensionless pressure gradient, $d^2/(\mu u_i)dp/dx$, for a 1:3 planar expansion ($X=x/(d\ Re)$)

reattachment to place one marching station beyond the step in the secondary eddy for d/D = 0.5.) Those solving the Navier-Stokes equations usually do not use a grid fine enough to resolve the secondary corner eddy.

c. Initial conditions Modifying the initial conditions along the face of the step as proposed by Acrivos and Schrader [27] to take into account the "collision velocity" at the face of the step as was discussed in Section II.A.4.b was found to be of minor importance. The algorithm to determine the necessary velocity at the step face [144] predicted nonzero velocities for moderately fine grids but predicted zero velocities as the grid was refined. To test the effect a "collision velocity" could have had on the solution, the effect of the following sinusoidal velocity along the face of the step was studied:

$$U(0,y) = -A \sin(\frac{2\pi y}{h}), \quad 0 \leq y < h \tag{4.2}$$

where A is an arbitrary amplitude. The predictions of the boundary-layer equations with global iteration for flow through a 1:2 planar expansion was used as a test case. An extreme case with A = 0.15, which caused velocities at the step to be greater than those normally in the recirculation region, predicted the reattachment length, location of Ψ_{min}, and value of Ψ_{min} to within 2% of the A = 0 case. (For a 1:2 expansion, the maximum speed of the fluid in the recirculation region was 0.12 in the negative X-direction.) Figure 20 shows that the difference between the c_f predicted by the A = 0 case and the A = 0.15

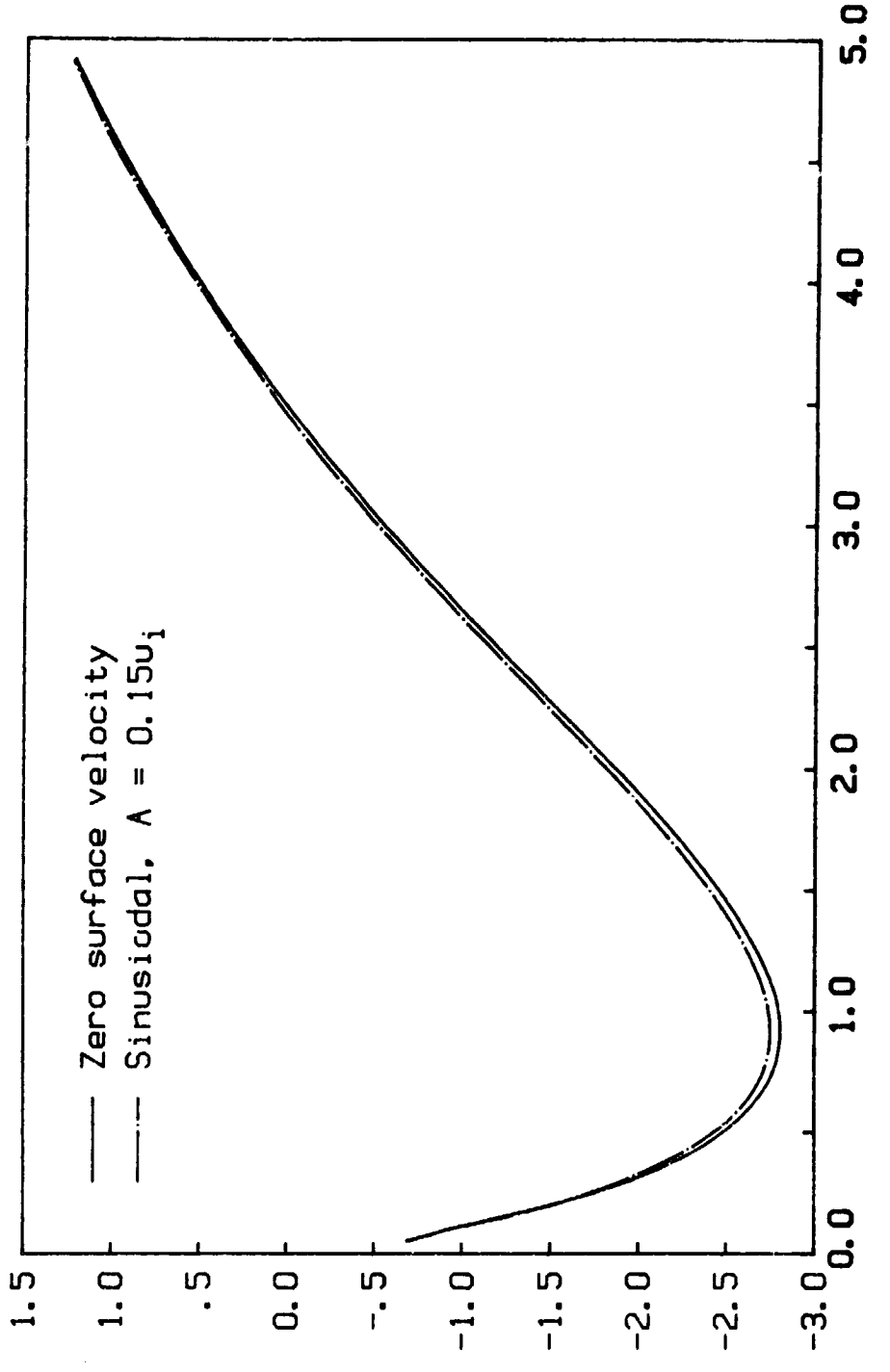

Figure 20 Effect of a nonzero face velocity on the friction coefficient for a 1:2 planar expansion (X=x/(d Re))

case is not significant. Since a "collision velocity" was not predicted and would have had very little effect if it were predicted, a zero face velocity was used for all other calculations of the present study.

d. Primitive variable results The primitive variable formulation was used to test methods for determining the pressure gradient in the channel. The most efficient method is similar to that used for the u-ψ variable formulation where the 2x2 matrices below the diagonal are eliminated. Then, Eq. (3.43) with $V_{NJ} = 0.0$ is used to algebraically give an expression for β in terms of known coefficients. The results using this method were the same as those predicted by the U-Ψ variable formulation. For internal flows, the U-V form is in fact somewhat easier to program.

If one desires to use one of the available general block solvers, the channel mass flow constraint cannot be included in the algorithm before the back-substitution step without adding an extra equation used to determine the pressure gradient to each block of equations as was done by Cebeci [145]. If the extra equation is not added, an iterative procedure as discussed in Section III.B.2.b of the previous chapter is required. The three different variations of the secant method investigated in this study had different levels of success. Variation 1 was by far the superior algorithm. A planar expansion with a 1:2 expansion provided a test case.

1) Variation 1 As described in Section III.C.2.b, variation 1 nested the pressure secant loop in the Newton linearization

loop. This ensured that an accurate value of the dimensionless pressure gradient, β, was obtained before making the next Newton linearization iteration. The secant iteration continued until the newly predicted β had a relative change from the old value less than some prescribed limit. The relative difference between the first and second secant predictions for β was less than 5.0×10^{-4} and usually less than 5.0×10^{-6}. (The first secant iteration is the first prediction after the two calculations were done using the guessed values of β.) A relative change of 5.0×10^{-5} was used as the criterion for convergence. Since only one secant iteration was usually sufficient, it appears that there is a nearly linear relationship between the pressure gradient error and the error in V at the centerline.

A comparison of the results using variation 1 and the U-Ψ variable solution showed the velocities, pressure, and c_f agreeing to four significant digits. In general, the results were within 0.5% of the U-Ψ scheme. There were no oscillations of c_f as predicted by Kwon and Pletcher [39] when the continuity and momentum equations were not coupled. The execution time was three times slower than the U-Ψ scheme. This ratio seems reasonable since the pressure secant method had to solve the system of equations three times in order to find the correct β.

The number of Newton linearization iterations was counted for each step down the channel. Generally, only one update of the provisional coefficients was necessary. For the smallest ΔX used, the relative

change between iterations was less than 0.0005 on the second calculation of the velocities at a given X-position.

2) Variation 2 The Newton linearization loop inside the pressure loop caused the solution to converge to an erroneous solution and then diverge when predicting the expansion flow. It makes little sense to use Newton linearization iteration when the initial pressure derivative is inaccurate. The failure of variation 2 shows the importance of leaving the pressure derivative as a variable and solving for it along with the velocities at each X-station. Variation 2 predicted the correct velocity profile when modeling the inlet flow between two parallel plates which involved no separation.

3) Variation 3 Removing the Newton linearization loop from variation 1 caused large oscillations for the first few X-stations beyond the step. Figure 21 compares the predictions of c_f for variation 1 and variation 3 for a Reynolds number of 50.

2. Heat transfer

The results of this section are for variable property flow unless specified otherwise. Both specified heat flux and specified wall temperature boundary condition predictions will be discussed. Global iteration was important when predicting the temperature field.

a. Comparison with other data sets As mentioned in the Literature Review, there are no experimental laminar heat transfer data sets for symmetric rapid expansions. For this reason, comparisons were made with pipe entry flows to check the program.

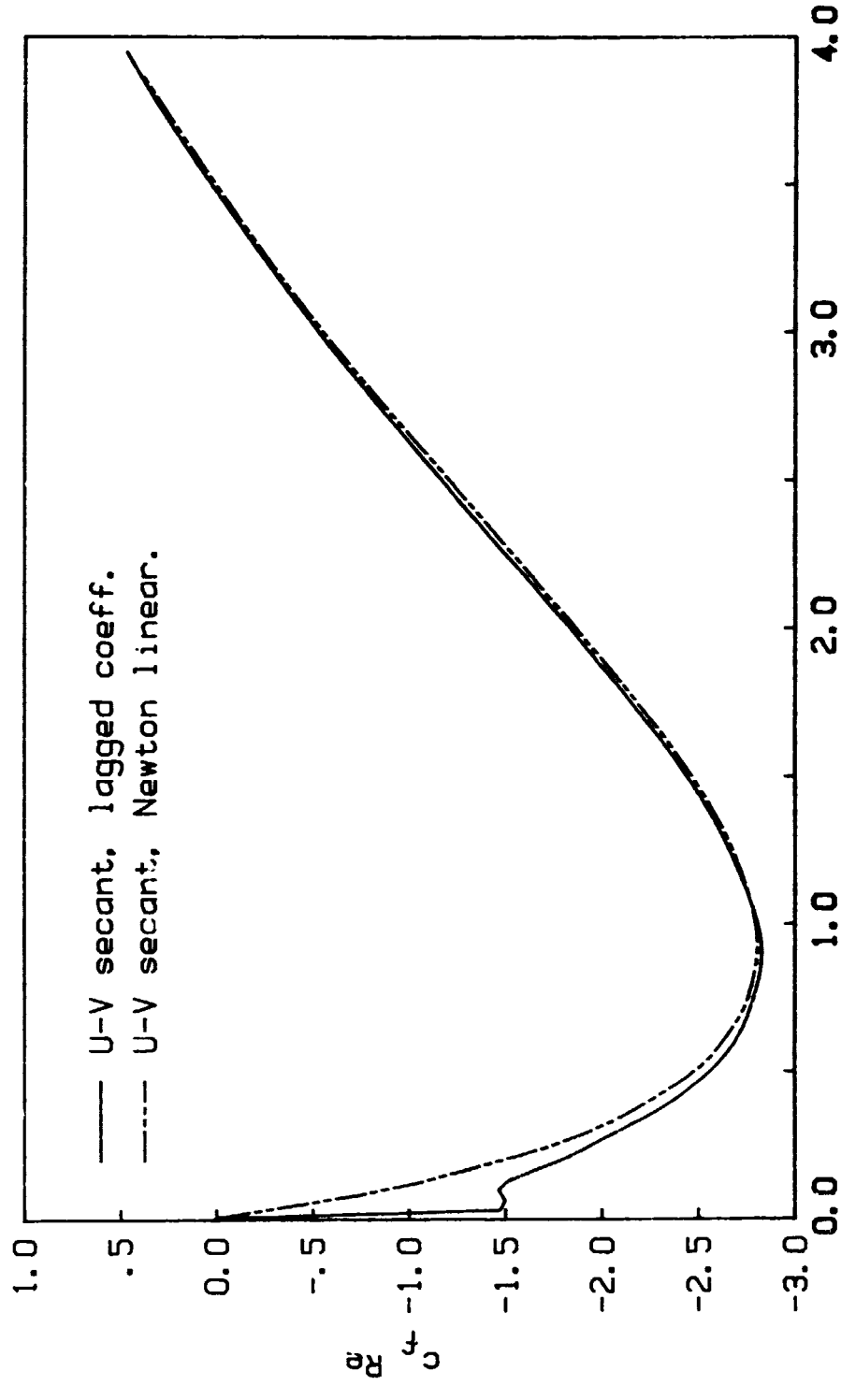

Figure 21. Primitive variable prediction of the friction coefficient for a 1:2 planar expansion using pressure derivative secant variations 1 and 3 (X=x/(d Re))

Figure 22 compares the Nusselt number predictions of the present study with a constant property eigen-function solution [127] for air flowing in a pipe. The temperature profile is uniform at the inlet and the velocity profile is fully-developed. The boundary condition at the wall is given by a constant wall temperature.

Figure 23 shows the predicted bulk temperature, T_b, for variable property inlet flow in a pipe with a constant specified heat flux at the wall. The velocity and temperature profiles at the inlet are both uniform. Figure 23 compares the finite-difference solution of the boundary-layer equations by Bankston and McEligot [146] with the present predictions using the ASHRAE property expressions given in Appendix A and the power-law property expressions used by Bankston and McEligot. The the wall heat flux was

$$\frac{q_w(d/2)}{k_i T_i} = 10$$

where k_i and T_i are respectively the thermal conductivity at the inlet and the absolute temperature at the inlet.

b. Predictions Flow through a 1:2 pipe rapid expansion was predicted for a constant wall temperature and a constant wall heat flux. The inlet diameter in both cases was 50mm; the inlet temperature profile was uniform at 10°C.

1) Constant heat flux For the specified heat flux boundary condition predictions, Re = 200 based on inlet conditions, and $q_w = 25\ W/m^2$. The constant heat flux prediction converged much slower

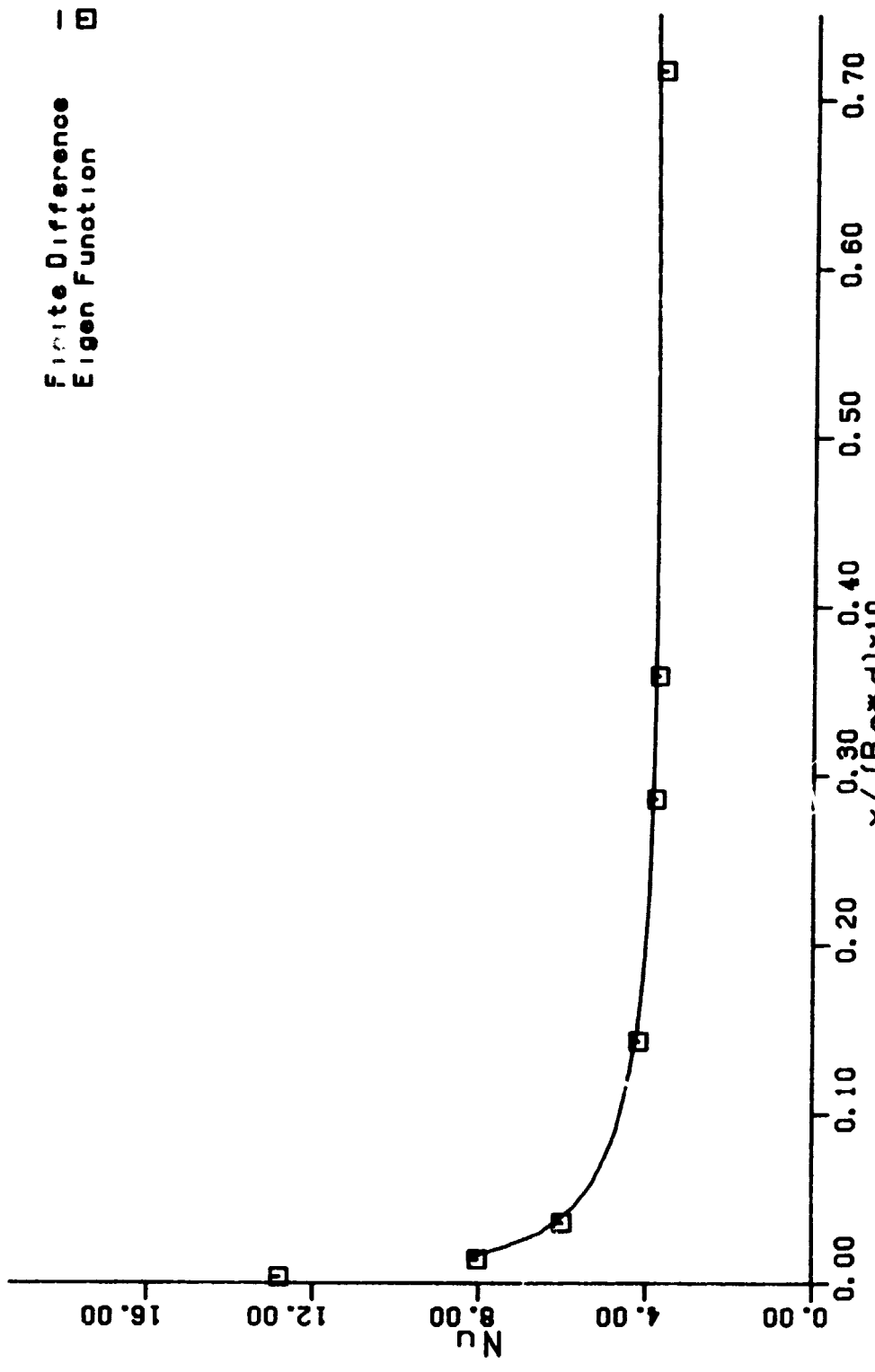

Figure 22. Predicted Nusselt number for inlet pipe flow having an initial fully developed velocity profile and uniform temperature profile compared with an analytical solution for a constant wall temperature boundary condition [127] (Pr = 0.7)

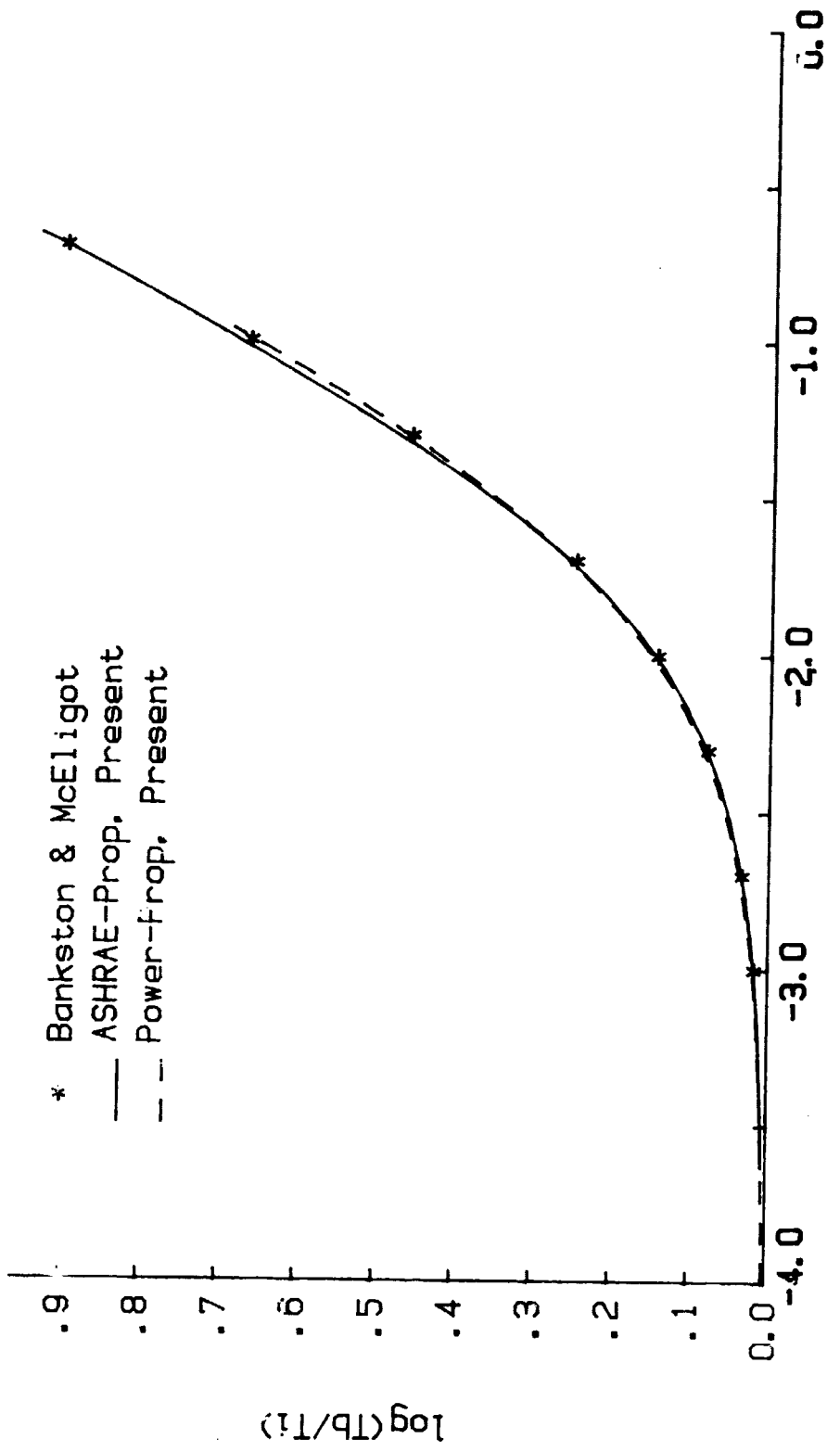

Figure 23. Comparison of the predicted bulk temperature for a pipe entry flow with a constant wall heat flux with the boundary-layer predictions of Bankston and McEligot [146] (absolute temperature ratio, $x^+ = x/(r_o Pe)$)

than the specified wall temperature prediction. For the specified heat flux, the temperature field boundary conditions are specified by the slope everywhere except at the inlet above the step. Since the actual value of the temperature is "tied" down only for a small portion of the boundary, the solution for the specified heat flux boundary condition converges very slowly. Figure 24 shows the relative change of the wall temperature at three different x-values with respect to global iteration. The momentum and continuity equations were not solved each time the solution of the energy equation was obtained due to the computational expense. A hydrodynamic solution was computed on energy global iteration numbers 1, 3, 10, 30, and 45-50. The large "burp" in Fig. 24 at iteration 30 is caused by the u-ψ values being recomputed. Figure 25 shows the effect of global iteration on the Nusselt number. There is very little difference between the 30th and 50th iterations. This indicates that 30 iterations are sufficient for convergence. Figure 26 shows the wall temperature and the bulk temperature computed by Eq. (2.81) and Eq. (2.82). Ideally, the two bulk temperature curves should exactly correspond.

2) Constant wall temperature The predictions for the constant wall temperature boundary condition were obtained for Re = 1000 based on inlet conditions and T_w = 100°C. Only six global iterations were required for convergence of the specified wall temperature predictions. By specifying the temperature along the wall as opposed to the slope of the temperature as for the specified wall heat flux, the

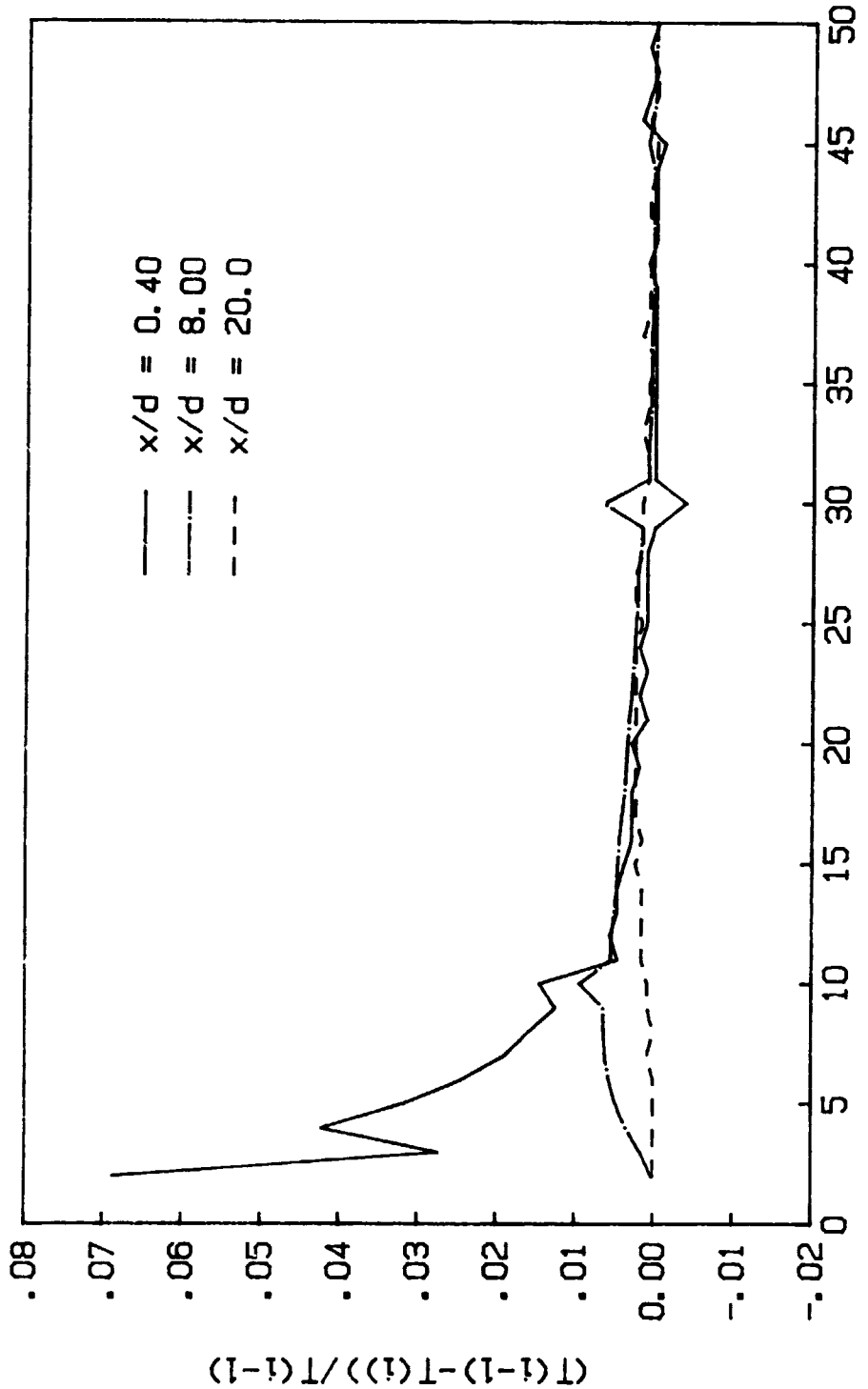

Figure 24. Relative change of the wall temperature at three different channel locations with global iteration for a 1:2 pipe expansion

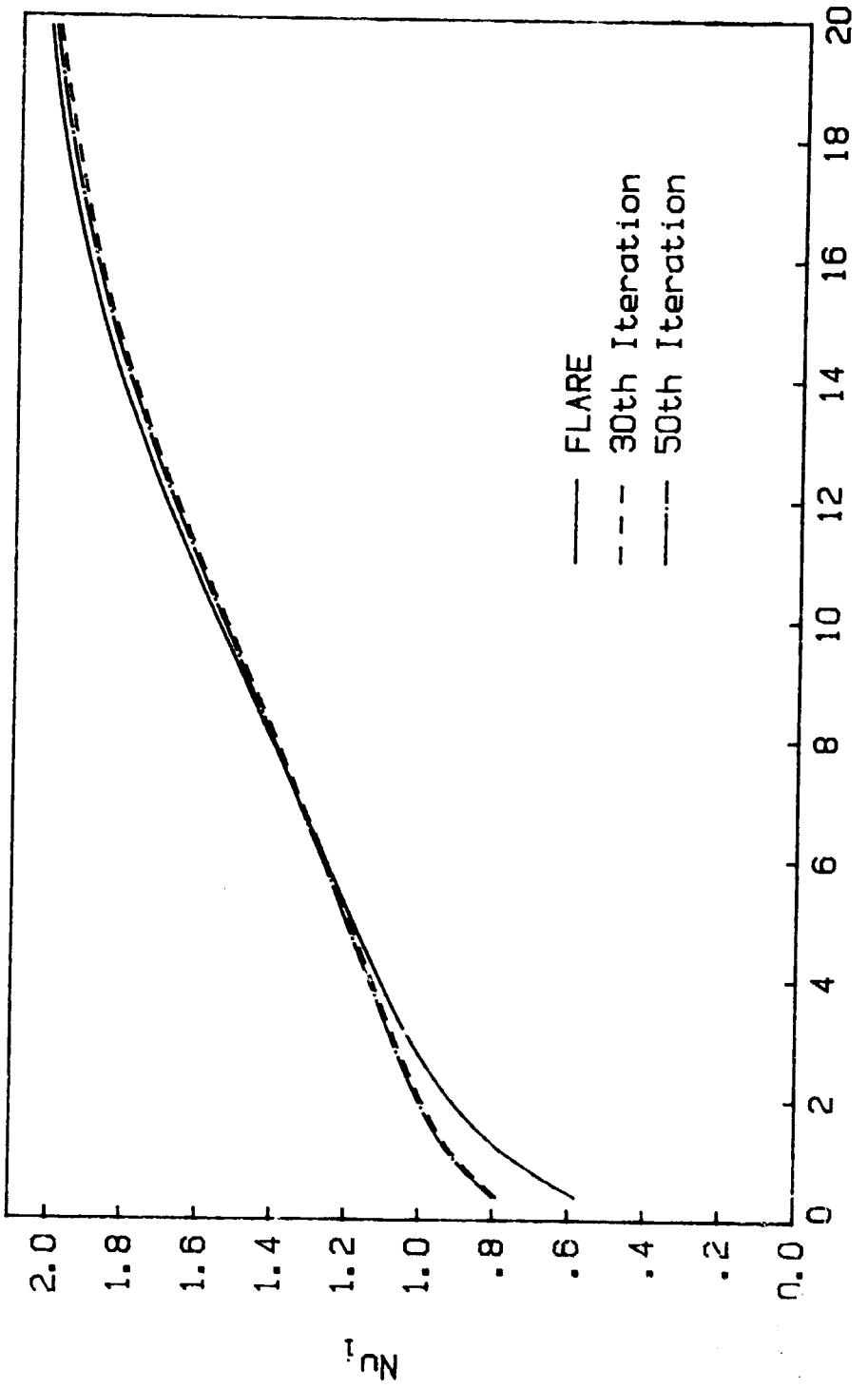

Figure 25. Nusselt number for a 1:2 pipe expansion with a heat flux boundary condition (Re_i=200, q_w=25 W/m^2, Pr=0.7, x is dimensional)

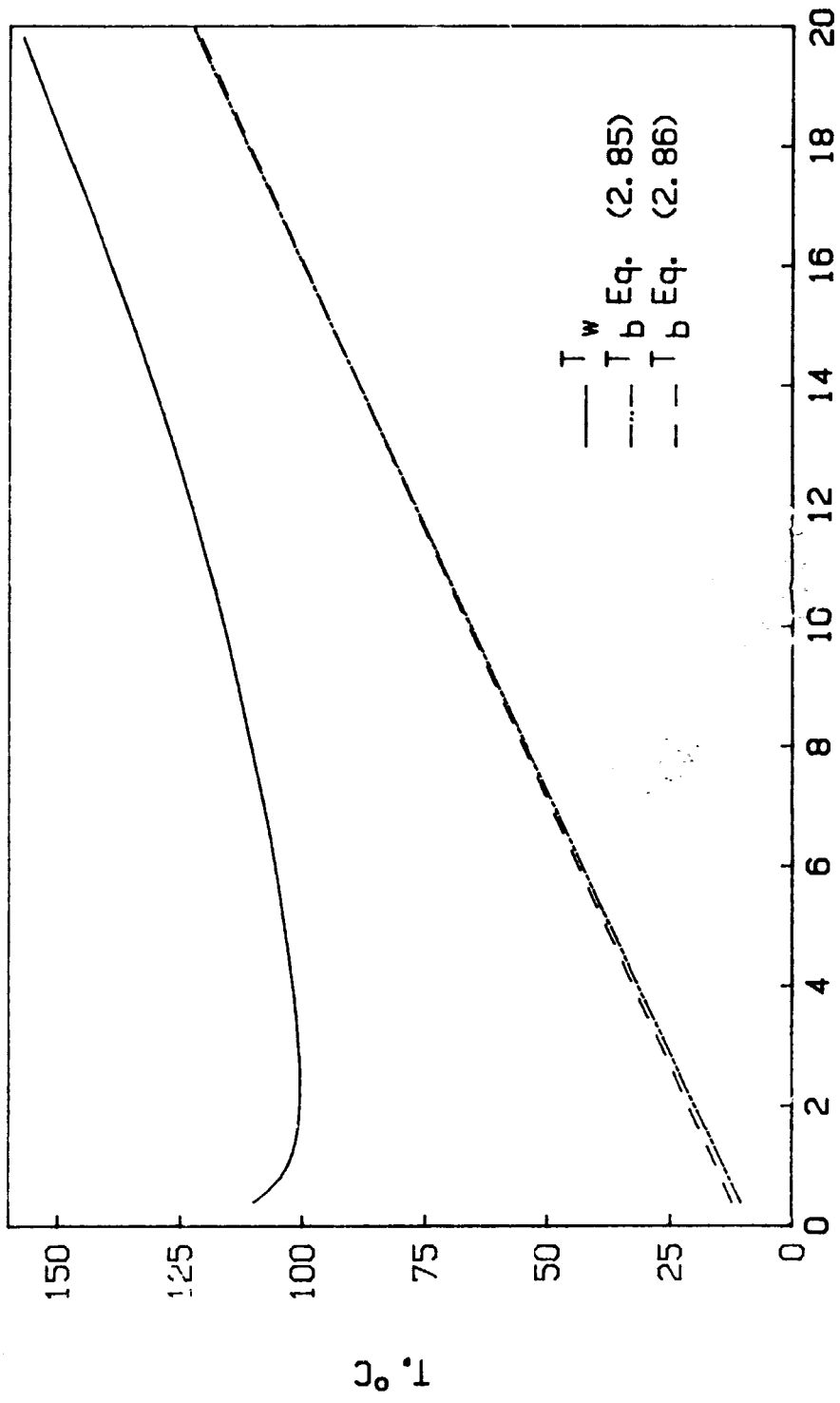

Figure 26. Wall temperature and bulk temperature for a 1:2 pipe expansion with a heat flux boundary condition (Re_i=200, q_w=25 W/m², Pr=0.7, inlet T_b=10°C, x is dimensional)

solution responds to the boundary conditions much quicker. Figure 27 shows the Nusselt number for the first and sixth global iterations for a constant wall temperature boundary condition. Figure 28 shows the Nusselt number for three different mesh sizes after convergence.

B. Turbulent

This section describes the turbulent flow results. The differences between the predictions using the low-Reynolds-number k-ε equations and the high-Reynolds-number k-ε equations with the different near-wall models will be presented.

The turbulent calculations were done using a Perkin Elmer 3240 computer. An average run using a 121x120 grid required 3.5 minutes of CPU time for the first iteration and 1.2 minutes for subsequent iterations. The reason for the different CPU time requirements is due to the linearization procedure used after the first global iteration for the turbulent flow calculations. For the turbulent flow calculations, the Newton linearization was dropped after the first global iteration and the nonlinear terms were linearized using values from the previous global iteration.

1. Hydrodynamic constant temperature

a. Fully developed pipe flow The hydrodynamic solution procedure was first tested by comparing with the well-documented fully developed pipe flow. Air at 17°C flowing in a pipe of internal radius of 0.1235m with a Reynolds number of 41,680 was used as a test case.

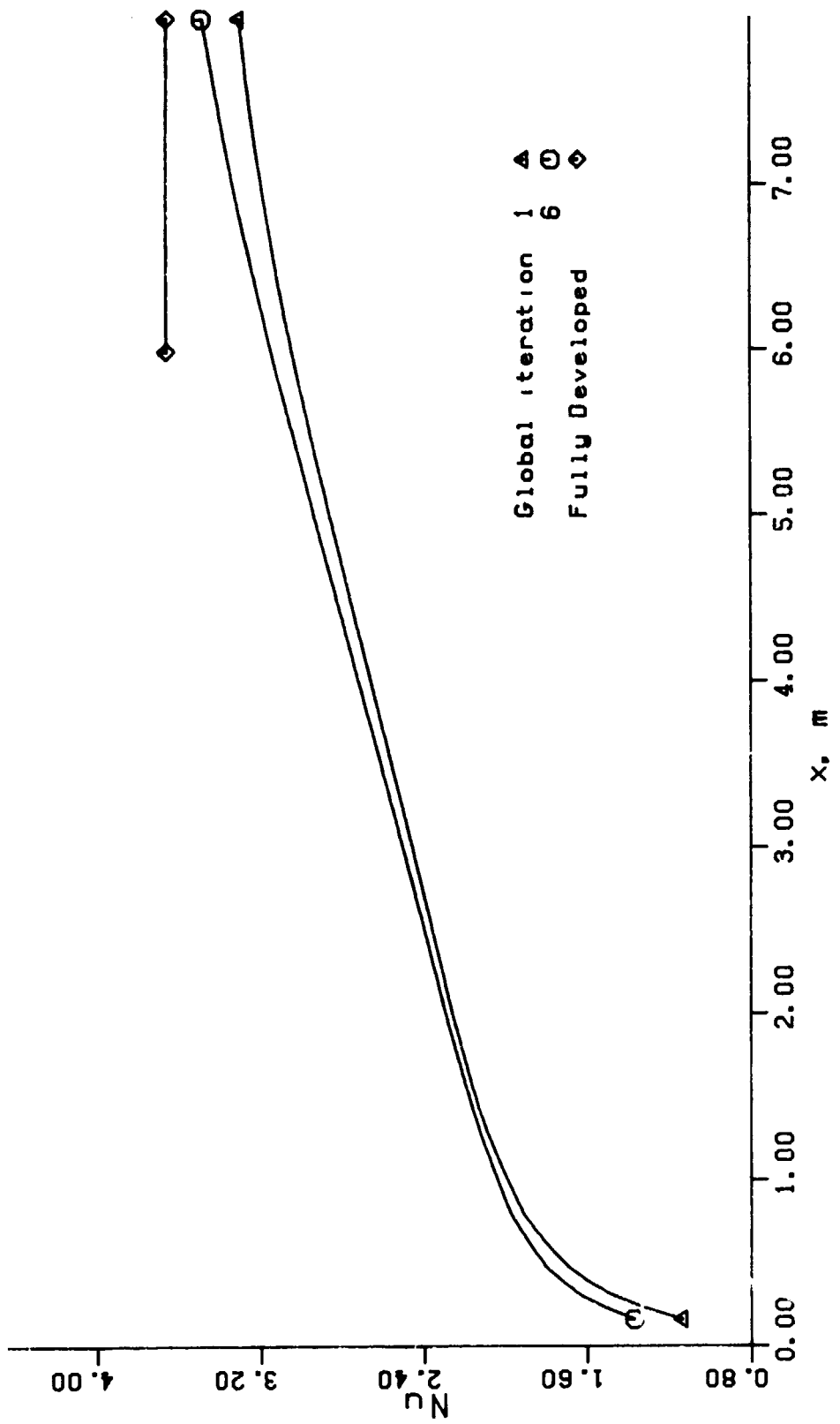

Figure 27. Nusselt number for a 1:2 pipe expansion with a wall temperature boundary condition (Re_i=1000, T_w=100°C, Pr=0.7, inlet T_b=10°C, x is dimensional)

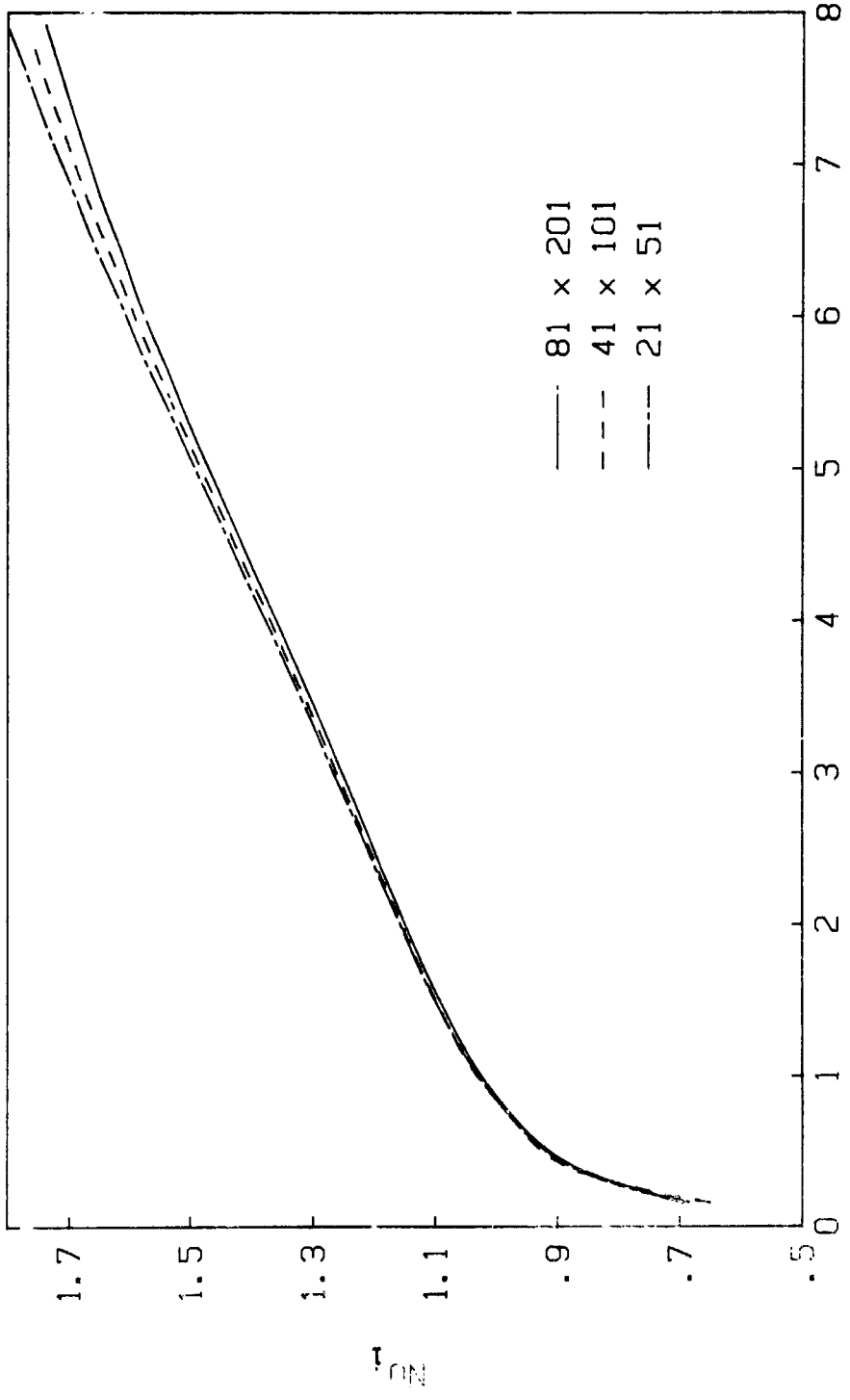

Figure 28. Effect of grid refinement on the Nusselt number for a 1:2 pipe expansion with a specified wall temperature (Re_i=1000, T_w=100°C, Pr=0.7, inlet T_b=10°C)

Uniform inlet conditions for u, k, and ε were specified; the inlet condition for ψ was obtained by integrating the u profile. There were 80 unequal grid divisions in y so that at least two grid points above the wall were in the viscous sublayer.

Figure 29 shows the computer predictions of the velocity compared with Eqs. (2.60) and (2.61) in law-of-the-wall coordinates. Three different methods of specifying the turbulent length scale were used in conjunction with the low-Reynolds-number k-equation: (1) an algebraic mixing length given by Eq. (2.56), (2) the high-Reynolds-number ε-equation with the ε boundary condition applied at $y^+ = 30$ and Eqs. (2.56) and (2.75) for $y^+ < 30$, and (3) the low-Reynolds-number ε-equation solved throughout the flow field. Figure 29 shows that for fully developed pipe flow, all three methods give similar velocity predictions.

Figures 30 and 31 show that the three different methods of specifying the near-wall mixing length predict widely varying values of k and Reynolds stress near the wall. The turbulent kinetic energy predicted by the low-Reynolds-number ε-equation is much closer to experimental values near the wall (Fig. 30). However, the Reynolds stress predictions using the low-Reynolds-number ε-equation do not correspond to the experimentally measured values as well as those using the high-Reynolds-number ε-equation.

For separated flow, the first global sweep with the low-Reynolds-number model predicted reattachment lengths that were more than twice as

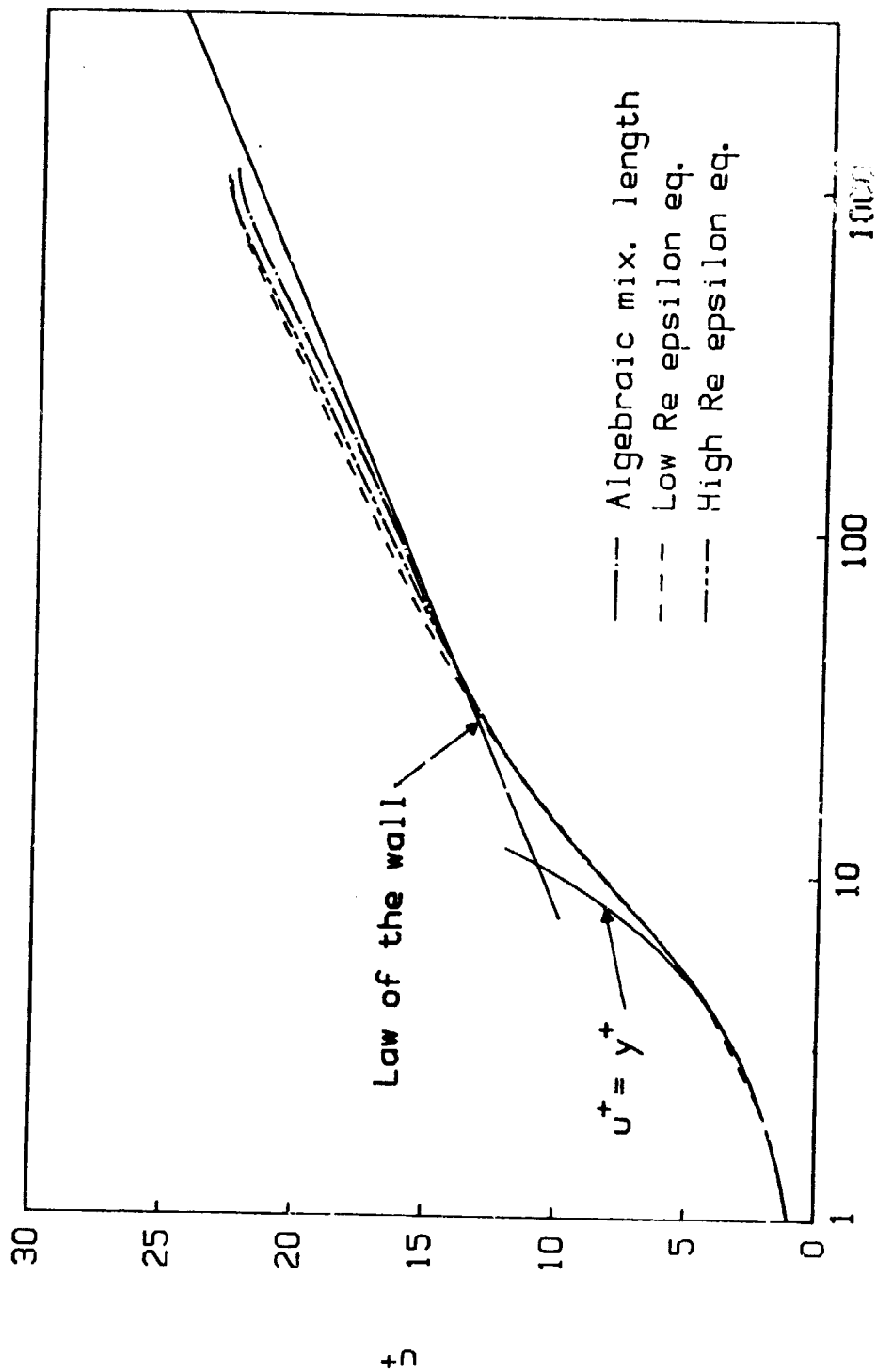

Figure 23 Fully developed pipe velocity profile in law-of-the-wall coordinates for three different length scale models used with a low-Reynolds-number k-equation

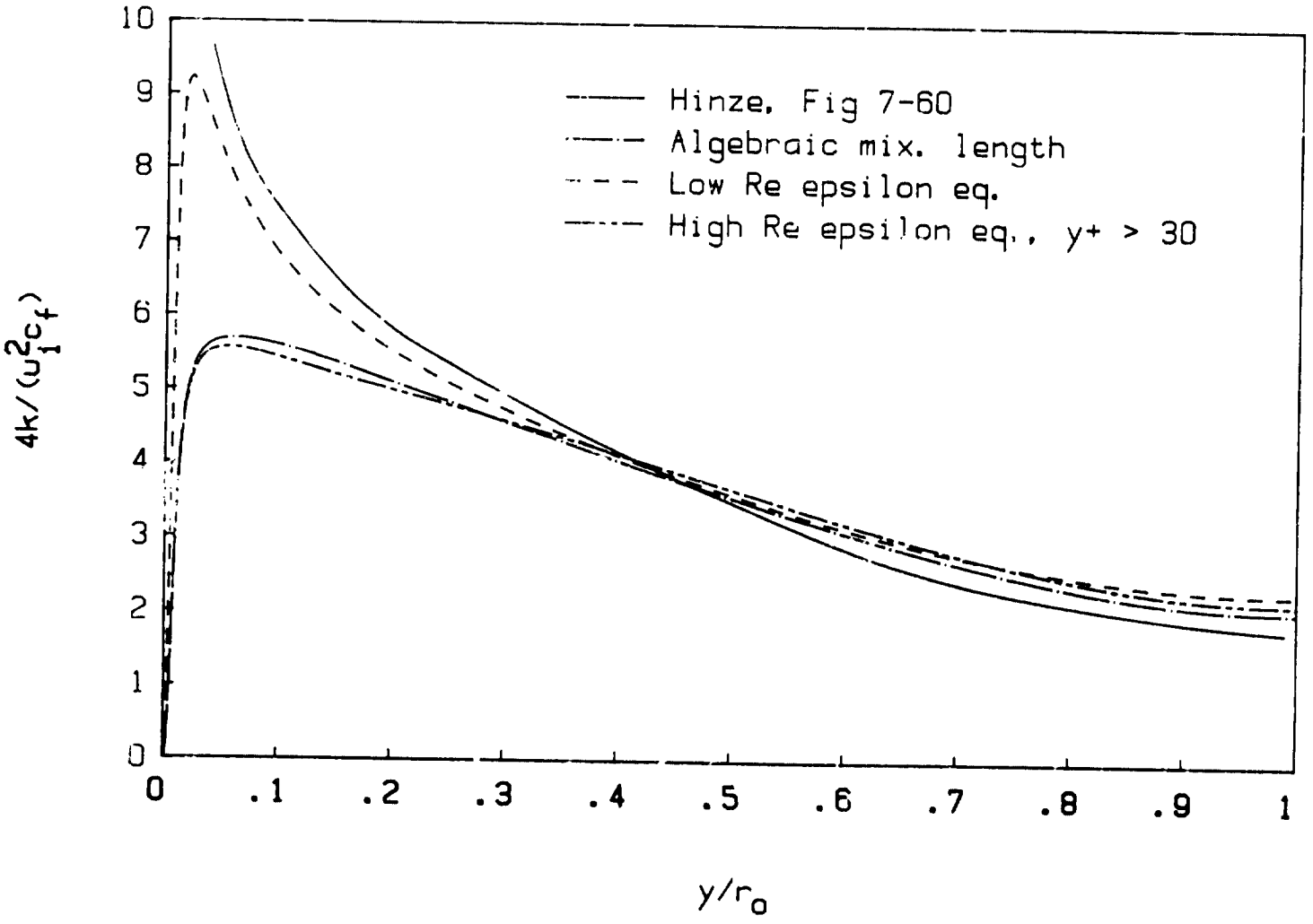

Figure 30. Fully developed pipe flow turbulent kinetic energy profiles for three different length scale models used with a low-Reynolds-number k-equation

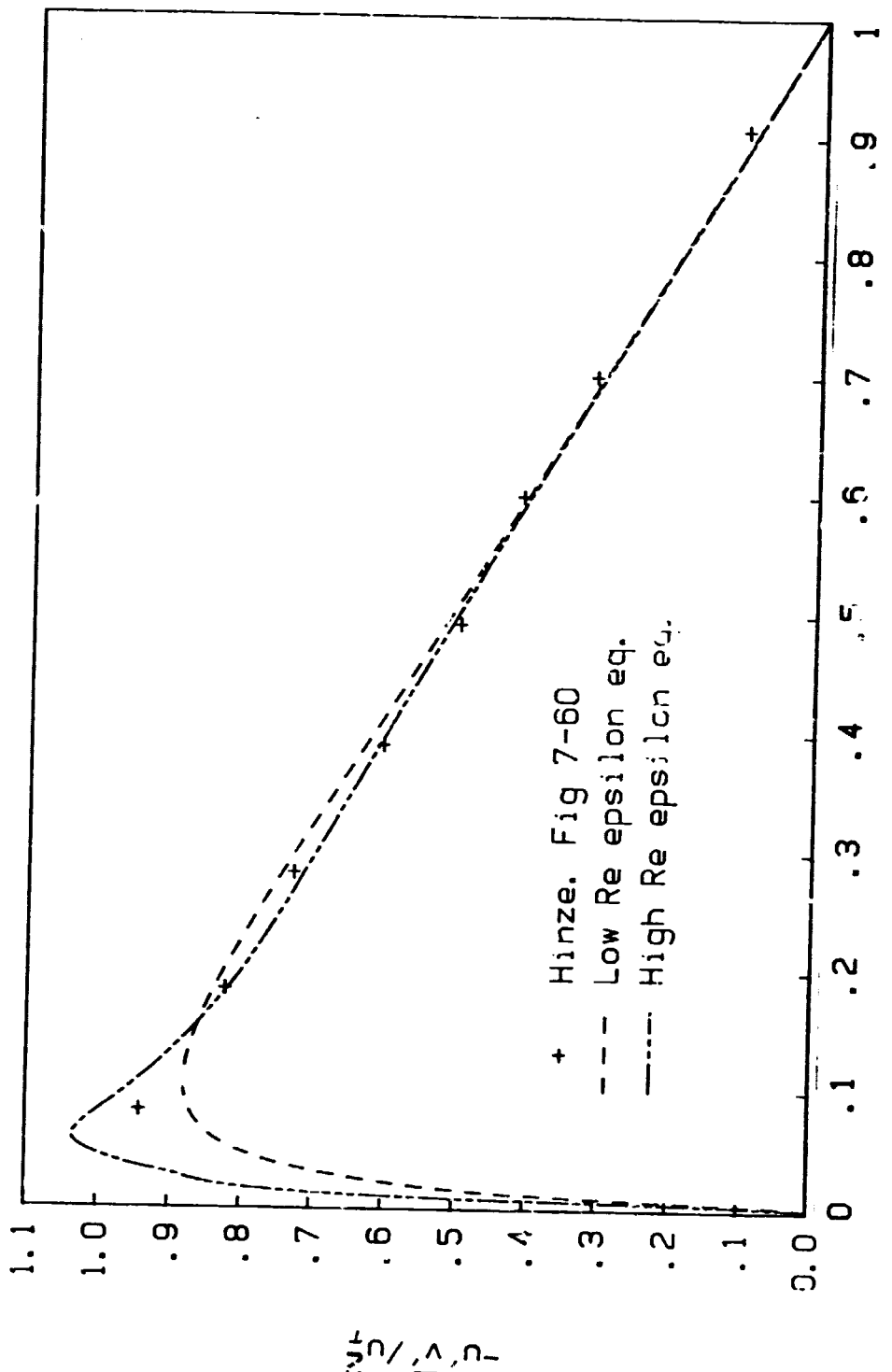

Figure 31. Fully developed pipe flow Reynolds stress profiles for two different length scale models used with a low-Reynolds-number k-equation

long as measurements. It also proved to be unstable when iterating globally. However, due to the good correlation between experimental measurements of k and those predicted by the low-Reynolds-number turbulence model, this model was used to provide the fully developed inlet values for u, ψ, k, and ε for the step flow predictions using the high-Reynolds-number k-ε models.

b. Rapid expansion flow The laser anemometer measurements of flow through a symmetric planar expansion obtained by Smyth [64] were used as the test case for the constant temperature hydrodynamic predictions since he gives the most extensive set of data to date for symmetric expansion flows. For Smyth's measurements, water flowed through a 1:1.5 planar expansion at a Reynolds number of 20,140 based on the inlet plate spacing and the inlet average velocity, u_i. The flow was fully developed at the step. The initial conditions for the computer predictions were obtained by solving the channel flow case upstream of the step using the low-Reynolds-number k-ε equations. An 88x81 computational grid was used for the computer predictions compared with the measurements of Smyth.

Of the three different near-wall models mentioned in Section III.B.6.b, the maximum-shear-stress model gave the best predictions. The variable-A^+ near-wall model gave generally better predictions than the constant-A^+ model in which the boundary conditions for k and ε were given at $y^+ = 30$. Only the results of the maximum-shear-stress and variable-A^+ models will be presented for the constant temperature turbulent flow calculations.

All of the predictions for the flow except very near the wall were similar regardless of the near-wall model that was used. Watkins and Gooray [115] noticed similar behavior for their predictions using the Navier-Stokes equations. When they modified the wall function used with the high-Reynolds-number turbulence model, the reattachment length and near-wall solution was affected but the predictions away from the wall were not. Since the predictions away from the wall are similar for all the near-wall models, they will be discussed below with the results of the maximum-shear-stress near-wall model.

The predicted reattachment lengths were longer than that measured experimentally. The experimental reattachment point, deduced from the velocity profiles provided by Smyth [54], was

$$1.2 < \ell_r/r_o < 1.5$$

The predicted reattachment lengths according to iteration number and near-wall turbulence model were

$\ell_r/r_o = 2.2$ variable-A^+, first iteration

1.8 variable-A^+, fiftieth iteration

2.2 maximum-Reynolds-stress, first iteration

2.1 maximum-Reynolds-stress, fiftieth iteration

Again, the reattachment length is a strong function of the near-wall turbulence model.

The two main short comings of the variable-A^+ model were slow convergence with respect to global iteration and the prediction of small unphysical irregularities near the wall. For the 88x81 grid used for

the comparisons with Smyth, 300 iterations were required for convergence of the variable-A^+ model. Figure 32 shows dp/dx at an x position approximately half-way to reattachment with respect to global iteration. Figure 32 shows that the computer predictions were not highly stable for the first 250 iterations even though all the variables were underrelaxed by 0.25 (the allowable change between global iterations was only 1/4 the predicted change). Due to the high number of iterations, the computational cost of solving the boundary-layer equations with this near-wall model is approaching the cost of solving the Navier-Stokes equations using coarse grids and wall functions near the wall.

Figures 33 through 35 show the unphysical irregularities near the wall for the variable-A^+ case. These irregularities are very noticeable in the velocity profile for $x/r_o = 0.8$ in Fig. 33, and the velocity and Reynolds stress profiles for $x/r_o = 1.2$ and 2.0 in Figs. 34 and 35. Figures 33 through 35 are the predictions for the converged solution after 300 iterations.

For the predictions of the present study, the same mass flow down the channel was used as was reported in Smyth [64]. However, Figs. 33 and 34 suggest that for some experimental profiles (especially the inlet profile), more fluid is flowing down the channel than the predictions indicate. The experimental profiles were integrated using a trapezoidal rule to find the mass flow rate in the channel. The mass flow measured experimentally was found to vary from 1% below to 13% above that reported by Smyth. If anything, the trapezoidal rule integration would

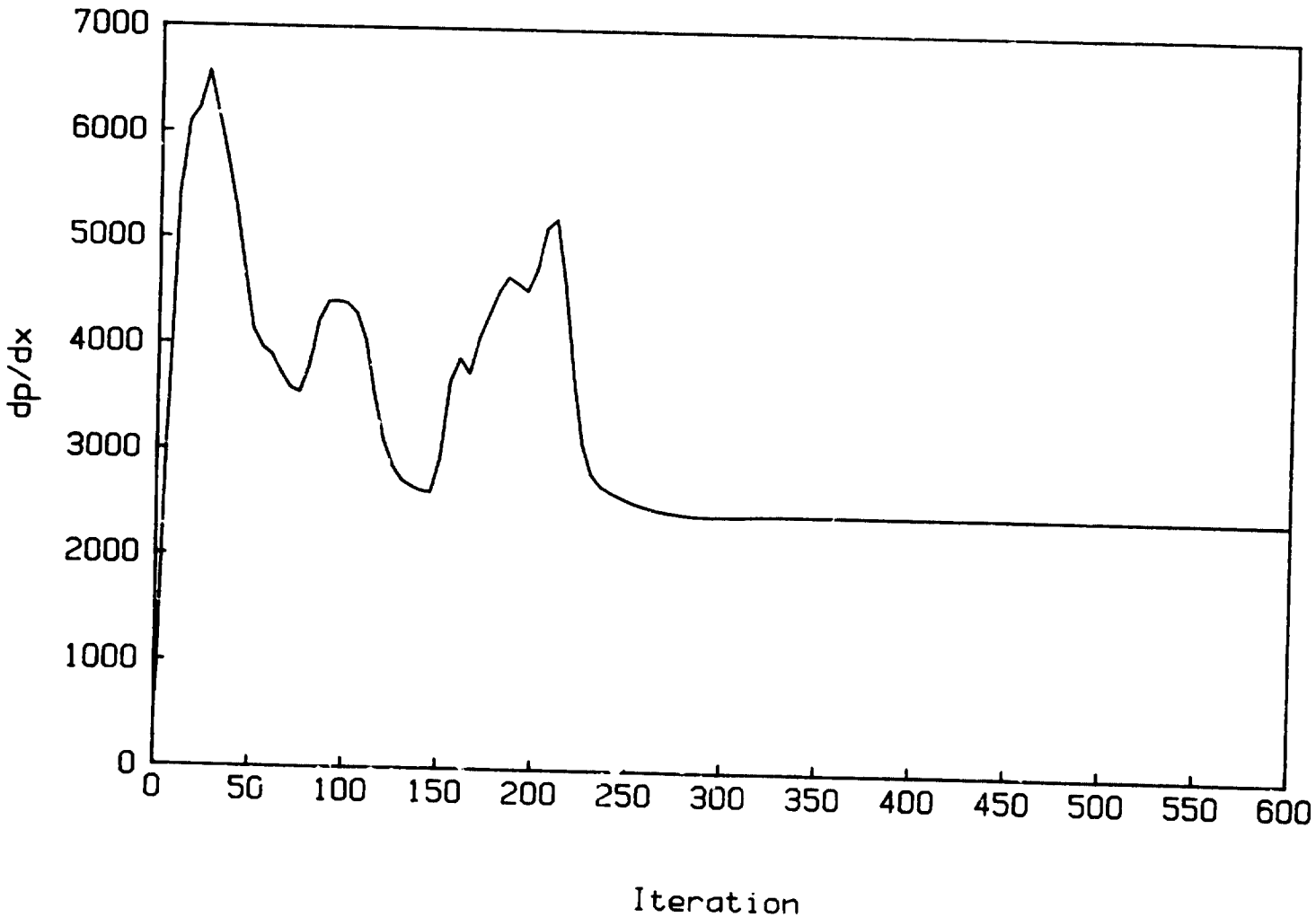

Figure 32. Convergence of the variable-A^+ near-wall model with global iteration for a planar expansion

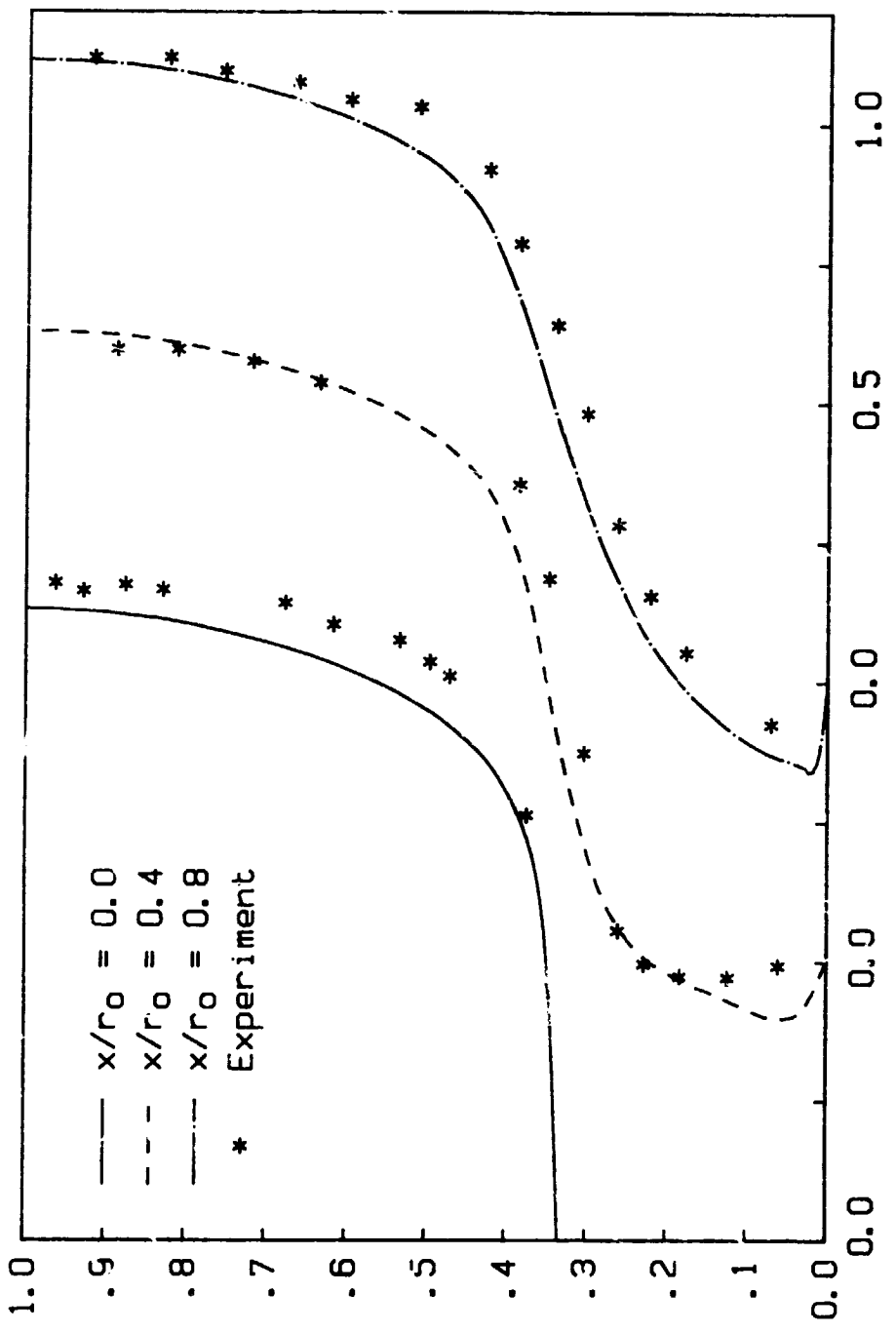

Figure 33. Comparison of velocity profile predictions using the variable-A^+ near-wall model and those measured by Smyth [64] for a planar expansion (d/D=2/3, Re_i=20140)

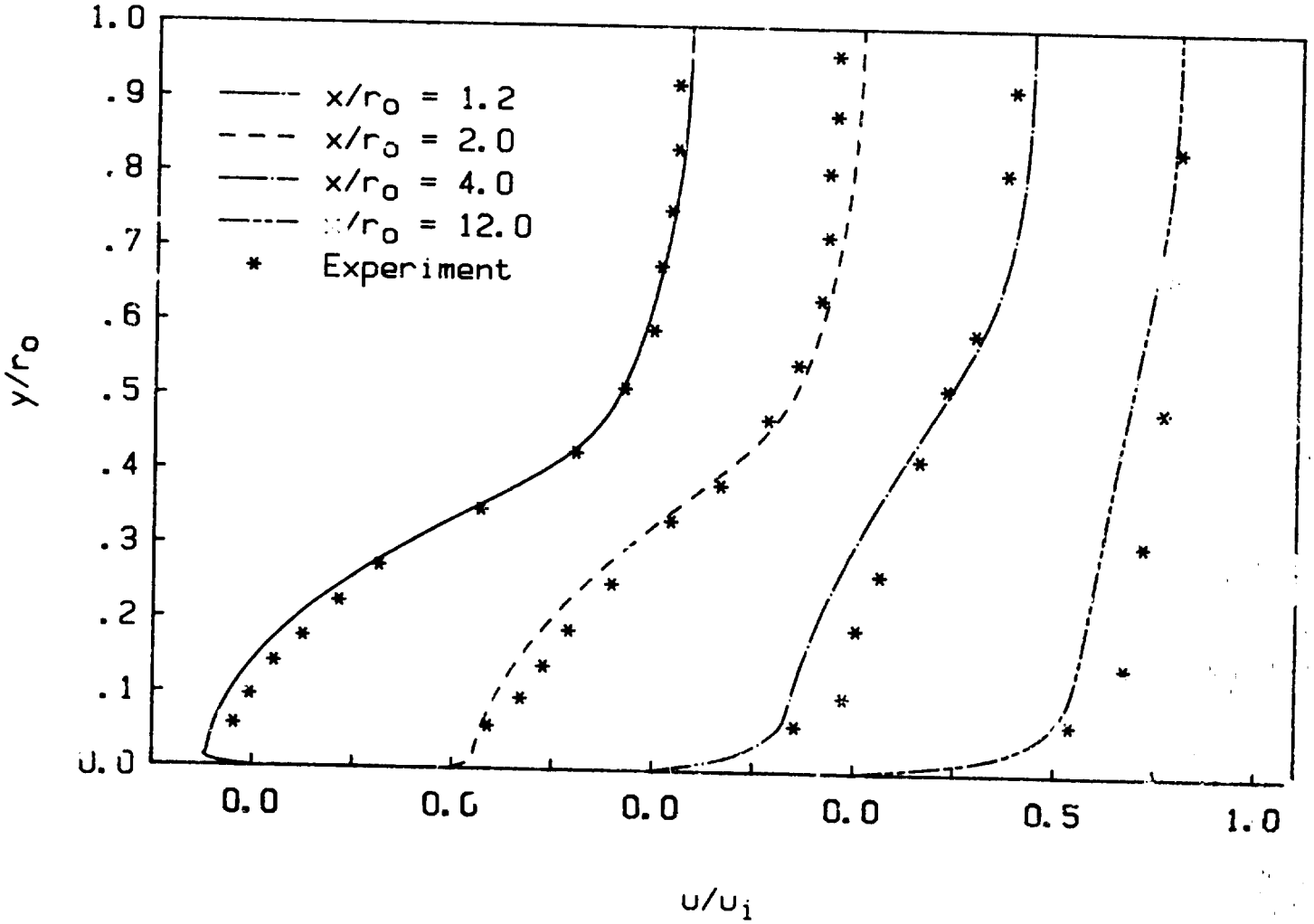

Figure 34. Comparison of velocity profile predictions using the variable-A^+ near-wall model and those measured by Smyth [64] for a planar expansion (d/D=2/3, Re_i=20140)

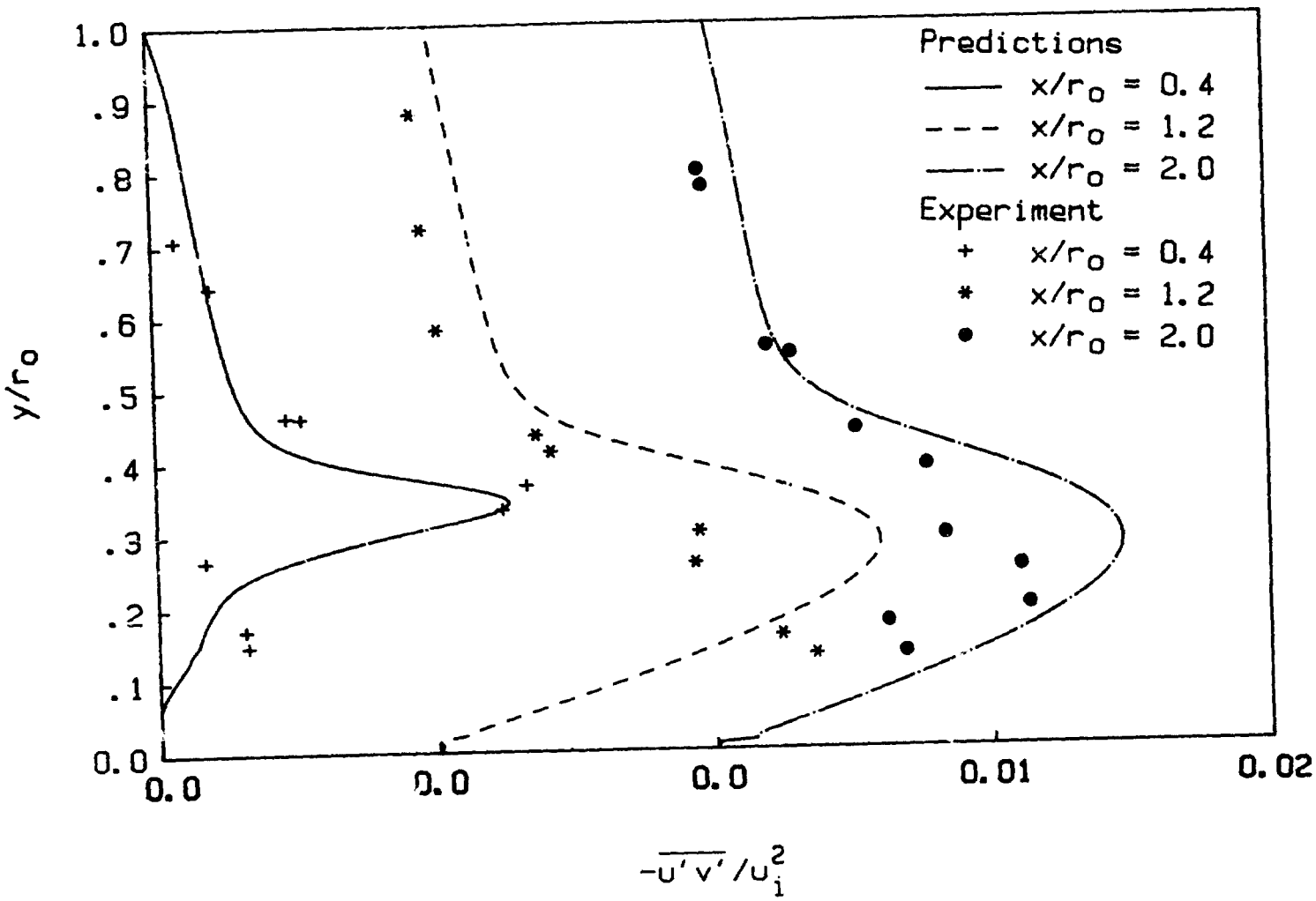

Figure 35. Comparison of Reynolds stress profile predictions using the variable-A^+ near-wall model and those measured by Smyth [64] for a planar expansion (d/D=2/3, Re_i=20140)

tend to underpredict the mass flow rate. Since Smyth gives the accuracy of his u/u_i measurements as ± 0.05, this author is uncertain of the cause of the discrepancy.

The wall functions based on the maximum Reynolds stress with the boundary conditions applied at a y position corresponding to a y^+ of 30 to 50 for a fully developed turbulent profile gave the overall best results. This method converged much faster than the variable-A^+ method. Only 50 global iterations were required for convergence with an underrelaxation factor of 0.5. The unphysical irregularities in the velocity profiles were not predicted with the maximum-shear-stress near-wall model. However, irregularities in the Reynolds stress profiles were still predicted near the wall.

Figures 36 through 39 compare the velocity profiles for the first and last (fiftieth) global iterations with the experimental measurements of Smyth [64]. The predictions for the last global iteration (Figs. 38 and 39) are generally better than the predictions for the first (Figs. 36 and 37) but not remarkably so. Other than in the separated region itself, global iteration has no noticeable effect on the velocity profiles. This indicates that the flow outside the separation bubble is not affected by the way the x-convective term is approximated. The reason for the different predictions for the first and last global iterations in the separation bubble is due to convection in the negative x-direction in this region. The velocity predictions on the first and the last global iterations in the recovery region downstream of

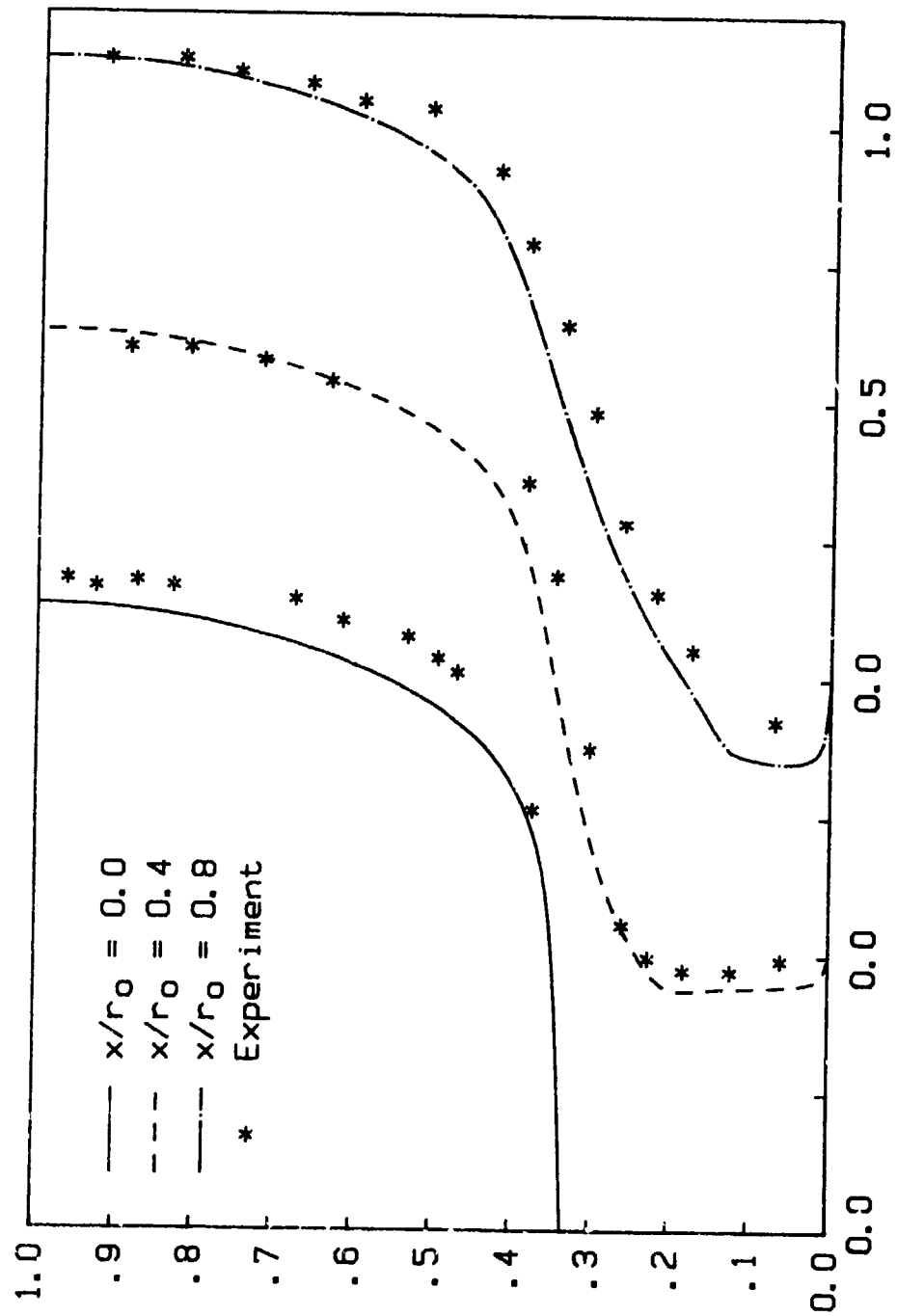

Figure 36. Comparison of velocity profile predictions using the maximum-shear-stress near-wall model and those measured by Smyth [64], first iteration ($d/D=2/3$, $Re_i=20140$)

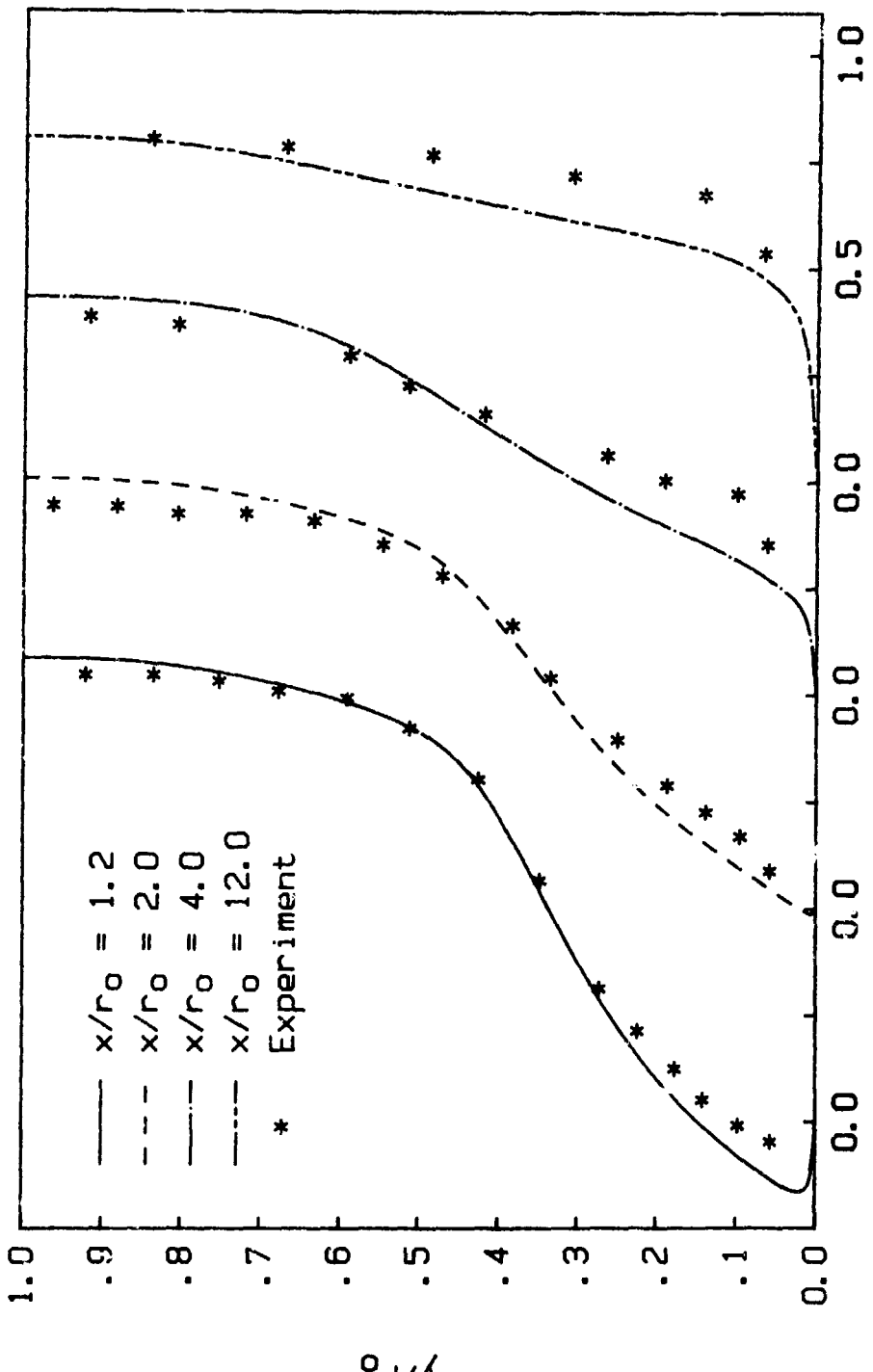

Figure 37. Comparison of velocity profile predictions using the maximum-shear-stress near-wall model and those measured by Smyth [64], first iteration (d/D=2/3, Re_i=20140)

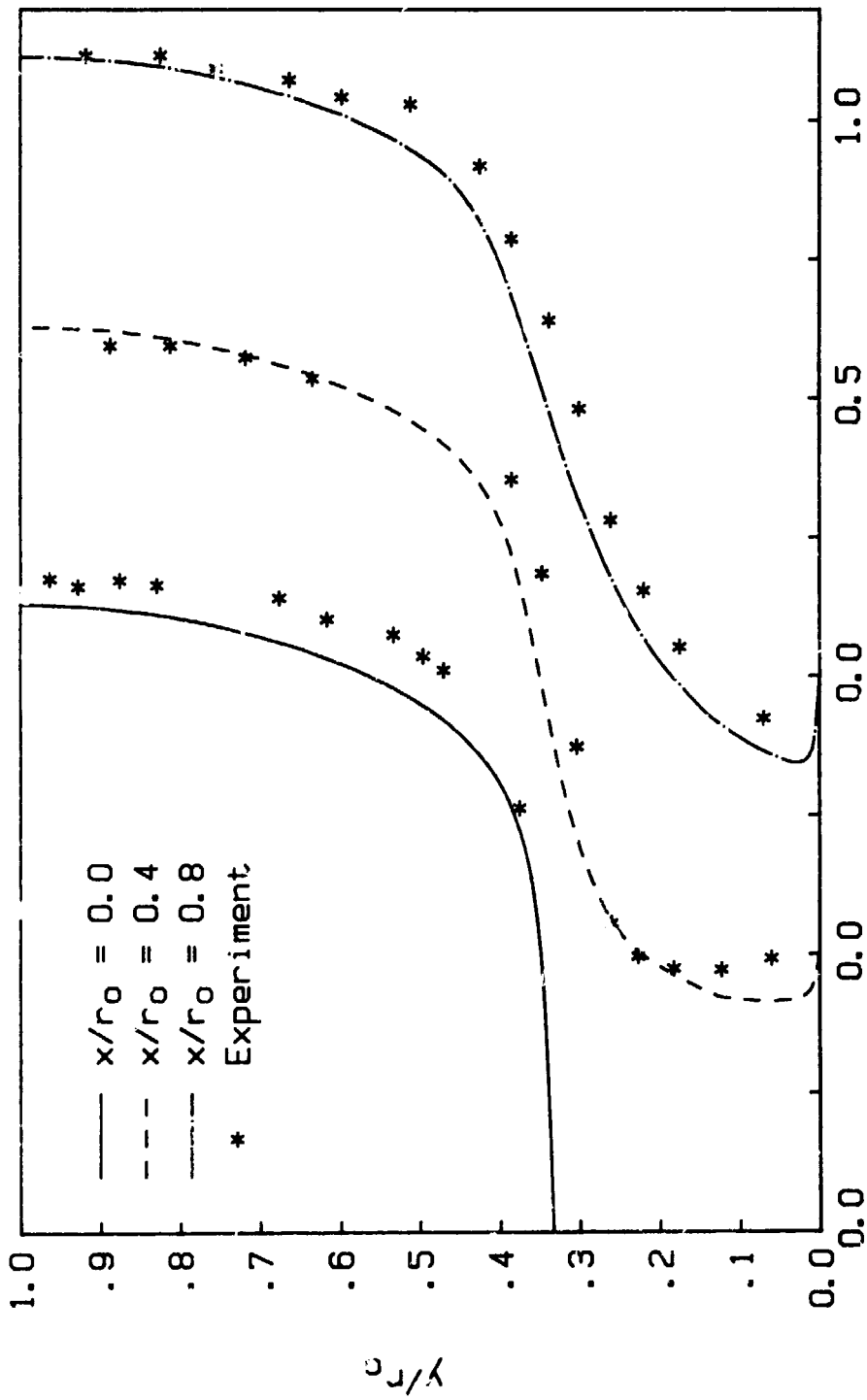

Figure 38. Comparison of velocity profile predictions using the maximum-shear-stress near-wall model and those measured by Smyth [64], fiftieth iteration (d/D=2/3, Re_i=20140)

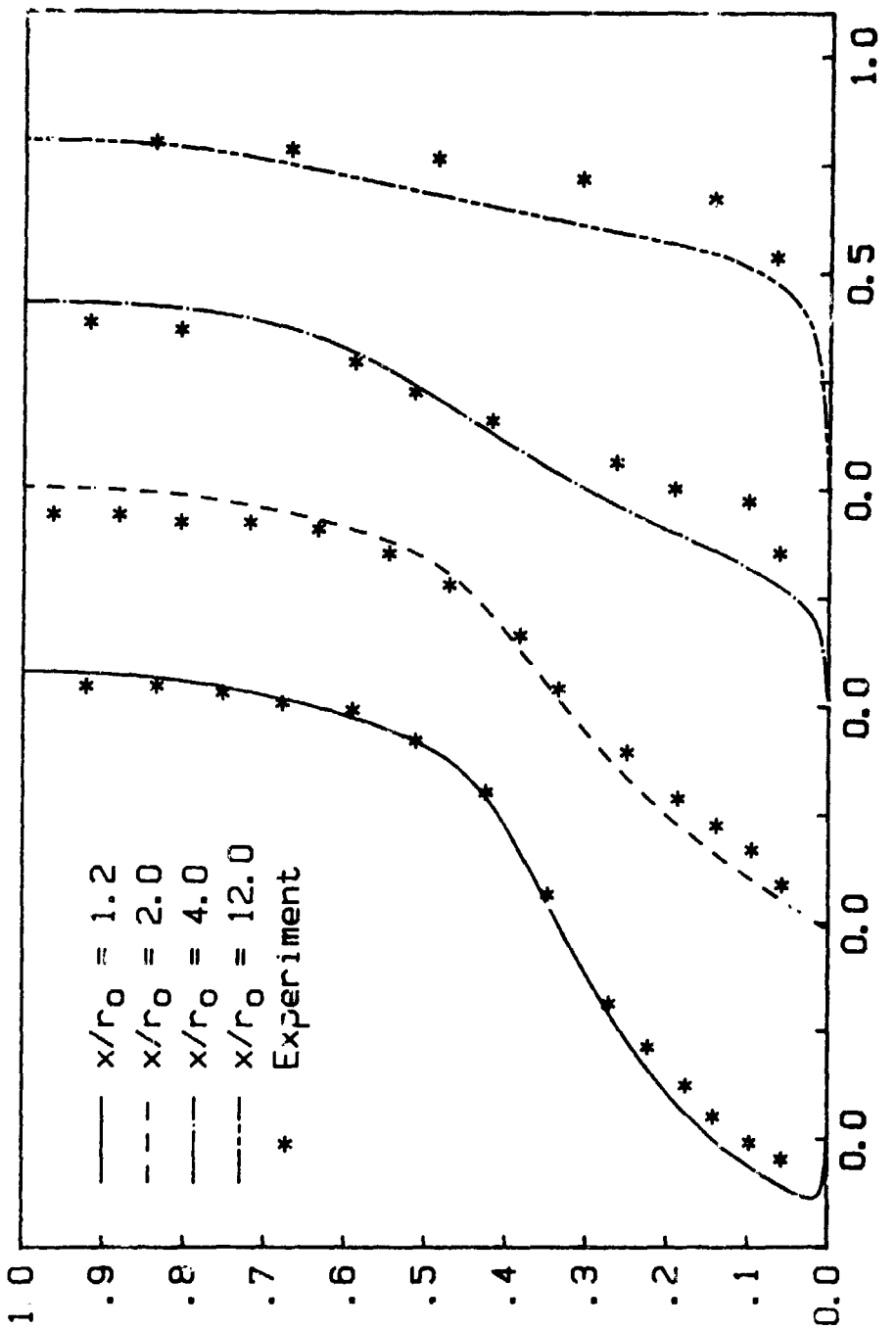

Figure 39. Comparison of velocity profile predictions using the maximum-shear-stress near-wall model and those measured by Smyth [64], fiftieth iteration ($d/D=2/3$, $Re_j=20140$)

reattachment are very similar to each other and are not in good agreement with experimental measurements.

Figures 40 and 41 compare the predictions of the turbulent kinetic energy on the first and last global iterations with the experimental measurements of Smyth. The predicted turbulent kinetic energy varied little between the first and last global iterations except near the step. The maximum k predicted numerically is less than that measured experimentally by Smyth. The k values also drop off too rapidly as the channel centerline is approached. This last point is not too important because near the centerline, $\partial u/\partial y$ is small so any error in the turbulent viscosity will not have a very large effect.

Global iteration has some effect on the Reynolds stress as is shown by Figs. 42 and 43. On the last iteration, the Reynolds stresses were observed to be higher in the recirculation region ($x/r_o = 0.4$) than on the first global iteration. The distance from the wall to the point of the peak Reynolds stress does not decrease as reattachment is approached and then increase after reattachment has been passed as experiments have shown should be the case [1]. The maximum Reynolds stress is also too large after reattachment in the redeveloping boundary layer.

2. Heat transfer

The turbulent heat transfer results are discussed in this section. For the predictions, the variable property relations for air given in Appendix A were used. The computational field had a 120x121 grid for the heat transfer predictions. The predictions of the present study

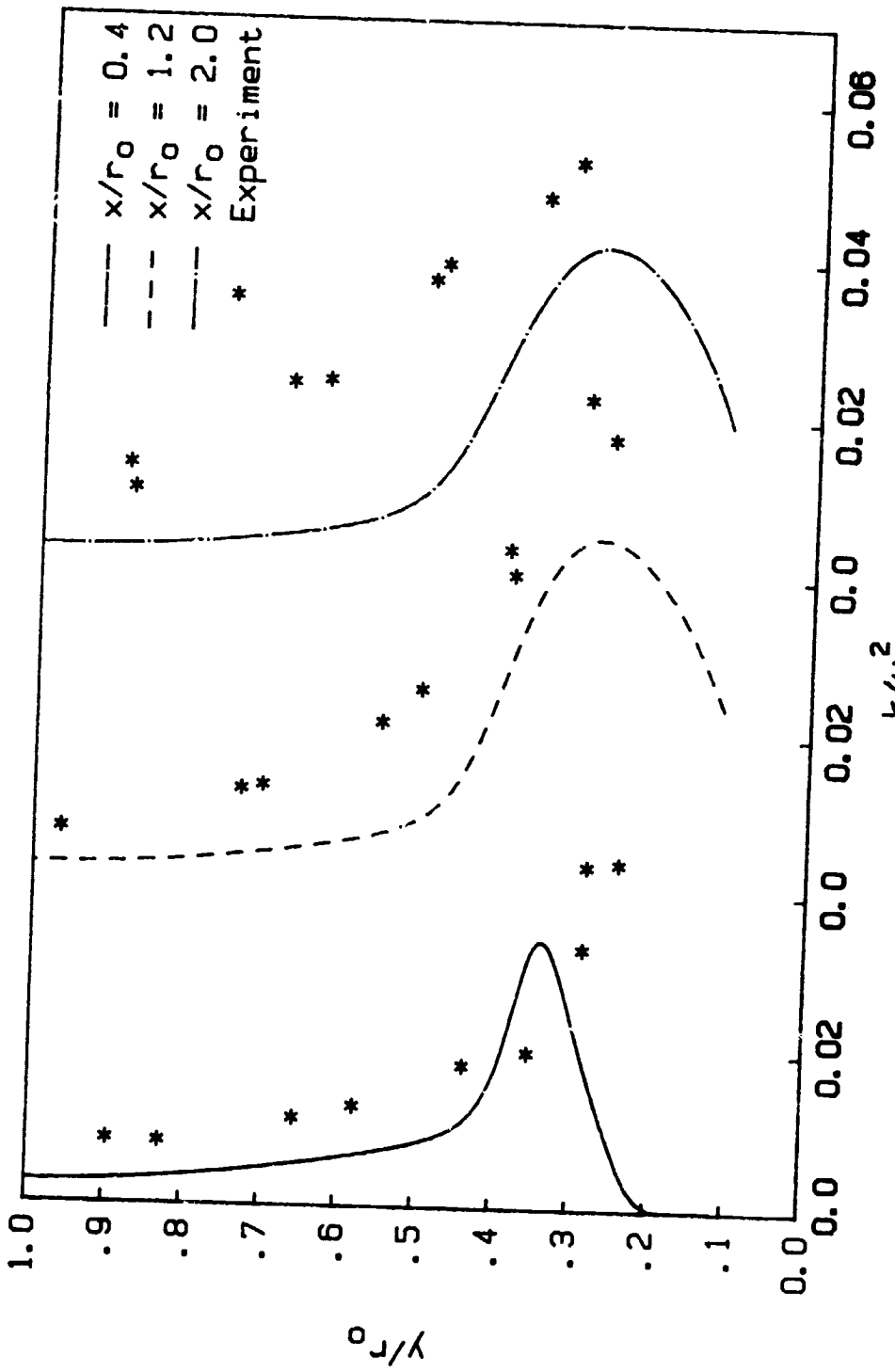

Figure 40. Comparison of turbulent kinetic energy profile predictions using the maximum-shear-stress near-wall model and those measured by Smyth [64], first iteration ($d/D=2/3$, $Re_i=20140$)

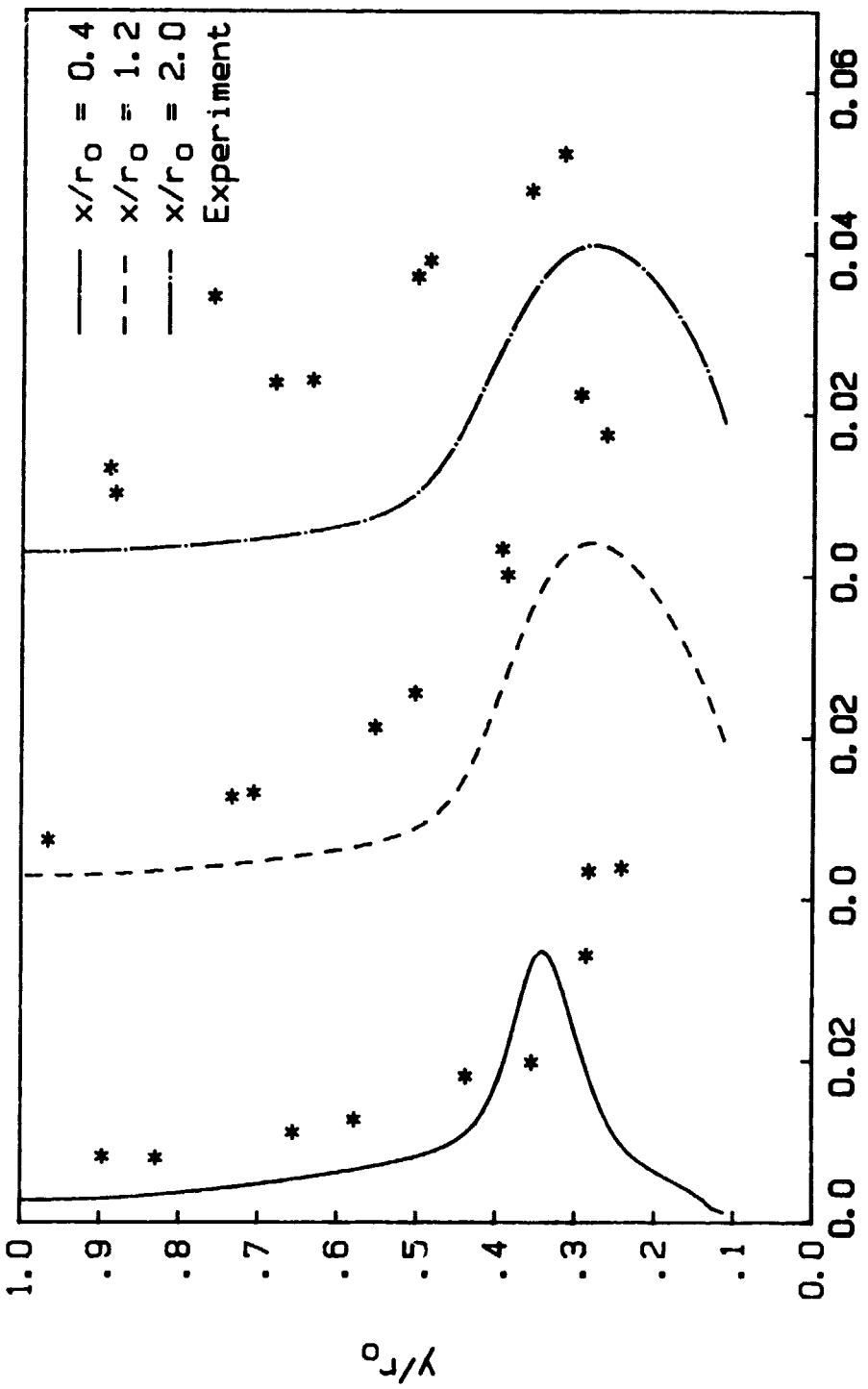

Figure 41. Comparison of turbulent kinetic energy profile predictions using the maximum-shear-stress near-wall model and those measured by Smyth [64], fiftieth iteration (d/D=2/3, Re_i=20140)

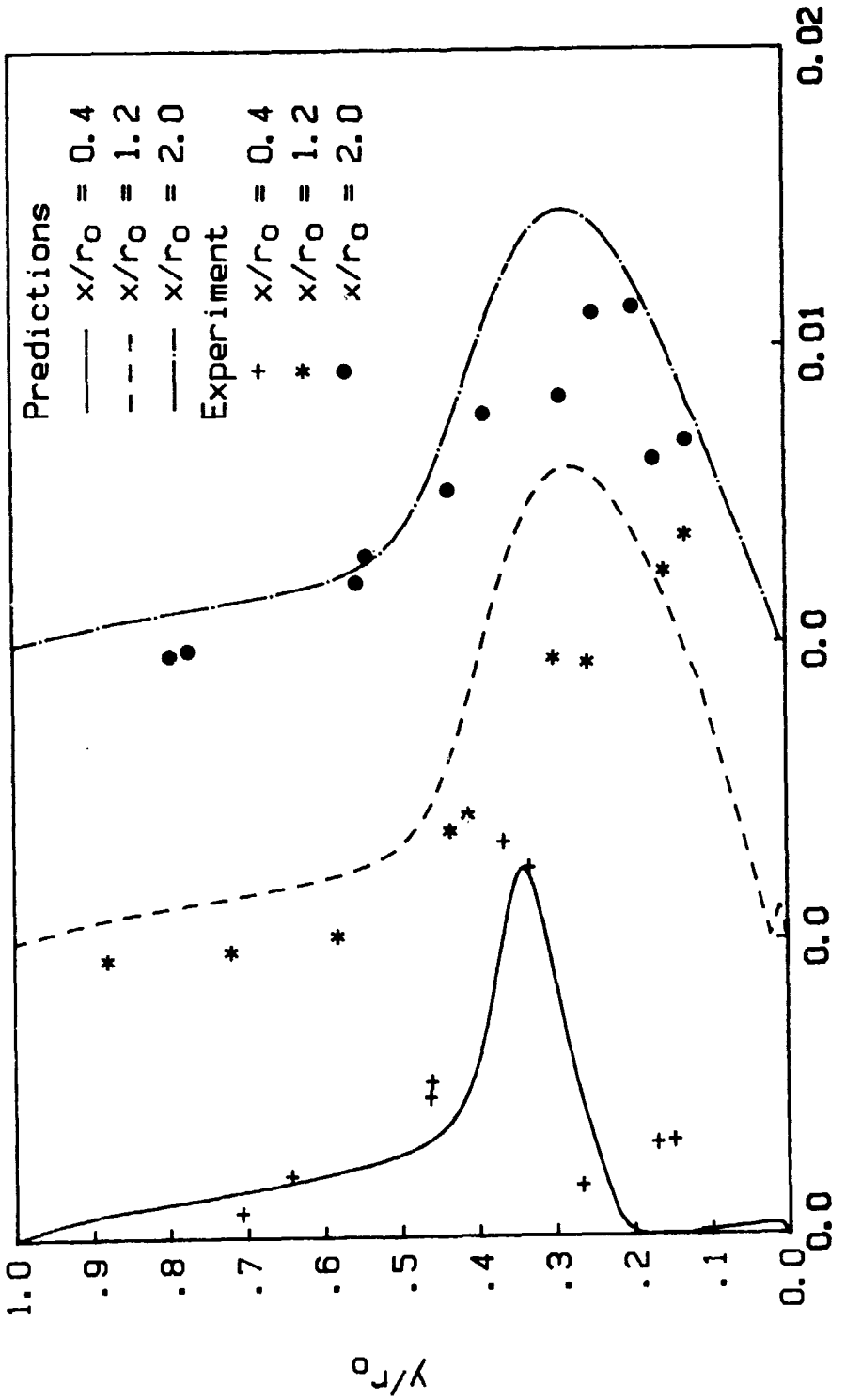

Figure 42. Comparison of Reynolds stress profile predictions using the maximum-shear-stress near-wall model and those measured by Smyth [64], first iteration (d/D=2/3, Re_i=20140)

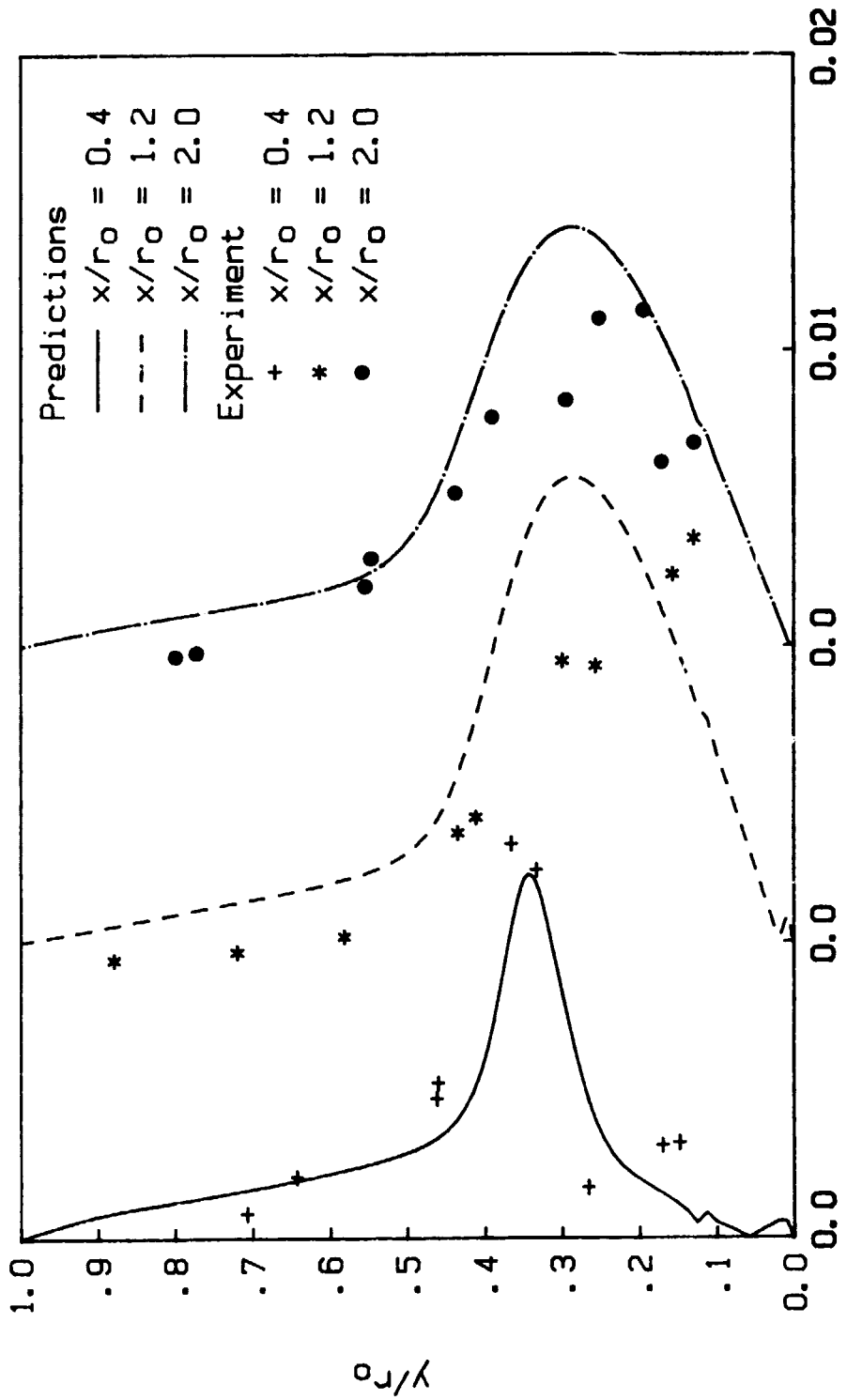

Figure 43. Comparison of Reynolds stress profile predictions using the maximum-shear-stress near-wall model and those measured by Smyth [64], fiftieth iteration (d/D=2/3, Re_i=20140)

will be compared with the Nusselt number measurements of Zemanick and Dougall [84] and Baughn et al. [90], and the numerical predictions of Johnson and Launder [113] and Watkins and Gooray [115].

To verify the computer program, the fully developed temperature profile in law-of-the-wall coordinates was calculated for pipe flow. The dimensionless temperature measured experimentally in a fully developed flat plate turbulent boundary layer [127] is compared with the predictions for fully developed turbulent pipe flow in Fig. 44. It would have been better to compare with experimental measurements of fully developed pipe flow but none were readily available. The velocity law-of-the-wall profiles for boundary-layer flow and fully developed pipe flow are very similar. For this reason, the temperature law-of-wall profiles for the two flows should also be very similar in the logarithmic region, although one might expect minor differences. The dimensionless temperature, T^+ is given by

$$T^+ = \rho c_p (T_w - T) u_\tau / q_w$$

The agreement between the two curves is acceptable.

The variable turbulent Prandtl number developed by Watkins and Gooray [115] reduces to a value near 0.2 for fully developed turbulent pipe flow (Eq. 2.81). Thus, one would expect the Pr_t expression of Watkins and Gooray to greatly increase the heat transfer predictions over those predicted using a constant Pr_t of 0.9. When the Pr_t expression of Watkins and Gooray was used in the computer program of the

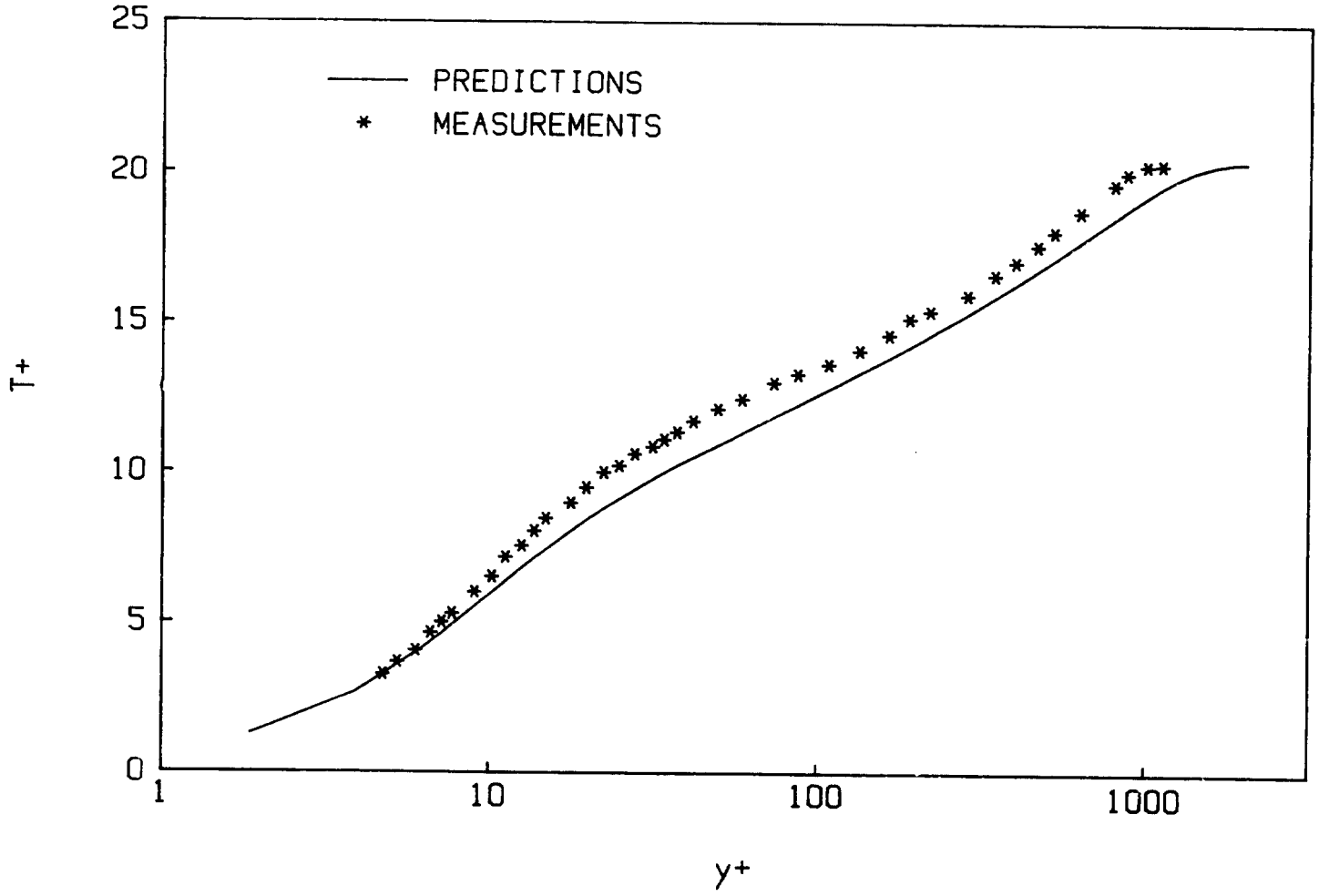

Figure 44. Temperature comparison between fully developed pipe flow predictions and boundary-layer measurements [127]

present study, the heat transfer predictions in the separated flow were generally more than 100% higher than the experimental measurements. Since predictions using the variable Pr_t expression given by Eq. (2.81) predicted extremely high heat transfer, the results using a variable Pr_t will not be discussed further. The remaining heat transfer predictions are for Pr_t equal to 0.9. Several other recent numerical predictions successfully used a constant Pr_t of 0.9 when predicting the heat transfer in a pipe expansion using the Navier-Stokes equations [89, 113, 119].

The maximum-shear-stress inner viscosity model given by Eqs. (2.65), (2.76), and (2.77) not only gave the best hydrodynamic predictions but also gave the best predictions for heat transfer. The Nusselt number predictions obtained using the maximum-shear-stress inner-model and the constant-A^+ model are compared to experimental measurements [84, 90] in Fig. 45 for d/D of 0.8 and Re near 20,000. Figure 45 shows that global iteration improves the heat transfer predictions in the recirculating flow. The overall agreement is quite good considering the difficulty in predicting turbulent heat transfer in separated flow.

Figure 46 is a comparison similar to Fig. 45 but for a more extreme expansion, d/D = 0.53, and a lower Reynolds number, Re = 10950. The predictions of Watkins and Gooray [115] and Johnson and Launder [113] for the same flow case are also included. For this large expansion, it was very difficult to specify initial values for k and ε along the face

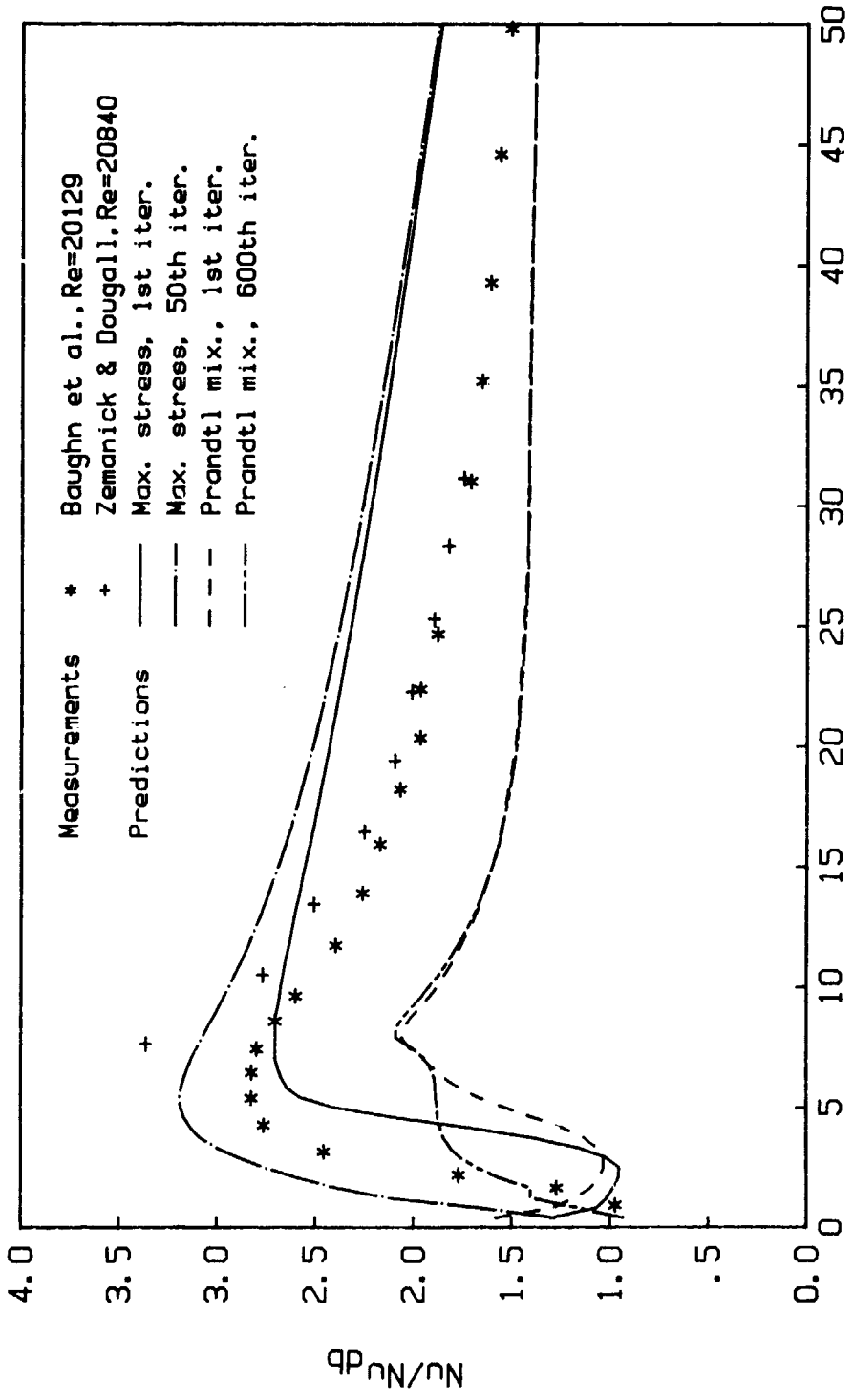

Figure 45. Comparison of the predicted Nusselt number using the Prandtl-mixing-length (A^+-25) and maximum-shear-stress near-wall models with experimental measurements [84,90] for an axisymmetric expansion (d/D = 0.8, Re_o = 20161, Nu based on D)

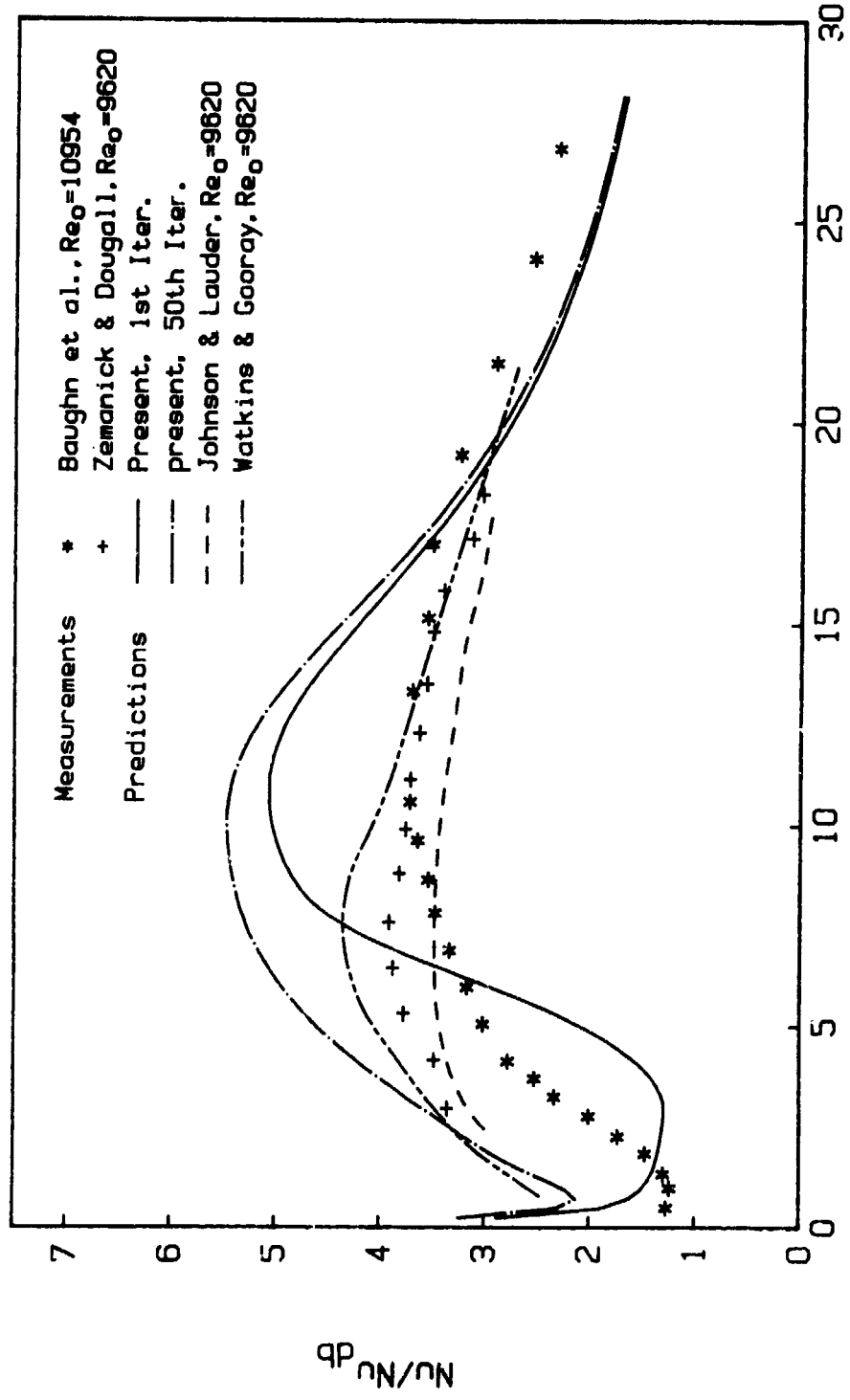

Figure 46. Comparison of the predicted Nusselt number using the maximum-shear-stress near-wall model with Navier-Stokes predictions [113,115] and with experimental measurements [84,90] for an axisymmetric expansion (d/D = 0.533, Re_o = 10954, Nu based on D)

of the step so that the prediction algorithm was stable for the first sweep down the channel. For the algorithm to be stable, the variable expression for c_μ (Eq. 2.80) had to be discarded in favor of a constant value of 0.09. Figure 46 shows that the heat transfer is overpredicted in the recirculating region and in the initial redeveloping boundary layer but is then underpredicted as the boundary layer develops. Again, as was indicated by Fig. 45, global iteration greatly affects the heat transfer predictions in the reversed flow region.

The predicted x-position of Nu_{max}, $x/h = 5.4$ for the fiftieth global iteration, was near the value measured by Baughn et al. [90] for $d/D = 0.8$ (Fig. 45). The predicted reattachment point was $\ell_r/h = 6.0$, slightly downstream of the point of maximum Nu. For $d/D = 0.553$, the predicted reattachment point was upstream of the predicted point of maximum Nu. The predicted reattachment length and point of maximum Nu were 9 2 and 10.1, respectively. This predicted point of maximum Nu was near the value measured by Baughn et al. but downstream of the other studies shown in Fig. 46.

V. CONCLUSIONS

A. Laminar

From the results of the laminar predictions mentioned in the previous section, one can draw the following conclusions.

1. The distance to flow reattachment and velocities outside of the trapped eddy are very well-predicted by the boundary-layer equations for Reynolds numbers above 20 and expansion ratios below 1:3.
2. The eddy structure is not well-predicted for low Reynolds numbers (Re < 200 for a 1:2 pipe and planar expansion). This is shown by the poor predictions of the magnitude and position of Ψ_{min}. For planar expansions, when the Reynolds number is approaching the point where the eddy structure can be predicted by the boundary-layer equations, experiments have shown the flow tends to be either asymmetric or unsteady [10].
3. The flow can be qualitatively divided into two regions. An elliptic region made up of the trapped eddy and a parabolic region including the rest of the flow field. The eddy asserts only a weak influence on the rest of the typically parabolic flow.
4. Global iteration over the flow field using the boundary-layer equations does not significantly change the hydrodynamic

constant temperature predictions and offers little improvement over the "once through" method using FLARE. However, global iteration is important when predicting the heat transfer for an insulated step face, as was the case for the present study. When the heat flux is specified at the wall, the convergence of the global iteration to determine the temperature field is approximately five times slower than when the wall temperature is specified as a boundary condition.

5. A zero velocity initial condition on the face of the step is adequate. A nonzero velocity on the step face was not predicted by the algorithm of Acrivos and Schrader [27] as the grid was refined. A small nonzero velocity on the face of the step did not significantly affect the solution.
6. The primitive variable formulation (U-V) predictions were the same as the U-Ψ formulation predictions. Thus, the "wiggles" previously noted with primitive variable solutions [39], were due to uncoupling of the continuity and momentum equations and not the choice of variables.

B. Turbulent

This section describes the conclusions that can be drawn from the turbulent hydrodynamic and heat transfer predictions.

1. Although the low-Reynolds-number k-ε turbulence model of Chien [135] gave excellent results for attached flow in channels and pipes, it greatly overpredicted the reattachment length when used for rapid expansion geometries. The low-Reynolds-number model was also unstable when iterating globally. The high-Reynolds-number k-ε turbulence model with near-wall turbulence models gave better predictions.
2. The near-wall turbulence model exerted a very weak influence on the flow field away from the wall. It had a very strong influence on the near-wall flow and the point of reattachment as was reported by Watkins and Gooray [115]. The near-wall model had a primary role in determining the heat transfer rate.
3. The near-wall maximum-shear-stress turbulent viscosity model based on the inner viscosity model of Johnson and King [121] gave better predictions than the near-wall models based on Prandtl's mixing length. The maximum-shear-stress model required less underrelaxation when iterating globally, required fewer global iterations to converge, and predicted the heat transfer much better than the Prandtl mixing length near-wall models. The maximum-shear-stress model did not predict small irregularities in the velocity profiles near the wall as did the variable-A^+ model.

4. A modification of the turbulent Prandtl number expression, Pr_t, derived by Watkins and Gooray [115] when used in the computer code of the present study, predicted values of Pr_t between 0.2 and 0.3. This caused the heat transfer predictions for attached pipe flow to be greatly overpredicted. The near-wall models based on Prandtl's mixing length underpredicted the heat transfer in the recirculating region when using $Pr_t = 0.9$. Using the expression for Pr_t of Watkins and Gooray with the near-wall models based on Prandtl's mixing length for the separated flow may give reasonable heat transfer predictions in separated flow but does not appear to be applicable for flows with no separation.
5. Global iteration, as for laminar flow, was not very important for the hydrodynamic predictions. However, it was even more important than for laminar flow when predicting the heat transfer.
6. The computer algorithm was sensitive to the initial values of k and ε specified at the step necessary to start the first sweep down the channel. The larger the expansion, the more critical the initial values of k and ε became.
7. As for laminar flow, the parabolic region of the flow outside the separation bubble was not affected by global iteration.

8. The predictions of the peak turbulent kinetic energy were less than those measured by Smyth [64].
9. The overprediction of the Reynolds stress in the redevelopment region caused the underprediction of u in this region. The predicted peak value of $-\overline{u'v'}$ did not dip toward the wall as reattachment was approached and then move away from the wall as it was passed as indicated by experiments [1].
10. For the less extreme of the two pipe expansions examined, the heat transfer was well-predicted in the separated region and slightly overpredicted as the flow developed. For the more extreme expansion, the heat transfer was overpredicted in the separated region and near reattachment.
11. The boundary-layer equation method of this study provided a relatively inexpensive way to evaluate turbulence models applicable to separated flow that occurs with such devices as turbines, heat exchangers, airfoils, and ramjets.

C. Recommendations for Future Research

The present study indicated that the near-wall model derived from the inner viscosity model of Johnson and King [121] improved the heat transfer predictions. It may be desirable to study the use of this near-wall model based on the maximum Reynolds stress with the Navier-Stokes equations to predict the heat transfer in separated flow. Since

the correct prediction of the heat transfer rate is so sensitive to the near-wall model, heat transfer predictions should not be ignored when developing turbulent models valid in reversed flow.

The use of wall functions for velocity for the near-wall flow, in contrast to solving the momentum, continuity, and energy equations up to the wall as was done in the present study, is becoming widely accepted as the most economical and robust method of predicting turbulent flow with separation. However, these three PDE's are valid near the wall and might be used to provide insight to turbulence modeling of the wall dominated region. The fact that the wall is not approached with the wall-function methods points to the lack of the ability to model the turbulence in this region. More research should be conducted in solving the actual momentum, continuity, and energy partial-differential equations with the turbulence model input as either a turbulent viscosity or the Reynolds stresses themselves in the near-wall region. This would clearly show the shortcomings of the near-wall turbulence models and hopefully lead to more universal ones. It is understood that solving the momentum, continuity, and energy equations in the near-wall region may not be the most cost effective way to predict turbulent flow at the present time, but information from doing so may help in the development of more universal wall models.

VI. REFERENCES

1. Eaton, J. K., and Johnston, J. P. "A Review of Research on Subsonic Turbulent Flow Reattachment." AIAA J. 19, No. 9 (1981): 1093-1100.

2. Westphal, R. V., Johnston, J. P., and Eaton, J. K. "Experimental Study of Flow Reattachment in a Single-Sided Sudden Expansion." NASA Contractor Report 3765. Stanford Univ., 1984.

3. Rodi, W. R. Turbulence Models and Their Application in Hydraulics. University of Karlsruhe, Karlsruhe, Federal Republic of Germany, 1980.

4. Anderson, D. A., Tannehill, J. C., and Pletcher, R. H. Computational Fluid Mech. and Heat Transfer. New York: McGraw-Hill, 1984.

5. Macagno, E. O., and Hung, T. K. "Computational and Experimental Study of *a* Captive Annular Eddy." J. Fluid Mech. 28, No. 1 (1967): 43-64.

6. Back, L. H., and Roshko, E. J. "Shear-Layer Flow Regions, Wave Instabilities and Reattachment Lengths Downstream of an Abrupt Circular Channel Expansion." J. Applied Mech. 39 (1972): 677-681.

7. Iribarne, A., Frantisak, F., Hummel, R. L., and Smith, J. W. "An Experimental Study of Instabilities and Other Flow Properties of a Laminar Pipe Jet." AIChE J. 18 (1972): 689-698.

8. Durst F., Melling A., and Whitelaw, J. H. "Low Reynolds Number Flow over a Plane Symmetric Sudden Expansion." J. Fluid Mech. 64, No. 1 (1974): 111-128.

9. Feuerstein, J. A., Pike, G. K., and Rounds, G. F. "Flow in an Abrupt Expansion as a Model for Biological Mass Transfer Experiments." J. Biomech. 8 (1975): 41-51.

10. Cherdron, W., Durst, F., and Whitelaw, J. H. "Asymmetric Flows and Instabilities in Symmetric Ducts with Sudden Expansions." J. Fluid Mech. 84 (1978): 13-31.

11. Restivo, A., and Whitelaw, J. H. "Turbulence Characteristics of the Flow Downstream of a Symmetric Plane Sudden Expansion." J. Fluids Engrg. 100 (1978): 308-310.

12. Pollard, A. "Entrance and Diameter Effects on the Laminar Flow in Sudden Expansions." In Momentum and Heat Transfer Processes in Recirculating Flows, pp. 21-26. Edited by B. E. Launder and J. A. C. Humphrey. New York: ASME, 1980.

13. Back, L. H., and Roshko, E. J. "The Influence of Upstream Conditions on Reattachment Lengths Downstream of an Abrupt Circular Expansion." J. Biomech. 9, No. 7 (1976): 481.

14. Moore, T. W. F. "Some Experiments on the Reattachment of Laminar Boundary Layer Separating from a Rearward Facing Step on a Flat Plate Airfoil." J. Royal Aeronautical Society 64 (1960): 668-672.

15. Leal, L. G., and Acrivos, A. "The Effects of Base Bleed on the Steady Separated Flow Past Bluff Objects." J. Fluid Mech. 34 (1968): 25-48.

16. O'Leary, R. A, and Mueller, T. J. "Correlation of Physical and Numerical Experiments for Incompressible Laminar Separation Flows." Technical Report No. THEMIS-UND-69-4. University of Notre Dame, 1969.

17. Goldstein, R. J., Eriksen, V. L., Olson, R. M., and Eckert, E. R. G. "Laminar Separation, Reattachment, and Transition of the Flow over a Downstream-Facing Step." J. Basic Engrg. 92 (1970): 732-741.

18. Denham, M. K., and Patrick, M. A. "Laminar Flow over a Downstream-Facing Step in a Two-Dimensional Flow Channel." Trans. Instn. Chemical Engineers 52 (1974): 361-367.

19. Matsui, T., Hiramatsu, M., and Hanaki, M. "Separation of Low Reynolds Number Flow around a Corner." In Turbulence in Liquid, pp. 283-288. Edited by T. J. Hanratty, R. J. Hansen, A. K. M. F. Hussain, and L. C. Thomas. Princeton: Science Press, 1977.

20. Armaly, B. F., and Durst, F. "Reattachment Length and Circulation Regions Downstream of a Two-Dimensional Single Backward Facing Step." In Momentum and Heat Transfer Process in Recirculating Flows pp. 1-7. Edited by J. A. C. Humphrey and B. E. Launder. New York: ASME, 1980.

21. Sinha, S. N., Gupta, A. K., and Oberai, M. M. "Laminar Separating Flow over Backsteps and Cavities Part I: Backsteps." AIAA J. 19 (1981): 1527-1530.

22. Armaly, B. F., Durst, F., Pereira, J. C. F., and Schonung, B. "Experimental and Theoretical Investigation of Backward-Facing Step Flow." J. Fluid Mech. 127 (1983): 473-496.

23. Aung, W. "Heat Transfer in Separated Region beyond a Rearward Facing Step." Ph.D. Thesis. University of Minnesota, 1969.

24. Aung, W. "An Experimental Study of Laminar Heat Transfer Downstream of Backsteps." J. Heat Transfer 105, No. 4 (1983): 823-829.

25. Armaly, B. F., Durst, F., and Kottke, V. "Momentum, Heat and Mass Transfer in Bacward-Facing Step Flows." Symposium on Turbulent Shear Flows 3. University of California, Davis, Sept., 1981.

26. Hung, T. K. "Laminar Flow in Conduit Expansions." Ph.D. Thesis. University of Iowa, Iowa City, Iowa, 1966.

27. Acrivos, A., and Schrader, M. L. "Steady Flow in a Sudden Expansion at High Reynolds Numbers." Phys. Fluids 25, No. 6 (1982): 923-930.

28. Agarwal, R. K. "A Third-Order-Accurate Upwind Scheme for Navier-Stokes Solutions at High Reynolds Numbers." AIAA Paper No. AIAA-81-0112, 1981.

29. Atkins, D. J., Maskell, S. J., and Patrick, M. A. "Numerical Prediction of Separated Flows." Int. J. Numerical Methods in Engrg. 15 (1980): 129-144.

30. Chen, C. J., Ho, K. S., and Cheng, W. S. "The Finite Analytic Method." IIHR Report No. 232-V. Iowa Institute of Hydraulic Research, University of Iowa, Iowa City, Iowa, 1982.

31. Giaquinta, A. R. "Numerical Modeling of Unsteady, Separated Viscous Flow." In Numerical/Laboratory Computer Methods in Fluid Mechanics, pp. 279-301. Edited by A. A. Pouring and V. L. Shah. New York: ASME, 279-301.

32. Hackman, L. P., Raithby, G. D., and Strong, A. B. "Numerical Predictions of Flows over Backward-Facing Steps." International J. Numerical Methods in Fluids 4 (1984): 711-724.

33. Halim, A., and Hafez, M. "Calculations of Separation Bubbles Using Boundary-Layer-Type Equations - Part I." In Recent Advances in Numerical Methods in Fluids 3. Edited by Habashi, 1984.

34. Hall, E. J., and Fletcher R. H. "Application of a Viscous-Inviscid Interaction Procedure to Predict Separated Flows with Heat Transfer." J. Heat Transfer, (1985), In press.

35. Hutton, A. G., and Smith R. M. "The Prediction of Laminar Flow over a Downstream Facing Step." C.E.G.B. Report RD/B/B 3600, 1979.

36. Huyakorn, P. S., Taylor, C., Lee, R. L., and Gresho, P. M. "A Comparison of Various Mixed-Interpolation Finite Elements in the Velocity-Pressure Formulation of the Navier-Stokes Equations." Computers and Fluids 6 (1978): 25-35.

37. Kumar, A., and Yajnik, K. S. "Internal Separated Flows at Large Reynolds Number." J. Fluid Mech. 97, No. 1 (1980): 27-51.

38. Kwon, O. K., Pletcher, R. H., and Lewis, J. P. "Prediction of Sudden Expansion Flows Using the Boundary-Layer Equations." J. Fluids Engrg. 106, No. 3 (1984): 285-291.

39. Kwon, O. K., and Pletcher, R. H. "Prediction of the Incompressible Flow over a Rearward-Facing Step." Technical Report No. HTL-26, CFD-4, ISU-ERI-Ames-82019. Engrg. Research Institute, Iowa State University, Ames, Iowa, 1981.

40. Leschziner, M. A. "Practical Evaluation of Three Finite Difference Schemes for the Computation of Steady-State Recirculating Flows." Computer Methods in Applied Mech. and Engrg. 23 (1980): 293-312.

41. Morihara, H. "Numerical Integration of the Navier-Stokes Equations." Ph.D. Thesis. University of New York at Buffalo, 1972.

42. Oosthuizen, P. H. "A Numerical Study of Laminar Flow through a Stepped Channel Using the Boundary Layer Equations with Particular Emphasis on 'Secondary' Separation." ASME Paper No. 84-FE-7, 1984.

43. Osswald, G. A., Ghia K. N., and Ghia, U. "Unsteady Navier-Stokes Simulation of Internal Separated Flows over Plane and Axisymmetric Sudden Expansions." AIAA Paper No. AIAA-84-1584, 1984.

44. Plotkin, A. "Spectral Method Solutions for some Laminar Channel Flows with Separation." AIAA J. 20, No. 12 (1982): 1713-1719.

45. Pollard, A. "A Contribution on the Effects of Inlet Conditions when Modeling Stenoses Using Sudden Expansions." J. Biomech. 14, No. 5 (1981): 349-355.

46. Roache, P. J., and Mueller, T. J. "Numerical Solutions of Laminar Separated Flows." AIAA J. 8, No. 3 (1970): 530-538.

47. Taylor, C., Thomas, C. E., and Morgan, K. "Confined Turbulent Flow Utilizing the Finite Element Method." In Finite Element Method for Convection Dominated Flows, pp. 213-224. Edited by T. J. R. Hughes. New York: ASME, 1979.

48. Thomas, C. E., Morgan, K., and Taylor, C. "A Finite-Element Analysis of a Flow over a Backward Facing Step." Computers and Fluids 9 (1981): 265-276.

49. Gosman, A. D., Pun, W. M., Runchal, A. K., Spalding, D., and Wolfshtein, M. Heat and Mass Transfer in Recirculating Flows. London: Academic Press, 1969.

50. Patankar, S. V., and Spalding, D. B. "A Calculation Procedure for Heat, Mass and Momentum Transfer in Three-Dimensional Parabolic Flows." Int. J. Heat Mass Transfer 15 (1972): 1787-1806.

51. Madavan, N. K. "Predictions of Incompressible Laminar Separated Flows Using the Partially-Parabolized Navier-Stokes Equations." M.S. Thesis. Iowa State University, Ames, Iowa, 1981.

52. Chiu, I. T. "Prediction of Laminar Flows over a Rearward-Facing Step Using the Partially-Parabolized Navier-Stokes Equations." M.S. Thesis. Iowa State University, Ames, Iowa, 1984.

53. Reyhner, T. A., and Flugge-Lotz, I. "The Interaction of a Shock Wave with a Laminar Boundary Layer." Int. J. Nonlinear Mech. 3 (1968): 173-199.

54. Denham, M. K. "The Development of a Laser Anemometer for Recirculating Fluid Flow Measurements." Ph.D. Thesis. University of Exeter, Great Britian, 1974.

55. Gosman, A. D., and Pun, W. M. Lecture notes for course entitled: "Calculation of Recirculating Flow." Heat Transfer Rep HTS/74/2. Imperial College, London, 1974.

56. Drewry, J. E. "Fluid Dynamic Characterization of Sudden Expansion Ramjet Combustor Flowfields." AIAA J. 16 (1978): 313-319.

57. Kangovi, S. and Page, R. H. "Subsonic Turbulent Flow Past a Downstream Facing Annular Step." ASME Paper No. 78-WA/FE-15, 1978.

58. Ha Minh, H. H, and Chassaing, P. "Perturbations of Turbulent Pipe Flows." In Turbulent Shear Flows I, pp. 178-197. New York: Springer-Verlag, 1979.

59. Mehta, P. R. "Separated Flow Through Large Sudden Expansions." J. Hyd. Div. ASCE 107 (1981): 451-460.

60. Abbot, D. E., and Kline, S. J. "Experimental Investigation of Subsonic Flow Over Single and Double Backward Facing Steps." J. Basic Engrg. 84 (1962): 317-325.

61. Chaturvedi, M. C. "Flow Characteristics of Axisymmetric Expansion." J. Hydraulics 89 (1963): 61-92.

62. Moon, L. F., and Rudinger, G. "Velocity Distributions in an Abruptly Expanding Circular Duct." J. Fluids Engrg. 99 (1977): 226-230.

63. Freeman, A. R. "Measurements of Velocity and Temperature in the Region Downstream of a Sudden Pipe Expansion." CEGB Report No. RD/B/N4306, July, 1978.

64. Smyth, R. "Turbulent Flow Over a Plane Symmetric Sudden Expansion." J. Fluids Engrg. 101 (1979): 348-353.

65. Lu, C. C. "Measurements of Turbulent Flow Velocity for Sudden Expansion Cylindrical Tube Using Laser Doppler Velocimenter (LVD)." AIChE J. 26 (1980): 303-305.

66. Stevenson, W. H., Thompson, H. D., Craig, R. R. "Laser Velocimeter Measurements in Highly Turbulent Recirculating Flows." J. Fluids Engrg. 106 (1984): 173-180.

67. Driver, D. M., and Seegmiller, H. L. "Features of a Reattaching Turbulent Shear Layer." AIAA Paper No. AIAA-82-1029, 1982.

68. Pronchick, S. W., and Kline, S. J. "An Experimental Investigation of the Structure of a Turbulent Reattaching Flow Behind a BackwardFacing Step." Report MD-42. Thermosciences Div., Mech. Engrg. Dept., Stanford University, Stanford, 1983.

69. Adams E. "Experiments on the Structure of Turbulent Reattaching Flow." Ph.D. Thesis. Stanford University, Stanford, 1984.

70. Cheun, B. S., Toy, N., and Moss, W. D. "The Effect of Upstream Boundary Layer Thickness Upon Flow Past a Backward-Facing Step." from the 1981 Conference at the University of Missouri-Rolla, 1981.

71. Moss, W. D., and Baker, S. "Recirculating Flows Associated with Two-Dimensional Steps." The Aeronautical Q. 31, No. 3 (1980): 151-172.

72. Chandrsuda, C., and Bradshaw, P. "Turbulence Structure of a Reattaching Mixing Layer." J. Fluid Mech. 110 (1981): 171-194.

73. Walterick, R. E., Jagoda, J. I., Richardson, C. R. C., DeGroot, W. A. Strahle, W. C., and Hubbartt, J. H. "Experiments and Computations on Two-Dimensional Turbulent Flow over a Backward-Facing Step." AIAA Paper No. AIAA-84-0013, 1984.

74. Vogel, J., and Eaton, J. P. "Heat Transfer and Fluid Mechanics Measurements in the Turbulent Reattaching Flow Behind a Backward-Facing Step." Report MD-44. Thermosciences Div, Mech. Engrg. Dept., Stanford University, Stanford, 1984.

75. Lamb, J. P., and McCotter, F. "Correlation of Mean Flow Parameters for Subsonic Recirculating Flows." ASME Paper No. 84-FE-8, 1984.

76. Simpson, R. L., Chew, Y. J., and Shivaprasad, B. G. "The Structure of a Separating Turbulent Boundary Layer, Part I: Mean Flow and Reynolds Stress." J. Fluid Mech. 113 (1981): 23-51.

77. Simpson, R. "A Model for the Backflow Mean Velocity Profile." AIAA J. 21, No. 1 (1983): 142-143.

78. Hanson F., and Richardson, P. "Mechanics of Turbulent Separated Flows as Indicated by Heat Transfer: A Review." from the ASME Symposium on Fully Turbulent Flows, New York, 1964.

79. Chilcott, R. E. "A Review of Separated and Reattaching Flows with Heat Transfer." Int. J. Heat and Mass Transfer 10 (1967): 783-797.

80. Fletcher, L. S., Briggs, D. G., and Page, R. H. "Heat Transfer in Separated and Reattached Flows: an Annotated Review." Israel J. Technology 12 (1974): 236-261.

81. Aung, W., and Watkins, C. B. "Heat Transfer Mechanisms in Separated Forced Convection." In Turbulent Forced Convection in Channels and Bundles - Theory and Applications to Heat Exchangers and Nuclear Reactors, pp. 233-256. Edited by S. Kakac and D. R. Spalding. Washington, D. C.: Hemisphere Pub. Corp., 1979.

82. Ede, A. J., Hislop, C. I., and Morris, R. "Effect on the Local Heat Transfer Coefficient in a Pipe of an Abrupt Disturbance of the Fluid Flow: Abrupt Convergence and Divergence of Dia. Ratio 2/1." Proceedings Institution Mech. Engineers 170, No. 38 (1956): 1113-1126.

83. Krall, K. M., and Sparrow, E. M. "Turbulent Heat Transfer in the Separated, Reattached and Redevelopment Regions of a Circular Tube." J. Heat Transfer 88, No. 1 (1966): 131-136.

84. Zemanick, P. P., and Dougall, R. S. "Local Heat Transfer Downstream of Abrupt Circular Channel Expansion." J. Heat Transfer 92 (1970): 53-60.

85. Runchal, A. K. "Mass Transfer Investigation in Turbulent Flow Downstream of Sudden Enlargement of a Circular Pipe for Very High Schmidt Numbers." Int. J. Heat and Mass Transfer 14 (1971): 781-791.

86. Back, L. H., Massier, P. F., and Roschke, E. J. "Partially Ionized Gas Flow and Heat Transfer in the Separation, Reattachment, and Redevelopment Regions Downstream of an Abrupt Circular Channel Expansion." J. Heat Transfer 94, No. 1 (1972): 119-127.

87. Kang, Y., Nishino, J., Suzuki, K., and Sato, T. "Applications of Flow and Surface Temperature Visualization Techniques to a Study of Heat Transfer in Recirculating Flow Regions." In Flow Visualization II. Edited by Wolfgang Merzkich. W. Germany: Hemisphere Pub. Corp., 1980.

88. Sparrow, E. M., and O'Brien, J. E. "Heat Transfer Coefficients on the Downstream Face of an Abrupt Enlargement or Inlet Constriction in a Pipe." J. Heat Transfer 102 (1980): 408-414.

89. Amano, R. S., Jensen, M. K., and Goel, P. "A Numerical and Experimental Investigation of Turbulent Heat Transport Downstream from an Abrupt Pipe Expansion." J. Heat Transfer 105 (1983): 862-869.

90. Baughn, J. W., Hoffman, M. A., Takahashi, R. K., and Launder, B. E. "Local Heat Transfer Downstream of an Abrupt Expansion in a Circular Channel with Constant Wall Heat Flux." J. Heat Transfer 106 (1984): 789-796.

91. Filetti, E. G., and Kays, W. M. "Heat Transfer in Separated, Reattached, and Redevelopment Regions Behind a Double Step at Entrance to a Flat Duct." J. Heat Transfer 89 (1967): 163-167.

92. Seki, N., Fukusako, S., and Hirata, T. "Effect of Stall Length on Heat Transfer in Reattached Region Behind a Double Step at Entrance to an Enlarged Flat Duct." Int. J. Heat and Mass Transfer 19 (1976): 700-702.

93. Seki, N., Fukusako, S., and Hirata, T. "Turbulent Fluctuations and Heat Transfer for Separated Flow Associated with a Double Step at Entrance to an Enlarged Flat Duct." J. Heat Transfer 98 (1976): 588-593.

94. Seban, R. A., Emery, A., and Levy, A. "Heat Transfer to Separated and Reattached Subsonic Turbulent Flows Obtained Downstream of a Surface Step." J. Aero/Space Sciences 26 (1959): 809-814.

95. Seban, R. A. "Heat Transfer to the Turbulent Separated Flow of Air Downstream of a Step in the Surface of a Plate." J. Heat Transfer 86 (1964): 259-263.

96. Aung, W., and Goldstein, R. J. "Heat Transfer in Turbulent Separated Flow Downstream of a Rearward-Facing Step." Israel J. Technology 10 (1972): 35-41.

97. Kottke, V. "Heat, Mass and Momentum Transfer in Separated Flows." Int. J. Chem. Engrg. 24, No. 1 (1984): 86-94.

98. Sogin, H. "A Summary of Experiments on Local Heat Transfer from the Rear of Bluff Obstacles to a Low-Speed Airstream." J. Heat Transfer 86 (1964): 200-202.

99. Briggs, M., Mellor, G., and Yamada, T. "A Second Moment Turbulence Model Applied to Fully Separated Flows." In Turbulence in Internal Flows, pp. 249-281. Edited by S. N. B. Murthy. Washington, D. C.: Hemisphere Pub. Corp., 1977.

100. Le Balleur, J. C., and Mirande, J. "Experimental and Theoretical Study of Two-Dimensional Turbulent, Incompressible Reattachment." AGARD Conference Proceeding, No. 168 (1975): 17.1-17.13.

101. Kim, J., Kline, S. J., and Johnston, J. P. "Investigation of Separation and Reattachment of a Turbulent Shear Layer: Flow over a Backward-Facing Step." Report MD-37. Thermosciences Div., Mech. Engrg. Dept., Stanford University, Stanford, 1978.

102. Ha Minh, H., and Chassaing, P. "Some Numerical Prediction of Incompressible Turbulent Flows." In Numerical Methods in Laminar and Turbulent Flow, pp. 287-300. Edited by C. Taylor, K. Morgan, and C. A. Brebbia. New York: John Wiley & Sons, 1978.

103. Gosman, A. D., Khail, E. E., and Whitelaw, J. H. "The Calculation of Two-Dimensional Turbulent Recirculating Flows." Paper Presented at Symposium of Turbulent Shear Flows, Pennsylvania State Univ., 1977.

104. Oliver, A. J. "A Finite Difference Solution for Turbulent Flow and Heat Transfer over a Backward Facing Step in an Annular Duct." In Numerical Methods in Laminar and Turbulent Flow, pp. 467-478. Edited by C. Taylor, K. Morgan, and C. A. Brebbia. New York: John Wiley & Sons, 1978.

105. Mehta, P. R. "Flow Characteristics in Two-Dimensional Expansions." J. Hydraulics 105 (1979): 501-517.

106. Atkins, D. J., Maskell, S. J., and Patrick, M. A. "Numerical Predictions of Separated Flows." Int. J. Numerical Methods in Engrg. 15 (1980): 129-144.

107. Kim, J., Kline, S. J., and Johnston, J. P. "Investigations of a Reattaching Turbulent Shear Layer: Flow over a Backward-Facing Step." J. Fluids Engrg. 102, No. 3 (1980): 302-308.

108. Lokrou, V. P., and Shen, H. W. "Analysis of the Characteristics of Flow in Sudden Expansion by Similarity Approach." J. Hydraulic Research 21, No. 2 (1983): 119-132.

109. Sindir, M. M. "Effects of Expansion Ratio on the Calculation of Parallel-Walled Backward-Facing Step Flows: Comparison of Four Models of Turbulence." ASME Paper No. 83-FE-10, 1983.

110. Sindir, M. M. "Calculation of Deflected-Walled Backward-Facing Step Flows: Effects of Angle of Deflection on the Performance of Four Models of Turbulence." ASME Paper No. 83-FE-16, 1983.

111. Chieng, C. C., and Launder, B. E. "On the Calculation of Turbulent Heat Transport Downstream from an Abrupt Pipe Expansion." Numerical Heat Transfer 3 (1980): 189-207.

112. Srinivas, K. and Fletcher, C. A. J. "Eddy Viscosity Models for Wakes and Separated Flows." AIAA J. 22, No. 1 (1984): 147-148.

113. Johnson, R. W., and Launder, B. E. "Discussion of 'On the Calculation of Turbulent Heat Transport Downstream from an Abrupt Pipe Expansion'." Numerical Heat Transfer 5 (1982): 493-496.

114. Kang, Y., and Suzuki, K. "Numerical Study of Wall Heat Transfer in Recirculating Flow Region of a Confined Jet." Heat Transfer - Japanese Research 11, No. 1 (1982): 44-69.

115. Watkins, C. B., and Gooray, A. M. "Numerical Calculations of Turbulent Recirculating Heat Transfer Beyond Two-Dimensional Back-Steps and Sudden Pipe Expansions." Final Report ONR Contract No. N0014-80C-0545, Howard University, 1982.

116. Gooray, A. M., Watkins, C. B., and Aung, W. "k-ε Calculations of Heat Transfer in Redeveloping Turbulent Boundary Layers Downstream of Reattachment." J. Heat Transfer 107 (1985): 70-76.

117. Jones, W. P., and Launder, B. E. "The Prediction of Laminarization with a 2-Equation Model of Turbulence." Int. J. Heat Mass Transfer 15 (1972): 301-313.

118. Chieng, C. C. "An Investigation of Turbulence Modeling for the Abrupt Pipe Expansion." ASME Paper 83-FE-15, 1983.

119. Amano, R. S. "A Study of Turbulent Flow Downstream of an Abrupt Pipe Expansion." AIAA J. 21, No. 10 (1938): 1400-1405.

120. Boussinesq, J. "Theorie de l'écoulement tourbillant." Mém. prés. Acad. Sci. 23 (1877): 46.

121. Johnson, D. A, and King, L. S. "A New Turbulence Closure Model for Boundary Layer Flows with Strong Adverse Pressure Gradients and Separation." AIAA Paper No. AIAA-84-0175, 1984.

122. Hinze, J. O. Turbulence. 2nd edition. New York: McGraw-Hill, 1975.

123. Cebeci, T., and Smith, A. M. O. Analysis of Turbulent Boundary Layers. New York: Academic Press, 1974.

124. Bird, R. B., Stewart, W. E., and Lightfoot, E. N. Transport Phenomena. New York: John Wiley & Sons, 1960.

125. Keenan, J. H., Frederick, C. K., Hill, P. G., and Moore, J. G. Steam Tables (SI Units). New York: John Wiley & Sons, 1978.

126. van Driest, E. R. "On Turbulent Flow near a Wall." J. Aeronautical Sciences 23 (1956): 1007-1011,1036.

127. Kays, W. M., and Crawford, M. E. Convective Heat and Mass Transfer. 2nd edition. New York: McGraw-Hill, 1980.

128. Reeves, B. L. "Two-Layer Model of Turbulent Boundary Layers." AIAA J. 12 (1974): 932-939.

129. McD Galbraith, R. A., and Head, M. R. "Eddy Viscosity and Mixing Length from Measured Boundary-Layer Developments." Aeronautical Q. 26 (1975): 133-154.

130. Carter, J. E., and Wornom, S. F. "Solutions for Incompressible Separated Boundary Layers Including Viscous-Inviscid Interaction." NASA Report No. NASA SP 347, 1975.

131. Pletcher, R. H. "Prediction of Incompressible Turbulent Separating Flow." J. Fluid Mech. 100 (1978): 427-433.

132. Kays, W. M., and Moffat, R. J. In Studies in Convection, Vol. 1, pp. 213-319. London: Academic Press, 1975.

133. Launder, B. E., and Spalding, D. B. "The Numerical Computation of Turbulent Flow." Computer Methods in Applied Mech. and Engrg. 3 (1974): 269.

134. Launder, B. E. "On the Effect of a Gravitational Field on the Turbulent Transport of Heat and Momentum." J. Fluid Mech. 67 (1975): 569-581.

135. Chien, K. Y. "Predictions of Channel and Boundary-Layer Flows with a Low-Reynolds-Number Turbulence Model." AIAA J. 20, No. 1 (1982): 33-38.

136. Gibson, M. M., and Launder, B. E. "On the Calculation of Horizontal Turbulent Free Shear Flow Under Gravitational Influence." J. Heat Transfer 98 (1976): 81-87.

137. Launder, B. E., Reece, G. J., and Rodi, W. "Progress in the Development of a Reynolds Stress Turbulence Closure." J. Fluid Mech. 68, No. 3 (1975): 537-566.

138. Roberts, G. O. "Computational Meshes for Boundary Layer Problems." Proceedings Second Int. Conf. Num. Methods Fluid Dyn. Lecture Notes in Physics, Vol. 8, pp. 171-177. New York: Springer-Verlag, 1971.

139. Patankar, S. V. Numerical Heat Transfer and Fluid Flow. Washington, D. C.: Hemisphere Pub. Corp., 1980.

140. Blottner, F. G. "Variable Grid Scheme Applied to Turbulent Boundary Layers." Computer Methods in Applied Mech. and Engrg. 4 (1974): 179-194.

141. Blottner, F. G. "Numerical Solution of Slender Channel Laminar Flows." Computer Methods in Applied Mech. and Engrg. 11, No. 3 (1977): 319-339.

142. Chiu, I. T. Personal Communication. Mech. Engrg. Dept., Iowa State University, Ames, Iowa, 1984.

143. Moffat, H. K. "Viscous and Resistive Eddies near a Sharp Corner." J. Fluid Mech. 18 (1964): 1-18.

144. Brady, J. F., and Acrivos, A. "Closed-Cavity Laminar Flows at Moderate Reynolds Numbers." J. Fluid Mech. 115 (1982): 427-442.

145. Cebeci, T. "Finite-Difference Solution of Boundary-Layer Flows with Separation." Report ME-84-4. Dept. Mech. Engrg., California State Univ., Long Beach, 1984.

146. Bankston, C. A., and McEligot, D. M. "Turbulent and Laminar Heat Transfer to Gases with Varying Properties in the Entry Region of Circular Ducts." Int. J. Heat and Mass Transfer 13 (1970): 319-344.

147. Thermophysical Properties of Refrigerants. New York: ASHRAE, 1973.

VII. ACKNOWLEDGMENTS

This work was financially supported by the National Aeronautics and Space Administration (NASA Training Grant No. NGT-016-002-801), the National Science Foundation (NSF Grant No MEA-8211713 redesignated as CBT-8211713), the Iowa State Engineering Research Institute, and the Iowa State University Mechanical Engineering Department.

VIII. APPENDIX A: VARIABLE PROPERTIES FOR AIR AND WATER

The equations used to approximate the properties of air and water as a function of temperature were taken from Thermophysical Properties of Refrigerants [145].

A. Air

The density of air is given by the perfect gas law

$$\rho(kg/m^3) = \frac{p}{RT} \tag{A.1}$$

where T is the absolute temperature, R is 287.0 J/(kg•K), and p is the pressure in Pascals.

The viscosity is approximated by

$$\mu(10^{-6}Ns/m^2) = \sqrt{T}/(0.671692 + 85.22974/T - 2111.475/T^2 + 106417/T^3) \tag{A.2}$$

for 60 < T < 1000 K. Equation (A.2) has a maximum deviation of ± 0.7% and an average deviation of ± 0.2%.

The thermal conductivity is given by

$$k(W/(m•K)) = \sqrt{T}/(A + B/T + C/T^2 + D/T^3) \tag{A.3}$$

where A, B, C, and D have the following values

Range (K)	A	B	C	D
80-300	385.859	9.11440×10^{4}	-2.68667×10^{6}	5.52604×10^{7}
300-600	328.052	1.67320×10^{5}	-3.02953×10^{7}	3.05682×10^{9}
600-1000	539.544	-3.32903×10^{5}	3.59756×10^{8}	-9.67202×10^{10}

The maximum error of Equation (A.3) is ± 0.23%.

The specific heat at one atmosphere is given by

$$c_p(kJ/(kg \cdot K)) = A + BT + CT^2 + DT^3 \qquad (A.4)$$

The constants in Eq. (A.4) have the following values

Range (K)	A	B	C	D
90-260	1.03200	-1.22500×10^{-4}	0.0	0.0
260-610	1.04466	-3.15967×10^{-4}	7.07909×10^{-7}	-2.70340×10^{-10}
610-900	1.00205	-1.62983×10^{-4}	5.69525×10^{-7}	-2.68081×10^{-10}

Equation (A.4) is accurate to within ± 0.018% for T > 260 K and accurate to within ± 0.8% for T < 260 K.

B. Water

Water is considered an incompressible fluid with ρ equal to 995.6 kg/m^3.

The viscosity of water is highly temperature dependent. The recommended equation is

$$\mu(10^{-3}Ns/m^2) = e^{(A + B/T + C/T^2)} \qquad (A.5)$$

the constants are

Range (K)	A	B	C
273-350	0.030185	-2191.60	6.38605×10^5
350-500	-3.22950	13.18574	2.65531×10^5
500-620	-8.77361	5875.8	-1.28275×10^5

The maximum deviation of Eq. (A.5) is ± 1.5% from measured values.

The thermal conductivity of water can be approximated by

$$k(W/(m\cdot K)) = A + BT + CT^2 + DT^3 \qquad (A.6)$$

to within ± 0.19% with the following constants

Range (K)	A	B	C	D
273-400	-0.61694	7.17851×10^{-3}	-1.16700×10^{-5}	4.70358×10^{-9}
400-600	-0.14532	4.02217×10^{-3}	-4.64993×10^{-6}	-4.89257×10^{-10}

The following equation gives the specific heat of water for 237 < T < 450 K to within ± 0.13%.

$$c_p(kJ/(kg\cdot K)) = 17.6611 - 0.147914T + 6.08619\times10^{-4}T^2 - 1.11867\times10^{-6}T^3 + 7.80297\times10^{-10}T^4 \qquad (A.7)$$

IX. APPENDIX B: RESULTING COEFFICIENTS FROM THE DISCRETIZATION OF THE MOMENTUM AND CONTINUITY EQUATIONS (u-ψ VARIABLES)

The coefficients in the continuity equation are

$$e_j = b_j = \frac{1}{2}(\rho^i_{j-\frac{1}{2}} r_{j-\frac{1}{2}} \Delta y_-)$$

The coefficients of Eq. (3.14) when the FLARE approximation is in use or when u is nonnegative ($j \neq NJ$) are

$$A_j = \frac{1}{\theta_j \Delta y_+}\left(\frac{\Delta y_-}{\Delta x_-}(\psi^i_j - \hat{\psi}_j) - \frac{2}{\Delta y_+}\left[\Delta y_- r_{j+\frac{1}{2}} M_{j+\frac{1}{2}} + M_j r_j (\Delta y_+ - \Delta y_-)\right]\right)$$

$$B_j = \frac{1}{\theta_j \Delta y_-}\left(\frac{\Delta y_+}{\Delta x_-}(\hat{\psi}_j - \psi^i_j) - \frac{2}{\Delta y_-}\left[\Delta y_+ r_{j-\frac{1}{2}} M_{j-\frac{1}{2}} - M_j r_j (\Delta y_+ - \Delta y_-)\right]\right)$$

$$C_j = \frac{1}{\Delta x_-}\left[c\rho^i_j (\hat{u}_j)^2 + \frac{1}{\theta_j}\hat{\psi}_j \left(\frac{\Delta y_+}{\Delta y_-}\hat{u}_{j-1} - \frac{\Delta y_-}{\Delta y_+}\hat{u}_{j+1} - \beta \hat{u}_j\right)\right]$$

$$D_j = \frac{1}{\Delta x_-}\left[c\rho^i_j (2\hat{u}_j - u^i_j) - \frac{\beta}{\theta_j}(\hat{\psi}_j - \psi_j{}^i)\right] +$$

$$\frac{2}{\theta_j}\left(\frac{\Delta y_-}{\Delta y_+^2} r_{j+\frac{1}{2}} M_{j+\frac{1}{2}} - \frac{\beta^2}{(\Delta y_+ + \Delta y_-)} M_j r_j + \frac{\Delta y_+}{\Delta y_-^2} r_{j-\frac{1}{2}} M_{j-\frac{1}{2}}\right)$$

$$E_j = \frac{1}{\theta_j \Delta x_-}\left(\frac{\Delta y_+}{\Delta y_-}\hat{u}_{j-1} - \frac{\Delta y_-}{\Delta y_+}\hat{u}_{j+1} - \beta \hat{u}_j\right)$$

$$H_j = 1.0$$

$$\beta = \left(\frac{\Delta y_+}{\Delta y_-} - \frac{\Delta y_-}{\Delta y_+}\right) \qquad \text{(B.1)}$$

$$\theta_j = r_j(\Delta y_+ + \Delta y_-) \qquad \text{(B.2)}$$

After the first global iteration, if u is negative the coefficients of Eq. (3.14) are

$$A_j = \frac{1}{\theta_j \Delta y_+}\left(\frac{\Delta y_-}{\Delta x_-}(\hat{\psi}_j - \psi^{i+2}_j) - \frac{2}{\Delta y_+}\left[\Delta y_- r_{j+\frac{1}{2}} M_{j+\frac{1}{2}} + M_j r_j (\Delta y_+ - \Delta y_-)\right]\right)$$

$$B_j = \frac{1}{\theta_j \Delta y_-}\left(\frac{\Delta y_+}{\Delta x_+}(\psi_j^{i+2} - \hat{\psi}_j) - \frac{2}{\Delta y_-}\left[\Delta y_+ r_{j-\frac{1}{2}} M_{j-\frac{1}{2}} - M_j r_j (\Delta y_+ - \Delta y_-)\right]\right)$$

$$C_j = \frac{1}{\Delta x_+}\left(\rho_j^i (\hat{u}_j)^2 + \frac{1}{\theta_j}\hat{\psi}_j \left(\frac{\Delta y_+}{\Delta y_-}\hat{u}_{j-1} - \frac{\Delta y_-}{\Delta y_+}\hat{u}_{j+1} - \beta \hat{u}_j\right)\right)$$

$$D_j = \frac{1}{\Delta x_+}\left[\rho_j^i (u_j^{i+2} - 2\hat{u}_j) + \frac{\beta}{\theta_j}(\hat{\psi}_j - \psi_j^{i+2})\right] +$$

$$\frac{2}{\theta_j}\left(\frac{\Delta y_-}{\Delta y_+^2} r_{j+\frac{1}{2}} M_{j+\frac{1}{2}} - \frac{\beta^2}{(\Delta y_+ + \Delta y_-)} M_j r_j + \frac{\Delta y_+}{\Delta y_-^2} r_{j-\frac{1}{2}} M_{j-\frac{1}{2}}\right)$$

$$E_j = \frac{1}{\theta_j \Delta x_+}\left(\frac{\Delta y_+}{\Delta y_-}\hat{u}_{j-1} - \frac{\Delta y_-}{\Delta y_+}\hat{u}_{j+1} - \beta \hat{u}_j\right)$$

$$H_j = 1.0$$

β and θ_j are the same as in Eqs. (B.1) and (B.2).

For j=NJ, the coefficients of Eq. (3.14) are

$$A_{NJ} = E_{NJ} = 0.0$$

$$B_{NJ} = -\frac{2^{m+1}}{\Delta y_-^2} M_{NJ-\frac{1}{2}}$$

$$C_{NJ} = \frac{1}{\Delta x_-}\rho_{NJ}^i (\hat{u}_{NJ})^2$$

$$D_{NJ} = \frac{1}{\Delta x_-}\rho_j^i (2\hat{u}_{NJ} - u_{NJ}^i) + \frac{2^{m+1}}{\Delta y_-^2} M_{NJ-\frac{1}{2}}$$

$$H_{NJ} = 1.0$$

X. APPENDIX C: MODIFIED THOMAS ALGORITHM

Upon reducing Eq. (3.20) to an upper triangular matrix, the diagonal submatrices $[D]_j^*$ and right hand vector of knowns $\{C\}_j^*$ are

$$[D]_j^* = \begin{bmatrix} D_j^* & E_j \\ e_j^* & -1 \end{bmatrix} ; \quad \{C\}_j^* = \begin{Bmatrix} H_j^* \chi + C_j^* \\ G_j \chi + d_j \end{Bmatrix}$$

E_j remains unchanged from the value given in Appendix B. The modified coefficients in terms of the coefficients of Appendix B are (j=2,NJ)

$$D_j^* = \gamma B_j A_{j-1} + D_j \tag{C.2}$$

$$e_j^* = \gamma A_{j-1}(b_j + e_{j-1}^*) + e_j \tag{C.3}$$

$$H_j^* = \gamma B_j (H_{j-1}^* + E_{j-1} G_{j-1}) + H_j \tag{C.4}$$

$$C_j^* = \gamma B_j (C_{j-1}^* E_{j-1} d_{j-1}) + C_j \tag{C.5}$$

$$G_j = \gamma [H_{j-1}^* (b_j + e_{j-1}^*) + G_{j-1}(b_j E_{j-1} - D_{j-1}^*)] \tag{C.6}$$

$$d_j = \gamma [C_{j-1}^* (b_j + e_{j-1}^*) + d_{j-1}(b_j E_{j-1} - D_{j-1}^*)] \tag{C.7}$$

$$\gamma = -1/(D_{j-1}^* + e_{j-1}^* E_{j-1}) \tag{C.8}$$

A_j and E_j are unchanged by the transformation to upper triangular form so are not starred.

The boundary conditions at the wall are used to determine the coefficients for j=1. The following is true for j=1,

$$\begin{bmatrix} D_1^* & E_1 \\ e_1^* & -1 \end{bmatrix} \begin{Bmatrix} u_1^{i+1} \\ \psi_1^{i+1} \end{Bmatrix} + \begin{bmatrix} A_1 & 0 \\ 0 & 0 \end{bmatrix} \begin{Bmatrix} u_2^{i+1} \\ \psi_2^{i+1} \end{Bmatrix} = \begin{Bmatrix} H_1^* \chi + C_1^* \\ 0 \end{Bmatrix} \tag{C.9}$$

Since $U_1^{i+1} = \psi_1^{i+1} = 0$, D_1^*, E_1, and e_1^* are arbitrary, they are set equal to 1. A_1, H_1^*, C_1^*, c_1^*, G_1, and $d_1 = 0$ cause Eq. (C.9) to be satisfied. Now that the coefficients for j=1 are specified, Eqs. (C.2) through (C.8) can be evaluated starting with j=2 and continuing until j=NJ.

Solving the reduced continuity and momentum equations for j=NJ (Eq. 3.24) gives the following expressions for u_{NJ}^{i+1} and χ.

$$u_{NJ}^{i+1} = [(E_{NJ}G_{NJ}+H_{NJ}^*)\psi_{NJ} - G_{NJ}C_{NJ}^* + d_{NJ}H_{NJ}^*]/(e_{NJ}^*H_{NJ}^* - G_{NJ}D_{NJ}^*)$$

$$\chi = (e_{NJ}^* u_{NJ}^{i+1} - \psi_{NJ} - d_{NJ})/G_{NJ}^*$$

Back substitution is now used to solve for the unknowns u_j^{i+1} and ψ_j^{i+1} for $2<j<NJ-1$ with the following expressions

$$u_j^{i+1} = [(H_j^*+E_jG_j)\chi - A_j u_{j+1}^{i+1} + C_j^* + E_j d_j](D_j^*+E_j e_j^*)$$

$$\psi_j^{i+1} = e_j^* u_j^{i+1} - G_j\chi - d_j$$

XI. APPENDIX D: RESULTING COEFFICIENTS FROM THE DISCRETIZATION OF THE ENERGY, k, AND ε EQUATIONS

The coefficients of Eqs. (3.26) and (3.31) using the FLARE approximation and when u is positive are

$$a_j = -\frac{1}{\theta_j \Delta y_+}\left[\frac{\Delta y_-}{\Delta x_-}(\psi_j^{i+1}-\psi_j^i) + P_1\right]$$

$$b_j = \frac{1}{\theta_j \Delta y_-}\left[\frac{\Delta y_+}{\Delta x_-}(\psi_j^{i+1}-\psi_j^i) - P_2\right]$$

$$c_j = \frac{1}{\Delta x_-} c\rho_j^i u_j^{i+1}\phi_j^i + S_{\phi,c}$$

$$d_j = \frac{1}{\Delta x_-}\left[c\rho_j^i u_j^{i+1} - \frac{\beta}{\theta_j}(\psi_j^{i+1}-\psi_j^i)\right] + P_3 - S_{\phi,d}$$

$$P_1 = \frac{2}{\Delta y_+}\left[\Delta y_- r_{j+\frac{1}{2}}\Gamma_{\phi,j+\frac{1}{2}} + (\Delta y_+ - \Delta y_-)\Gamma_{\phi,j} r_j\right]$$

$$P_2 = \left[\frac{2}{\Delta y_-}\Delta y_+ r_{j-\frac{1}{2}}\Gamma_{\phi,j-\frac{1}{2}} - (\Delta y_+ - \Delta y_-)\Gamma_{\phi,j} r_j\right]$$

$$P_3 = \frac{2}{\theta_j}\left[\frac{\Delta y_-}{\Delta y_+^2} r_{j+\frac{1}{2}}\Gamma_{\phi,j+\frac{1}{2}} - \frac{1}{\Delta y_+ + \Delta y_-}\beta^2 \Gamma_{\phi,j} r_j + \frac{\Delta y_+}{\Delta y_-^2} r_{j-\frac{1}{2}}\Gamma_{\phi,j-\frac{1}{2}}\right]$$

where β and θ_j are the same as in Eqs. (B.1) and (B.2) and ϕ takes the value of H, k or ε depending on the transport equation being solved.

The source terms for the cases when ϕ is k or ε are given in Section III.B.6.1. For the energy equation,

$$S_{H,c} = \frac{1}{\theta_j}\left(\frac{\Delta y_-}{\Delta y_+^2} r_{j+\frac{1}{2}} L_{j+\frac{1}{2}}\left[(u_{j+1}^{i+1})^2 - (u_j^{i+1})^2\right] + \frac{1}{\Delta y_+ + \Delta y_-}\beta L_j r_j\left[\frac{\Delta y_-}{\Delta y_+}(u_{j+1}^{i+1})^2 + \beta(u_j^{i+1})^2 - \frac{\Delta y_+}{\Delta y_-}(u_{j-1}^{i+1})^2\right] - \frac{\Delta y_+}{\Delta y_-^2} r_{j-\frac{1}{2}} L_{j-\frac{1}{2}}\left[(u_j^{i+1})^2 - (u_{j-1}^{i+1})^2\right]\right)$$

$$S_{H,d} = 0.0$$

where $L = \Gamma_u - \Gamma_H$ as given in Table 4.

After the first iteration when the FLARE approximation was not used, the following coefficients apply when $u < 0$:

$$a_j = -\frac{1}{\theta_j \Delta y_+}\left[\frac{\Delta y_-}{\Delta x_+}(\psi_j^{i+2}-\psi_j^{i+1}) + P_1\right]$$

$$b_j = \frac{1}{\theta_j \Delta y_-}\left[\frac{\Delta y_+}{\Delta x_+}(\psi_j^{i+2}-\psi_j^{i+1}) - P_2\right]$$

$$c_j = -\frac{1}{\Delta x_+}\rho_j^i u_j^{i+1}\phi_j^{i+2} + S_{\phi,c}$$

$$d_j = -\frac{1}{\Delta x_+}\left[\rho_j^i u_j^{i+1} + \frac{\beta}{\theta_j}(\psi_j^{i+2}-\psi_j^{i+1})\right] + P_3 - S_{\phi,d}$$

P_1, P_2, P_3, $S_{\phi,c}$ and $S_{\phi,d}$ are defined above.

For j=NJ, the following set of coefficients apply

$$a_{NJ} = 0\ 0$$

$$b_{NJ} = -\frac{1}{\Delta y_-^2} 2^{m+1}\Gamma_{\phi,j-\frac{1}{2}}$$

$$c_{NJ} = \frac{1}{\Delta x_-}\rho_j^i u_j^{i+1}\phi_j^i + S_{\phi,c}$$

$$d_{NJ} = \frac{1}{\Delta x_-}\rho_j^i u_j^{i+1} + \frac{1}{\Delta y_+^2} 2^{m+1}\Gamma_{\phi,j-\frac{1}{2}} - S_{\phi,d}$$

Equation (3.30) implements the wall boundary condition for the energy equation when a heat flux is specified. The coefficients are obtained from a three-point finite-difference approximation of $\partial T/\partial y$ and are given as follows:

$$d_1 = -\frac{2\Delta y_1+\Delta y_2}{\Delta y_1(\Delta y_1+\Delta y_2)}$$

$$a_1 = \frac{\Delta y_1+\Delta y_2}{\Delta y_1 \Delta y_2}$$

$$\lambda = - \frac{\Delta y_1}{\Delta y_2 (\Delta y_1 + \Delta y_2)}$$

$$c_1 = - \frac{q(x)}{\Gamma_{H,1}} + \frac{1}{2}[a_1 (u_2^{i+1})^2 + \lambda (u_3^{i+1})^2]$$

where

$$\Delta y_1 = y_2 - y_1 \; ; \; \Delta y_2 = y_3 - y_2$$

XII. APPENDIX E: RESULTING COEFFICIENTS FROM THE DISCRETIZATION OF THE MOMENTUM AND CONTINUITY EQUATIONS (U-V VARIABLES)

The coefficients of Eq. (3.42) are

$$A_j = \frac{1}{\Delta Y_+ + \Delta Y_-}\left(\hat{V}_j - \frac{2}{\Delta Y_+}\right) \tag{E.1}$$

$$B_j = -\frac{1}{\Delta Y_+ + \Delta Y_-}\left(\hat{V}_j - \frac{2}{\Delta Y_-}\right) \tag{E.2}$$

$$D_j = \frac{c}{\Delta X_-}(2\hat{U}_j - U_j^i) + \frac{2}{\Delta Y_+ + \Delta Y_-}\left(\frac{1}{\Delta Y_+} + \frac{1}{\Delta Y_-}\right) \tag{E.3}$$

$$C_j = \frac{c}{\Delta X_-}(\hat{U}_j)^2 - \frac{1}{\Delta Y_+ + \Delta Y_-}(-\hat{U}_{j+1}\hat{V}_j + \hat{U}_{j-1}\hat{V}_j) \tag{E.4}$$

$$E_j = \frac{1}{\Delta Y_+ + \Delta Y_-}(\hat{U}_{j+1} - \hat{U}_{j-1}) \tag{E.5}$$

$$H_j = 1.0 \tag{E.6}$$

$$b_j = e_j = \frac{\Delta Y_-}{2\Delta X_-} \tag{E.7}$$

$$d_j = b_j(U_j^i + U_{j-1}^i) \tag{E.8}$$

$$G_j = 0.0 \tag{E.9}$$

Equations (E.1) through (E.9) are valid for j=1 to NJ except that B_{NJ} is twice the value given by Eq. (E.2).

After the system of equations (Eq. 3.41) is reduced to upper triangular form, the elements of $[D]_j^*$ and $\{C\}_j^*$ are

$$D_j^* = D_j - \frac{1}{\delta}A_{j-1}B_j$$

$$e_j^* = e_j - \frac{1}{\delta}A_{j-1}(e_j + e_{j-1}^*)$$

$$H_j^* = H_j - \frac{1}{\gamma}B_j(H_{j-1}^* - G_{j-1}^* E_{j-1})$$

$$C_j^* = C_j - \frac{1}{\gamma}B_j(C_{j-1}^* - d_{j-1}^* E_{j-1})$$

$$G_j^* = G_j - \frac{1}{\gamma}[e_j(H_{j-1}^* - G_{j-1}^* E_{j-1}) + (e_{j-1}^* H_{j-1}^* - D_{j-1}^* G_{j-1}^*)]$$

$$d_j^* = d_j - \frac{1}{\gamma}[e_j(C_{j-1}^* - d_{j-1}^* E_{j-1}) + (e_{j-1}^* C_{j-1}^* - D_{j-1}^* d_{j-1}^*)]$$

$$\gamma = D_{j-1}^* - E_{j-1} e_{j-1}^*$$

The above equations give the modified coefficients at the j level as a function of those at the j-1 level. A_j and E_j are not affected by the change to upper triangular form. Those for j=1 are found from the boundary conditions $U_1^{i+1}=V_1^{i+1}=0$. Taking A_1^*, H_1^*, C_1^*, G_1^*, d_1^*, E_1^*, and e_1^* all equal to zero and D_1^* equal to one satisfies the boundary conditions.

After reducing the coefficient matrix to block upper triangular form, Eq. (3.43) with j=NJ is used to solve for U_{NJ}^{i+1} and β. The result is

$$U_{NJ}^{i+1} = (d_{NJ}^* H_{NJ}^* - C_{NJ}^* G_{NJ}^*)/(e_{NJ}^* H_{NJ}^* - D_{NJ}^* G_{NJ}^*)$$

$$\beta = (e_{NJ}^* U_{NJ}^{i+1} - d_{NJ}^*)/G_{NJ}^*$$

After knowing β and U_{NJ}^{i+1}, back substitution can be used to find the rest of the Us and Vs for j=NJ-1 to j=2. U_j^{i+1}, and V_j^{i+1} are given by

$$U_j^{i+1} = \frac{1}{\Omega}[-A_j U_{j+1}^{i+1} + (H_j^* - E_j G_j^*)\beta + C_j^* - E_j d_j^*]$$

$$V_j^{i+1} = \frac{1}{\Omega}[e_j^* A_j U_{j+1}^{i+1} + (\Omega G_j - e_j^*(H_j^* - E_j G_j^*))\beta +$$
$$d_j^* \Omega - e_j^*(C_j^* - E_j d_j^*)]$$

$$\Omega = D_j^* - E_j e_j^*$$

XIII. APPENDIX F: Y-GRID STRETCHING TRANSFORMATIONS

The inverses of the general stretching transformations of Roberts [138] as cited in Anderson et al. [4] were used to transform a uniform grid spacing (ζ-space, $\Delta\zeta$ = constant) to a nonuniform grid spacing (y-space). The x = 0 line was divided into two regions, the step face and the inlet region. In both of these regions, $0 \le \zeta \le 1$.

Along the face of the step, $0 \le y \le h$, the transformation was given by

$$y = \left\{ \frac{(\sigma+1)\left(\frac{\sigma+1}{\sigma-1}\right)^{(2\zeta-1)} - \sigma + 1}{2\left[1 + \left(\frac{\sigma+1}{\sigma-1}\right)^{(2\zeta-1)}\right]} \right\} h$$

At the inlet, $h < y \le y_{NJ}$, the transformation was

$$y = \left\{ \frac{\sigma+1 - (\sigma-1)\left(\frac{\sigma+1}{\sigma-1}\right)^{(1-\zeta)}}{\left(\frac{\sigma+1}{\sigma-1}\right)^{(1-\zeta)} + 1} \right\} r_i + h$$

The values of NJ, σ, and the number of grid points below the lip of the step (y = h) were adjusted until there was a smooth variation of Δy near y = h and enough grid points near the wall to resolve the laminar sublayer regions. The values of σ typically ranged from 1.005 to 1.05.